Effect of Austenite Deformation and Continuous Cooling on the Microstructural Evolution in a Microalloyed Steel

Haitao Zhao

Thesis submitted for the degree of Doctor of Philosophy

Department of Materials Science and Engineering
The University of Sheffield

September 2016

Abstract

In this thesis, the effect of various thermomechanical controlled processing parameters on the transformed microstructural evolution and grain refinement of an API X-80 high temperature processing steel was investigated by conducting plane strain compression tests followed by continuous cooling.

Increasing the strain magnitude below the recrystallisation-stop temperature ($T_{5\%}$) from 0 to 0.5 with a cooling rate of 20˚C/s, a transition from bainitic ferrite (BF) to acicular ferrite (AF) occurs and grain refinement, microhardness and martensite/retained austenite (M/A) constituent refinement is improved. Once the magnitude of strain2 is increased to 0.7, dynamic recrystallisation (DRX) and subsequent static recrystallisation/meta-dynamic recrystallisation (SRX/MDRX) were triggered, weakening the beneficial influences of the austenite deformation.

Applying continuous cooling with various cooling rates, ranging from 0.5˚C/s to 50˚C/s, to both fully recrystallised and fully unrecrystallised austenite, the effect of continuous cooling rate was investigated. Based on the results of the effects of austenite deformation and continuous cooling rate on AF transformation, the introduction of intragranular nucleation sites and halting of BF laths nucleated on austenite grain boundaries are found as two conditions that should be fulfilled for the occurrence of acicular ferrite transformation in pipeline steels.

The effect of prior-austenite grain size (PAGS) on the microstructural evolution from both recrystallised and unrecrystallised austenite was studied. For microstructures transformed from recrystallised austenite, increasing the PAGS from 22.3 μm to 62.8 μm, the morphology of the transformed BF microstructure is changed and the effective grain size is reduced. For microstructures transformed from unrecrystallised austenite, reducing the PAGS from 62.8 μm to 37.0 μm, the volume fraction of AF is increased and the effective grain size is reduced from 4.5 μm to 2.9 μm. However, further reducing the PAGS from 37.0

μm to 22.3 μm, there are not significant changes on the transformed microstructures and the grain refinement.

Acknowledgements

First and foremost, I would like to express my greatest appreciation to my supervisor, Dr Eric Palmiere, for his support, understanding, encouragement and guidance through all these years. When I encounter difficulties in research or in life, Eric always does his utmost to help and encourage me. Without him, I could not have completed this research project.

I am also greatly indebted to my second supervisor, Prof. Bradley Wynne. It is his help during those painful and helpless days that I will treasure for my life. Those inspiring discussions on crystallography and plasticity with him really help me gain a more thorough understanding of this research project.

I would like to thank Dr Peter Korgul, Dr Le Ma, Dr Peng Zeng, Mr. Michael Bell, Mr. Dean Haylock, Mr. Ian Watts and Dr Luke Marshall for trainings and helps on the works of microscopy and TMC testing.

Chinese scholarship council (CSC) and Companhia Brasileira de Metalurgia e Mineração (CBMM) are sincerely acknowledged for providing financial supports and experimental materials.

I would also like to acknowledge my fellow co-workers, Zhe Cui, Feng Qian and Omar Khalid, and all my friends in H6 and surface engineering research group for their helps and all the good times, meals and beers we had together.

Special thanks to my wife, Xin Gao who carries the burden of life and raises our child alone all these years. I own her so much that I cannot pay her back in my whole life. Words fail to convey my deepest appreciation to my parents for all the things they have done and sacrificed for me.

Finally, I would like to thank my son, Tianze Zhao. Your birth is the best gift in my life. This thesis is dedicated to you.

Nomenclature

ACC	Accelerated Cooling
AF	Acicular Ferrite
BF	Bainitic Ferrite
CB	Cell Block
CL	Confidence Level
CP	Close-Packed Plane
DBTT	Ductile-Brittle Transition Temperature
DQ	Direct Quenching
DRX	Dynamic Recrystallisation
DWTT	Drop Weight Tear Test
EBSD	Electron Backscattering Diffraction
EBSP	Electron Backscattering Diffraction Pattern
FCC	Face-Centred Cubic
FE	Finite Element
FEGSEM	Field Emission Gun Scanning Electron Microscope
FTTU	Fast Thermal Treatment Unit
GB	Granular Bainite
GNB	Geometrically Necessary Boundary
GND	Geometrically Necessary Dislocation
G-T	Greninger-Troiano
HAGB	High Angle Grain Boundary
HSLA	High Strength Low Alloy
HTP	High Temperature Processing
IAC	Interrupted Accelerated Cooling

IDB	Incidental Dislocation Boundary
IPF	Inverse Pole Figure
IPS	Invariant-Plane Strain
K-S	Kurdjumov-Sachs
LAGB	Low Angle Grain Boundary
LB	Lath Bainite
LEDS	Low Energy Dislocation Structures
LSCM	Laser Scanning Confocal Microscopy
M/A	Martensite/Retained Austenite
MDRX	Meta-Dynamic Recrystallisation
ND	Normal Direction
N-W	Nishiyama-Wasserman
ODF	Orientation Density Function
OM	Optical Microscopy
OR	Orientation Relationship
PA	Parent Austenite
PAGB	Prior-Austenite Grain Boundary
PAGS	Prior-Austenite Grain Size
PF	Polygonal Ferrite
PSC	Plane Strain Compression
QF	Quasi-Polygonal Ferrite
QST	Direct Quenching Plus Self-Tempering
RD	Rolling Direction
SEM	Scanning Electron Microscopy
SFE	Stacking Fault Energy
SRX	Static Recrystallisation
SSD	Statistically Stored Dislocation

TEM	Transmission Electron Microscopy
TMC	Thermomechanical Compression
TMCP	Thermomechanical Controlled Processing
TWIP	Twinning-Induced Plasticity
WF	Widmanstätten Ferrite
b	Burgers Vector
C_1	Constant
C_2	Constant
D	Austenite Grain Size
d	Grain Diameter
$D_{c10\%}$	Grain Size that 10% Area Fraction of Grains possessing a Size Greater than this Value
G	Shear Modulus
K	Constant
k_y	Constant
l_1	Average Slip Length for Statistically Stored Dislocations
l_2	Average Slip Length for Geometrically Necessary Dislocations
R	Reduction Ratio
s	Shear Strain
S_v	Effective Interfacial Area per Unit Volume
$S_v(DB)$	Total Area of Intragranular Planar Defects per Unit Volume
$S_v(GB)$	Total Area of Deformed Austenite Grain Boundary per Unit Volume
T	Temperature
$T_{5\%}$	Recrystallisation-Stop Temperature
$T_{95\%}$	Recrystallisation-Limit Temperature
v	Poisson's Ratio
α	Constant

β	Resistance of Grain Boundary Against Cleavage Fracture
δ	Dilation Strain
ΔG	Chemical Free Energy Change
ε	Deformation Strain
ε_c	Critical Strain of Dynamic Recrystallisation
ε_p	Peak Strain
ε_{ss}	Steady State Strain
ε_T	Minimum Strain for Meta-Dynamic Recrystallisation Becoming Dominant
θ	Boundary Disorientation Angle
ρ	Dislocation Density
ρ_g	Density of Geometrically Necessary Dislocations
ρ_s	Density of Statistically Stored Dislocations
σ	Flow Stress
σ_0	Friction Stress
σ_y	Yield Strength
τ	Mean Shear Stress Needed to Force Dislocation Past Each Other
τ_T	Shear Stress Driving the Motion of the Interface
Φ	Constant

Table of Contents

Chapter 1 Introduction

1.1 Thermomechanical controlled processing of microalloyed steels

Thermomechanical controlled processing (TMCP), including controlled rolling and accelerated cooling, has been widely applied to the production of microalloyed steels and has gained great commercial success. Through controlled rolling, austenite grains are refined and then heavily deformed at temperatures with no recrystallisation and minimum recovery to increase the density of nucleation sites for subsequent phase transformations. By applying accelerated cooling, medium to low-temperature transformation products are favoured to improve the strength. The addition of microalloy elements such as niobium, vanadium and titanium with very small amounts (<0.1wt%) can benefit the practical application of TMCP by retarding the restoration of deformed austenite and by increasing the hardenability, especially when niobium is added. In addition, fine precipitates of microalloy elements as carbides, nitrides or carbonitrides can significantly increase the strength.

The advances in TMCP techniques and alloy design of microalloyed steels have significantly promoted the development of pipeline steels. Pipeline steels have long been used for building pipelines to transport massive natural gas and oil from deposits to harbours and refineries [1]. By increasing the strength of pipeline steels, a significant pipe thickness reduction can be achieved which will markedly reduce the pipe weight, the building cost and the welding difficulty [2]. Even when the wall thickness is not the main concern, raising the pipeline steels strength can allow a higher operating transmission pressure which will promote the transmission efficiency and lower the cost. Thus, great efforts in the steel industry have been devoted to the development of high strength pipeline steels [3-5] and the pipeline steel grades progressed from API X60 to API X120 since

the 1970s as shown in Figure 1-1 (a), with yield strengths increasing from 420 MPa (60 ksi) to ~830 MPa (120 ksi) and microstructures evolving from ferrite-pearlite to bainite-martensite [6]. The representative stress-strain curves and types of transformation products for pipeline steels with different grades are shown in Figure 1-1 (b) [7].
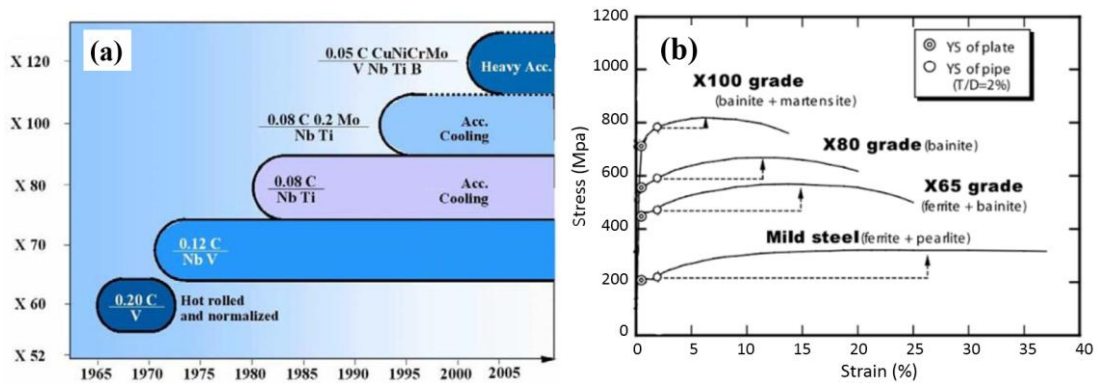
Figure 1-1 (a) Development history of pipeline steels [6], (b) representative stress-strain curves and microstructure components for pipeline steels with different grades [7].

1.2 Acicular ferrite in pipeline steels

It is clear from Figure 1-1 (a) that increasing hardenability and changing cooling conditions, and thus altering austenite decomposition products are necessary to meet the strength requirement. However, since many gas and oil exploitations have been undertaken in extreme conditions like severe low temperatures or deep seas [1], it is imperative that the increase in strength of pipeline steels is done so without compromising the toughness. A decrease in toughness will promote the stress-induced cracking especially in corrosive atmospheres, and will reduce the formability which will cause failures in the pipe shaping processes. Thus, high strength in association with high toughness is an important requirement for pipeline steels [3-5].

To meet this requirement, an optimal microstructure should be obtained during the steel plate production. Acicular ferrite (AF) dominant microstructures

2

provide more potential to improve the strengthening and toughening components, including grain refinement, dislocation density and easily controlled precipitation hardening, than those obtainable in ferrite-pearlite microstructure [8]. As a result, pipeline steels with an acicular ferrite (AF) microstructure possess a better property combination (e.g., higher strength [9], better toughness [9], superior H_2S resistance [10], and better fatigue behaviour [11]) than those steels exhibiting a ferrite-pearlite microstructure. Additionally, the strength associated with an AF microstructure is relatively lower than that of a bainitic ferrite (BF) microstructure, but the toughness of an AF microstructure is considerably higher [12].

Although there have been extensive investigations on the AF microstructure since the 1970s and API X80 pipeline steels with an AF dominant microstructure have already been successfully used to build several pipeline projects, there are still many unclear aspects of AF microstructures, including the transformation mechanism and the formation conditions. Knowledge of these aspects is necessary to understand the reason for the good strength and toughness of the AF microstructure and to further improve its properties.

1.3 Aim and scope of this thesis

The aim of this thesis is to investigate the effects on the microstructure evolution, especially AF transformation, of various TMCP parameters, including austenite deformation, continuous cooling rates and austenite grain sizes. Not only their individual effects but also their combined influences were studied. Along with the discussion on the influences of these TMCP parameters, the conditions for the occurrence of AF microstructure in pipeline steels were analysed and the related implications on the industrial production were also provided. In order to achieve these purposes, the layout of this thesis is presented as follows:

Chapter 2 presents a literature review on various aspects of the background

necessary for this thesis. Firstly, the thermomechanical controlled processing of high strength low alloy (HSLA) steels is illustrated generally. After that, several physical metallurgy phenomena related to this thesis are introduced, covering the hot deformation of austenite, the decomposition of supercooled austenite and the characteristics of acicular ferrite in different microstructures. Finally, the crystallography characteristics of BF microstructure are briefly explained.

Chapter 3 mainly introduces the material used in this thesis, which is a high temperature processing (HTP) pipeline steel, together with the experimental apparatuses. The microscopy techniques adopted in this thesis to characterise microstructures are also presented and emphasis is placed on the description of the electron backscattering diffraction (EBSD) mapping and the post-processing procedures for EBSD data. In the end, the as-received microstructure of the tested steel is characterised.

Chapter 4 discusses the effect of austenite deformation below the recrystallisation-stop temperature ($T_{5\%}$) on the austenite restoration behaviour, the evolution of transformed microstructures and the grain refinement. The possible nucleation mechanism of AF is presented and the importance of AF transformation on grain refinement is also emphasized.

Chapter 5 is concerned with the influence of different continuous cooling rates, for both recrystallised austenite and deformed austenite, on the evolution of transformed microstructures and the grain refinement. The conditions for the occurrence of AF transformation are proposed and explained in terms of the mechanical stabilisation of austenite. Subsequently, the impact of cooling rates on the grain refinement effect of austenite deformation is presented.

Chapter 6 presents the effect of different austenite grain sizes, for both recrystallised austenite and deformed austenite, on the evolution of transformed microstructures and the grain refinement. Austenite with different grain sizes are generated before the continuous cooling or the finishing deformation, by altering the heat treatment time and the roughing deformation magnitude. Possible

4

mechanisms that are responsible for the differences in morphologies of the transformed microstructures with different austenite grain sizes are proposed.

Chapter 7 concludes the main findings of this thesis based on the result of each chapter. Chapter 8 suggests the possible work that could be done in the future to complete the results and testify the mechanisms proposed in this thesis.

Chapter 2 Background

2.1 Introduction

In this chapter, a literature review on various aspects of the background necessary for this thesis is presented. First, the thermomechanical controlled processing of high strength low alloy (HSLA) steels is illustrated in general terms. After that, several physical metallurgy phenomena related to this thesis are introduced, covering the hot deformation of austenite, the decomposition of supercooled austenite and the characteristics of acicular ferrite in different microstructures. Finally, the crystallography characteristics of BF microstructure are briefly explained.

2.2 Overview of TMCP for HSLA steels

Based on the well-acknowledged Hall-Petch equation [13, 14], the yield strength σ_y can be expressed as:

$$\sigma_y = \sigma_0 + k_y d^{-\frac{1}{2}} \tag{2.1}$$

where σ_0 is the friction stress , d the grain diameter and k_y a positive constant of yielding related to the stress required to extend activities of dislocations to adjacent grains. Furthermore, when polygonal ferrite dominates the final microstructure, the ductile-brittle transition temperature (DBTT) can be expressed as:

$$T = \alpha - \beta d^{-\frac{1}{2}} \tag{2.2}$$

where α is a constant depending on the chemical composition and β is the resistance of a grain boundary against the progress of cleavage fracture [15]. From the above two relationships, it is clear that unlike other strengthening mechanisms, grain refinement not only increases the strength but also improves the toughness.

The aim of TMCP for HSLA steels is to obtain refined transformation microstructures through the conditioning of austenite and the controlling of cooling processes.

In general, the grain size of ferrite depends on the density of nucleation sites. It was found that in undeformed austenite, ferrite grains mainly nucleate at grain triple junctions, grain edges and grain boundaries with increasing activation energy for nucleation as shown in Figure 2-1 (a) [16]. While in deformed austenite, additional nucleation sites of ferrite transformation were found to be effective, such as deformation bands and prior annealing twin boundaries as shown in Figure 2-1 (b) [16]. The reason why it is called a prior annealing twin boundary is because, during austenite deformation, twin boundaries will lose coherency and transit into normal high angle grain boundaries (HAGBs).
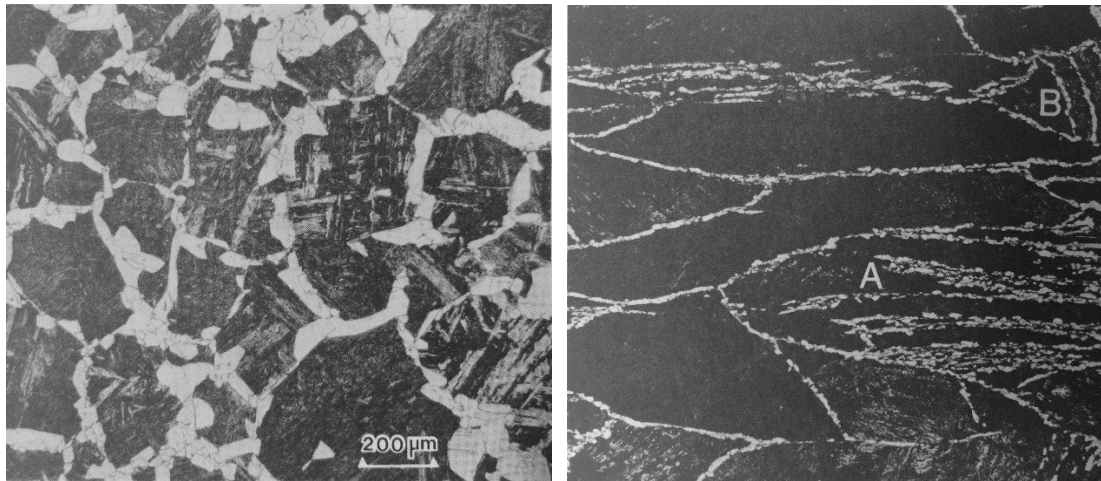
Figure 2-1 Nucleation of ferrite at (a) undeformed austenite grain boundary, (b) deformed austenite grain boundaries, deformation bands A and prior annealing twins B [16].

A stereological parameter S_v has been proposed to quantify the total effective nucleation sites area per unit volume for ferrite transformation [16], and the relationship between ferrite grain size and S_v in both recrystallised and deformed austenite is shown in Figure 2-2. We can see that the ferrite grain diameter has a

reciprocal relationship with S_v, and therefore increasing S_v is the primary method to refine ferrite microstructures.
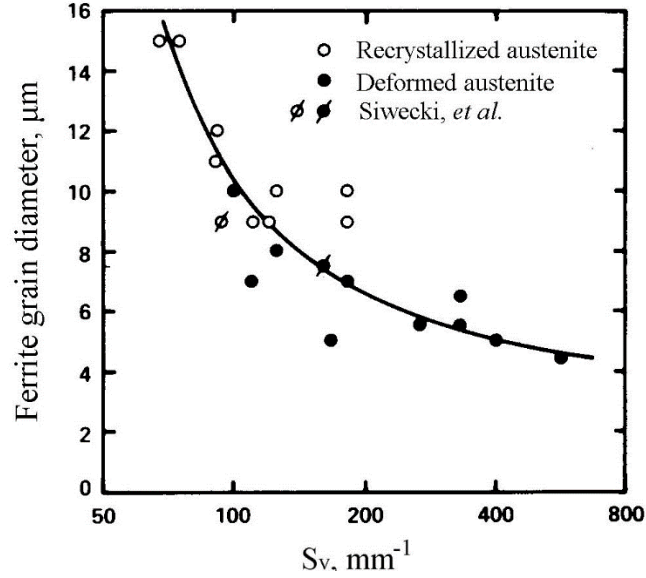
Figure 2-2 Relationship between ferrite grain size and S_v value in austenite [16].

The expression of S_v for recrystallised austenite was proposed as:

$$S_v = \frac{2}{D} \qquad (2.3)$$

where D is the austenite grain size measured by mean linear intercept length [17]. The expression of S_v for deformed austenite was presented as:

$$S_v = S_v(\text{GB}) + S_v(\text{DB}) = [1.67(R - 0.1) + 1](\frac{2}{D}) + 0.63(R - 0.3) \qquad (2.4)$$

where $S_v(\text{GB})$ stands for the total area of deformed austenite grain boundary per unit volume, $S_v(\text{DB})$ the total area of intragranular planar defects per unit volume, D the austenite grain size and R the reduction ratio [18].

Based on these equations, to archive a large S_v, there are two methods, obtaining recrystallised austenite with small grain diameters or deforming austenite to generate additional nucleation sites. These two methods lead to two different rolling strategies, the recrystallisation controlled rolling and the non-recrystallisation controlled rolling. At a given strain, strain rate, temperature and

8

interpass time, deformed austenite may exhibit different restoration behaviours, including complete recrystallisation, partial recrystallisation and no recrystallisation at decreasing temperatures as schematically illustrated in Figure 2-3. The lower and upper temperature limits for partial recrystallisation are termed as the recrystallisation-stop temperature ($T_{5\%}$) and the recrystallisation-limit temperature ($T_{95\%}$). For the recrystallisation controlled rolling, austenite deformation is conducted above $T_{95\%}$ so that recrystallised and refined austenite grains are obtained. While for the non-recrystallisation controlled rolling, austenite deformation is performed below $T_{5\%}$ so that austenite is deformed with no recrystallisation and minimum recovery, generating a high density of nucleation sites for subsequent phase transformations. Usually, austenite deformation between $T_{95\%}$ and $T_{5\%}$ is avoided due to the inhomogeneous microstructure transformed from partially recrystallised austenite grains.
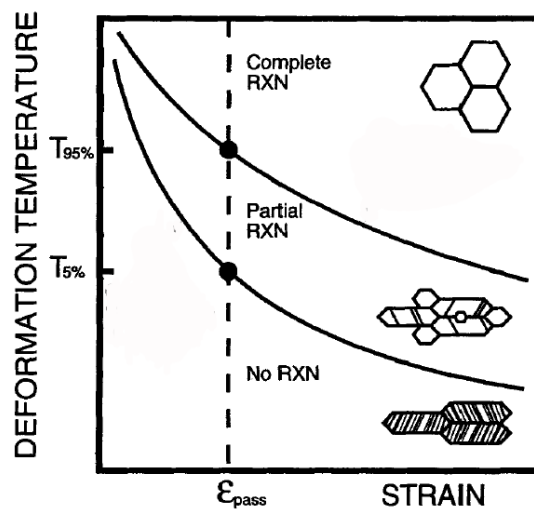
Figure 2-3 Schematic illustration of austenite grains at the same strain level but different deformation temperatures [19]. RXN stands for recrystallisation.

According to the S_v expression for deformed austenite, Equation (2.4), a smaller austenite grain size before deformation can also help increase S_v and this can be more directly understood by the relationship between S_v, austenite grain size and rolling reduction as shown in Figure 2-4.

9
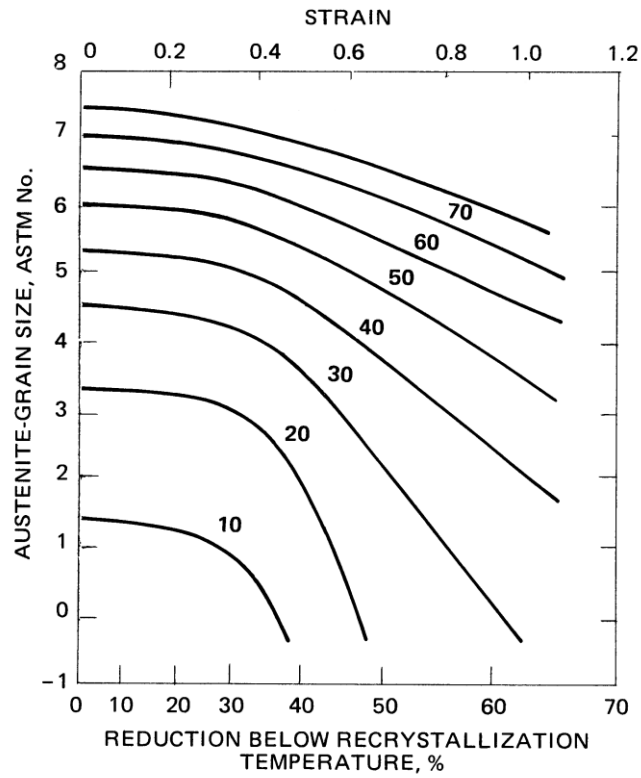
Figure 2-4 Change of S_v with rolling reduction below the recrystallisation-stop

temperature for a 0.03%-Nb steel [20].

Based on the above information, the typical thermomechanical controlled processing for HSLA steels is schematically shown in Figure 2-5, including reheating, rough rolling, finish rolling and continuous cooling.

10
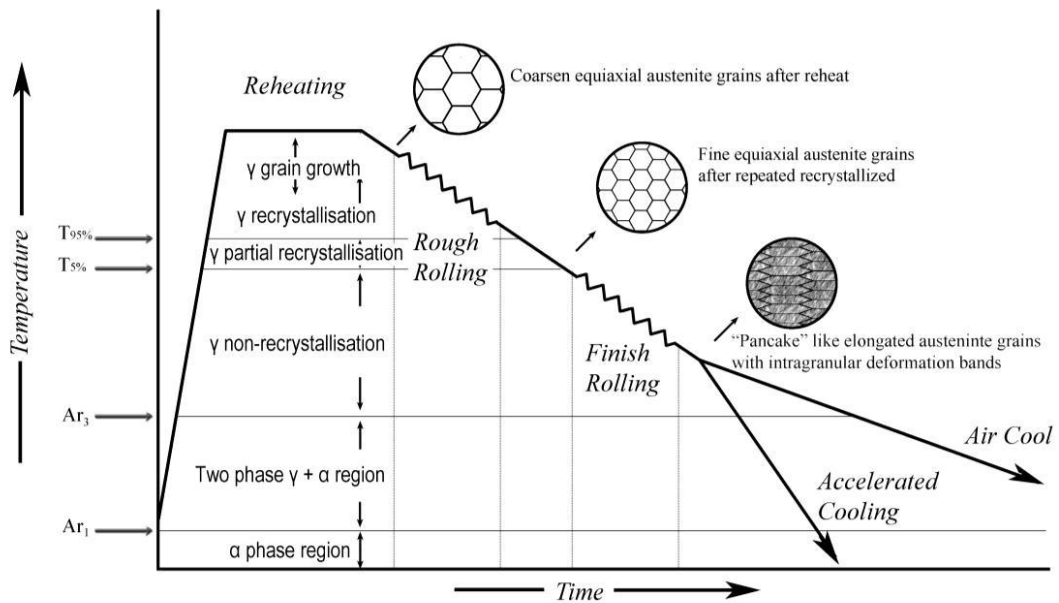
Figure 2-5 Schematic illustration of the thermomechanical controlled processing (TMCP) [21].

During the reheating process, ingots are heated to the austenite single-phase region and there are two major influences of the reheating process on the following thermomechanical treatment, grain coarsening of austenite and dissolution of microalloy element precipitates [22]. The grain coarsening of austenite during the reheating process is affected by the temperature and duration of reheating. Lower reheating temperatures and shorter reheating times can reduce the initial austenite grain size, which benefits the following austenite conditioning. However, the reheating temperature and duration must be adequate for enough dissolution of microalloy element precipitates. It can be seen from Figure 2-6 that increasing the initial solute content of various alloy elements, the recrystallisation-stop temperature ($T_{5\%}$) is raised to higher temperatures which facilitates the finish rolling process. The dissolved microalloy elements can also increase the hardenability of steels and form fine precipitates during continuous cooling, both strengthening the final microstructure. Past research [22] has shown that the reheating temperature very strongly affected the strength and low-temperature toughness properties of HSLA steels, which could be attributed to

11

the higher amount of Nb(C,N) in solution at higher reheating temperatures.
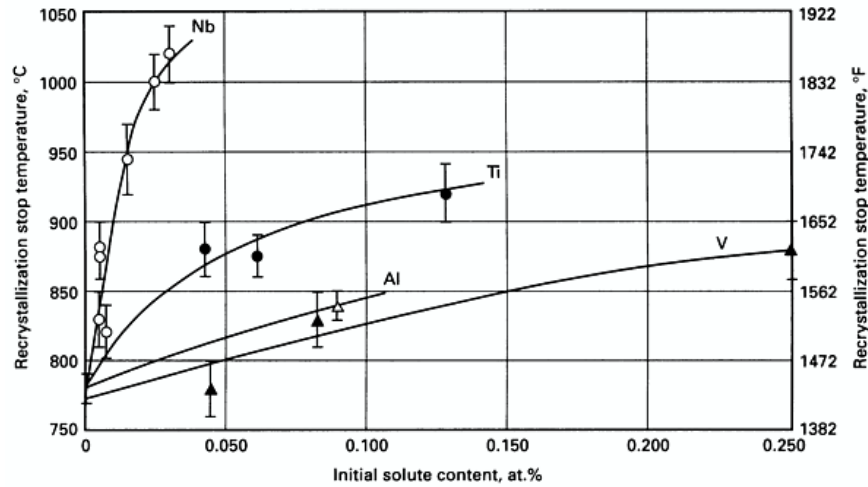
Figure 2-6 Effect of addition of microalloying elements on recrystallisation-stop temperature of a 0.07C-1.4Mn-0.25Si steel [16].

During rough rolling, ingots are deformed above $T_{95\%}$ to refine the coarse-grained austenite through repeated deformation and recrystallisation. After that, finish rolling is conducted below $T_{5\%}$ to pancake the refined austenite grains and introduce intragranular nucleation sites.

Finally, the pancaked (i.e., unrecrystallised) austenite is cooled continuously to get the final transformed microstructure. For controlled rolled microalloyed steels, subjected to air cooling often leads to a ferrite-pearlite microstructure with mechanical properties commonly below an X70 grade. To further improve the properties, accelerated cooling (ACC) is necessary. Based on the understanding of the transformation behaviours of deformed austenite during continuous cooling, the advantages of ACC for the improvement of both strength and toughness were studied during the 1970's [23]. The wide application of online ACC equipment not only increases the productivity significantly in steel plate mills [24] but also brings good control of the transformed microstructures [25].

For low carbon microalloyed pipeline steels, ACC after finish rolling exploits the enhanced hardenability of these steels to produce low-temperature

transformation products, mainly acicular ferrite (AF) which has a good combination of strength and toughness. A good example of the effect of ACC on the improvement of mechanical properties is shown in Figure 2-7. We can see that replacing the air cooling with an ACC with a cooling rate of 15°C/s, not only the strength is increased from X70 grade to X80 grade, also the toughness is improved as shown by the lower temperature of 85% shear in a drop weight tear test (DWTT).
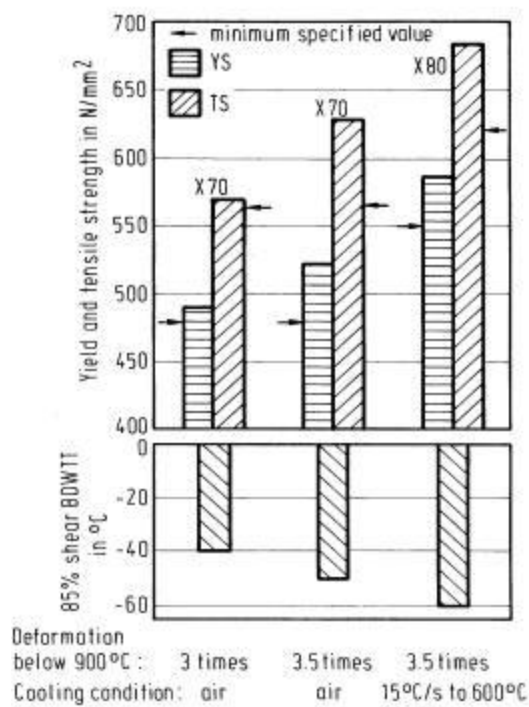
Figure 2-7 Strength and toughness properties of 18 mm pipeline steel plate (0.03% C–0.10% Nb–1.75% Mn) as a function of cooling conditions [26].

Additionally, the microstructure inhomogeneity across the plate thickness, mainly observed as banded structures, caused by solidification-induced chemical segregation, can be reduced or eliminated by applying ACC [24, 27].

2.3 Hot deformation of austenite

The essence of TMCP for HSLA steels is austenite deformation below the

13

$T_{5\%}$ which significantly increases the density of nucleation sites for the subsequent phase transformations from austenite. Therefore, in this part, the deformation mechanisms of austenite are introduced and the evolution of deformation substructures are reviewed.

2.3.1 Deformation mechanisms of austenite

It is well known that the deformation mechanisms of face-centred cubic (FCC) metals strongly depends on the stacking fault energy (SFE) [28]. For the FCC phase of iron, austenite, its SFE is one of a number of factors that determine whether dislocation glide, twinning or martensite transformation will occur during deformation [29].

In austenite, a perfect <110> dislocation can dissociate into two Shockley partial dislocations with Burgers vectors in directions of <112>, as shown in Figure 2-8 (a). Between these two partial dislocations, an area with a perturbed local stacking sequence on the slip plane exists as shown by the area A in Figure 2-8 (b), which is called a stacking fault. If the dislocation energy can be reduced by dissociating perfect dislocations into partial dislocations, stacking faults are likely to be generated. Furthermore, there is a repulsive force between these two partial dislocations and the surface tension of the stacking fault tend to pull them together. The partial dislocations will settle at an equilibrium separation determined primarily by the stacking fault energy. Therefore, the width of stacking faults, namely the separation distance between two partial dislocations has an inverse relationship with the SFE of austenite. Low SFE leads to wide stacking faults, while high SFE results in narrow ones. The narrow stacking faults in high SFE materials means the separated partial dislocations could be easily recombined to form a perfect dislocation to climb or cross-slip. On the other hand, for low SFE materials, due to the wide stacking faults and thus the difficulty of climb and cross-slip, other deformation mechanisms may be activated in addition to dislocation slip.
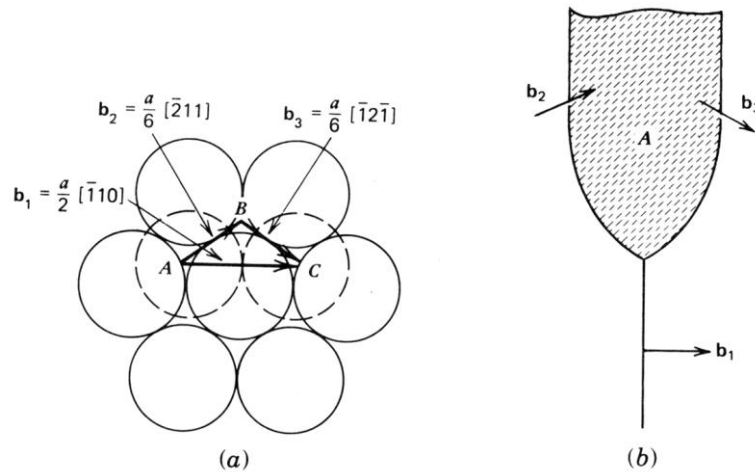
Figure 2-8 (a) A dislocation b_1 dissociate into two Shockley partial dislocations b_2 and b_3 in FCC crystal; (b) The stacking fault region with an area of A between two Shockley partials b_2 and b_3 [30].

The mechanisms both of ε-martensite transformation and mechanical twinning can be associated with the dissociation of perfect <110> dislocations and thus to the SFE of the material as well. From a crystallographic viewpoint, the formation of twins can be explained by packing of the same Shockley partial dislocations on every close-packed {111} plane, while packing of Shockley partials on every second close-packed {111} plane leads to the occurrence of ε-martensite [31]. Therefore, the occurrence of mechanical twinning and ε-martensite transformation is linked to the probability of forming stacking faults and thus to the SFE [32, 33].

It was reported that with increasing SFE, the active deformation mechanism of austenite will change from martensitic transformation, mechanical twinning to dislocation glide [34]. With a SFE smaller than 18 mJ/m^2, and simultaneously a high enough driving force for a martensite transformation, martensite transformation is favoured. If the SFE is higher than 18 mJ/m^2 but lower than 45 mJ/m^2, mechanical twinning becomes active. When the SFE is higher than 45 mJ/m^2, dislocation glide is the only deformation mechanism [29]. Besides

15

chemical composition, the SFE of materials also increases with an increase in temperature [33]. Therefore, various deformation mechanisms can be observed within different temperature ranges for the same material. An example of twinning-induced plasticity (TWIP) steel is shown in Figure 2-9 [29]. From it, we can see that at the same temperature, the SFE varies with different chemical compositions and with increased temperatures, SFEs of all three kinds of TWIP steels rises dramatically.
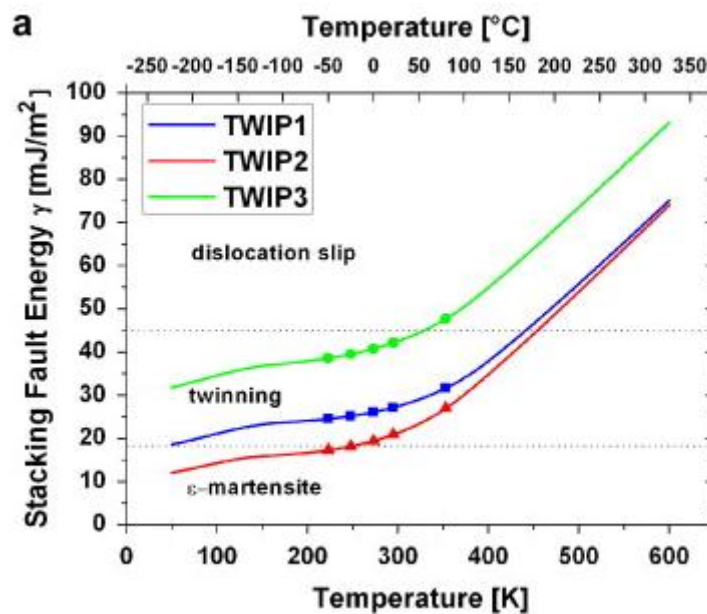
Figure 2-9 Stacking fault energy (SFE) of various TWIP steels at different temperatures [29].

The SFE of the austenite in C-Mn steels as measured by Charnock and Nutting at high temperatures is around 75 mJ/m^2 [35]. Therefore, based on the description of the dependence of deformation mechanism on SFE, dislocation slip is the main deformation mechanism during hot deformation of austenite.

2.3.2 Evolution of deformation substructures

During the deformation of metals, the mechanical energy required for deformation is largely transformed into heat and only a small fraction (~1-10%)

16

of the mechanical energy is stored in the deformed metals as crystal defects, mainly dislocations [28]. The arrangement of these dislocations depends on the material and deformation parameters, and generally these dislocations are accumulated in dislocation boundaries and only a small amount of dislocations exist in the regions separated by those dislocation boundaries [36]. The occurrence of this dislocation accumulation behaviour can be attributed to the reduction of strain energy by forming low energy dislocation structures (LEDS). Although the LEDS theory provides guidelines and principles for the analysis of deformation microstructures, it cannot allow the prediction of certain dislocation arrangement [36].

The evolution of deformation induced dislocation boundaries during rolling has been characterised extensively in FCC metals, such as Al [37], Ni [38] and Cu [39]. The general evolution pattern is illustrated as follows: at small strains, cell block (CB) structures are generated as schematically shown in Figure 2-10 (a); while at large strains, typical lamellar structures, with almost planar boundaries and short coadjacent boundaries generating a bamboo-like structure, are dominant as shown in Figure 2-10 (b) [40].
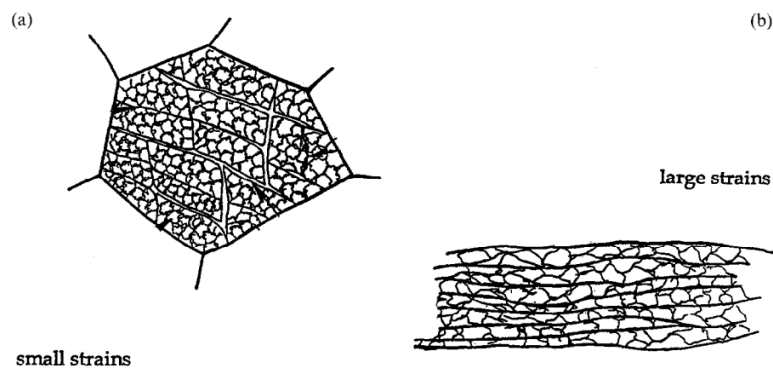
Figure 2-10 Schematic illustration of the deformation substructure evolution: (a) strain between 0.06 and 0.80, (b) strain higher than 1 [40].

For the cell block structures, cell blocks consisting of multiple equiaxed ordinary cells are delineated by extended planar dislocation boundaries and cells

17

are separated by cell boundaries [41]. These two types of dislocation boundaries are intrinsically different. The extended planar dislocation boundaries separating CBs are geometrically necessary boundaries (GNBs) produced by a deterministic mechanism while the ordinary cell boundaries are incidental dislocation boundaries (IDBs) formed by stochastic processes [36].

The formation mechanisms for these two different types of dislocation boundaries are schematically described in Figure 2-11 [36]. For GNBs, Figure 2-11 (a), different slip systems are activated in each cell block, which leads to an increased misorientation between adjacent cell blocks, and this difference in orientation will further aggravate the difference in slip systems activated. Therefore, dislocation boundaries with relatively large misorientation angles are geometrically necessary to accommodate the orientation misorientations between adjacent CBs and this process is deterministic during deformation. As for IDBs, mutual trapping of moving dislocations on a single slip system is the main mechanism to generate these boundaries and thus this process is stochastic in nature.
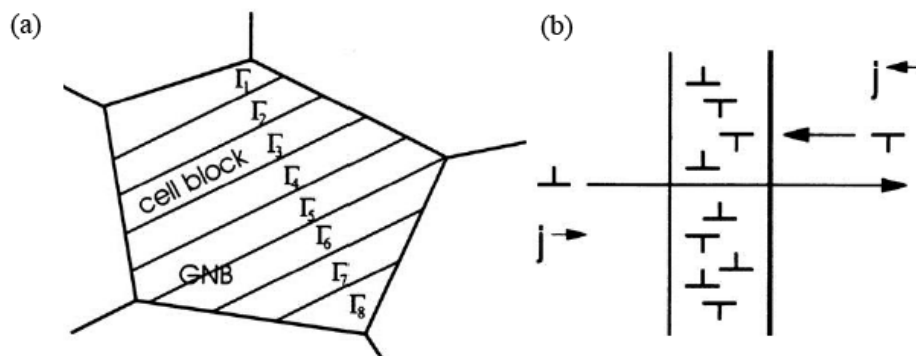
Figure 2-11 Formation mechanisms for two types of dislocation boundaries: (a) GNBs such as cell block boundaries are produced by different active slip systems (Γ) within individual cell blocks; (b) IDBs such as cell walls are formed by mutual trapping of moving dislocations on a single slip system [36].

To quantify the evolution of deformation substructures, microstructural

parameters, including the spacing between dislocation boundaries and the misorientation angles across these boundaries have been extensively investigated. One example is shown in Figure 2-12 for cold-rolled nickel specimens [42]. It can be seen clearly that the spacings of both GNBs and IDBs decrease with the increased Von Mises strain, while the averaged misorientation angles of both GNBs and IDBs increase with the raised Von Mises strain. Furthermore, the mean misorientation angle of GNBs increases with Von Mises strain more rapidly that that of IDBs, which can be seen more clearly in Figure 2-13. The more rapid increase in the average misorientation angle of GNBs was attributed to its deterministic nature and modelling and calculation using dislocation mechanisms based on the different formation processes of GNBs and IDBs successfully predict this difference as shown by the dashed lines in Figure 2-13 [43].
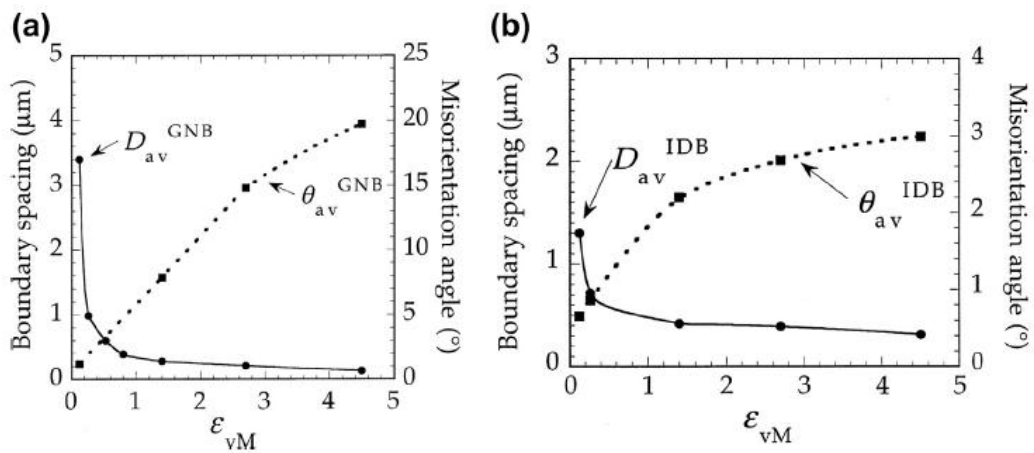
Figure 2-12 Spacings (D_{av}) and average misorientation angles (θ_{av}) at different Von Mises strains for cold-rolled nickel: (a) GNBs and (b) IDBs [42].
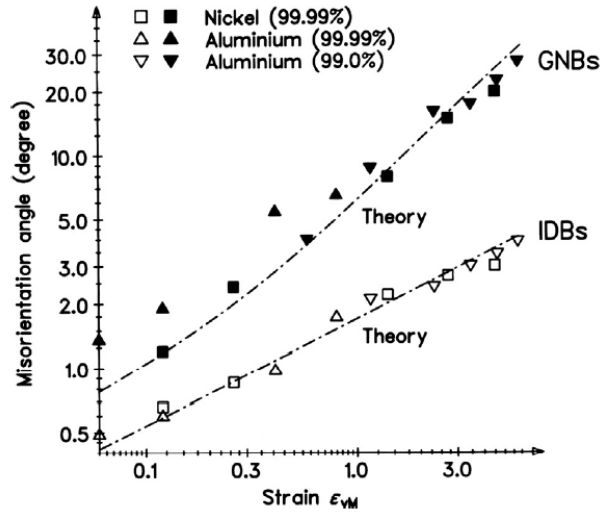
Figure 2-13 Experimental measurements and theoretical calculation of mean misorientation angles at different Von Mises strains for IDBs and GNBs [43].

Besides strain magnitude, deformation induced substructures can also be significantly affected by orientations of the parent grains. An example of tensile strained Cu is given in Figure 2-14 [44]. It is clear from Figure 2-14 (b)~(c) that three different types of deformation substructures can be identified and this substructure difference can be associated with the orientations of the parent grains as shown in the inverse pole figure (IPF) of tensile axes in Figure 2-14 (a).
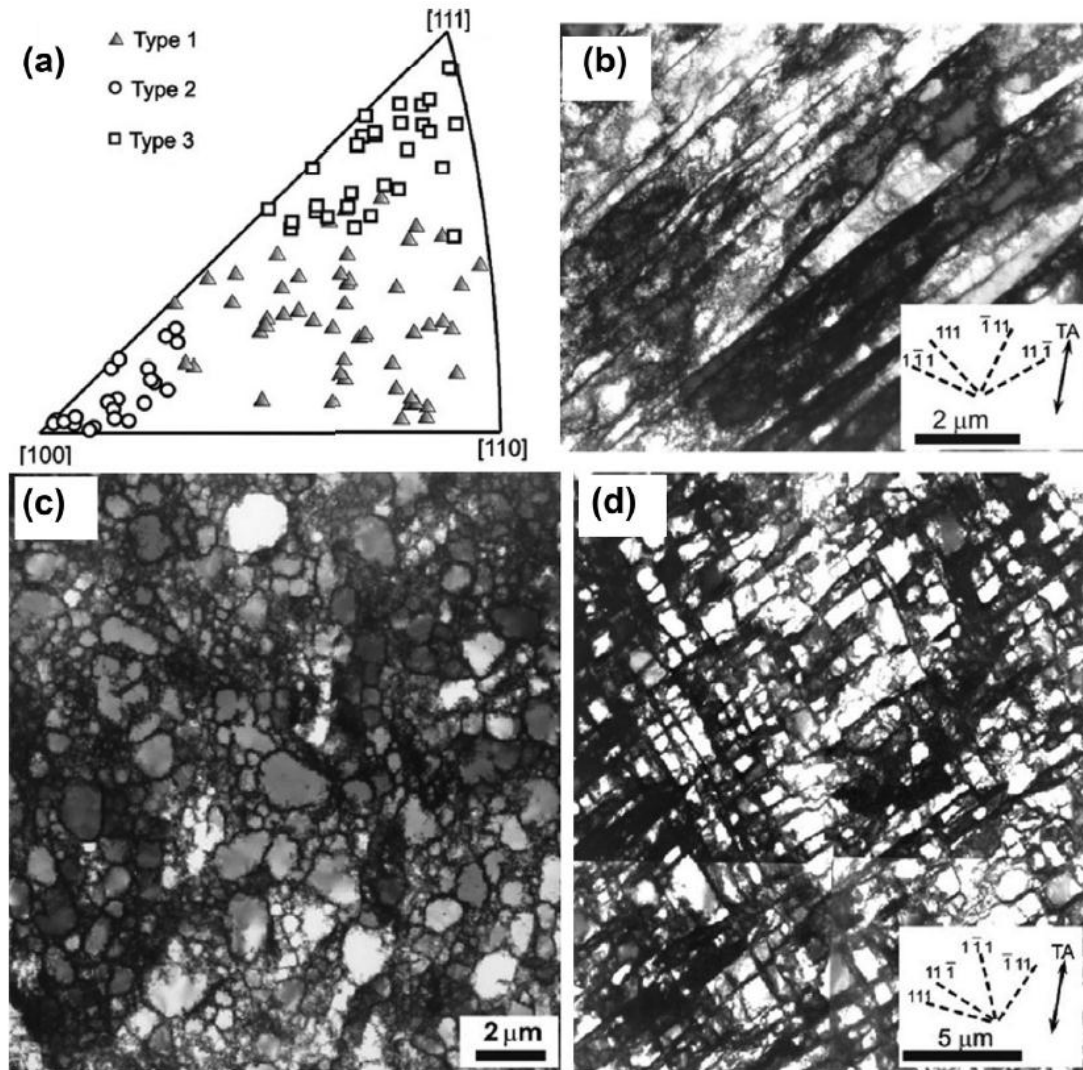
Figure 2-14 The dependence of deformation induced substructures on grain orientations in a tensile strained copper: (a) inverse pole figure (IPF) of tensile axes orientations of 120 grains, (b) type 1 substructures, (c) type 2 substructures and (d) type 3 substructures [44].

With tensile axes locating in the centre of the IPF, a cell block deformation substructure developed, Figure 2-14 (b). The GNBs in this type of microstructure are straight, parallel and aligned nearly with the activated slip planes (within 10˚). If tensile axes are near to the <111> direction of the parent grains, a cell block deformation substructure is also generated, Figure 2-14 (d), but the GNBs deviate substantially from the activated slip planes (>10˚). When tensile axes are

21

near to the <100> direction of the parent grains, a cell structure without GNBs is developed, Figure 2-14 (c), with cell boundaries randomly orientated and extended along the tensile axes. A similar dependence of deformation substructure on parent grain orientations was also found in cold-rolled Cu. Detailed descriptions can be found in reference [44].

Through extensive and careful transmission electron microscopy (TEM) characterisation of various deformation substructures in pure copper and aluminium [45, 46], the strong effect of the parent grain orientations on the deformation substructures was found to originate from the dependence of deformation substructures on the active slip systems. Different combinations of slip systems will give rise to different types of dislocation boundaries and most of the GNBs align with certain crystallographic planes. Based on the characteristics of the GNBs generated after deformation, different combinations of slip systems were classified into 5 fundamental slip classes [45]. More importantly, the slip activities of all slip systems largely depend on the orientations of parent grains. Therefore, different parent orientations lead to distinct active slip systems and finally result in different deformation substructures.

The slip activity distribution within a parent grain is also very important. According to the classic Taylor theory [47], each grain is subjected to the same homogeneous strain undergone by the bulk material, which needs the simultaneous operation of the same five independent slip systems in different parts. This homogeneous slip activity will generate a homogeneous deformation substructure as schematically shown in Figure 2-15. Nevertheless, in experimental work, inhomogeneous slip patterns are generally observed, and it is believed that the quantity of active independent slip systems is commonly less than 5 in each region of the parent grain. More importantly, the active slip systems in each region of the parent grain are different and therefore cause the parent grains to be subdivided into cell blocks separated by GNBs as shown in

22
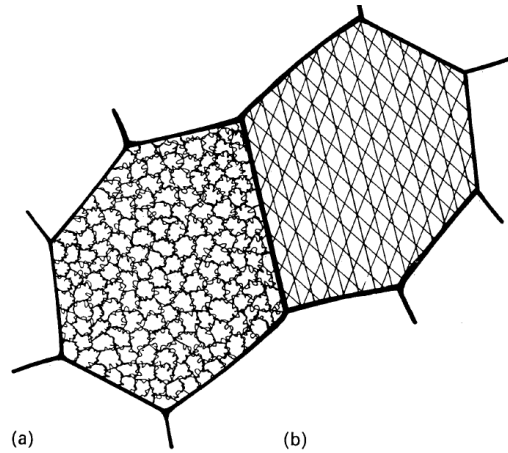
Figure 2-16 [48].

Figure 2-15 Homogeneous deformation based on the Taylor assumption: (a) deformation substructures (b) slip line pattern [48].
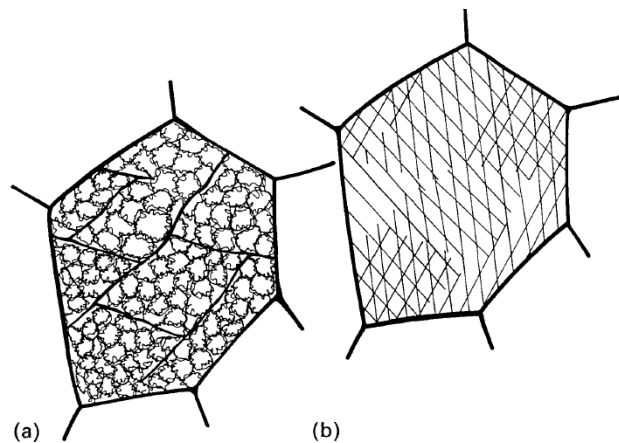
Figure 2-16 Inhomogeneous deformation with various combination of slip systems operating in different regions: (a) deformation substructures (b) slip line pattern [48].

Although most of the experiments mentioned above were conducted at room temperature, the underlying principles and general descriptions are suitable for both cold and hot deformation [44]. Direct characterisations of austenite deformation substructures for C-Mn steels are difficult due to the phase transformation during quenching, but similar evolutions of deformation substructures were observed in hot deformed austenitic stainless steels and Fe-Ni model alloys [49, 50]. Therefore, the general description of deformation

23

substructures should be applicable to the hot deformation of austenite for HSLA steels.

Deformed austenite is thermodynamically unstable because of the presence of crystal defects generated during deformation. At high temperatures, restoration processes such as recovery and recrystallisation occurring during (dynamic) or after (static) deformation can proceed readily by the help of thermally activated diffusion. For further details about the mechanisms and microstructure evolution characteristics of various restoration processes, comprehensive textbooks such as *Recrystallization and related annealing phenomena* [28] can be referred to.

2.4 Decomposition of austenite

During the continuous cooling of HSLA steels, various transformation products can be formed and specific terms have been introduced to describe these phases. The classification of these transformation products usually is conducted according to the systems proposed by Araki et al. [51] and Krauss and Thompson [52]. In this section, the morphology characteristics and the transformation mechanisms of these transformation products are introduced.

2.4.1 Morphologies of austenite decomposition products

The classification of ferritic microstructures proposed by Krauss and Thompson [52] is used in this thesis, including polygonal ferrite (PF), quasi-polygonal ferrite (QF), Widmanstätten ferrite (WF), granular bainite (GB), acicular ferrite (AF) and lath bainite (LB). Since acicular ferrite (AF) has been designated to a specific type of microstructure which is illustrated at length in Section 2.5, the term lath bainite (LB) is used to describe the bainite microstructures with an apparent parallel morphology. The morphology characteristics of all types of microstructure except AF are illustrated below and

the typical optical micrographs are shown in Figure 2-17.
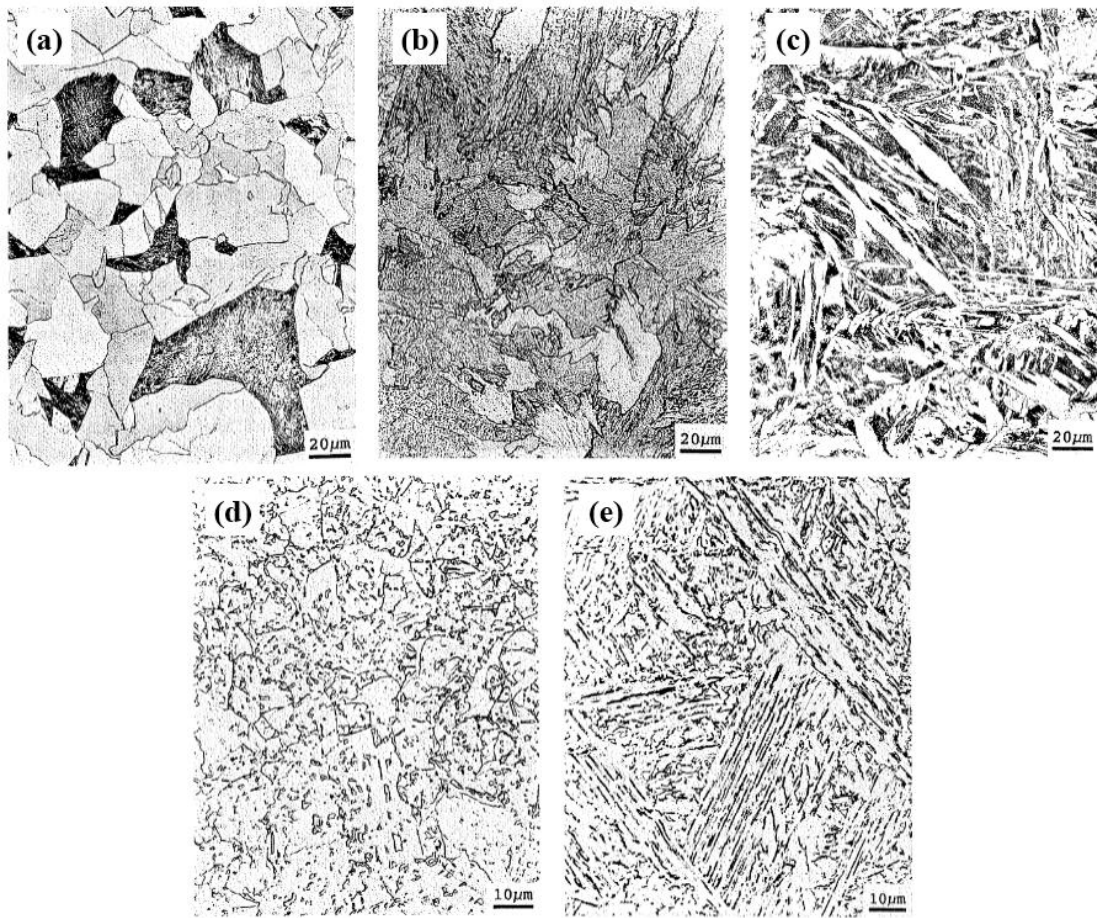
Figure 2-17 Optical micrographs of various transformation products: (a) polygonal ferrite (light grains), (b) quasi-polygonal ferrite, (c) Widmanstätten ferrite (large elongated white grains), (d) granular bainite and (e) lath bainite.

PF forms at the slowest cooling rates and the highest transformation temperatures, and nucleates at austenite grain boundaries and grows into equiaxed shapes [52]. Due to the very low dislocation density and the high transformation temperature [53], this microstructure can be easily identified, under a optical microscope, with bright colour and smooth boundaries as shown in Figure 2-17 (a). The dark areas in Figure 2-17 (a) are martensite formed during quenching after isothermal holding.

During the continuous cooling of very-low-carbon steels, if the cooling rate

is rapid enough, with decreased temperatures, austenite can go through the two-phase field of austenite/ferrite without any initiation of transformation, and reach the single-phase field of ferrite. Within the single-phase field of ferrite, massive transformations could occur and quasi-polygonal ferrite (QF or massive ferrite) could be generated from austenite without any change of bulk chemical composition [54, 55]. QF has irregular grain boundaries and sub-boundaries with high densities of dislocations [56], as shown in Figure 2-17 (b).

WF is usually referred to coarse and elongated ferrite grains and due to the lack of substructures within each grain, WF in optical micrographs appears uniformly white as shown in Figure 2-17 (c). WF forms at faster cooling rates or lower transformation temperatures than those of PF and QF. It nucleates on austenite grain boundaries or pre-existed PF grains and develops into long, thin and parallel lath-like or plate-like microstructures.

At even lower transformation temperatures or higher cooling rates, granular bainite (GB) and then lath bainite (LB) transformations occur [57, 58]. GB microstructures usually consist of coarse plates with an almost entirely granular aspect together with equiaxed M/A (martensite and retained austenite) constituents distributing among this featureless matrix as shown in Figure 2-17 (d) [2]. In GB microstructures, prior-austenite grain boundaries (PAGBs) are also retained. Differently, parallel morphologies can be seen clearly from LB microstructures and M/A constituents in them have an acicular shape as shown in Figure 2-17 (e). The terms GB and LB were given mainly to distinguish different bainite morphologies [55]. Actually, GB has many similarities to LB [51] and Bhadeshia [2] suggested that GB is not different from ordinary LB in terms of transformation mechanism, despite the existence of morphological differences between them. They both consist of packets of parallel ferrite laths separated by low-angle disorientation boundaries and contain high densities of dislocations [59]. Since in this research ferritic microstructure evolution is the main focus, we term both GB and LB as bainitic ferrite (BF).

2.4.2 Mechanisms of phase transformation from austenite

The various austenite transformation products illustrated above can be divided into two groups, reconstructive transformations and displacive transformations, based on their transformation mechanisms [60]. PF and QF belong to the group of reconstructive transformations while WF, GB and LB fall into the group of displacive transformations. During reconstructive transformations, to form the lattice structure of the target phase (bcc in this case), all of the atom bonds in the parent lattice (FCC in this case) need to be broken and all the atoms are needed to be rearranged through diffusion [54]. As for displacive transformations, the lattice structure of the target phase is formed through uniform deformation of the austenite lattice and the movement of atoms are synchronized. These two transformation mechanisms are schematically illustrated in Figure 2-18.
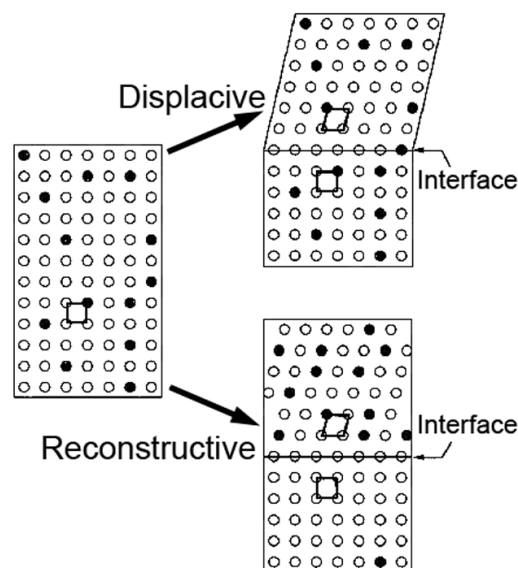
Figure 2-18 Schematic illustration of the lattice change mechanisms from a parent lattice (left) to a product lattice (above the interface) through a displacive transformation (right and upper) and a reconstructive transformation (right and lower) [60].

For displacive transformations in steels, the transformation product is

27

generated by an invariant-plane strain (IPS) deformation consisting of a small dilation component, δ, and a large shear component, s, as shown in Figure 2-19. The approximate values of the shear component, s, and the dilatation component, δ, for various transformation products are listed in Table 2-1. The shape strains of displacive transformations are significantly larger than those of reconstructive transformations, and the relief of these large shape strains will cause surface displacement for polished and unconstrained samples as shown in Figure 2-20. But if the sample is constrained during displacive transformation, a thin plate or lath morphology will be adopted by the transformation products to minimize the strain energy induced by transformation. This thin plate or lath morphology can be seen in all displacive transformation products [2]. Besides morphology, displacive transformation products will also have many crystallographic characteristics and these will be introduced in section 2.6.
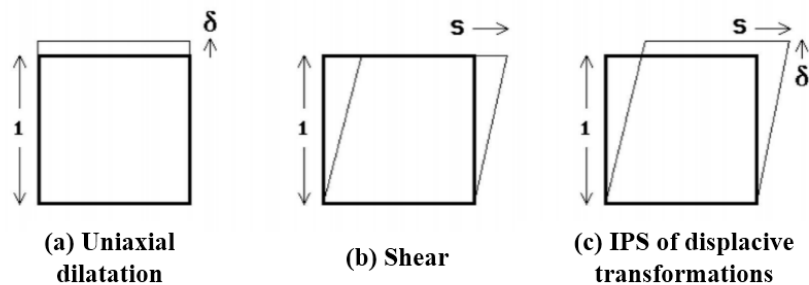
Figure 2-19 Different strain conditions (a) uniaxial dilatation, (b) shear and (c) IPS of displacive transformations [2].

It was found that bainite possesses a higher density of dislocations than that of PF even when PF and bainite transformed at similar temperatures [2]. The existence of a high density of dislocations in bainite is usually attributed to the large shape strain corresponding to the bainitic transformation. When the shape deformation is relaxed by the plastic deformation of austenite and bainite, dislocations introduced by this plastic relaxation in austenite will be inherited by

28

the bainite, which finally leads to a high density of dislocations in bainite [2]. The plastic relaxation can be seen in Figure 2-21.

Table 2-1 Approximate values of the shear strain, *s*, and dilatational strain, δ, for a variety of transformation products in steels [2].

Transformation	*s*	δ
Widmanstätten ferrite	0.36	0.03
Bainite	0.22	0.03
Bainite	0.26	
Martensite	0.24	0.03
Allotriomorphic ferrite	0	0.03
Idiomorphic ferrite	0	0.03
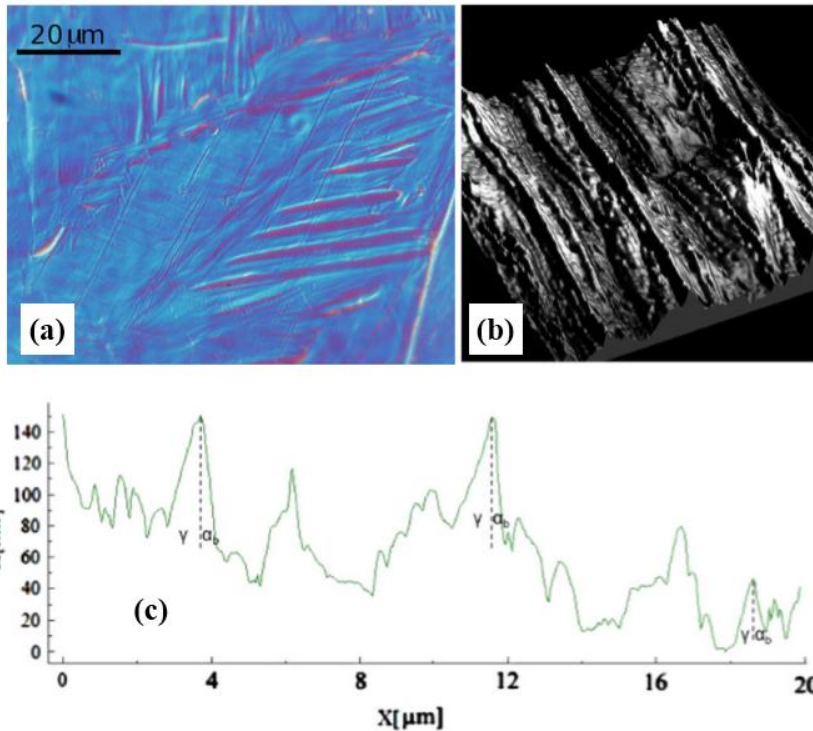
Figure 2-20 Surface relief after bainitic transformation in a pipeline steel: (a) optical differential interference contrast microscopy, (b) topography using atomic force microscopy and (c) a line scan [61].

29
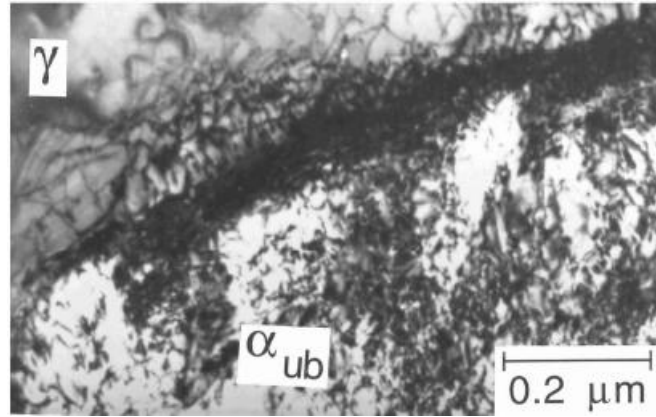
Figure 2-21 Dislocations in austenite and bainite near an austenite/bainite interface [2].

The main characteristics of many important phase transformations in steels are listed in Table 2-2 [61]. For more details, comprehensive textbooks such as *Steels: Microstructure and Properties* [60] can be useful.

Table 2-2 Key Transformation Characteristics in Steels [61].

Table I. Key Transformation Characteristics in Steels

Comment	α'	α_{lb}	α_{ub}	α_a	α_w	α	α_i	P
Nucleation and growth reaction	=	=	=	=	=	=	=	=
Plate shape	=	=	=	=	=	≠	≠	≠
IPS shape change with large shear	=	=	=	=	=	≠	≠	≠
Lattice correspondence during growth	=	=	=	=	≠	≠	≠	≠
Co-operative growth of ferrite and cementite	≠	≠	≠	≠	≠	≠	≠	=
High dislocation density	=	=	=	=	●	≠	≠	≠
Necessarily has a glissile interface	=	=	=	=	=	≠	≠	≠
Always has an orientation within the bain region	=	=	=	=	=	≠	≠	≠
Grows across austenite grain boundaries	≠	≠	≠	≠	≠	=	=	=
High interface mobility at low temperatures	=	=	=	=	=	≠	≠	≠
Reconstructive diffusion during growth	≠	≠	≠	≠	≠	=	=	=
Bulk redistribution of X atoms during growth	≠	≠	≠	≠	≠	●	●	●
Displacive transformation mechanism	=	=	=	=	=	≠	≠	≠
Reconstructive transformation mechanism	≠	≠	≠	≠	≠	=	=	=
Diffusionless nucleation	=	≠	≠	≠	≠	≠	≠	≠
Only carbon diffuses during nucleation	≠	=	=	=	=	≠	≠	≠
Reconstructive diffusion during nucleation	≠	≠	≠	≠	≠	=	=	=
Often nucleates intragranularly on defects	=	≠	≠	=	≠	≠	=	≠
Diffusionless growth	=	=	=	=	≠	≠	≠	≠
Local equilibrium at interface during growth	≠	≠	≠	≠	≠	●	●	●
Local paraequilibrium at interface during growth	≠	≠	≠	≠	=	●	●	≠
Diffusion of carbon during transformation	≠	≠	≠	≠	=	=	=	=
Carbon diffusion-controlled growth	≠	≠	≠	≠	=	●	●	●
Incomplete reaction phenomenon	≠	=	=	=	≠	≠	≠	≠

Martensite α', lower bainite α_{lb}, upper bainite α_{ub}, acicular ferrite α_a, Widmanstätten ferrite α_w, allotriomorphic ferrite α, idiomorphic ferrite α_i, pearlite P, substitutional solutes X. Consistency of a comment with the transformation concerned is indicated by =, inconsistency by ≠ ; a bullet ● identifies the case where the comment is only sometimes consistent with the transformation. The term *parent γ* implies the γ grain from which the product phase grows. Adapted from.[14]

2.5 Acicular ferrite

Acicular ferrite was firstly introduced by Y. E. Smith [8] in 1972. However, it has been designated to several slightly different microstructures over the years [62].

2.5.1 AF in steel welds

In steel welds, acicular ferrite has been known as ferrite laths nucleating on intragranular non-metallic inclusions in austenite, as shown in Figure 2-22 and Figure 2-23, and leads to an excellent combination of strength and toughness [63] which can be attributed to the high densities of dislocations and HAGBs in these AF microstructures [64].
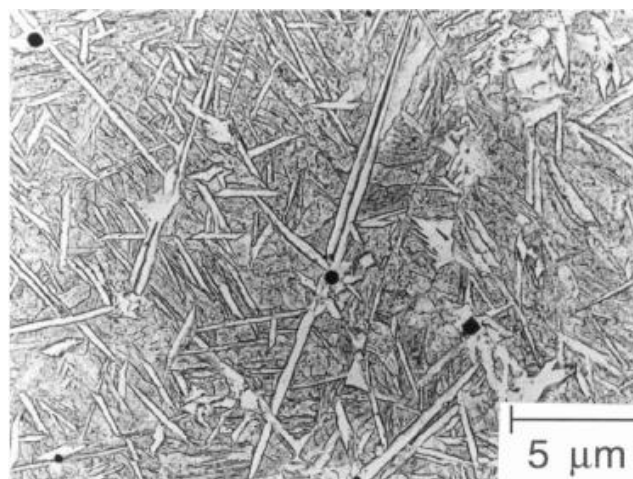
Figure 2-22 Replica TEM micrograph of acicular ferrite in a steel weld [2].
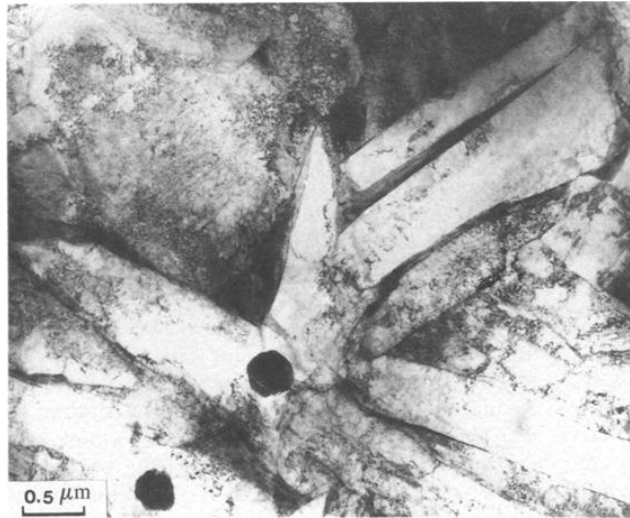
Figure 2-23 TEM micrograph of AF plates nucleated on inclusions [65].

Based on extensive investigations on the nature of AF [2, 66-70], it was found that the transformation mechanism of AF in steel welds is similar to that of bainite, except for the requirement of intragranular inclusions for AF nucleation. Therefore, AF in steel welds has been known as intragranularly nucleated bainite [2]. Acicular ferrite laths usually do not develop into parallel packets like bainite as the formation of packets is prohibited by impingement of adjacently nucleated plates in AF microstructures [2].

Although, the transformation mechanisms of bainite and AF are analogous, because of the existence of more crystallographic variants in AF microstructures and thus a higher density of HAGB, the toughness of AF microstructures in steel welds is better than that of bainite microstructures [71] which is a highly organized microstructure with packets containing parallel plates with similar crystallographic orientation [2], as shown in Figure 2-24.
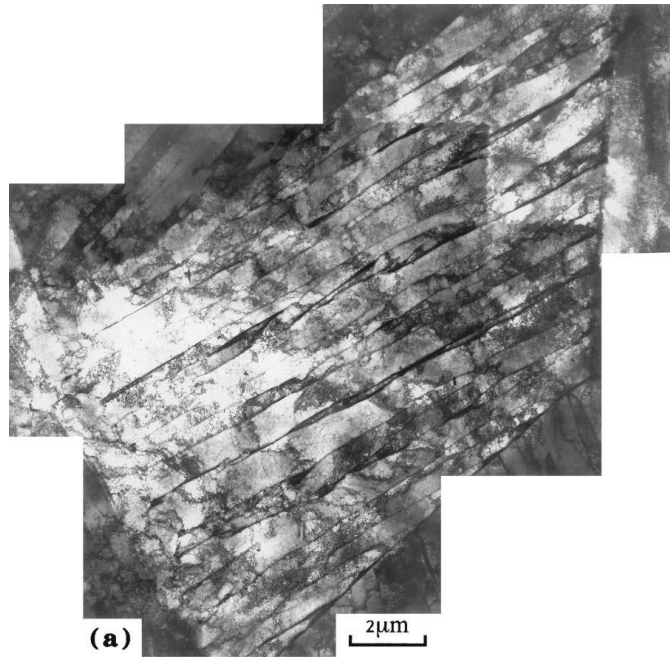
Figure 2-24 TEM micrograph of a bainite packet [12].

2.5.2 Inoculated Acicular Ferrite Steels

To obtain the weld-metal AF-like microstructures in structural steels, inclusion particles which are effective in stimulating AF nucleation are deliberately brought in by controlling the deoxidation process during steel making [2]. The particles formed are generally a mixture of various oxides and sulphides, but the effective phase in promoting the AF nucleation is Ti_2O_3 [72]. The formation of weld-metal AF-like microstructures can greatly improve the steel's toughness through the increase of the density of HAGBs which can arrest or deflect the propagation of cracks. A huge number of inoculated AF steels have been produced for the constructions in the offshore gas and oil industries, especially in various deep, cold and hostile environments [2]. The optical micrograph of an inoculated acicular ferrite steel is shown in Figure 2-25.
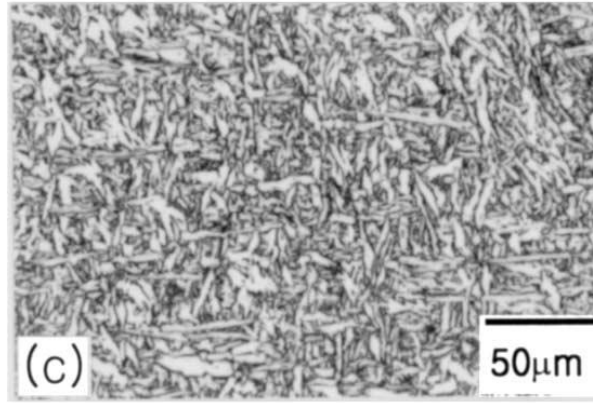
Figure 2-25 Optical micrograph of acicular ferrite in an inoculated acicular ferrite steels [73].

Based on the introduction above, it is reasonable to say that the AF microstructures in inoculated AF steels and steel welds are the same.

2.5.3 AF in pipeline steels

In pipeline steels, acicular ferrite was defined by Smith in 1972 [8] as "a highly substructured, non-equiaxed ferrite that forms on continuous cooling by a mixed diffusion and shear mode of transformation that begins at a temperature slightly higher than the upper bainite transformation range." Nowadays, AF dominant microstructures have become the optimal candidates in the production of pipeline steels for their excellent combination of strength and toughness. Actually, pipeline steels with AF dominant microstructures have already been applied in the 3000 km Alliance Pipeline Project from British Columbia to Chicago in North America [74] and also in the 4000 km West–East Natural Gas Transmission Project from Xinjiang to Shanghai in China [75].

As for the nature of AF in pipeline steels, its transformation mechanism is still controversial. Some researchers regarded AF as a kind of GB [76], while AF was classified as quasi-polygonal ferrite (QF) or massive ferrite in some investigations [77, 78]. Xiao et al. [75] proposed that the phase transformation mechanism of acicular ferrite was in diffusion mode. Collins et al. [79] indicated that AF transformation was similar to that of WF. Various investigators [80, 81]

34

proposed that AF was almost similar to BF because of the similar mechanical properties, while Coldren and Mihelich [82] suggested that AF was different from bainite for the disappearance of PAGBs. Differently, Wang et al. [83] argued that AF complexly consisted of QF, GB and BF with dispersed islands of second phases in the matrix. And a complicated mixture of PF, upper bainite, lower bainite, auto tempered martensite with retained austenite was treated as AF in the literature [84].

However, after analysing the characteristics of the AF transformation and its microstructure carefully, it is more proper to classify AF as a kind of bainitic transformation product. In an isothermal holding test [85], it was found that by increasing the austenite deformation strain, there was a transition from BF to AF, which means both AF and BF transformations can occur at the same thermodynamic conditions. Furthermore, in an investigation [85], after isothermal holding at 600˚C, the AF transformation was nearly finished and the final volume fraction of acicular ferrite was only 51%, corresponding well to the typical incomplete transformation phenomenon of bainite [2], and the total transformation time of AF was 13s, which suggests that the transformation of AF proceeds very quickly by transformation behaviour associated with a shear mechanism. The incomplete transformation phenomenon is related to the transformation mechanism of bainite. During bainite transformation, laths grow without diffusion and after the formation of a lath, supersaturated carbon atoms in this lath partition into the surrounding residual austenite, leading to the increased carbon concentration in the residual austenite. Therefore, during bainite transformation, laths grow from austenite with gradually increased carbon concentrations as schematically shown in Figure 2-26 [2]. Bainite transformations will cease when the carbon concentration of austenite reaches a critical value, x'_{T0} which is defined as the critical carbon concentration below which the driving force of the transformation from FCC to BCC without a composition change is higher than the transformation strain energy, and is around

400J/mol for bainite [2]. Differently, for paraequilibrium transformations, e.g. WF, the transformation can proceed until the carbon concentration of austenite reaches the Ae_3' curve [2], which is higher than x'$_{T0}$ at the same temperature as shown in Figure 2-26, indicating that a higher fraction of austenite can transform into paraequilibrium transformation products than into bainite. Therefore, bainite transformations appear 'incomplete' compared with paraequilibrium transformations.
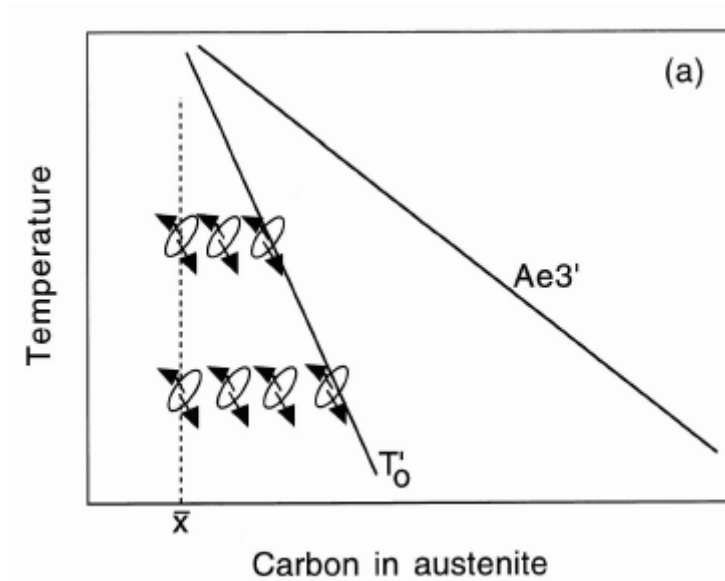
Figure 2-26 Schematic illustration of the incomplete transformation phenomenon of bainite [2].

Furthermore, in several TEM observations [85-88], it was found that AF laths contained a higher density of dislocations than that in the reconstructive transformation products, which is a characteristic of low-temperature transformation products [2]. And in research [85], the microstructure of AF was found to be composed of several parallel sub-units, which are possibly formed by side-by-side sympathetic nucleation and the size of each sub-unit was less than 1 μm. This morphology characteristic can also be observed in the literature [86] which resembles the sheaf morphology of bainite sub-units proposed by

36

Bhadeshia [2].

The displacive transformation characteristic of the AF microstructure can also be seen from the boundary density distributions against disorientation angles shown in Figure 4-6. This is explained at length in Section 4.3.3.

In summary, acicular ferrite in pipeline steels shows a similar transformation behaviour to that of bainitic ferrite, which is agreed by many other researchers [1, 85, 88].

2.5.4 Microstructure characteristics of acicular ferrite in pipeline steels

Acicular ferrite in pipeline steels has many microstructural characteristics, such as consisting of non-equiaxed ferrite grains with high dislocation densities, the existence of a microphase, mostly M/A constituents, the veined appearance [89] and the boundary protrusions of ferrite lath groups [79]. These characteristics are illustrated below under different microscopy techniques.

(1) Optical microscopy (OM)

Optical micrographs of microstructures with different fractions of AF are shown in Figure 2-27. It is found that these microstructures are mainly composed of AF and PF. Acicular ferrite usually appears grey in these micrographs and consists of fine non-equiaxed ferrite laths with a chaotic arrangement as schematically illustrated in Figure 2-28. The boundaries of acicular ferrite are very obscure and less evident than those of PF which appear white in these micrographs. This may be attributed to the fact that the grain boundaries within acicular ferrite are mainly with low disorientation angles [85] and the standard 2% nital is less effective for revealing these boundaries [88]. Some microphases, possibly fine M/A constituents, appearing black, are distributed throughout the matrix and the formation of this microphase can be attributed to the partitioning of carbon from ferrite to austenite during the AF transformation [90].

37
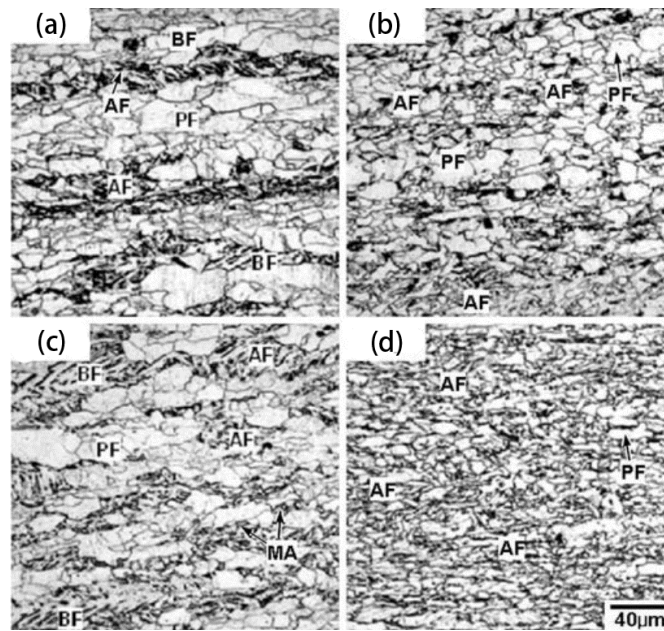
Figure 2-27 Optical micrographs of microstructures with different fractions of AF: (a) 0.23, (b) 0.48, (c) 0.25 and (d) 0.82 [1].
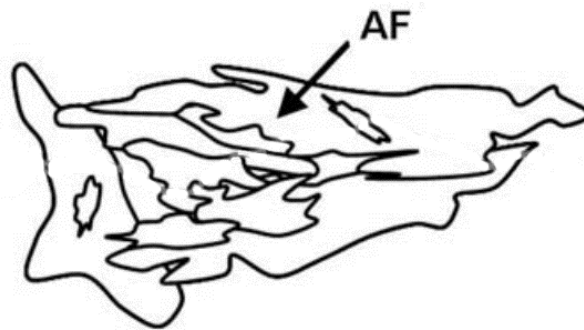
Figure 2-28 Schematic illustration of acicular ferrite grains [1].

(2) Scanning electron microscopy (SEM)

In SEM micrographs, the randomly oriented and non-equiaxed ferrite laths with dispersed M/A islands can be seen in Figure 2-29. But in practical acicular ferrite dominant microstructures, PF/QF not only forms on the austenite grain boundaries but also on the deformation induced substructure formed within the austenite grains as shown in Figure 2-1 (b). Furthermore, some of the acicular ferrite boundaries cannot be clearly etched [89]. Therefore, it is hard to distinguish between these two phases, PF/QF and AF, even under SEM. However,

it was found in research [88] that under high-resolution SEM after a long time etching, PF/QF is etched very lightly while AF is etched much more deeply and also contains fine and veined substructures as shown in Figure 2-30.
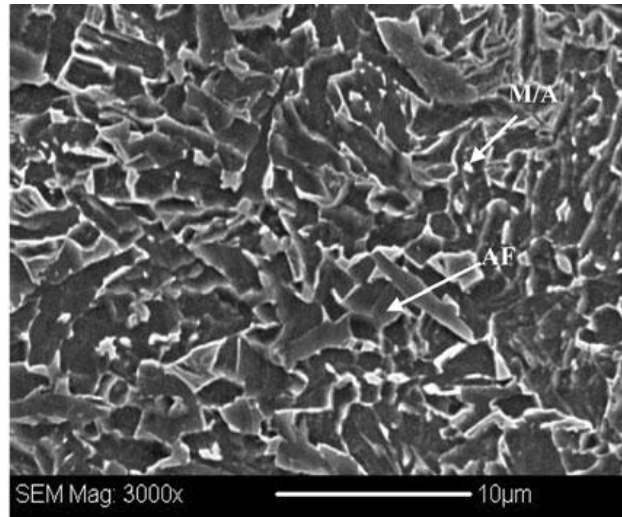
Figure 2-29 SEM micrograph of acicular ferrite [91].
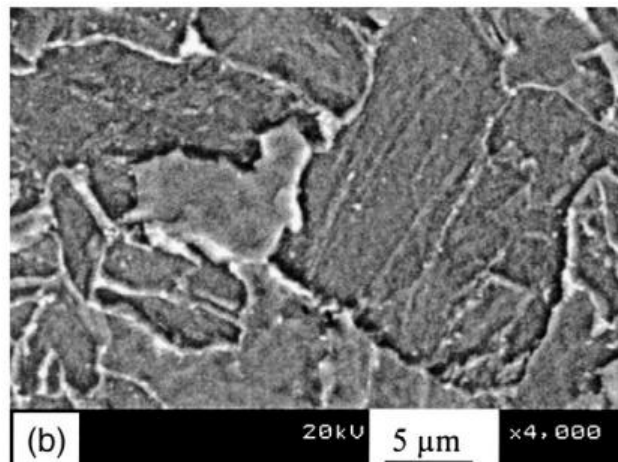
Figure 2-30 SEM micrograph of AF and PF/QF under a high magnification [89].

(3) Transmission electron microscopy (TEM)

At the initial transformation stage, since the interference from other nucleation sites is quite small, it is feasible to obtain accurate acicular ferrite microstructures. The microstructure of acicular ferrite at the initial stage isothermally held at 600°C [85] is shown in Figure 2-31 and schematically

illustrated in Figure 2-32. The microstructure of acicular ferrite was found to be consisting of several parallel sub-units, and size of each sub-unit was less than 1 μm. The sub-units are possibly formed by a side-by-side sympathetic nucleation. This morphology characteristic can also be observed in the literature [86] which quite resembles the sheaf morphology of bainite sub-units proposed by Bhadeshia [2].
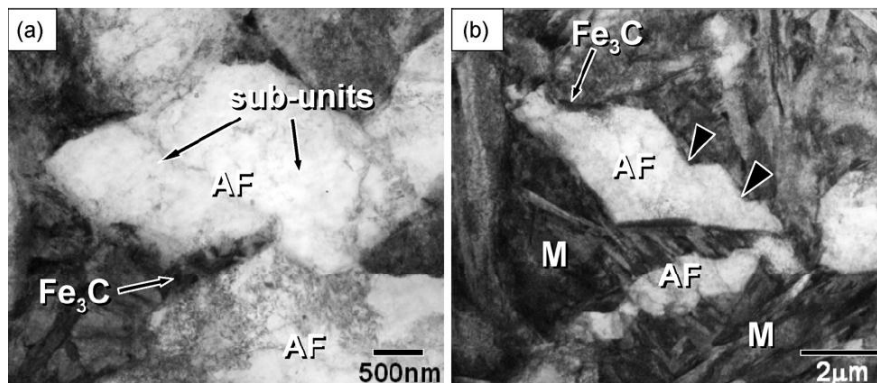
Figure 2-31 TEM micrographs of acicular ferrite at the starting stage of transformation [85].
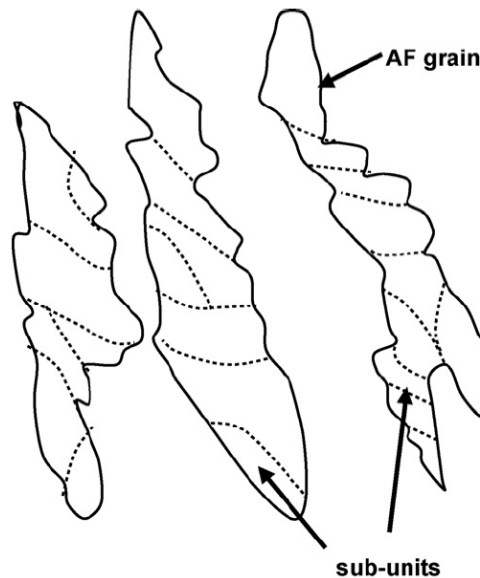
Figure 2-32 Schematic illustration of acicular ferrite laths [85]

After the AF transformation, the acicular ferrite grains are shown in Figure

40

2-33 (a), it can be found that the sub-units of the AF grains are also clear despite the boundaries being curved and not as flat as in the initial stage, Figure 2-31. The sheaf-like morphology changes into one that is more irregular-shaped. This may be explained by the occurrence of some diffusional processes like coalescence and thickening of acicular ferrite grains similar to what happens in bainite transformation [92], given the relatively high transformation temperatures of acicular ferrite.
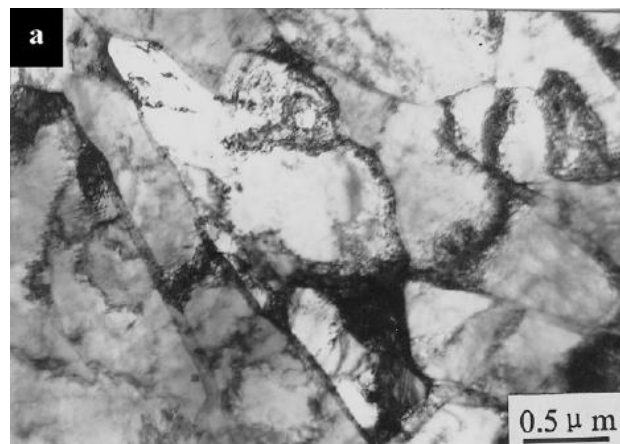
Figure 2-33 TEM micrographs of as-rolled acicular ferrite microstructure [87].

In research [88], the thin foil TEM observation revealed that the AF microstructure consisted of parallel laths forming groups which were separated by PF regions, as shown in Figure 2-34. Where the groups with different lengthening directions met, chaotic and interweaving arrangements of ferrite laths were also found, as shown in Figure 2-35. Thus, there are two different morphologies existing simultaneously in the microstructure, parallel laths and interweaving laths. It has been shown that the parallel laths have a similar crystallographic orientation and are separated by low-angle boundaries [91].
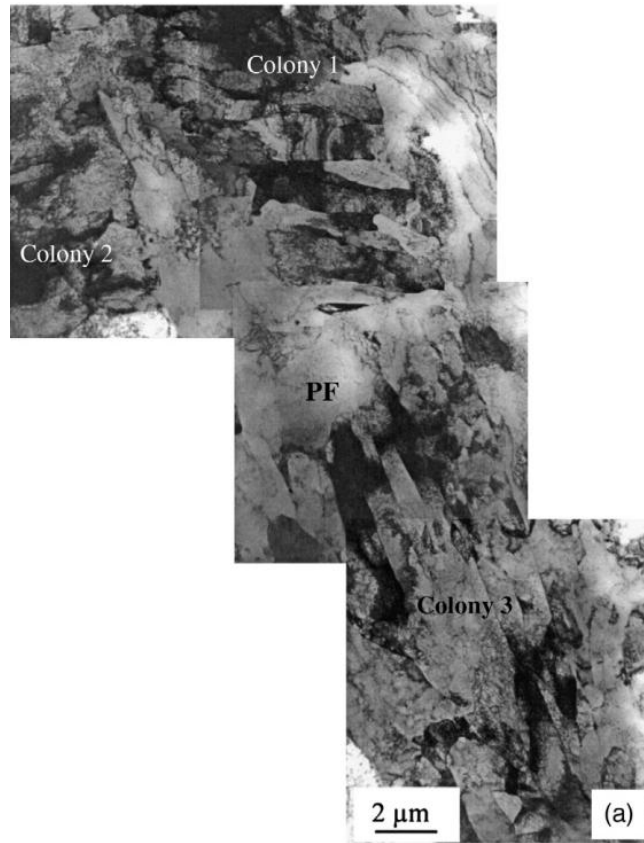
Figure 2-34 TEM micrographs of AF colonies separated by PF areas [88].
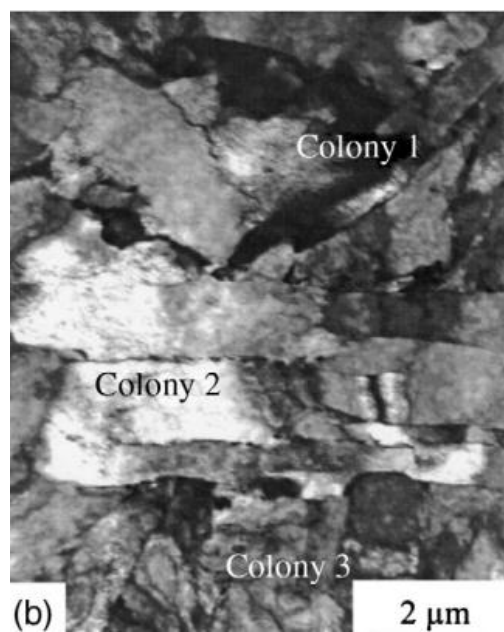
Figure 2-35 TEM micrographs of chaotic arrangement of ferrite laths [88].

In all the TEM observations above [85-88], it was found that AF laths all

contain a higher density of dislocations than PF, which is a characteristic of displacive transformation products [2]. All these microstructure characteristics observed by TEM indicate that AF has a similar transformation mechanism to that of bainite.

2.6 Crystallographic characteristics of Bainite microstructures

2.6.1 Orientation relationships

For displacive transformations like BF and martensite, transformation interfaces cannot cross austenite grain boundaries and the transformed ferritic products and their parent austenite grains are crystallographically related by an orientation relationship (OR) within the Bain region [2]. Although various ORs have been proposed, including the Kurdjumov-Sachs (K-S) OR [93], the Nishiyama-Wasserman (N-W) OR [94, 95], the Kelly OR [96] and the Greninger-Troiano (G-T) OR [97], according to the phenomenological theory of martensite transformation [98], this OR is actually irrational and the close-packed planes of BF and parent austenite are not exactly parallel. It was found that the angular deviation between close-packed planes of bainite and austenite increases with the increased transformation temperature, while the change of angular deviation between close-packed directions are very small, which was explained by the temperature related plastic accommodation of bainite transformation strain in austenite [99].

2.6.2 24 K-S variants

Owing to the OR between bainite and austenite and the crystallographic symmetry of austenite, there are 24 possible BF orientation variants for each austenite grain. Since the Kurdjumov–Sachs (K–S) orientation relationship ($\{111\}\gamma//\{110\}\alpha$, $<110>\gamma//<111>\alpha$) generally provides good predictions for BF

transformations in steels [100], it is taken as the OR to illustrate the BF orientation variants. With the K–S OR, there are 24 BF orientation variants for each austenite grain, V1~V24 as listed in Table 2-3 [99]. The 24 K-S variants can be divided into four close-packed plane groups (CP groups), each of which consists of six variants sharing the same parallel relationship of close-packed planes with austenite. The arrangement of the close-packed planes and close-packed directions of these 24 K-S variants and the misorientation between these variants can be seen clearly in Figure 2-36 [101]. K–S variants can also be discriminated into three Bain groups based on three variants of the Bain correspondence [102]. Variants belonging to the same Bain group have their <100> directions surrounding a specific <100> direction of the prior austenite, shown in Figure 2-37 as black dots around an open diamond. The corresponding CP and Bain groups for these 24 K-S variants are also shown in Table 2-3.

Table 2-3 24 K–S variants and their corresponding CP and Bain groups [99].

Variant no.	Plane parallel	Direction parallel	CP group	Bain group	Misorientation from V1 (°)
V1	$(111)_\gamma//(011)_\alpha$	$[\bar{1}01]_\gamma//[\bar{1}\bar{1}1]_\alpha$	CP1	B1	–
V2		$[\bar{1}01]_\gamma//[\bar{1}\bar{1}1]_\alpha$		B2	60.0
V3		$[01\bar{1}]_\gamma//[\bar{1}\bar{1}1]_\alpha$		B3	60.0
V4		$[01\bar{1}]_\gamma//[\bar{1}\bar{1}1]_\alpha$		B1	10.5
V5		$[1\bar{1}0]_\gamma//[\bar{1}\bar{1}1]_\alpha$		B2	60.0
V6		$[1\bar{1}0]_\gamma//[\bar{1}\bar{1}1]_\alpha$		B3	49.5
V7	$(1\bar{1}1)_\gamma//(011)_\alpha$	$[10\bar{1}]_\gamma//[\bar{1}\bar{1}1]_\alpha$	CP2	B2	49.5
V8		$[10\bar{1}]_\gamma//[\bar{1}\bar{1}1]_\alpha$		B1	10.5
V9		$[\bar{1}\bar{1}0]_\gamma//[\bar{1}\bar{1}1]_\alpha$		B3	50.5
V10		$[\bar{1}\bar{1}0]_\gamma//[\bar{1}\bar{1}1]_\alpha$		B2	50.5
V11		$[011]_\gamma//[\bar{1}\bar{1}1]_\alpha$		B1	14.9
V12		$[011]_\gamma//[\bar{1}\bar{1}1]_\alpha$		B3	57.2
V13	$(\bar{1}11)_\gamma//(011)_\alpha$	$[0\bar{1}1]_\gamma//[\bar{1}\bar{1}1]_\alpha$	CP3	B1	14.9
V14		$[0\bar{1}1]_\gamma//[\bar{1}\bar{1}1]_\alpha$		B3	50.5
V15		$[\bar{1}0\bar{1}]_\gamma//[\bar{1}\bar{1}1]_\alpha$		B2	57.2
V16		$[\bar{1}0\bar{1}]_\gamma//[\bar{1}\bar{1}1]_\alpha$		B1	20.6
V17		$[110]_\gamma//[\bar{1}\bar{1}1]_\alpha$		B3	51.7
V18		$[110]_\gamma//[\bar{1}\bar{1}1]_\alpha$		B2	47.1
V19	$(111)_\gamma//(011)_\alpha$	$[\bar{1}10]_\gamma//[\bar{1}\bar{1}1]_\alpha$	CP4	B3	50.5
V20		$[\bar{1}10]_\gamma//[\bar{1}\bar{1}1]_\alpha$		B2	57.2
V21		$[0\bar{1}\bar{1}]_\gamma//[\bar{1}\bar{1}1]_\alpha$		B1	20.6
V22		$[\bar{1}\bar{1}0]_\gamma//[\bar{1}\bar{1}1]_\alpha$		B3	47.1
V23		$[101]_\gamma//[\bar{1}\bar{1}1]_\alpha$		B2	57.2
V24		$[101]_\gamma//[\bar{1}\bar{1}1]_\alpha$		B1	21.1
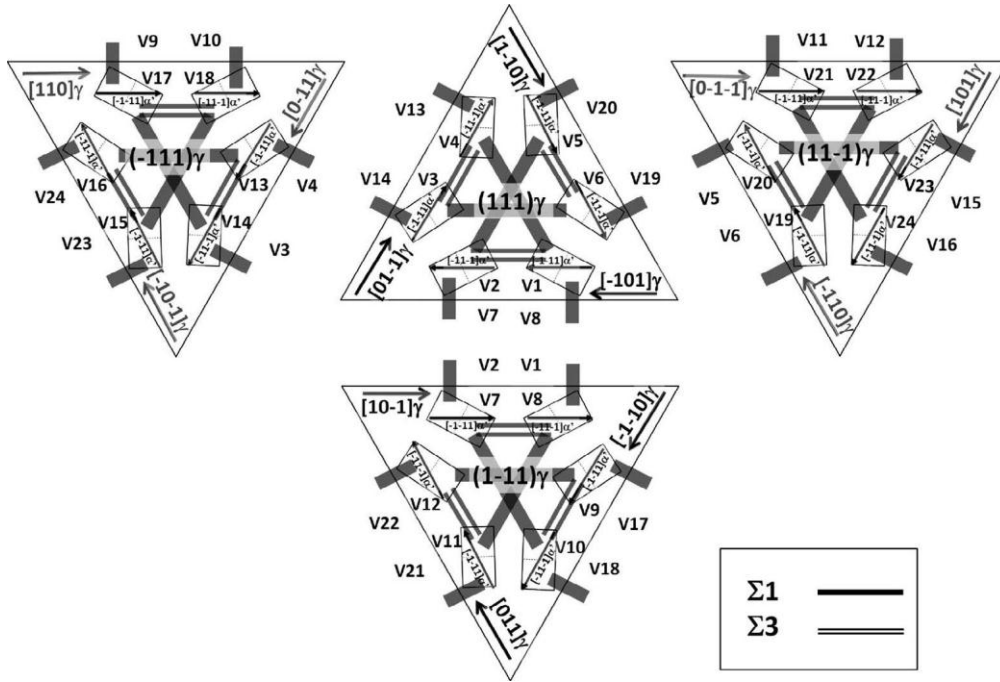
Figure 2-36 Arrangement of close-packed planes and close-packed directions of the 24 K-S variants and the misorientation between these variants [101].
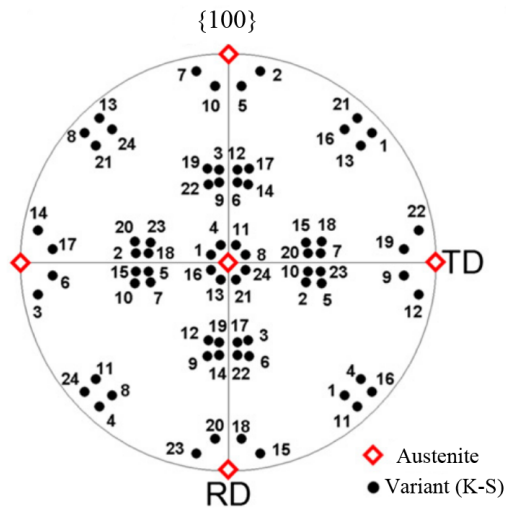
Figure 2-37 Austenite <001> {100} pole figure showing 24 K-S variants with their variant numbers labeled. Prior austenite orientation is marked by red open diamonds [103].

The connections between variants and bainite microstructures can be shown in Figure 2-38 [104]. A parent austenite grain is usually divided into several

45

packets during BF transformations and each packet can be further segmented into several blocks which consist of a few BF laths. This packet-block structure is defined from the viewpoint of variants. Each block contains several bainite laths with the same variant and the variants within the same packet belong to the same close-packed plane group. In martensite microstructures, each block can be further segmented into two sub-blocks with two variants belonging to the same CP group and the same Bain group [105-107].
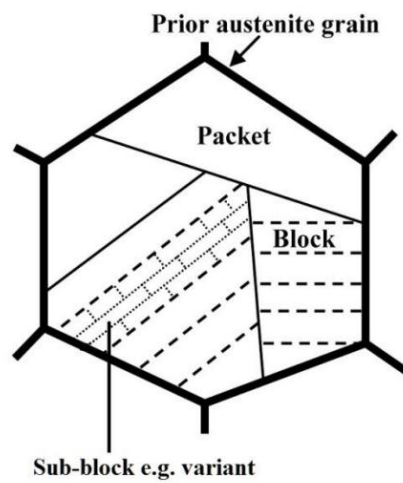
Figure 2-38 Schematic illustration of bainite lath martensitic structure [104].

The formation of blocks of several BF laths with the same variant can be attributed to an autocatalytic effect. In reference [108] the stress field surrounding a martensite plate of an oblate spheroid shape was established with the application of micromechanics theory and it was found that at the tip of the martensite plate the nucleation of a new plate with the same variant is favoured. Similarly, in reference [109] it was disclosed that the formation of a stacking fault at the tip of a martensite plate also promotes the development of a new plate with the same variant. This repetitive autocatalytic nucleation during martensite transformation results in the formation of a block structure consisting of laths/plates with the same variant.

The formation of packets can be related to the accommodation of large

transformation strains. During displacive transformations, the shape strain can be accommodated through different mechanisms, plastic deformation of austenite and bainite, elastic deformation of austenite and bainite or self-accommodation when different variants are formed adjacently [101]. Therefore, when austenite is difficult to deform plastically, different variants have to be formed adjacently to self-accommodate the transformation strain and the strain that can be elastically accommodated is very limited [68, 110, 111]. Due to the same reason, when plastic accommodation of transformation strain is feasible, the packet structure will be changed and this will be discussed in the next section.

2.6.3 Variant selection

During transformation, not all of the 24 K-S variants are necessarily formed in each austenite grain and the favour of certain variants is called variant selection. When transformation products nucleate at lattice defects in the matrix, the variant selected depends on the characteristics of these defects [112]. Since bainite usually nucleates on the austenite grain boundaries, the characteristics of austenite grain boundaries may have great impact on the variant selection of bainite, which has been observed experimentally [113, 114]. These investigations show that variant selection occurs through various mechanisms, including the reduction of the bainite/austenite interface energy through the elimination of the larger austenite grain boundary area at nucleation or through the reduction of transformation strain energy by plastic accommodation. Since an individual austenite grain boundary has its distinct characteristic, the bainite nucleation potency for each austenite grain boundary is different. In research [114], some austenite grain boundaries are still free from bainite laths, whereas others are fully covered with bainite laths and tilt grain boundaries are chosen as nucleation sites more evidently than twist grain boundaries. Similarly, in research [115], it was found that certain types of austenite grain boundaries have higher potencies for martensite nucleation than annealing twin boundaries and

47

normal HAGBs, and symmetric tilt boundaries with the rotation axis of <112> possess a similar dislocation arrangement to the nucleation model proposed in research [116]. Later the high potency of <112> symmetric tilt boundaries was confirmed and the potency of these boundaries was found to be higher than that of the twist boundary which was attributed to the better strain compatibility at the tilt boundary than at the twist boundary [117, 118].

Besides austenite grain boundary characteristics, variant selections can also be influenced by other factors. As previously reported [119], bainite formed at high temperatures exhibits a strong variant selection and with a decrease in the transformation temperature, more BF variants formed at each austenite grain boundary as shown in Figure 2-39. The factors that weaken the variant selection are the increased bainite transformation driving force and the onset of self-accommodation of transformation strain. For a larger driving force obtained by lowering the transformation temperature, the differences in the activation energy for nucleation between various variants are smaller and more types of variants can nucleate. But even when lowering the transformation temperature, variant selection can still happen in the initial stages of transformation [119].
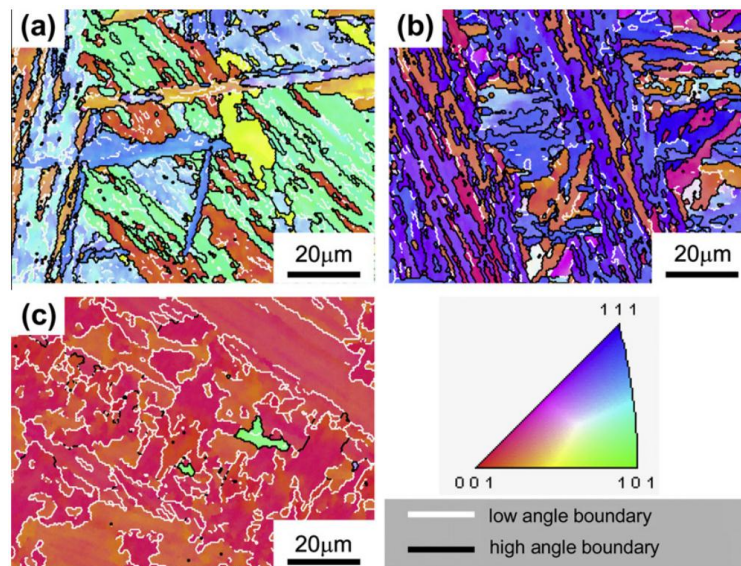
Figure 2-39 Inverse pole figure coloured orientation maps of (a) lath martensite, (b) bainite transformed at 450°C and (c) bainite transformed at 580°C [119].

48

Self-accommodation of the transformation shape strain also plays an important part in weakening variant selection. By forming different variants adjacently, the bainite transformation strain can be self-accommodated when the plastic accommodation in austenite and also in BF is difficult. As shown in reference [120], the formation of all 6 variants belonging to the same CP group can successfully self-accommodate the transformation shape strain and reduce the shape strain from 0.242 to 0.024. Such self-accommodation can be activated by strengthening the austenite through lowering transformation temperatures or increasing carbon contents.

The change in the bainite transformation driving forces and the transformation strain self-accommodation conditions can also influence the packet structure of BF as schematically illustrated in Figure 2-40 [99].
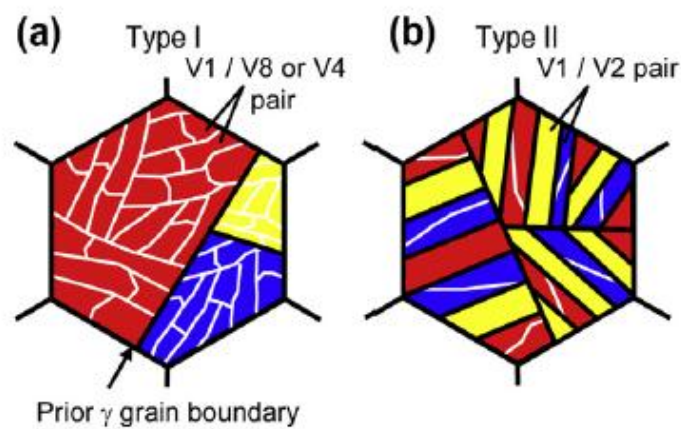
Figure 2-40 Schematic illustrations of packet structures in (a) bainite transformed at 580˚C and (b) bainite transformed at 450˚C. Different colours represent different Bain groups and different boundary directions represent different close-packed plane groups [99].

At a relatively low transformation temperature (450˚C), Figure 2-40 (b), normal BF packets in which variants of the same CP group are formed to self-accommodate the transformation strain as mentioned above.

At a relatively high transformation temperature (580°C), Figure 2-40 (a), variants belong to the same Bain group are formed adjacently and a variant pairing of V1-V8 is favoured in addition to the well acknowledged variant pairing of V1-V4 [119]. Although V1 and V8 belong to the same Bain group, they come from different CP groups. Therefore, at relatively high temperatures bainite microstructures cannot be divided into packets. The possible formation mechanism of a variant pair with two variants belonging to different CP groups but the same Bain group can be explained as follows. When the BF transformation happens at high temperatures, the transformation shape strain is accommodated plastically in the austenite and the BF, and thus dislocations could be introduced into the austenite which have characteristics that are strongly related to the first nucleated variant [2]. According to the variant selection model introduced by Butron-Guillen et al. [100], the development of each variant can be closely linked to a particular slip system. Therefore, it is possible that the dislocations introduced by the first nucleated variant in the austenite are suitable nucleation sites for other BF variants, which is defined as strain-induced nucleation [2], and indeed, a two-stage nucleation behaviour has been observed before [121]. The initial stage is associated with the nucleation of primary plates at austenite boundaries and these plates grow gradually towards the interior of the austenite grains. The following stage is the nucleation of secondary plates on the primary plates and these plates grow in different directions compared with the primary plates [121]. Furthermore, Lambert-Perlade et al. [110] suggested this particular variant pair, V1-V8, becomes favoured because this particular spatial and crystallographic kind of variant pair is able to reduce the plastic deformation in the austenite phase, which could help the growth of the BF laths. Differently, a separate investigation by Takayama et al.[99] proposed that reducing the boundary energy between variants may be the reason for the formation of this particular variant pair as variant pairs of the same Bain group usually have smaller disorientation angles and the boundary energy decreases

significantly with the reduction of disorientation angle below about 15°. Preferential formation of specific variant pairs that are disoriented by a relatively low angle (approximately, 10°) in a packet was also revealed in low carbon lath martensite [120, 122, 123] and bainite [68, 110, 119].

2.7 Phase identification

2.7.1 Discrimination between QF and AF

Since AF grains usually consist of several laths as shown in Figure 2-34 and these lath boundaries normally cannot be clearly revealed by nital [89], AF grains sometimes appear as granular grains with irregular boundaries as shown schematically in Figure 2-28 which resemble the morphology of QF as shown in Figure 2-17 (b). Therefore, sometimes it is difficult to distinguish whether a specific microstructure is AF dominant or QF dominant just by morphology characteristics, e.g. in Figure 4-4. Similarly, it was found in research [124] that some grains with the same morphology belong to different phases and it is very difficult to differentiate QF grains from GB packets using OM or SEM. But according to the phase transformation characteristics of steels, phases transformed at different temperatures or with different transformation mechanisms have different defect densities and thus different microhardness values as shown in Figure 2-41 for an ultra-low carbon steel [125]. It is evident that there is a large microhardness difference between QF and BF. Since AF can be regarded as intragranularly nucleated BF, it should have a similar hardness value to that of BF. Therefore, microhardness values can be used to determine whether a microstructure is AF dominant or QF dominant. For example, in Figure 4-8 we can see that most of the microstructures have hardness values higher than HV210 indicating that these microstructures should be AF/BF dominant.
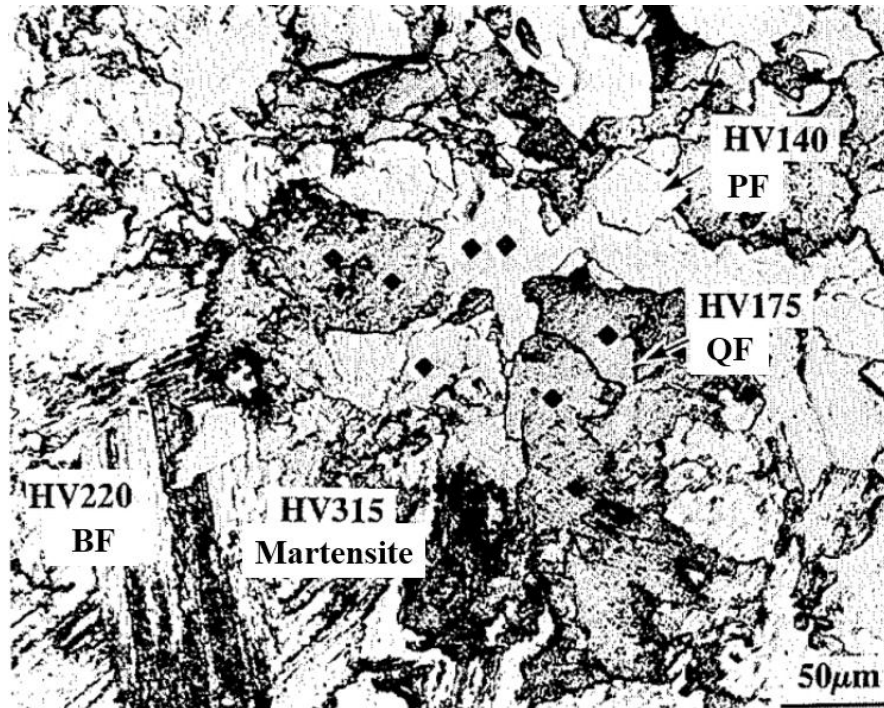
Figure 2-41 Optical microstructures and microhardness of various transformation products of an ultra-low carbon steel. Adapted from [125].

Another way to determine whether a microstructure is QF or AF dominant depends on the distribution of disorientation angles. Since PF/QF grains usually do not have a near K-S OR with the prior-austenite grains they grow into, the disorientation angle distribution of PF/QF grains will be quite random as shown in Figure 2-42, especially for disorientation angles between 21°~47° [126]. As listed in Table 2-3, for displacive transformations, variants following K-S OR within the same prior-austenite grain do not have disorientation angles between 21°~47°, so for displacive transformation products, e.g. AF and BF, the frequencies for disorientation angles between 21°~47° should be significantly lower than for others as shown in Figure 4-6. Therefore, the distribution of disorientation angles can generally be used to differentiate AF and QF dominant microstructures.
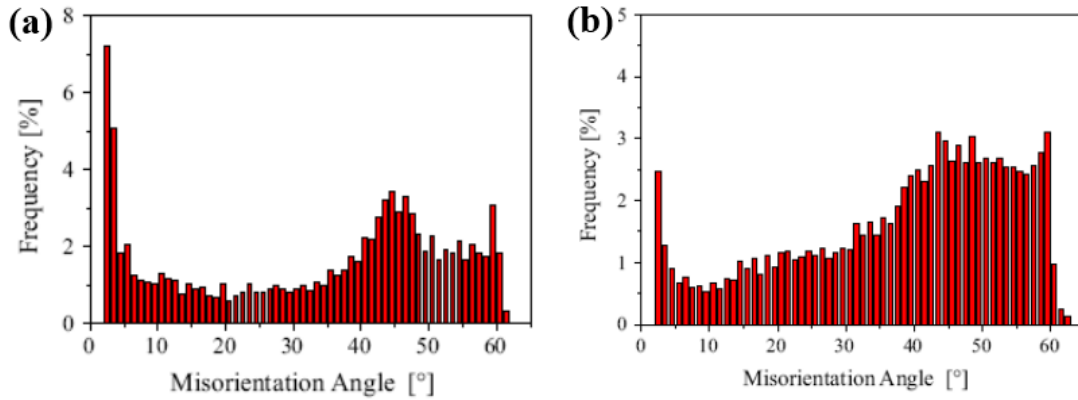
Figure 2-42 Histograms showing the boundary misorientation angle distributions of PF/QF grains transformed from: (a) recrystallised austenite and (b) deformed austenite of a low carbon Mo-Nb pipeline steel. Adapted from [126].

However, to determine whether a specific grain is AF or QF is still very difficult. Due to the similar morphology characteristics, it is hard to distinguish AF and QF even under SEM. Although it was found in research [88] that after a long time etching and under a SEM with a high resolution, a difference in etching status can be seen between PF/QF and AF as shown in Figure 2-30, it can not be used under the normal magnification needed to reflect the transformation microstructure. By the help of crystallographic data provided through EBSD mapping, QF and AF can be discriminated from each other by the differences in electron backscatter pattern (EBSP) clarity [127] and orientation gradients [128], due to different dislocation densities in these grains. Furthermore, it was found in this research that, QF can be differentiated from AF by carefully comparing the pole figure characteristics to see whether a specific grain has a near K-S OR with the prior-austenite grain.

2.7.2 Discrimination between BF and AF

Based on the description in Section 2.5, there are three characteristics of AF microstructure: intragranular nucleation, intersecting and irregular morphology and a high density of high angle grain boundaries (HAGBs). The latter two

53

characteristics indicate that in AF microstructures variants belong to different CP groups and at the same time different Bain groups are formed adjacently. For BF microstructure transformed at relatively high temperatures, Figure 2-40 (a), although intersecting laths are formed, these laths come from the same Bain group, suggesting a low density of HAGBs. For BF microstructure transformed at relatively low temperatures, Figure 2-40 (b), although variants from different Bain groups are formed side by side and a high density of HAGBs exist, these laths come from the same CP group, suggesting evident parallel morphology of this BF microstructure. Therefore, BF microstructures can be readily distinguished from AF by morphological characteristics and HAGB densities.

Some may argue that in both Figure 2-40 (a) and (b), in the centre part of the prior-austenite grains where different packets collide, variants from different Bain groups and at the same time different CP groups exist, so these laths should be named as AF. But it is clear that the existence of these packet-colliding regions are an inevitable and intrinsic characteristic of BF microstructures so long as more than one BF packet is formed in each austenite grain. And these packets nucleate on prior-austenite grain boundaries instead of intragranular features. Therefore, it is not appropriate to identify these packet-colliding regions as AF. However, the possibility that the sympathetic nucleation of BF results in a new lath belonging to both different CP group and different Bain groups can not be overlooked, although this kind of sympathetic nucleation hasn't been observed in Bainite. If it does exist, further investigations are needed to distinguish the sympathetically nucleated BF and AF intragranularly nucleated on deformation substructures.

Based on the description above, microhardness values and disorientation angle distributions obtained by EBSD were used in this thesis to determine whether the transformed microstructure is QF dominant or AF dominant. Furthermore, morphological characteristics, parallel for BF and chaotic for AF, and boundary maps plotting HAGBs were used to discriminate AF from BF.

Chapter 3　Experimental Details

In this chapter the material, experiment apparatus and microstructure characterisation methods used in this thesis are introduced, together with some illustrations about the post-processing procedures for EBSD data. But the detailed thermomechanical processing parameters for each specimen are given in the following chapters separately.

3.1 Material

Since both the thermomechanical processing parameters and the chemical composition of the steel can influence the final microstructure, to investigate the effect of thermomechanical processing parameters accurately, only one pipeline steel was used in the entire thesis, which is an API X-80 high temperature processing (HTP) pipeline steel.

The material used in this thesis was received as a half diameter of a steel pipe section provided by Companhia Brasileira de Metalurgia e Mineração (CBMM), Brazil. The as-received microstructure was characterised in Section 3.4. The chemical composition of this HTP steel is listed in Table 3-1. Due to the high niobium content, the retardation of austenite recrystallisation can be achieved at significantly higher temperatures as shown in Figure 2-6. Consequently, finish rolling can be carried out at higher temperatures, which is called high temperature processing.

Table 3-1 Chemical compositions (wt%)

C	Mn	Si	S	P	Nb	Cr	Ni	Cu	Ti	N
0.045	1.43	0.14	<0.003	<0.01	0.09	0.21	0.12	0.21	0.01	0.0039

The carbon content of this steel was lowered to 0.045% to improve the weldability, toughness, ductility, solubility of such high concentration of niobium, segregation reduction and thus corrosion resistance [26]. Titanium was

55

added to fix the nitrogen and to form thermodynamically stable nitrides to control the austenite grain size during reheating. The fix of nitrogen by the addition of titanium effectively prevents the formation of niobium carbonitride, allowing for a higher niobium content to be dissolved during reheating. Compared with the typical composition of HTP steels [26], the manganese concentration of this steel is reduced to alleviate the segregation of manganese and thus the banded structures formed during cooling. Chromium, nickel and copper are added as solid solution strengthening elements to compensate the reduced manganese and lower the corrosion rate under medium severe sour conditions [26].

The high temperature processing leads to a significant reduction of the finish rolling load, compared to the high strain and low temperature deformation required for conventional Nb-V microalloyed steels. This helps older plate mills which cannot accommodate high rolling loads to enter the profitable pipeline steel production. Moreover, the high processing temperature results in less evident textures associated with the final microstructure, which can improve the H_2S resistance. In addition, HTP steels are more economical than those steels relying extensively on vanadium or molybdenum microalloying [26, 129].

3.2 Plane strain compression and continuous cooling tests

3.2.1 Plane strain compression

Various laboratory-based mechanical testing methods, including plane strain compression (PSC), axisymmetric compression, tensile testing and torsion have been used to study the hot working behaviour of metals under different strain conditions. Since during industrial rolling, materials are subjected to a plane strain deformation, the plane strain compression test is the closest and thus the most commonly employed method to conduct laboratory physical simulations of the commercial hot rolling [130]. Furthermore, the PSC test has some additional

advantages over other physical simulation techniques. It can be used to achieve high-strain deformations unlike the tensile test and the volume of material undergoing deformation is relatively large, which is convenient for subsequent microstructure characterisation and mechanical property testing [130]. Therefore, in this thesis, plane strain compression is adopted to simulate the thermomechanical processing of pipeline steels.

All the PSC tests in this thesis were conducted using the servo-hydraulic Thermomechanical Compression (TMC) machine at The University of Sheffield shown in Figure 3-1. Some important features of the TMC machine are listed in Table 3-2. The operating system of the TMC machine is fully digitised and computer controlled to allow a precise control of many deformation parameters including temperatures, strains and constant true strain rates.

Table 3-2 Key features of the servo-hydraulic Thermomechanical Compression machine [131].

	Machine characteristics
Actuators	Servo-hydraulic
Maximum strain	~2
Maximum strain rate	$150 - 200s^{-1}$
Maximum Deformation temperature	1200°C
Maximum load	500 kN
Machine Stiffness	410 kN/mm
Maximum FTTU Reheating Temperature	1300°C
Full Quench start time	< 0.5second from end of deformation
Controllable cooling variables	Forced air, mist and water quench
Reheating rate	Rapid and controlled heating (up to 1300°C)
Atmosphere control	None (natural air)
Temperature measurement	Up to 3 thermocouples inside PSC specimen
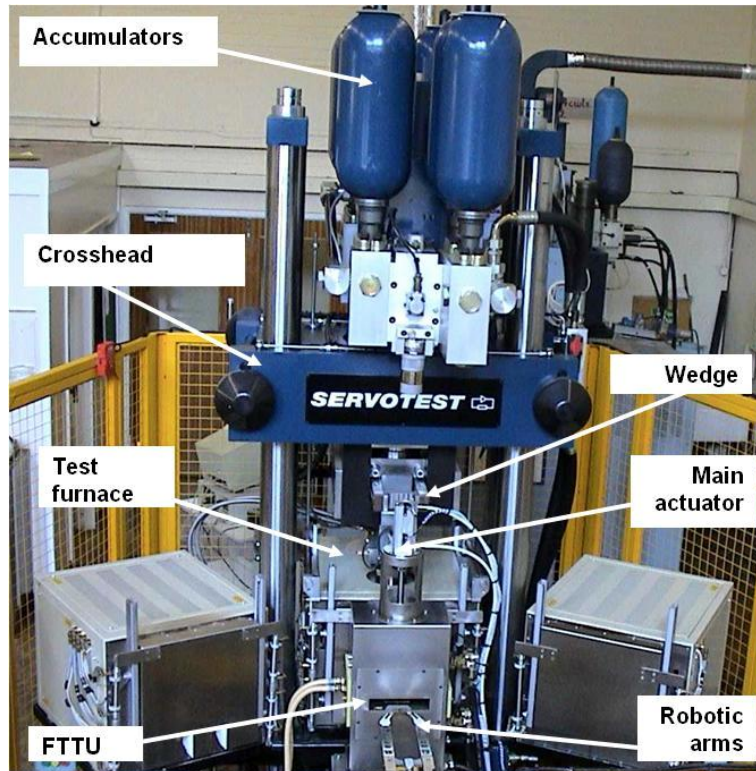
Figure 3-1 Outline structure of main components of TMC machine [131].

The configuration of the PSC test is shown in Figure 3-2. PSC specimens with a dimension of 60 mm $\times$ 30 mm $\times$ 10 mm were machined from the received HTP steel pipe section, according to the engineering drawing shown in Figure 3-3. The notches on the two sides of the PSC sample are machined for robotic arms holding the PSC sample. During the PSC test, a specimen is deformed between two flat parallel tools (with a width of 15 mm at room temperature) and the load-displacement data are recorded accurately. The tools are made of a nickel-based superalloy which are hard enough to withstand the load required for high temperature deformations.
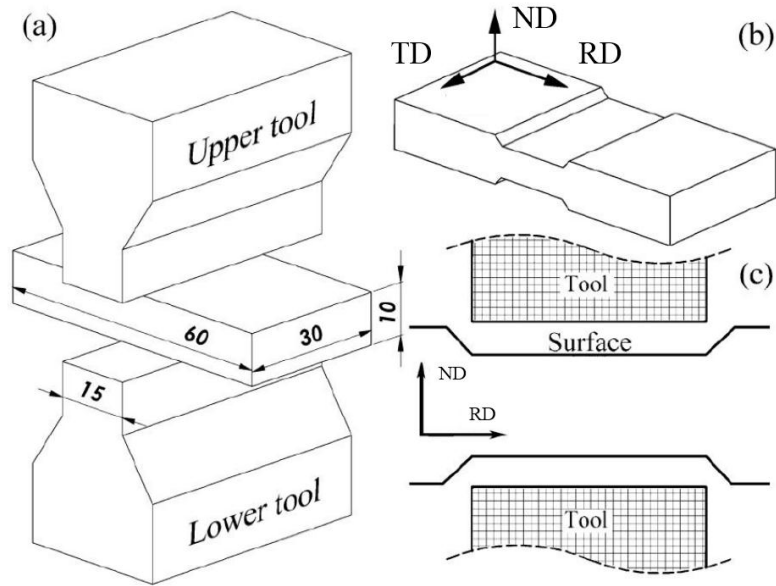
Figure 3-2 Schematic illustration of the configuration of plane strain compression test, (a) positions and geometries of PSC specimen and deformation tools, (b) deformed specimen and (c) the normal direction-rolling direction (ND-RD) plane of deformed PSC specimen for microstructure characterization [21].
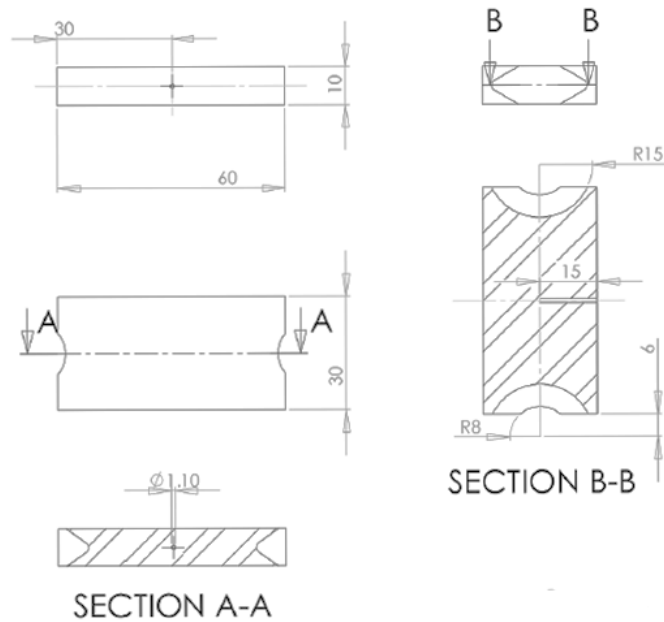
Figure 3-3 Engineering drawing of steel PSC specimen in the unit of millimetre [21].

It needs to be mentioned that for PSC tests on the TMC machine, before each deformation, the upper tool is lifted so that there is enough distance between the

59

upper tool and the specimen to accelerate the upper tool to a velocity required for the desirable strain rate when it contacts with the specimen. By doing that the instant strain rate of a PSC test on the TMC machine can be controlled precisely and the tool acceleration needed is finished when the tools and the specimen start to contact, which is far better than the PSC test on a Gleeble-like machine where the tool acceleration needed begins when the tools and the specimens are contacting. Furthermore, prior to each hot deformation, the wedge which is a mechanical stop device shown in Figure 3-1, automatically moves to a pre-defined position for the desirable strain so that the actual deformation strain does not exceed the desirable strain. The temperature of the specimens can also be precisely controlled over a uniform area, which is introduced in the next section.

3.2.2 Reheating and cooling

The temperature control of the specimens during the tests is fulfilled in the fast thermal treatment unit (FTTU) located in front of the test furnace as shown in Figure 3-1. The FTTU consists of an induction heating coil, a specimen cooling system (capable of air blasting, mist cooling and water quenching), an induction heating coil cooling system and an electrical converter. The temperature of the specimen is sampled through a thermocouple embedded into the PSC specimen.

To fully exploit the benefit of Nb addition on the deformation restoration retardation and the hardenability improvement, it is necessary to dissolve the Nb carbide or carbonitride precipitates back into solid solution during the reheating process. Given the high niobium concentration (0.09%) in the tested steel, a high reheating temperature and a long isothermal holding duration are needed.

To determine the dissolution temperature of Nb carbide or carbonitride precipitates in the tested steel, a thermodynamic calculation was conducted using the Thermo-calc software with the database TCFE6. The mole fractions of each phase at different temperatures are shown in Figure 3-4 (a). Because of the small

60

mole fractions of various precipitates, the region in Figure 3-4 (a) with mole fraction between 0 and 0.006 is enlarged and shown in Figure 3-4 (b). The dissolution temperatures for various precipitates are given in brackets. It is clear from Figure 3-4 (b) that at a temperature higher than 1156˚C, NbC should be dissolved according to the thermodynamic calculation.
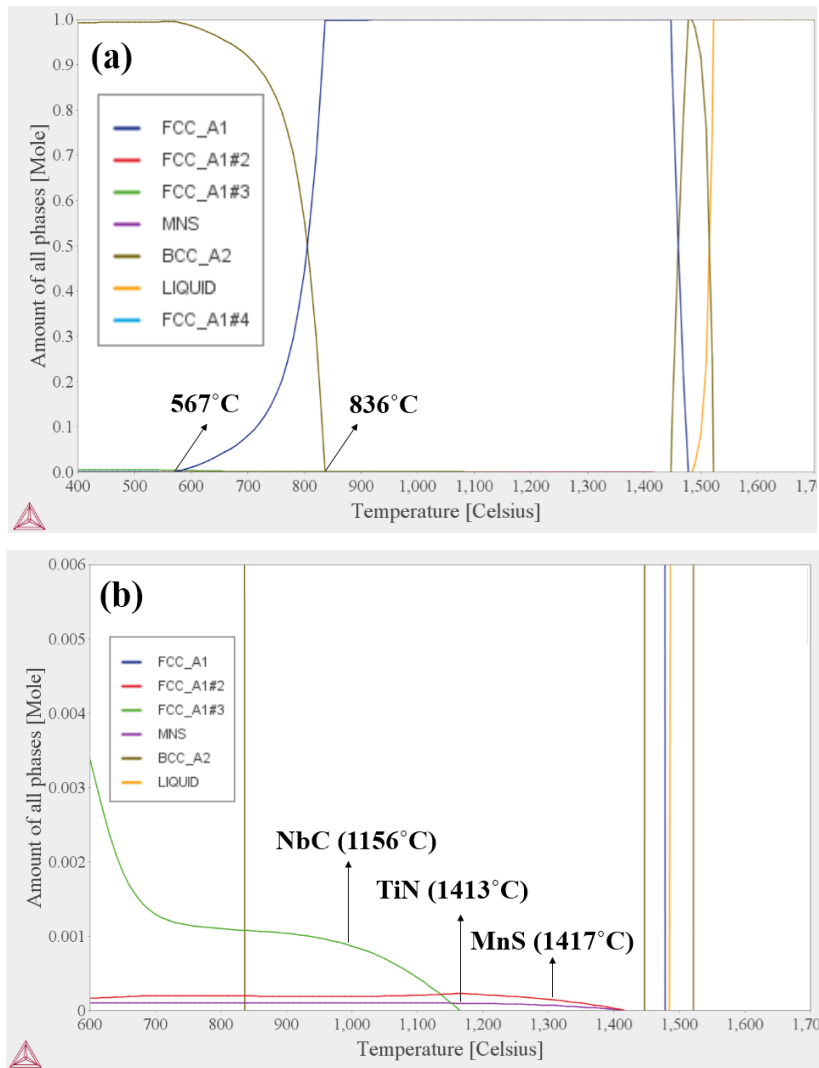
Figure 3-4 Thermodynamic calculation of phase constitution of the tested HTP steel at different temperatures using Thermo-calc software.

However, it was argued that thermodynamic calculations of solubility products tend to overlook the interaction between different elements and thus the activity coefficients are supposed to be unity. Consequently, activities are

represented by their weight percents, which is unrealistic [132]. Since most of the nitrogen in the tested steel is fixed by the addition of titanium, NbC should dominate the Nb related precipitates. Therefore, a solubility product, based on atom probe data and expressed as [132]:

$$\log[\text{Nb}][\text{C}] = 2.06 - \frac{6700}{T} \tag{3.1}$$

was adopted and the lowest temperature required to dissolve NbC in the tested steel is 1232°C.

Since the operating duration of FTTU at high temperatures above 1200°C cannot exceed 0.5 hours due to the limitation of the coil cooling system, all machined PSC specimens were subjected to an additional solid solution heat treatment before the PSC tests to shorten the reheating time in the FTTU. During the solid solution heat treatment, most of the specimens were individually heated to 1250°C in a tube furnace with Ar atmosphere protection, held for 30 minutes, and then directly quenched in ice water to keep the solute elements in solution.

Besides reheating, continuous cooling is also fulfilled in the FTTU. During the TMCP of steel plates, there are several cooling processes depending on the cooling rates and cooling interrupt temperature as shown in Table 3-3, including interrupted accelerated cooling (IAC), continuous ACC, direct quenching plus self-tempering (QST) and direct quenching (DQ) [133]. The typical cooling rates achieved for steel plates with different thickness on the MULPIC water cooling system from SIEMENS VAI is shown in Figure 3-5 [134] and we can see that the achievable cooling rates are largely between 1~60°C/s.

Through a previous systematic investigation on the maximum controllable linear cooling rates in the FTTU of the TMC machine, it was found that the largest cooling rates for air blasting and mist cooling are 25°C/s and 67°C/s respectively [135], which means the various cooling processes for industrial plate production can be successfully simulated in the FTTU. Furthermore, the above results were obtained from 10 mm thick undeformed PSC specimens, therefore for deformed PSC specimens the reduction in thickness can result in a

larger controllable linear cooling rate.

Table 3-3 Classification of different cooling process and corresponding cooling rate(dependent on plate thickness) in the TMCP [133].

	Stop Cooling Temperature	Cooling Rate
IAC	above M_S temperature	5-80°C/s
Continuous ACC	down to 200°C	
Interrupted Direct Quenching or QST	below B_S or M_S Temperature	10-60°C/s
DQ	down to 200°C	
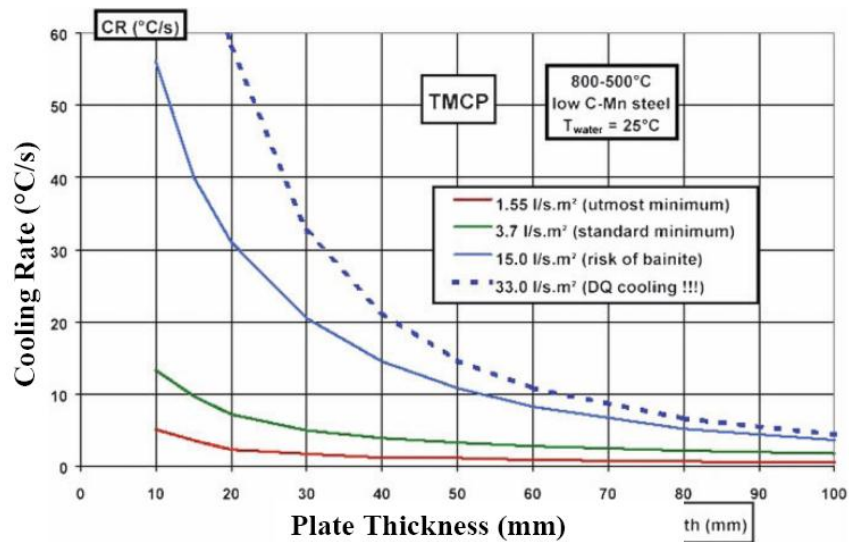
Figure 3-5 Typical cooling rates achieved for steel plates with different thickness on the MULPIC water cooling system from SIEMENS VAI [134].

3.3 Microstructure characterisation methods

3.3.1 Optical microscopy and scanning electron microscopy

After the plane strain compression and the continuous cooling, specimens were cut on the normal direction-rolling direction (ND-RD) plane, and then mechanically ground and polished down to 1 μm using silicon carbide abrasive papers and monocrystalline diamond suspensions, respectively. To reveal the

continuous cooling transformation products, a 2% Nital solution was used as an etchant on the polished surface. While saturated aqueous picric acid solution with the addition of surfactant Teepol and 3 drops of HCl was heated to 65˚C and was utilized as an etchant to reveal the prior-austenite grain boundaries (PAGBs) [136, 137]. The etched surface was observed under a Nikon Eclipse LV150 optical microscope to check the morphologies of the transformation products and the prior-austenite grains. Two scanning electron microscopes, JEM JEOL 6400 and FEI InspectF, were used to observe the transformed microstructure in greater detail.

Although during the plane strain compression on the TMC machine, specimens can be successfully deformed to the designed nominal compression strains, through a systematic thermomechanically coupled finite element (FE) analysis carried out by Mirza and Sellars [130, 138, 139], it was found that the equivalent strain distributions are not homogeneous in the deformed specimen as shown in Figure 3-6. The inhomogeneity of strain distribution can cause non-uniform microstructures during the subsequent continuous cooling. Therefore, to accurately investigate the microstructure evolution, the observation area must be selected carefully. According to the results shown in Figure 3-6, the suitable area actually is not located in the longitudinal centre of the specimen, deviating 1 mm to 4 mm from it along RD as shown by the area between positions A and B in Figure 3-6. Furthermore, due to the existence of intense friction on the specimen surface contacting with the tools during deformation, the strain conditions near these contacting surfaces will be far from plane strain conditions. Therefore the area in the centre along ND and between positions A and B along RD was selected for all microstructure and textural characterisation in this entire thesis.
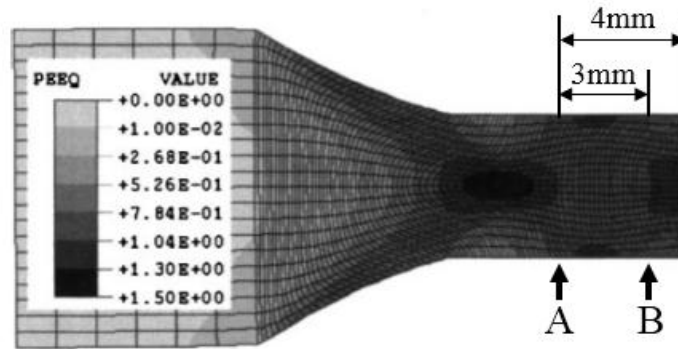
Figure 3-6 Predicted distributions of equivalent strain for a 316L stainless steel specimen after a plane strain compression with nominal equivalent strain of 1 and strain rate of 10s^{-1} at 1000°C [138].

3.3.2 Electron backscattering diffraction mapping

Additionally, electron backscattering diffraction (EBSD) mappings were also carried out in this research. The necessity of using EBSD mappings in AF microstructure related research can be explained from the following aspects. In AF dominant microstructures, PF/QF not only forms on the austenite grain boundaries but also on the substructures formed within the deformed austenite grains as shown in Figure 2-1, and the AF lath boundaries cannot be clearly revealed by nital [89] as shown in Figure 2-27. Given that, it is hard to distinguish different phases even under the SEM. Although, it was found in research [88] that after long time etching and under a SEM with a high resolution, a difference in etching status can be seen between PF/QF and AF. This discrimination can only be conducted under high magnifications (4000X in research [88]) and thus is not suitable for quantification. Differently, a number of phase quantification methods based on EBSD data were proposed and successfully applied to complex transformation microstructures in steels [124, 128, 140, 141]. Furthermore, using only OM and SEM, it is difficult to examine the effect of different degrees of deformation and cooling conditions on the grain refinement of the transformed microstructures. This is because the AF microstructures

observed by optical microscopy are usually finer than the crystallographic effective grain whose refinement is important for the improvement of toughness [85] and for displacive transformation products, the absence of EBSD techniques may lead to incorrect conclusions on grain refinement. In reference [142] it was found that the packet size is reduced after ausforming, which results in a refined microstructure when viewed under the optical microscope. But it was shown that the block width become larger after ausforming, which means that the crystallographic effective grain size actually becomes larger. Last but not the least, the orientation information of the transformed microstructures can be obtained through EBSD mappings, which can be used to analyse various crystallographic characteristics of the transformed microstructures.

To prepare the samples particularly for EBSD mapping, after grinding and polishing as mentioned in section 3.3.1, the samples were then polished with a colloidal silica suspension for an additional 2 minutes. EBSD mappings were performed on the RD-ND plane of the specimen in a FEI Sirion Field Emission Gun Scanning Electron Microscope (FEGSEM) with a working distance of 14 mm and accelerating voltage of 20 kV. The specimen was tilted around RD to 70° to the horizontal plane. The electron backscattering diffraction patterns (EBSPs) were acquired by an Oxford Instrument HKL Nordlys F+ Camera which was positioned to 164.7 mm, and these patterns were transformed into orientation data by an HKL Channel 5 Flamenco package.

For EBSD mappings, an appropriate selection of step size is significantly important. A step size of one-tenth of the average grain size is often utilised for microtexture and grain misorientation measurements, and an appropriate step size also depends on the scale of the feature investigated and the status of the material [143]. A step size equal to the smallest grain size can be used to observe the spatial distribution of texture components in an area, while for a detailed map illustrating microstructure morphologies or subtle orientation spreads within grains, a smaller step size compared to the average grain size is required.

Furthermore, typically, a step size of 1 μm might be required for a recrystallised microstructure, whereas for a unrecrystallised microstructure, the step size may have to be as small as 0.01~0.1 μm [143]. Since for the AF dominant microstructures, the grain size measured by EBSD is largely within the range of 1.6~3.0 μm [83] and there is a high density of substructures within AF laths, inherited or generated during transformations, a step size of 0.2 μm was used throughout this research except for the PF/QF dominant microstructures where 0.5 μm was chosen as the step size instead. As the ferritic phase was the main focus in this research, α iron (BCC) was chosen as the only matching unit in the HKL Channel 5 Flamenco package during the mapping to reduce the mis-indexing of phases in the complex transformation microstructures.

The obtained EBSD data were analysed using several in-house programs in C language together with the HKL Channel 5 post-processing software including Tango, Mambo and Salsa packages.

During the EBSD data analysing, it is universally found that the index rate of an EBSD mapping is below 100% and the rest of the pixels are zero solution. The existence of these non-indexed points can be attributed to their low quality EBSPs which cannot be recognised by the acquisition software. The non-indexed points are usually located near or at dislocations substructures, damage/contamination on the sample surface and grain boundaries. Differently, due to the poor quality of EBSPs near or at these locations, the orientations could also be wrongly indexed which is called spikes. It is obvious that these non-indexed points or spikes which together are called noise points, will have a negative effect on the crystallographic analysis of the EBSD data. Therefore, a reduction of the non-indexed points and spikes is necessary. However, it was found that these noise reduction procedures could have an effect on the results of the effective grain size measurement [144, 145]. A conservative progressing noise reduction method proposed in research [146] that could eliminate as many noise points as possible without introducing additional fictitious data points to

bias grain size measurement was used throughout this thesis. This method was conducted using the noise reduction function in the Channel 5 Tango package and can be described as follows: first, remove the spike points; second, fill the non-indexed points with the most common orientation of their 8 neighbouring pixels if they have; then, repeat the second step with 7, 6 and 5 neighbouring pixels respectively.

As for the grain size measurement, there are two approaches provided in the HKL Channel 5 Tango package. The first one is based on the linear intercepts in both horizontal and vertical directions and the geometric mean of them can be used as the grain size. The other method is based on the grain detection by setting a critical disorientation angle and detecting grains surrounded by boundaries with disorientation angles higher than the critical values, and the average values of both grain areas and diameters of equivalent circles around grains could represent the grain size. Since the latter one is more susceptible to the noise points in the EBSD data [146], the method based on the linear intercepts was adopted throughout this thesis. To measure the grain size, disorientation threshold values should be selected. Different disorientation threshold values have been used to define microstructure parameters that can be related to certain mechanical properties, and the microstructural unit size that controls strength may differ from that which controls toughness. Disorientation threshold values of 4° and 15° are typical threshold values to define the grain size for strengthening and toughening, respectively [83, 147]. Low angle disorientation (4°) grain size is one of the factors that controls the yield and tensile strength of steel because boundaries with disorientation angles above this value are expected to be able to oppose dislocation movements, while high angle boundaries (15°) provide effective barriers to cleavage fracture [147, 148]. The grain size measured against the high disorientation angle (15°) is usually called the effective grain size.

3.3.3 Microhardness

Besides microscopy, the hardness testing result is still an effective tool to identify different transformation products during continuous cooling [58, 125]. Since various transformation products have different transformation temperatures and thus distinct dislocation densities and grain sizes, there is a certain hardness range for each product. Vickers microhardness values were obtained with a 500 g applied load and a 20 second dwelling time on a Mitutoyo hardness testing machine. Ten indentations were measured on each specimen.

3.4 Initial microstructure characterisation

To characterise the as-received microstructure of the tested steel, specimens were sectioned from the original pipe on the RD-ND plane and then prepared carefully for the OM and SEM observation and the EBSD mapping. The optical micrograph and SEM secondary electron micrograph of the as-received microstructure are shown in Figure 3-7 (a)~(b) respectively. It can be seen that the final microstructure may consist of chaotic arranged AF laths or irregular QF grains. Within the matrix, granular-shaped microphases, probably M/A constituents appear black in the optical micrograph while white in the SEM secondary electron micrograph.
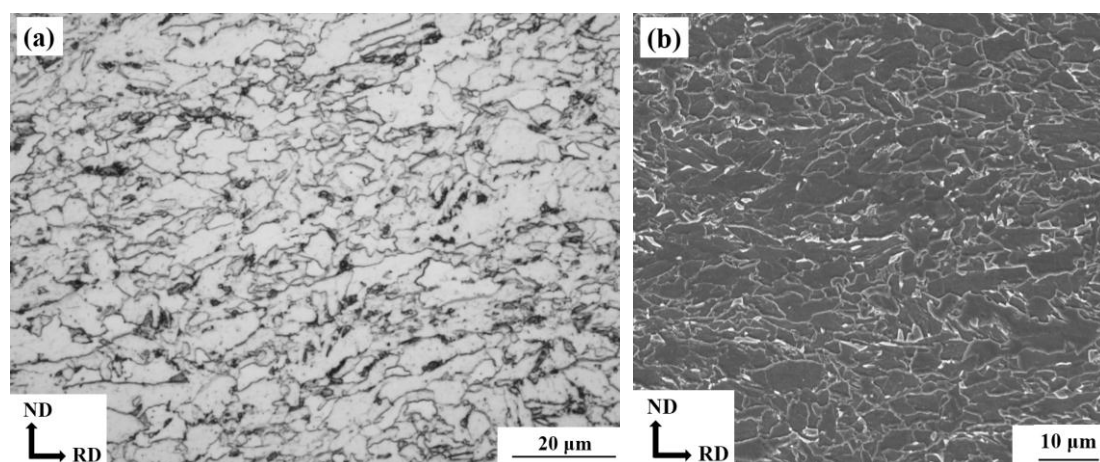
Figure 3-7 Optical micrograph (a) and SEM secondary electron micrograph (b)

69

depicting the as-received microstructure on the ND-RD plane.

An EBSD mapping was also performed on the RD-ND plane of the as-received steel with a step size of 0.2 μm. After the aforementioned noise reduction procedures, the inverse pole figure (IPF) coloured orientation map and the corresponding boundary map with red lines representing high angle grain boundaries (HAGBs) and blue lines indicating low angle grain boundaries (LAGBs) are shown in Figure 3-8 (a)~(b) respectively. The fine-grained characteristic of the as-received microstructure can be seen clearly from these EBSD maps. LAGBs can be found in most of the fine grains indicating that the transformed microstructure mainly consists of acicular ferrite. Meanwhile, there are still some regions with a lack of HAGBs but rich in LAGBs which can be identified as BF regions.
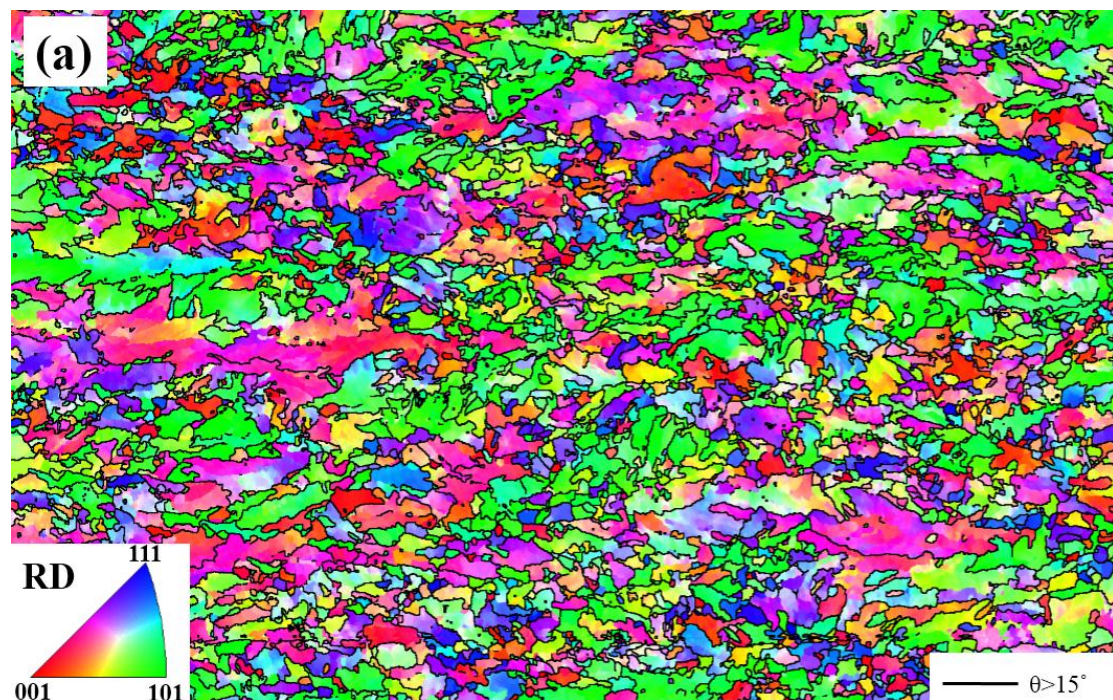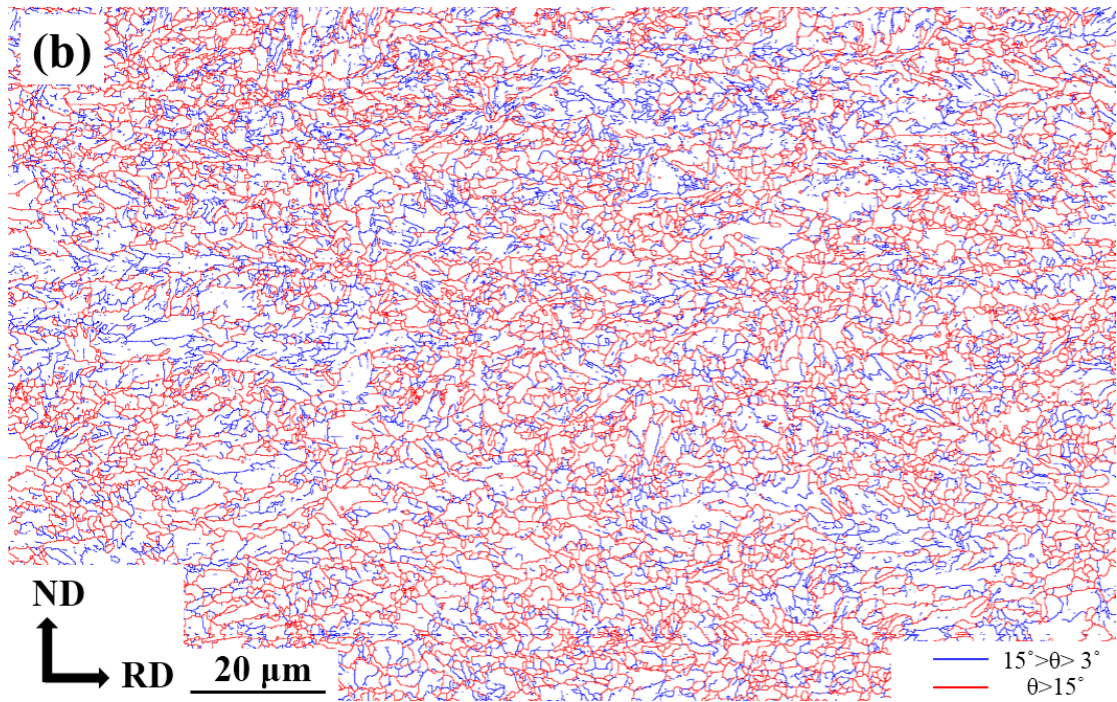
Figure 3-8 IPF coloured orientation map (a) and boundary map (b) with red lines representing HAGBs (disorientation angle >15˚) and blue lines indicating LAGBs (disorientation angle >3˚) on the RD-ND plane of the as-received steel.

Chapter 4 Effect of austenite deformation on microstructure evolution

4.1 Introduction

An important aspect of the thermomechanical processing of pipeline steels is the deformation below the recrystallisation-stop temperature ($T_{5\%}$), which renders the austenite grains highly elongated and deformed. This austenite conditioning strongly affects the transformed microstructure and, hence, the final mechanical properties [2, 91]. The effect of austenite deformation on the accelerated cooled transformation products has been studied by many researchers but the results are still controversial. Considering the effect of austenite deformation on the grain refinement as an example, in some investigations [85, 149, 150], it was found that the transformed microstructure is refined by the austenite deformation and the fraction of AF increases with increasing deformation. Contradicting this were results from another investigation [151] in which it was shown that the effective grain size of bainite was raised from 3.2 μm to 3.8 μm when the austenite was deformed by 30%. Furthermore, the block size of the bainite was found to be increased after austenite deformation [142], and the quantity of packets in each austenite grain also decreased after the austenite deformation [152]. More importantly, it was revealed from these investigations that even after significant austenite deformation, the transformation product still consisted of parallel BF laths and the typical AF microstructure was absent.

Therefore, in this chapter, different strains were applied to austenite before the continuous cooling to investigate the effect of deformed austenite on the microstructure evolution, including the transition between AF and BF, the grain refinement and the refinement of M/A constituents. Furthermore, the post-deformation softening behaviour of austenite was also illustrated.

72

4.2 Experimental

As mentioned in Section 2.2, the rough rolling is usually conducted above the recrystallisation-limit temperature ($T_{95\%}$) so that the austenite grain size can be refined by repeated recrystallisation, while the finish rolling should be performed below the recrystallisation-stop temperature ($T_{5\%}$) so that the deformation-induced substructures can be well-retained, leading to refined and homogeneous transformed microstructures. If the austenite deformation temperature is set between the $T_{95\%}$ and $T_{5\%}$, partial recrystallisation of deformed austenite will occur resulting in inhomogeneous transformed microstructures. Therefore, austenite deformations at temperatures between $T_{95\%}$ and $T_{5\%}$ are generally avoided.

The $T_{95\%}$ and $T_{5\%}$ are susceptible to the influences of steel's chemical composition [19], austenite deformation conditions (deformation mode, temperature, strain and strain rate) and inter-pass delay time [153]. Therefore, it is necessary to determine these temperatures for the specific steel and processing parameters to define the processing window, using the interrupted plane strain compression or double-hit tests. Since the evolution of transformed microstructure is the focus, double-hit tests were not conducted in this thesis. The deformation temperature below $T_{5\%}$ was firstly set according to various results in the literature and then testified through the observation of the deformed austenite microstructures.

Since the typical $T_{95\%}$ for HTP steels is around 1050˚C [26], the deformation temperature below $T_{5\%}$ was selected as 950˚C, and the strain was increased from 0 to 0.7. The processing route is illustrated in Figure 4-1. The solid solution heat treated specimens illustrated in section 3.2.2 were reheated to 1200˚C at a rate of 10˚C/s, held for 2 minutes for equilibration, then cooled at a rate of 5˚C/s to 1100˚C for a roughing deformation (strain1) of 0.3 at a constant true strain rate of 10s⁻¹. After that, the specimens were cooled immediately to 950˚C at a rate of 5˚C/s for the finishing deformation with strain2 varying between 0~0.7. This

73

second deformation was also performed at a constant true strain rate of 10s^{-1}, and was followed by an accelerated cooling from 950˚C to 500˚C at a rate of 20˚C/s, a slow cooling from 500˚C to 350˚C at a rate of 1˚C/s, and finally a water quenching from 350˚C to room temperature. Furthermore, another three specimens were also heat treated and deformed but were water quenched directly before strain2 and after strain2 of 0.5 and 0.7 to examine the as-deformed austenite microstructures.
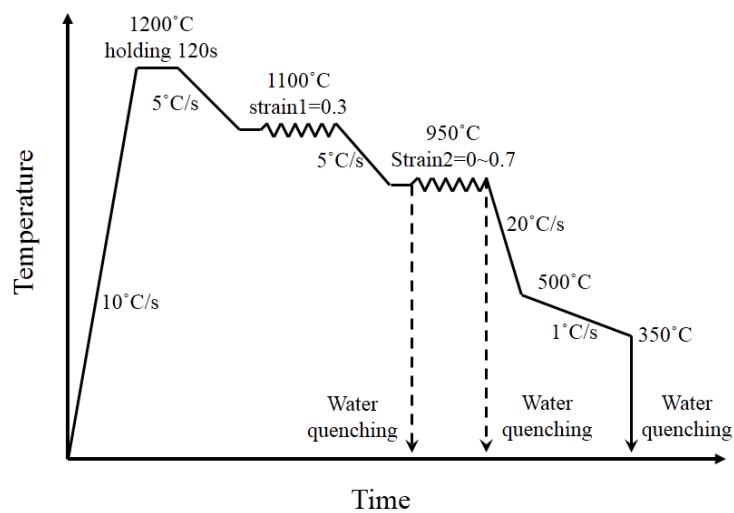
Figure 4-1 Schematic illustration of the thermomechanical testing profile.

Specimens for OM and SEM observation and EBSD mapping were prepared carefully as illustrated in Section 3.3. A 2% nital solution was used to show the transformed microstructures and a saturated aqueous picric acid solution was used to reveal the prior-austenite grain boundaries (PAGBs). Besides microscopy, mechanical properties of the transformed products were characterised by Vickers microhardness as described in Section 3.3.3.

EBSD analyses were carried out with a step size of 0.2 µm and accelerating voltage of 20 kV on the RD-ND plane of each specimen. Noise reduction and grain size measurement were performed as introduced in Section 3.3.2.

4.3 Results

4.3.1 Flow behaviour

The load-displacement data recorded during austenite deformation was converted into the von Mises equivalent stress-strain data according to a standard procedure [154]. The flow stress curve with strain2 of 0.7 is shown in Figure 4-2. It can be seen that during the second deformation (strain2) the flow stress increased gradually with strain2 and started to decrease after reaching a peak strain of 0.53, which is a characteristic of dynamic recrystallisation (DRX). However, this flow stress curve reflects the average, macroscopic deformation condition of the entire specimen. Due to the existence of strain gradients in the current plane strain compression tests as shown in Figure 3-6, optical micrographs depicting the PAGBs before strain2 and after strain2 of 0.5 and 0.7 are shown in Figure 4-3 respectively, to determine the austenite deformation behaviour accurately.
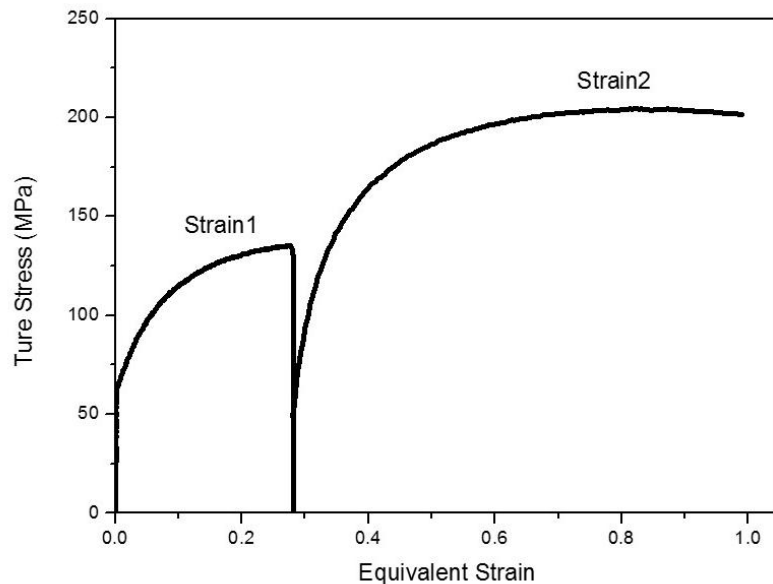
Figure 4-2 Macroscopic flow behaviour from testing scheme of strain2 of 0.7.
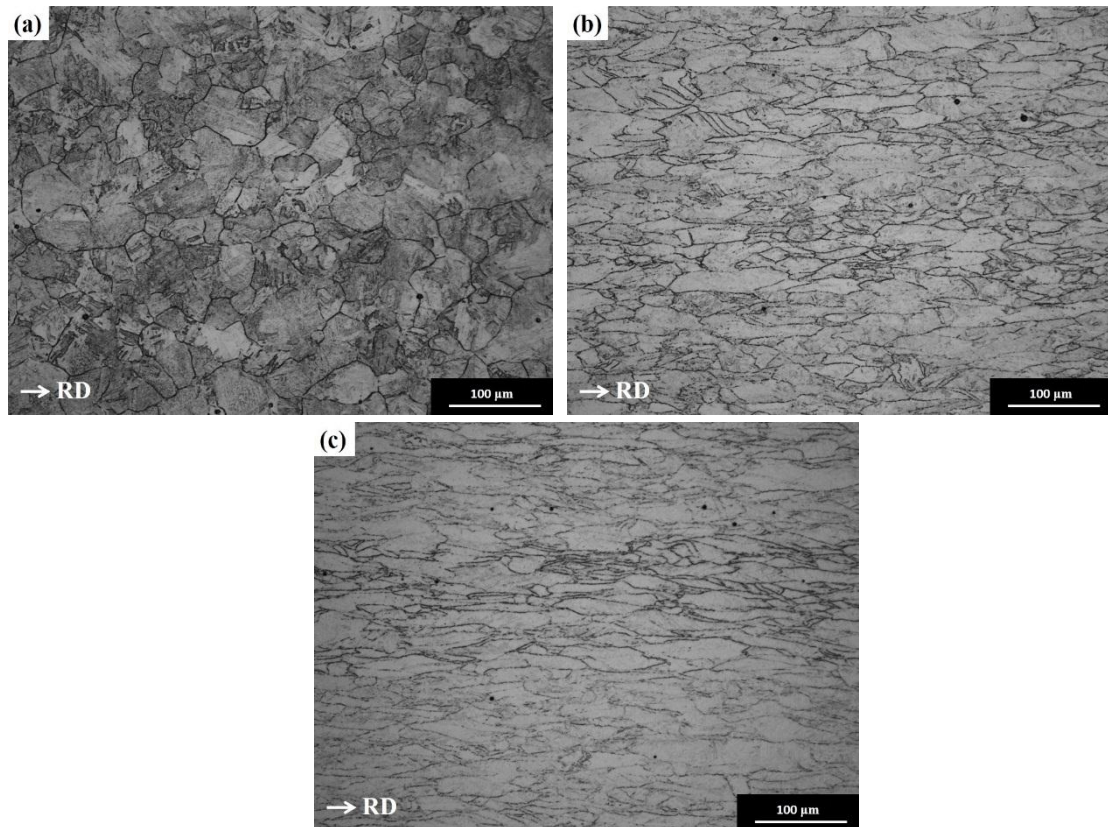
Figure 4-3 Optical micrographs showing PAGBs of water-quenched specimens: (a) after strain1 of 0.3, (b) after strain2 of 0.5 and (c) after strain2 of 0.7.

In Figure 4-3 (a), it is evident that before strain2, austenite grains are fully recrystallised with an average linear intercept length of 37.0 μm measured from multiple micrographs. In Figure 4-3 (b), the austenite microstructure remains in an unrecrystallised condition, while in Figure 4-3 (c) there are some small dynamically recrystallised austenite grains at the triple junctions of the elongated austenite grains. The recrystallisation fraction was measured as 6%, which means that at strain2 of 0.7, dynamic recrystallisation (DRX) was just triggered during austenite deformation, and the recrystallisation fraction is quite low at the end of deformation.

4.3.2 Microstructures

To observe the microstructure evolution with the increase of strain2, SEM secondary electron micrographs of the transformed microstructure are shown in

Figure 4-4 (a)~(e). In Figure 4-4 (a) and (b), a parallel morphology of the transformation products can be seen clearly. PAGBs remain, and the parallel laths developed from the PAGBs extended into the austenite grain, sometimes across the whole grain, which is a typical BF morphology. From Figure 4-4 (c) to (d), with an increase in strain2, the microstructure becomes finer, and the parallel BF laths get shorter. The fraction of parallel BF laths is gradually reduced and the rest are non-equiaxed ferrite laths with a chaotic arrangement which can be classified as AF. This indicates that with the increase of austenite deformation a transition from BF to AF occurs, consistent with previous research [85, 149, 150]. Finally, in Figure 4-4 (e), despite the further increased strain2, the fraction of AF is not increased and the microstructure becomes inhomogeneous with coarse BF packets surrounding fine AF laths.
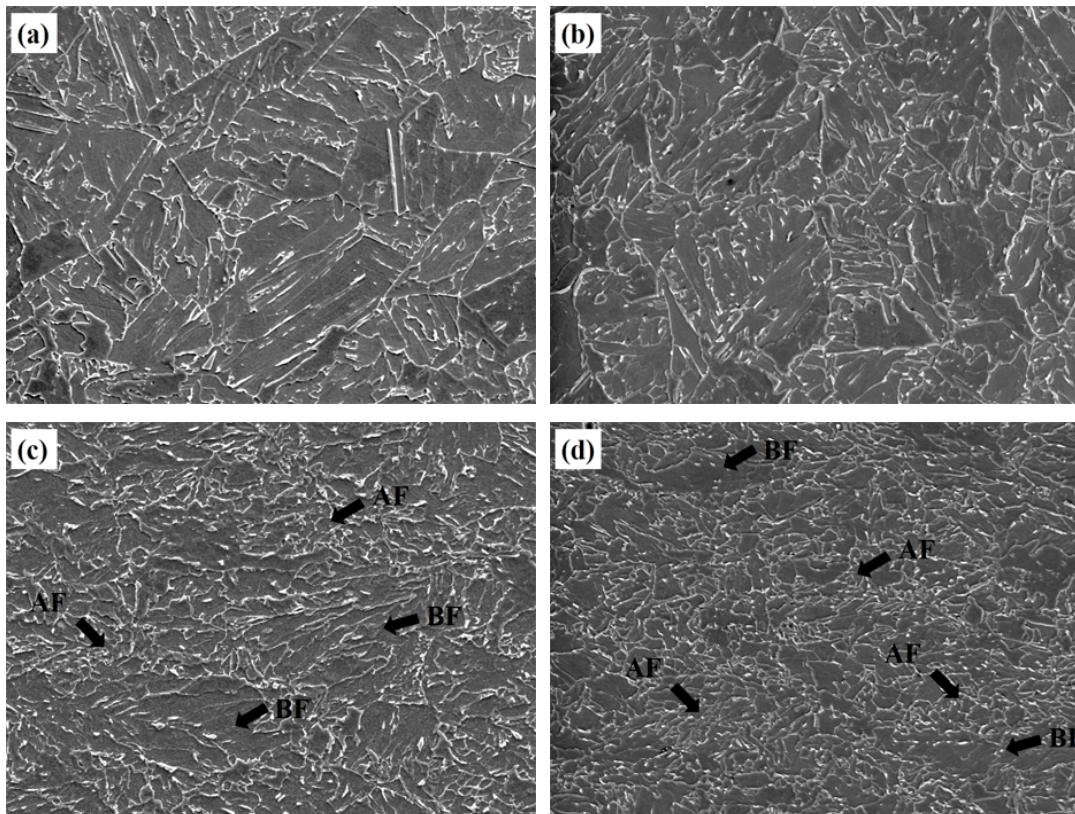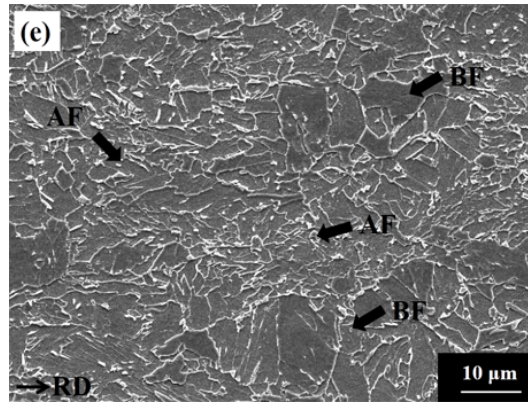
Figure 4-4 SEM secondary electron micrographs depicting the transformed microstructures after different strain2: (a) 0, (b) 0.1, (c) 0.3, (d) 0.5 and (e) 0.7.

Throughout all the micrographs above, microphases, possibly M/A constituents, appearing white can be found distributed within the matrix. In HSLA steels subjected to accelerated cooling processes, M/A constituents are a typical microstructural feature and they are considered as another factor affecting the toughness of steels, depending on their volume fraction, size and morphology. In general, the existence of M/A constituents causes a detrimental effect on the toughness. Hence, reduction and refinement of the M/A constituents will decrease the ductile–brittle transition temperature, promoting an improvement in the toughness of steels [11, 90].

It is clear in Figure 4-4 (a)~(d) that the shape of M/A constituents changes from elongated rods to dispersed, equiaxed particles with the increase of strain2 from 0 to 0.5. This shape change can be related to the transition from BF to AF. When the transformation product mainly is BF, which is a highly organised microstructure with packets of parallel laths with similar crystallographic orientations [2], the retained austenite mainly exists between laths, leading to the coarse, elongated rod shape of M/A constituents. In contrast, when the transformation product is AF dominant, which exhibits a relatively chaotic microstructure [88], the retained austenite is located mainly in the gaps between AF laths with different shapes and directions, resulting in the fine, equiaxed shape of M/A constituents. This morphology change of M/A constituents has also

78

been observed by another investigation [155]. The formation of coarse M/A constituents normally has a detrimental effect on toughness, therefore the refinement of M/A constituents through austenite deformation can alleviate the negative effect of M/A constituents on toughness.

4.3.3 EBSD mappings

Following the noise reduction procedures illustrated in Section 3.3.2, a small area of each EBSD data set was used to plot a boundary map. For a statistical analysis of boundary density distribution and boundary interception length, each whole data set was used.

The selected area boundary maps are shown in Figure 4-5. From Figure 4-5 (a)~(d), although BF microstructures revealed by parallel low angle grain boundaries (LAGBs) can be seen clearly in all figures, the length and fraction of parallel BF laths reduce gradually with increased austenite deformation. Additionally, the BF microstructure is replaced by non-equiaxed AF laths with curved boundaries and an irregular arrangement, indicating a transition from BF to AF as austenite deformation is increased. Together with these morphological changes, the densities of both HAGBs and LAGBs significantly increases with the augment of strain2 from 0 to 0.5. However, further increasing strain2 from 0.5 to 0.7, the densities of both HAGBs and LAGBs were reduced as shown in Figure 4-5 (d)~(e). The characteristics of microstructure evolution observed in the boundary maps correspond very well to those micrographs from optical and SEM microscopy. However, due to the advantages of EBSD mapping, these microstructure changes can be well quantified.
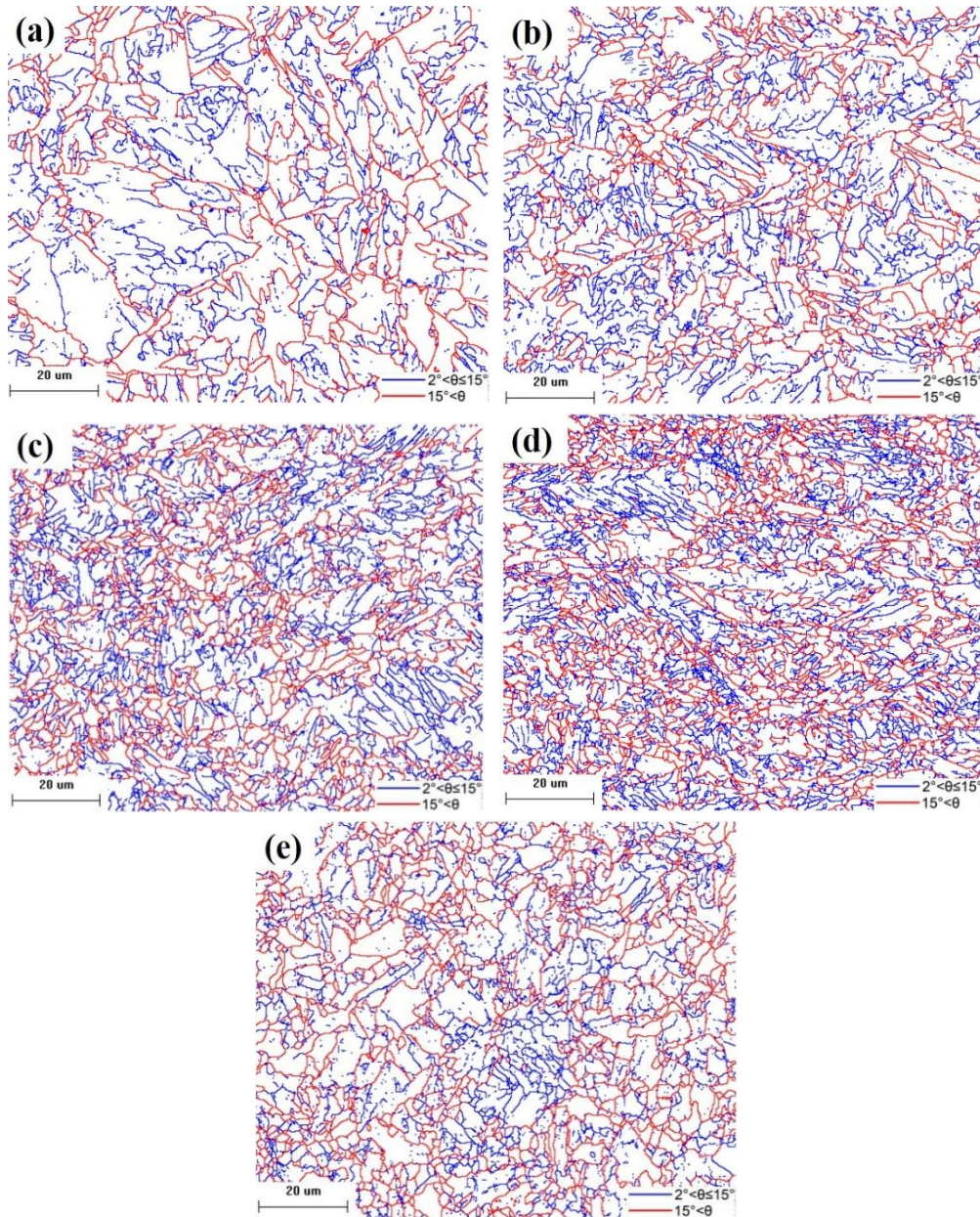
Figure 4-5 EBSD boundary maps of transformed microstructures after strain2 of (a) 0, (b) 0.1, (c) 0.3, (d) 0.5 and (e) 0.7, where blue lines represent low angle boundaries with disorientation between 2° and 15° whilst red lines represent high angle boundaries with disorientation greater than 15°.

Based on the EBSD maps covering relatively large areas of the tested specimens, the boundary densities in terms of absolute number per unit area are plotted against the disorientation angle values as distribution histograms in Figure 4-6, to reveal the boundary characteristics of the transformed

80

microstructures. For cubic crystals, there are 24 symmetrical operations and thus 24 angle-axis pairs to represent the misorientation between two orientations. Among these 24 misorientation angles, the smallest angle is called the disorientation angle. Therefore, a disorientation angle is a special kind of misorientation angle. Since the disorientation angle provide the small least rotation angle between two orientations, it is easy and accurate to use the disorientation angle to compare misorientations. Therefore disorientations angles were used throughout this thesis to represent the misorientation between two orientations. The whole disorientation angle scope can be divided into four ranges, range 1 ($\theta<10°$), range 2 ($10°\leq\theta<21°$), range 3 ($21°\leq\theta<47°$) and range 4 ($47°\leq\theta\leq62.8°$), due to different formation mechanisms.
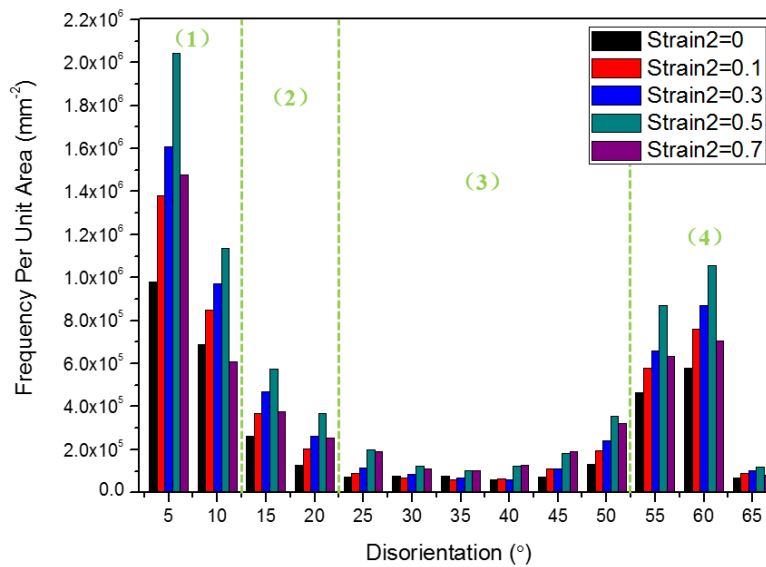
Figure 4-6 Histograms showing the boundary densities in terms of absolute number per unit area with different disorientation angles from 2° to 62.8°.

The displacive transformation characteristic of the microstructures formed under accelerated cooling can be seen directly from the boundary density distributions shown in Figure 4-6. For all transformed microstructures, the densities (frequencies) of boundaries with disorientation angles in range 3 are very low. This is because both AF and BF are displacive transformation products,

81

following a near K-S (Kurdjumov-Sachs) or N-W (Nishiyama-Wasserman) orientation relationship with parent austenite grains [89, 91]. For the K-S or N-W orientation relationships, the disorientation angles of boundaries between different laths transformed in the same parent austenite grain do not fall into range 3 between 21˚ and 47˚ as shown in Table 2-3. The boundaries with disorientations angles within range 3 shown in Figure 4-6 are the boundaries between laths transformed from different austenite grains at PAGBs, but not vice versa. Since the total area of PAGBs only accounts for a small portion of the total boundary area of the transformed microstructure, and it increases with austenite deformation as shown by Equation (2.4), the boundary densities in range 3 (21˚~47˚) are considerably lower than others and increase with the augment of strain2. Based on these results, the characteristics of boundary density distributions shown in Figure 4-6 add as evidence that the transformation mechanisms of both AF and BF are similar and displacive.

It can be seen in Figure 4-6 that the boundary densities (frequencies) of all EBSD data sets in other disorientation angle ranges, 1, 2 and 4, increase with the augment of strain2 from 0 to 0.5 and fall at strain2 of 0.7. The reason is explained in Section 4.4.3. It can also be observed that the boundary density in range 4 will increase with the rise of the AF volume fraction as strain2 increases from 0 to 0.5.

To quantify the microstructural refinement, the grain size defined by different disorientation threshold values, 4˚ and 15˚ are measured by a linear intercept method in the Channel 5 software respectively, owing to the reason explained in Section 3.3.2. The geometric mean of linear intercept lengths in both horizontal and vertical directions were calculated as in reference [146] and are shown in Figure 4-7.
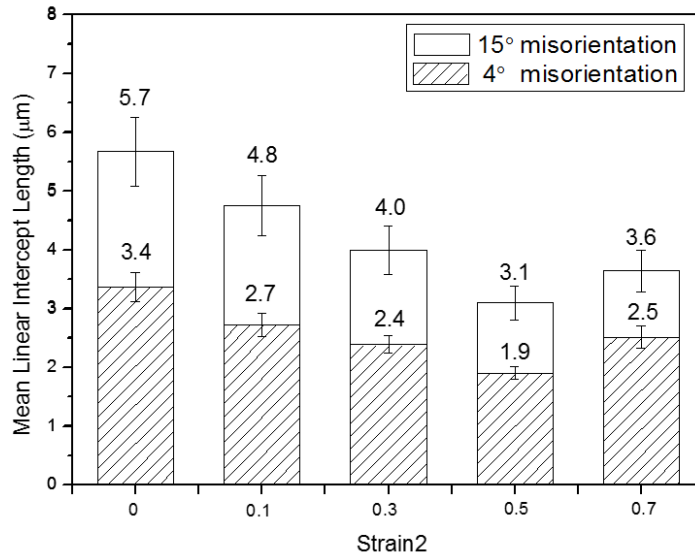
Figure 4-7 Microstructure size parameter as geometric mean of the linear interception lengths in horizontal and vertical direction from the EBSD maps measured against two disorientation criteria, 4˚ and 15˚. Error bar represent 95% confidence levels of the measurement.

It can be seen that the mean linear intercept lengths following both disorientation threshold values decrease with strain2, but increase again at a strain2 of 0.7, and the grain size range is very similar to another investigation [83]. Furthermore, the difference among all the specimens is statistically significant as there is very limited overlapping of their 95% CL error bars. The adjacent laths with disorientation below 15˚ make up the effective grains [85]. Since the effective grain boundaries ($\theta \geq 15˚$) act as obstacles to cleavage crack propagation, the reduction of effective grain size can result in a better toughness, especially in terms of the ductile–brittle transition temperature (DBTT) [85].

4.3.4 Microhardness

Microhardness values of the transformed microstructure versus the amount of strain2 are shown in Figure 4-8. The hardness increases slightly with increasing strain2 but decreases when strain2 reaches 0.7. This microhardness changing behaviour corresponds very well to that of the linear interception

lengths with threshold value of 4°.
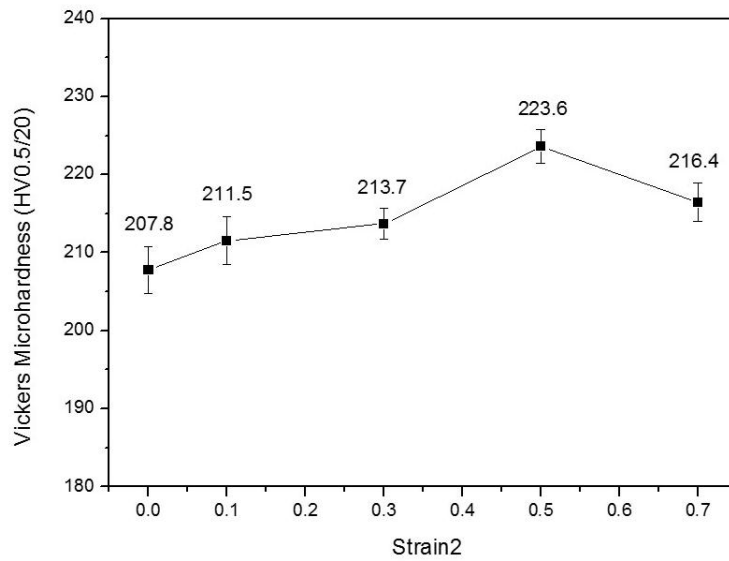
Figure 4-8 Vickers microhardness of the transformation products after various deformation strain. Error bars represent the 95% confidence interval of the measurement.

4.4 Discussion

4.4.1 Restoration of deformed austenite before phase transformation

It is evident from the results above that the microstructural refinement and strengthening effect of the austenite deformation is weakened when strain2 reaches 0.7. Despite the onset of DRX during strain2 of 0.7, the fraction of austenite recrystallisation is only 6% at the end of deformation, which is quite small compared to the hardness drop and microstructure coarsening.

Therefore, there should be another restoration mechanism occurring after deformation, but before the subsequent phase transformation. Under the cooling conditions used in this research, displacive transformations dominate as proved by the boundary density distribution histograms in Figure 4-6. Therefore, PAGBs before phase transformation can also be revealed by etching with a saturated aqueous picric acid solution similar to that used for water quenched specimens.

The optical micrographs depicting the PAGBs before phase transformation after strain2 of 0.5 and 0.7 are shown in Figure 4-9 (a) and (b) respectively. In Figure 4-9 (a), after strain2 of 0.5 and after continuous cooling, the prior-austenite still remains deformed which suggests that with strain2 of 0.5, deformation temperature of 950°C and strain rate of $10s^{-1}$, strain can be successfully accumulated in the austenite. While from Figure 4-9 (b), it can be seen clearly that many small equiaxed grains exist among unrecrystallised austenite grains. The fraction of those small equiaxed grains was measured at 38.5%. Since DRX was triggered at strain2 of 0.7 and the deformation temperature is relatively high (950°C), this leaves a relatively long time gap for post-dynamic softening to proceed.
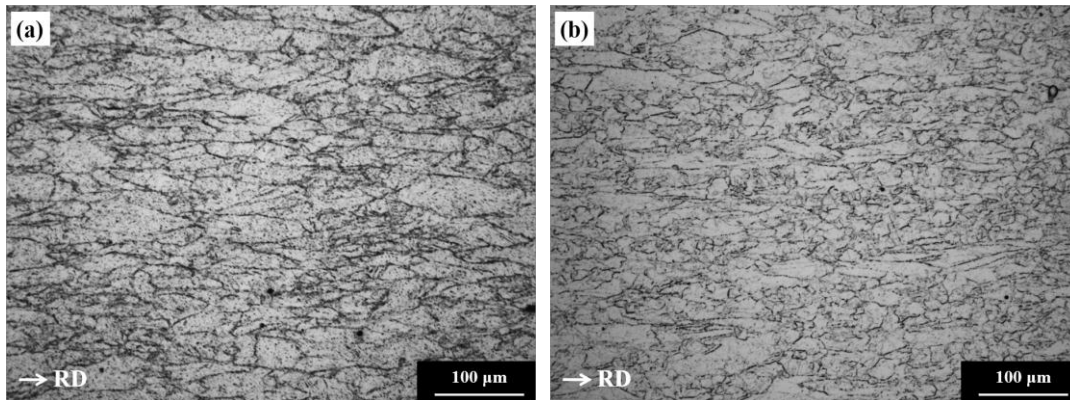
Figure 4-9 Optical micrographs depicting PAGBs of continuous cooled specimens after strain2 of (a) 0.5 and (b) 0.7.

As for the specific post-dynamic softening mechanism, some authors used to assume that static recrystallisation (SRX) is the dominant softening mechanism when deformation strain is lower than the critical strain of DRX, ε_c, while as long as the deformation strain is higher than ε_c, the following post-dynamic softening is dominated by meta-dynamic recrystallisation (MDRX) mechanisms which only involves growth of previously formed dynamic recrystallised grains. However, when the fraction of dynamic recrystallisation is low, MDRX cannot be accounted for a high post-dynamic softening fraction and in previous studies

[156], MDRX only became dominant after a minimum strain ε_T, was reached. This minimum strain ε_T is smaller than the steady state strain ε_{ss}, but can be significantly larger than ε_c. ε_T has been determined experimentally leading to a relationship:

$$\varepsilon_T = K\varepsilon_p \qquad\qquad (4.1)$$

where ε_p is the peak strain with the constant K of 1.7. Therefore, a transition between the strain-range was proposed [156], where SRX works as the dominant post-dynamic softening mechanism ($\varepsilon<\varepsilon_c$), and where MDRX takes over ($\varepsilon>\varepsilon_T$). Between ε_c and ε_T, both mechanisms contribute simultaneously to post-dynamic softening. Based on the information provided above, after strain2 of 0.7 both SRX and MDRX contributed to the softening, and resulted in the hardness drop and subsequent microstructure coarsening when strain2 reaches 0.7.

Therefore, based on the results shown above, the occurrence of SRX/MDRX during accelerated cooling is very hard to notice unless specimens with different strains are compared or the continuously cooled specimens are etched to reveal PAGBs. Moreover, the strain magnitude and deformation temperature of finish rolling should be selected carefully, especially for HTP steel, to minimise restoration processes such as MDRX and SRX from occurring prior to the phase transformation during accelerated cooling.

4.4.2 Transition from BF to AF

Despite the similarity in the transformation mechanism, AF has a quite different morphology compared to that of BF. The formation of AF can be explained by the effect of austenite deformation on introducing intragranular nucleation sites.

In Bhadeshia's research [2], the nucleation mechanism of bainite was proved to be related to spontaneous dissociation of specific dislocations that are already present in the parent austenite, which was originally proposed for martensite

nucleation by Olson and Cohen [116]. The first step of nucleation is faulting on the close-packed planes. Embryos consisting of stacking fault groups usually develop from the dissociation of existing dislocations with an appropriate number and spacing. These groups of stacking faults, embryos, turn unstable and start to spontaneously transform during cooling. These dislocations are glissile therefore diffusion of iron and substitutional solid solution atoms is not required for this nucleation mechanism, which corresponds well to the low transformation temperature for bainite at which thermal activation is in short supply. Although bainite and martensite are thought to have similar nucleation mechanisms, one difference is that carbon partitioning is required during the bainite nucleation stage to guarantee a reduction in free energy, due to the higher transformation temperatures and lower driving forces of bainite transformations compared with those of martensite transformations [2].

The hypothesis that martensite preferentially nucleates at dense stacking dislocation arrays has been widely accepted [157-160], and it was suggested that the potency of the nucleation site is determined by the number of dislocations in the array. For the nucleation site becoming potent enough, the quantity of dislocations inside should be higher than a critical value [116, 161]. The defect size necessary to account for a spontaneous nucleus formation was found to be directly proportional to the interfacial energy which is largely determined by the dislocation array energy [116]. Therefore, besides austenite grain boundaries where dense stacking dislocation arrays can be found and which is thought to be one of the most potent nucleation sites, intragranular dislocation arrays introduced by austenite deformation or strain related with intragranular inclusions can also act as nucleation sites for bainite and martensite transformation products. Furthermore, Magee [162] and Christian [163] argued that severely deformed regions could become potent nucleation sites for martensitic transformation. This can be attributed to the strain field interaction between martensite embryos and severely deformed regions which can lower the

free energy barrier for martensite nucleation. Actually, a mechanism for the strain-induced nucleation of martensite has been proposed by Olson and Cohen [158] involving two intersecting shear systems. In a three-dimensional phase-field study of strain-induced martensitic transformation in a stainless steel [160], martensite nucleates along the grain edges as well as in the austenite grain interior where the plastic strains are relatively larger compared to the rest of the material. Most importantly, the validity of deformation defects acting as nucleation sites for martensite transformation has been proved by in-situ laser scanning confocal microscopy (LSCM) observation and it was found that martensite blocks developed from sub-grain boundaries and the development of blocks were also stopped at subgrain boundaries [164].

Since the AF transformation mechanism is bainitic, the nucleation mechanisms of both AF and BF should be similar. Therefore, for specimens undeformed or slightly deformed, BF laths nucleate primarily on PAGBs where dense stacking dislocation arrays can be accommodated, and these laths finally developed into packets with a parallel morphology as shown in Figure 4-4 (a)~(b). On the other hand, when austenite is heavily deformed, a high density of dislocations and stacking faults will be introduced into the austenite, which can also act as nucleation sites in addition to PAGBs, leading to the AF dominant microstructures shown in Figure 4-4 (c)~(d). Moreover, it is worth noticing that in Figure 4-4 (e), a mixture of AF microstructure surrounded by blocky BF grains is evident. This inhomogeneous microstructure can be attributed to the mixture of unrecrystallised and recrystallised austenite grains as shown in Figure 4-9 (b). The remaining unrecrystallised austenite transforms into an AF microstructure, while the recrystallised austenite grains change into a BF microstructure because of the lack of intragranular nucleation sites.

The nucleation of AF has also been observed on many deformation substructures, like deformation bands [12, 165, 166] and dislocation cell walls [167]. Laths nucleated at these defects do not develop into a parallel morphology

on a large scale because the development of a parallel morphology is prohibited by impingement between adjacently nucleated AF laths [2]. Actually, several adjacent parallel AF laths form a packet on a small scale and different packets have different lengthening directions. AF packets will impinge with other packets formed at nearby nucleation sites, which prevents the parallel morphology on a large scale and brings about the irregular morphology of AF. This morphology characteristic has been proved by thin foil TEM observation in research [88] as shown in Figure 2-34 and Figure 2-35. Therefore, austenite deformation is required for the AF transformation in pipeline steels.

4.4.3 Grain refinement

The change of boundary densities in the disorientation angle range 3 with increased strain2 from 0 to 0.7 has been explained in Section 4.3.3. Differently, it can be seen in Figure 4-6 that the boundary densities (frequencies) of all EBSD data sets in the disorientation angle ranges, 1, 2 and 4, increase with the augment of strain2 from 0 to 0.5 and fall at strain2 of 0.7. A common reason is that with the increase of strain2 from 0 to 0.5, the density of intragranular nucleation sites introduced by austenite deformation is raised and thus the BF and AF laths become increasingly smaller and shorter as shown in Figure 4-4, leading to increased lath boundary densities. Due to the formation of blocky BF packets from the recrystallised austenite grains with strain2 of 0.7, the lath boundary density drops as strain2 reaches 0.7. However, the reason for the boundary density change in each disorientation angle ranges are slightly different.

Boundaries with disorientation angles in range 1 ($\theta<10°$), are mainly resulted from the plastic strains of austenite and ferrite to accommodate the displacive transformation shape strain [168, 169]. The main phase components, AF and BF, in all specimens are displacive transformation products with similar transformation shape strains. Therefore, the boundary density in range 1 should

be very similar. However, since the main characteristic of displacive transformations is the coordinated movement of lattice atoms [2], the substructure induced by austenite deformation will be inherited by the displacive transformation products. Therefore, the increase in strain2 will introduce more deformation substructures inherited by the transformation products and finally leads to the increased boundary density in range 1. The occurrence of SRX/MDRX after strain2 of 0.7 lowers the deformation substructure density, and results in a decrease of boundary density in range 1.

Boundaries with disorientation angles in range 4 ($47° \leq \theta < 62.8°$), are mainly the boundaries between variants transformed in the same austenite grain but belonging to different Bain groups as shown in Table 2-3. The rise in boundary density in range 4 as strain2 increases from 0 to 0.5 can be mainly attributed to the formation of intragranular nucleated AF. During the BF transformation, strong variant selection occurs and results in certain variant pairs in the transformation product and thus high boundary densities in certain disorientation values [99]. Under relatively slow cooling rates or high transformation temperatures, the variant selection will mainly favour the variant pairs with low disorientation angles between them [99]. However, for the AF dominant microstructures, austenite deformation increases the intragranular nucleation sites, which will weaken the variant selection mechanisms and more variants and variant pairs can be formed in each austenite grain. This is consistent with previous research [44], which found that plates formed on the primary plates have been found to be related with each other in low disorientation angles, between 5° and 15°, despite the considerable spatial disorientation between them. In other words, the HAGB found in research [44] is mainly attributed to the intragranular nucleation of the primary plates, and not the plate interwoven morphology. Therefore, the boundary density in range 4 will increase with the rise of the AF volume fraction as strain2 increases from 0 to 0.5. The occurrence of SRX/MDRX after strain2 of 0.7 eliminates some of the intragranular

nucleation sites, leading to the reduced AF volume fraction and thus the decreased boundary density in range 4.

Boundaries with disorientation angles in range 2 ($10° \leq \theta < 21°$), are mainly the boundaries between variants transformed in the same austenite grain and belonging to the same Bain group as shown in Table 2-3. The change of boundary density in this range can be explained mainly by the change of lath boundary density as illustrated in the beginning of this section.

It is also worth noticing that besides the disorientation angle range 4, the disorientation angles of boundaries formed between laths transformed from different austenite grains can also fall into other disorientation angle ranges 1, 2 and 4. But due to the limited fractions of PAGBs, their influences are very small in the ranges 1, 2 and 4.

Due to the increased boundary density in the high angle range ($\theta > 15°$) with strain2 from 0 to 0.5, Figure 4-6, it can be seen clearly that the effective grain size with threshold value of 15° reduces with the increase of accumulated strain in the austenite in this research. This is consistent with other previous research results [85, 149, 150]. As for the controversial influence of austenite deformation on effective grain size, it is discussed in Section 5.4.4.

4.5 Summary

In this chapter, the effect of austenite deformation (strain2) below the recrystallisation-stop temperature, $T_{5\%}$, on microstructural evolution was investigated. It was found that:

(1) With an increase of strain2 from 0 to 0.5 in the austenite, transition from bainitic ferrite to acicular ferrite occurs, and the grain boundary density and microhardness increase with the rise of the acicular ferrite fraction in the transformed microstructure. Meanwhile effective grain size decrease with increased strain2 indicating toughness improvement.

(2) Increasing strain2 further from 0.5 to 0.7 leads to reduced microhardness and inhomogeneous and coarse microstructure with AF regions surrounded by blocky BF grains, which is attributed to the occurrence of dynamic recrystallisation and subsequent post-dynamic softening resulting in the drop of the accumulated strain.

(3) Some of these microstructural evolution characteristics including effective grain size are opposite to those observed in bainitic ferrite dominant microstructures. The active intragranular nucleation sites under the transformation condition in this research are the main reason for this discrepancy.

(4) Based on the result of this research, to get AF dominant microstructures under industrial continuous cooling conditions, deformation below $T_{5\%}$ should be high enough to encourage the transition from BF to AF but not so high that DRX and subsequent SRX/MDRX can be triggered which will lower the accumulated strain in austenite and weaken the effect of austenite deformation on AF transformation, grain refinement and strengthening.

Chapter 5 Effect of cooling rates on microstructure evolution

5.1 Introduction

It is shown in Chapter 4 that the austenite deformation below the recrystallisation-stop temperature ($T_{5\%}$) can promote the transition from BF to AF. But besides austenite deformation, the effect of continuous cooling rates on the AF transformation is also under debate and the conditions for the occurrence of the AF transformation are still unclear. In the research of Xiao et al. [170], a low carbon Mn-Mo-Nb pipeline steel was used to investigated the static and dynamic transformation products and it was found that the final microstructure with cooling rates below 10°C/s can be identified as AF. However, in the research of Yakubtsov et al. [155], for a low carbon microalloyed commercial grade 550 steel, it was found that at slow cooling rates, the transformation microstructure is BF dominant, while at higher cooling rates (≥35°C/s), AF transformation occurs, due to the low bainite transformation temperature and thus the high thermodynamic driving force which promotes the intragranular nucleation of AF. Moreover, some researchers [89, 149, 170] proposed that AF-like microstructures can be formed without austenite deformation but at slow cooling rates.

Therefore, in this chapter, continuous cooling at different cooling rates was applied to either undeformed or deformed austenite to investigate the effect of cooling rates on the microstructure evolution and the conditions for the occurrence of the AF transformation. Furthermore, the influence of cooling rates on the grain refining effect of austenite deformation below the recrystallisation-stop temperature ($T_{5\%}$) is discussed.

5.2 Experimental

Given the controllable linear cooling capacity of the FTTU introduced in Section 3.2.2, the fastest rate of the controlled continuous cooling used in this thesis was set at 50˚C/s. During continuous cooling at rates slower than the natural air cooling rate, instead of using cooling mediums, the FTTU actually needs to heat the specimen to maintain the slow cooling rates. Based on the limitation of the coil cooling system of the FTTU and time efficiency, the slowest rate of the controlled continuous cooling used in this thesis was set at 0.5˚C/s.

The processing route is illustrated in Figure 5-1. The solid solution heat treated specimens illustrated in Section 3.2.2 were reheated to 1200˚C at a rate of 10˚C/s, held for 2 minutes for equilibration, and then cooled at a rate of 5˚C/s to 1100˚C for a roughing deformation (strain1) of 0.3 at a constant true strain rate of $10s^{-1}$. After that, the specimens were cooled immediately to 950˚C at a rate of 5˚C/s for the second deformation with strain2 of, either 0 or 0.5. This second deformation was also performed at a constant true strain rate of $10s^{-1}$, and was followed by a controlled cooling from 950˚C to 500˚C at rates of 0.5˚C/s, 1˚C/s, 5˚C/s, 10˚C/s, 20˚C/s and 50˚C/s. After that, specimens were slowly cooled from 500˚C to 350˚C at a rate of 1˚C/s and finally water quenched from 350˚C to room temperature.
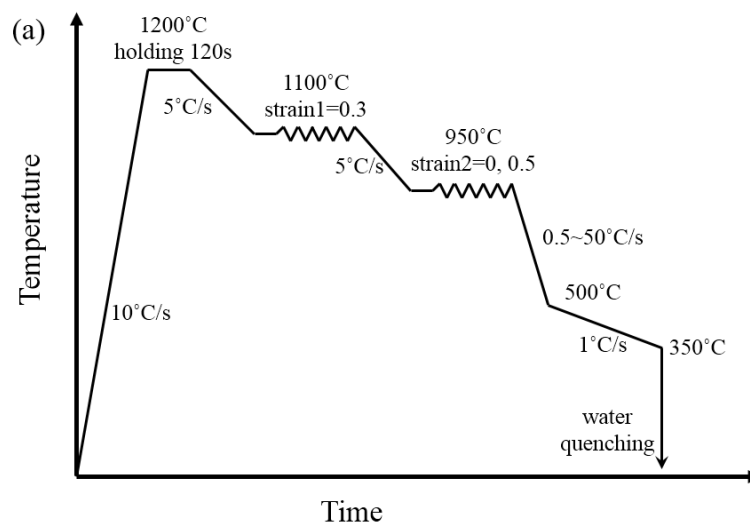
Figure 5-1 Schematic illustration of the thermomechanical testing profile.

94

Specimens for OM and SEM observation and EBSD mapping were prepared carefully as illustrated in Section 3.3. A 2% nital solution was used to show the transformed microstructure. EBSD analyses were also carried out with an accelerating voltage of 20 kV on the RD-ND plane of each specimen. The step size for the transformed microstructures with cooling rates of 0.5°C/s and 1°C/s is set as 0.5 μm because under these conditions coarse PF/QF grains dominate the transformed microstructures. The step size for the rest of the cooling rates is still set as 0.2 μm. Noise reduction and grain size measurement were performed as introduced in Section 3.3.2.

5.3 Results

5.3.1 Microstructures

The morphologies of the prior-austenite grains with strain2 of 0 and 0.5 have been shown in Figure 4-3 (a)~(b). As can been from these two figures, with strain2 of 0, the prior-austenite grains are recrystallised and the mean linear intercept length measured is 37.0 μm, while with a strain2 of 0.5, the prior-austenite microstructure remains in an unrecrystallised condition. Therefore, the selected austenite deformation parameters are suitable to investigate the effect of continuous cooling rates on the transformed microstructure evolution of recrystallised and deformed austenite.

The microstructures transformed from the recrystallised austenite (strain2 = 0) with different continuous cooling rates are shown in Figure 5-2. At cooling rates of 0.5°C/s and 1°C/s, Figure 5-2 (a)~(b), a mixture of PF/QF grains and BF packets was found in the transformed microstructures and with the increase of cooling rates, the volume fraction of BF raises and the grain size of PF/QF becomes smaller.

At cooling rates higher than 1°C/s, Figure 5-2 (c)~(f), a parallel morphology

95

of the transformed products can be seen clearly in all microstructures. PAGBs remain, and the parallel laths developed from the PAGBs extended into the austenite grain, sometimes across the whole grain, which is a typical BF morphology. Therefore, BF dominates the transformed microstructures continuously cooled at 5~50°C/s without austenite deformation. At the cooling rate of 5°C/s, Figure 5-2 (c), the microstructure mainly consists of coarse BF laths and some of the lath boundaries can only be seen vaguely. Differently, at the cooling rate of 50°C/s, Figure 5-2 (f), BF laths become thinner and the lath boundaries are clearer. With the increase of cooling rate from 5°C/s to 50°C/s, the transformed microstructure gradually changed from coarse BF laths to thin BF laths, and the boundaries between laths are increasingly clear.

The microstructures transformed from deformed austenite (strain2 = 0.5) with different continuous cooling rates are shown in Figure 5-3. At cooling rates of 0.5°C/s and 1°C/s, Figure 5-3 (a)~(b), a mixture of PF/QF grains and dark phases was found and increasing the cooling rate, the grain size of PF/QF becomes smaller. The phases appearing dark in the optical micrographs could be bainite or degenerated pearlite and a detailed TEM observation of thin foils is required to give a definite answer, which is out of the scope of this research. In contrast to the microstructures transformed from recrystallised austenite under the same low cooling rates, paralleled BF laths no longer exist in the microstructures transformed from deformed austenite as shown in Figure 5-3 (a)~(b).

With cooling rates between 5~20°C/s, Figure 5-3 (c)~(e), the transformed microstructures maybe consist of AF laths together with a small fraction of PF/QF grains at the lower cooling rate (5°C/s) while parallel BF laths are seen at the higher cooling rates (10~20°C/s). Increasing the cooling rate further to 50°C/s, a parallel morphology of the transformed product becomes evident and many sheaves developed across the whole austenite grains, which is a typical BF dominant microstructure. From Figure 5-3 (c)~(e), it is interesting to notice that

96

the fraction of BF in the transformed microstructures raises with the increased cooling rates, which means under the same austenite deformation condition (strain2 = 0.5), a transition from AF to BF happens with the increase of cooling rates.
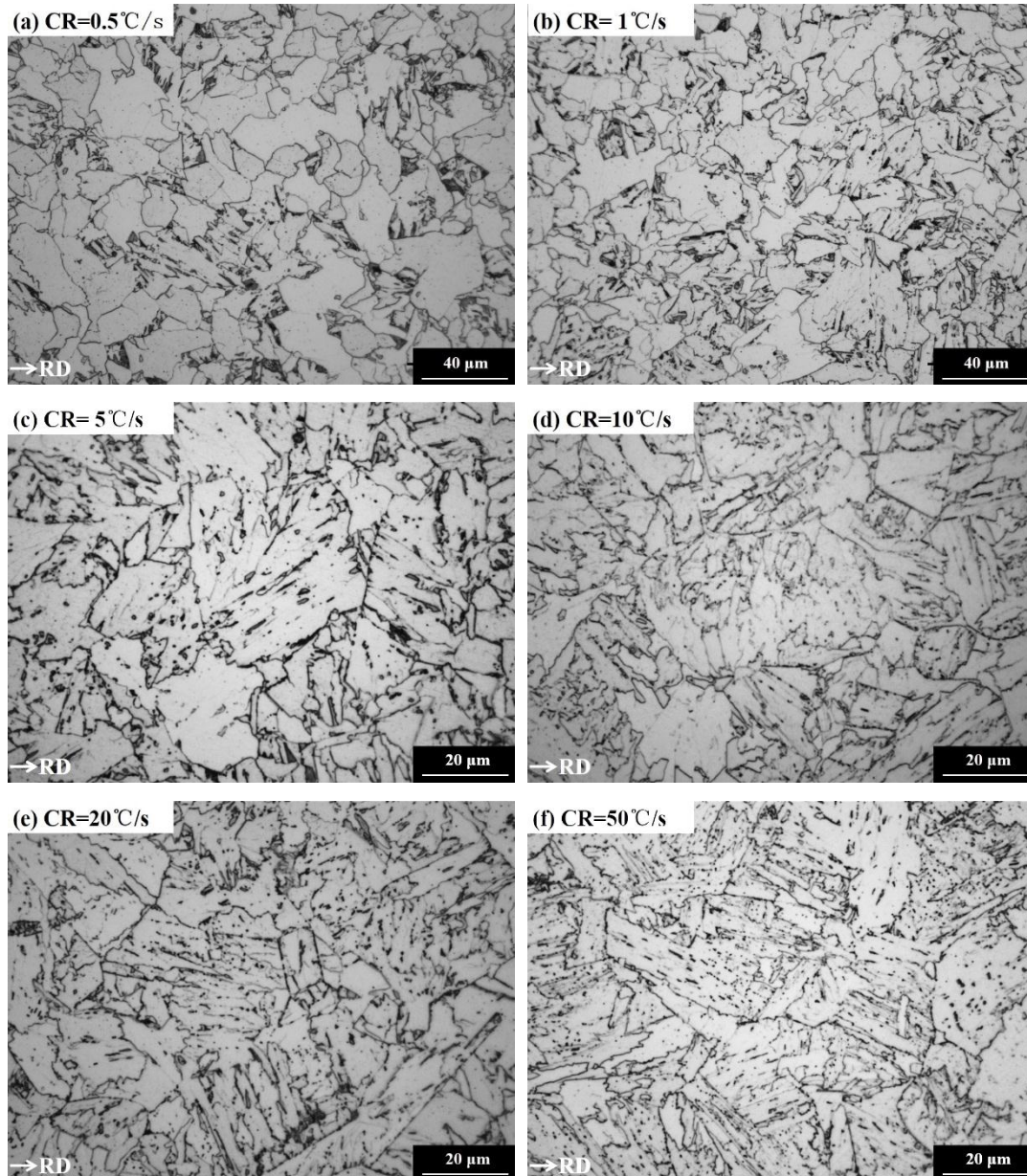
Figure 5-2 Optical micrographs depicting microstructures transformed from recrystallised austenite (strain2 = 0) with different continuous cooling rates: (a) 0.5°C/s, (b) 1°C/s, (c) 5°C/s, (d) 10°C/s, (e) 20°C/s and (f) 50°C/s.
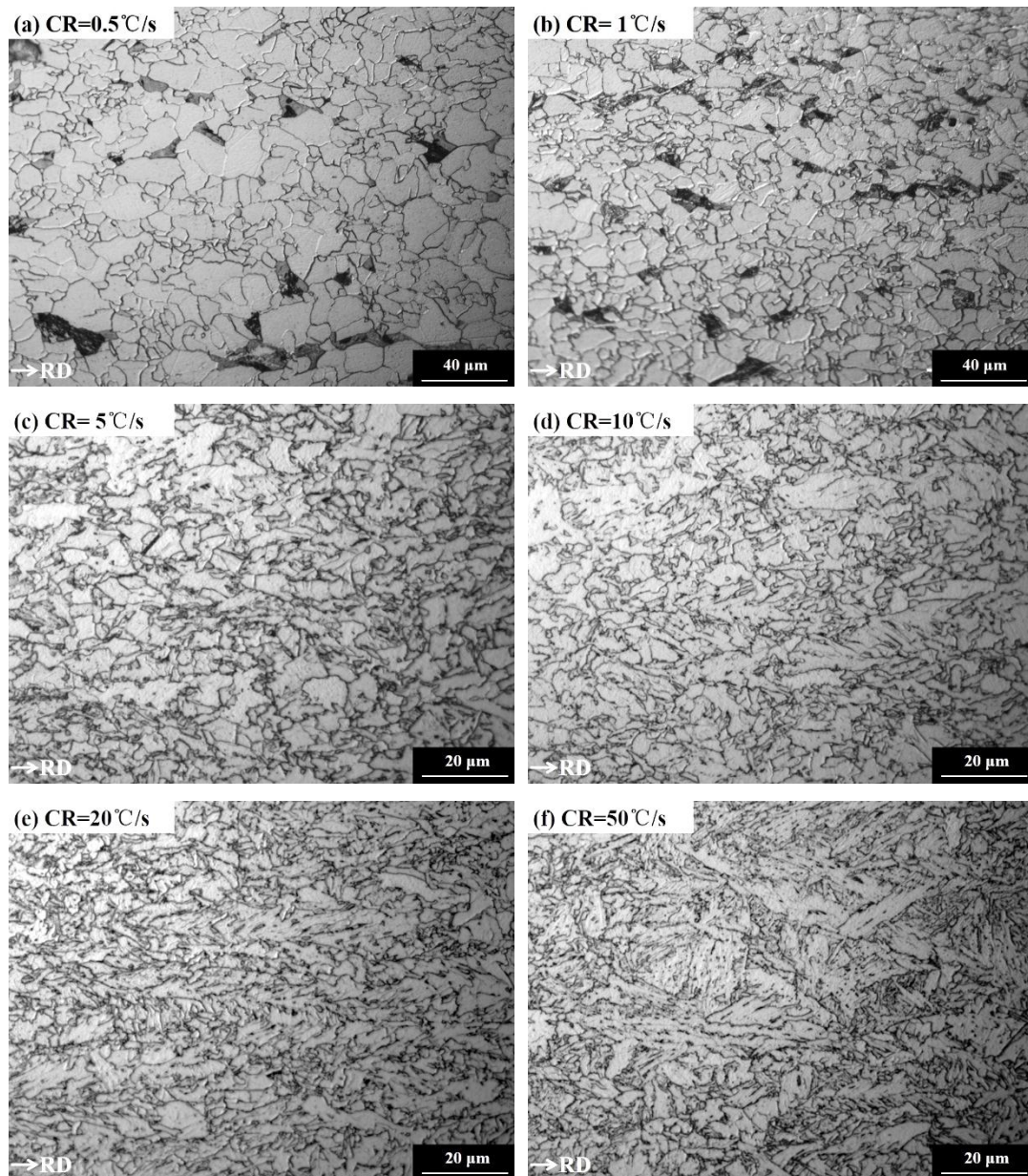
Figure 5-3 Optical micrographs depicting microstructures transformed from deformed austenite (strain2 = 0.5) with different continuous cooling rates: (a) 0.5°C/s, (b) 1°C/s, (c) 5°C/s, (d) 10°C/s, (e) 20°C/s and (f) 50°C/s.

Since PF/QF dominant microstructures at the low cooling rates, 0.5~1°C/s, are less intricate than the AF or BF dominant microstructures at higher cooling rates, 5~50°C/s, the following microstructure characterisation mainly focuses on the BF and AF dominant microstructures.

98

To observe the microstructures in greater detail, SEM secondary electron micrographs of the microstructures transformed from recrystallised and deformed austenite with different cooling rates are shown in Figure 5-4 and Figure 5-5, respectively. In Figure 5-4, with increased cooling rate, BF laths become thinner and the boundaries between BF laths revealed by nital etching are clearer.

In Figure 5-5, similar microstructural changes can be observed compared to optical micrographs as well. In Figure 5-5 (b)~(c), at the cooling rates of 10˚C/s and 20˚C/s, although the dominant microstructure is AF, some short parallel BF laths forming short wide packets along PAGBs can be seen in the microstructures, and AF microstructure exists between these wide packets. This actually is an important microstructural characteristic of AF and this will be discussed in Section 5.4.3. Finally increasing the cooling rate further to 50˚C/s, parallel BF laths dominate the transformed microstructure, Figure 5-5 (d), and many BF laths extended across the whole austenite grains.
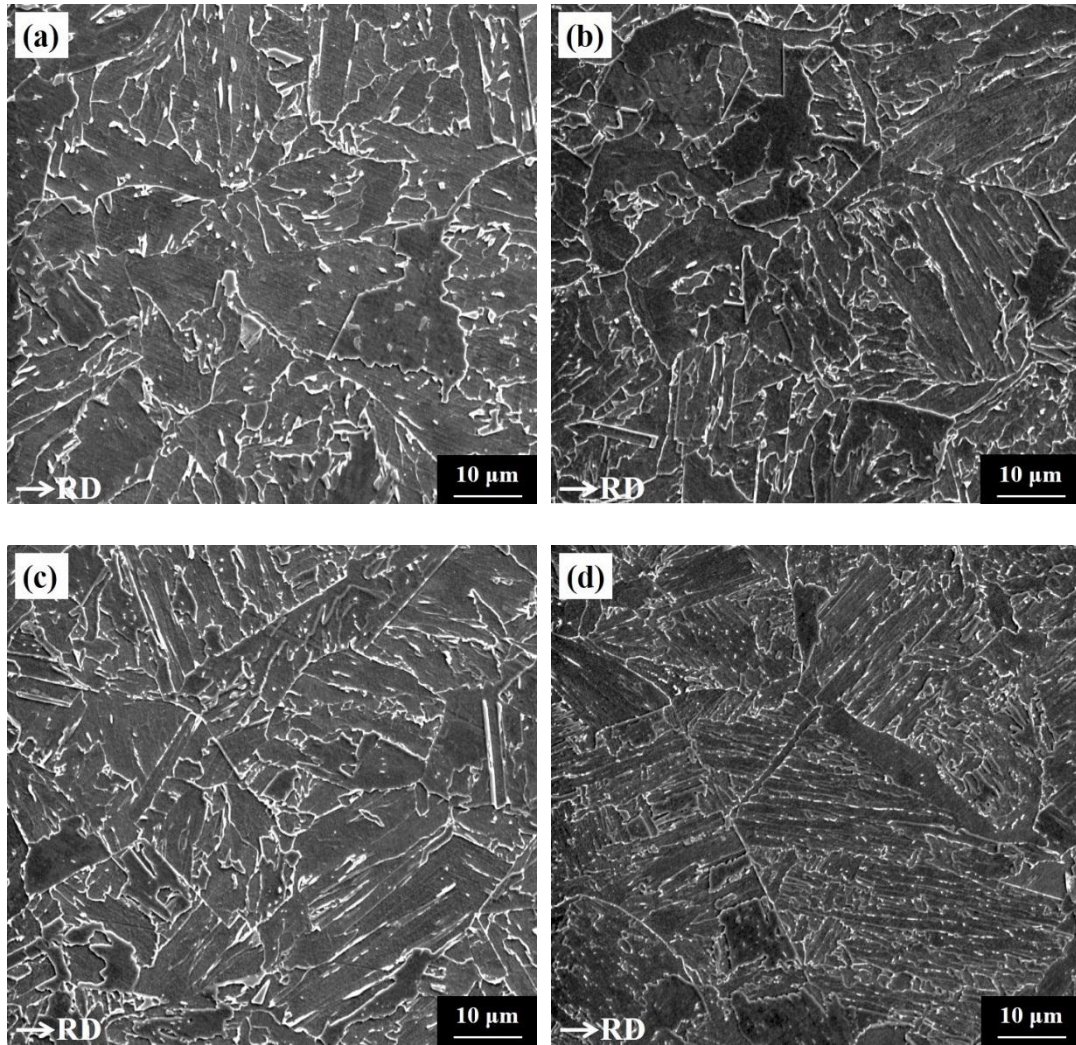
Figure 5-4 SEM secondary electron micrographs showing microstructures transformed from recrystallised austenite (strain2 = 0) with different continuous cooling rates: (a) 5˚C/s, (b) 10˚C/s, (c) 20˚C/s and (d) 50˚C/s.
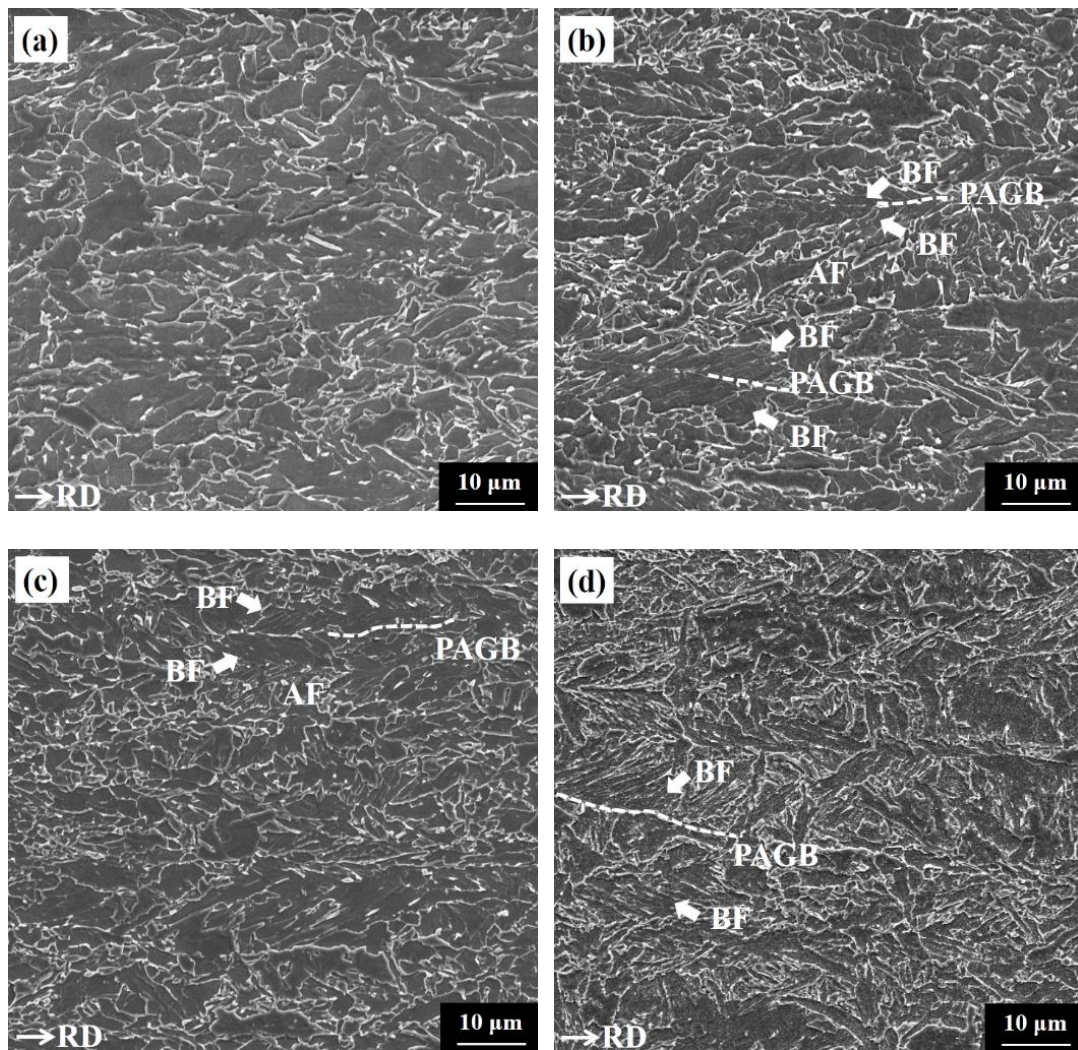
Figure 5-5 SEM secondary electron micrographs showing microstructures transformed from deformed austenite (strain2 = 0.5) with different continuous cooling rates: (a) 5°C/s, (b) 10°C/s, (c) 20°C/s and (d) 50°C/s, where white dashed lines represent the traces of the parent austenite grain boundaries.

5.3.2 EBSD mappings

Following the noise reduction procedures illustrated in Section 3.3.2, a small area of each EBSD data set was used to plot an inverse pole figure (IPF) coloured orientation map and a boundary map. For a statistical analysis of the boundary interception length, each whole data set was used.

The selected area IPF coloured orientation maps and corresponding

boundary maps of the microstructures transformed from recrystallised and deformed austenite with different cooling rates are shown in Figure 5-6 and Figure 5-7, respectively.

Transformed from recrystallised austenite, increasing the cooling rate from 5˚C/s to 20˚C/s, Figure 5-6 (a)~(c), the change in the effective grain size is not evident from these IPF coloured orientation maps and it can be seen that the transformed microstructures mainly consist of coarse BF packets and HAGBs exist mainly between packets instead of between laths within packets. Furthermore, from the corresponding boundary maps, Figure 5-6 (e)~(g), it can be found that within each packet LAGBs were generated and the influence of cooling rate on the densities of both HAGB and LAGB is not evident. However, increasing the cooling rate further to 50˚C/s, the densities of both HAGB and LAGB are increased significantly and HAGBs exist not only between packets but also between laths within packets as shown by the black parallel lines in Figure 5-6 (d).
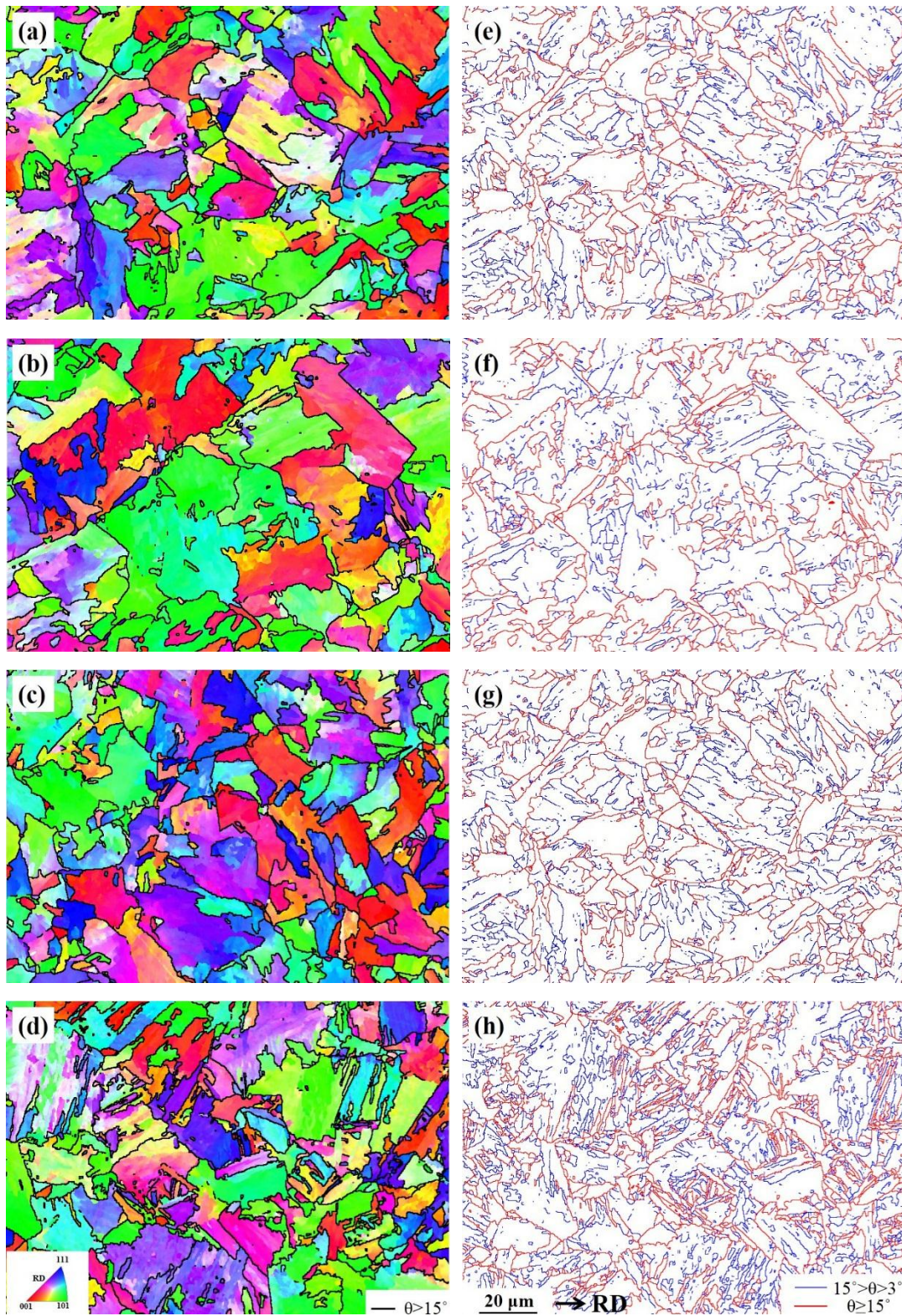
Figure 5-6 EBSD maps of the microstructures transformed from recrystallised austenite (strain2 = 0) with different continuous cooling rates: (a)~(d) inverse pole figure coloured orientation maps corresponding to microstructures with cooling rates of 5°C/s, 10°C/s, 20°C/s and 50°C/s respectively, where black lines represent high angle

103

boundaries with disorientation greater than 15˚; (e)~(h) boundary maps corresponding to the same area in (a)~(d) respectively, where blue lines represent low angle boundaries with disorientation between 3˚ and 15˚ whilst red lines represent high angle boundaries with disorientation greater than 15˚.

Transformed from deformed austenite, Figure 5-7 (e)~(h), the density of LAGBs increases constantly with the cooling rate raising from 5˚C/s to 50˚C/s. Coarse effective grains pointed to by black arrows can be found within all the transformed microstructures. Therefore all the microstructures can be divided into two parts, coarse effective grains composed of parallel BF laths and fine effective grains composed of AF laths with an irregular arrangement. From Figure 5-7 (a) to (b), the density of HAGBs is increased because the relatively coarse PF/QF grains in Figure 5-7 (a) are replaced by the fine AF laths in Figure 5-7 (b). But raising the cooling rate from 10˚C/s to 50˚C/s, the area of coarse effective grains increases and finally leads to a quite inhomogeneous microstructure at the cooling rate of 50˚C/s. The increase of the coarse effective grain area suggests that a transition from AF to BF happens with the cooling rate increasing from 10˚C/s to 50˚C/s. Furthermore, the change of the density of effective grains implies the differences of nucleation site density at various cooling rates.
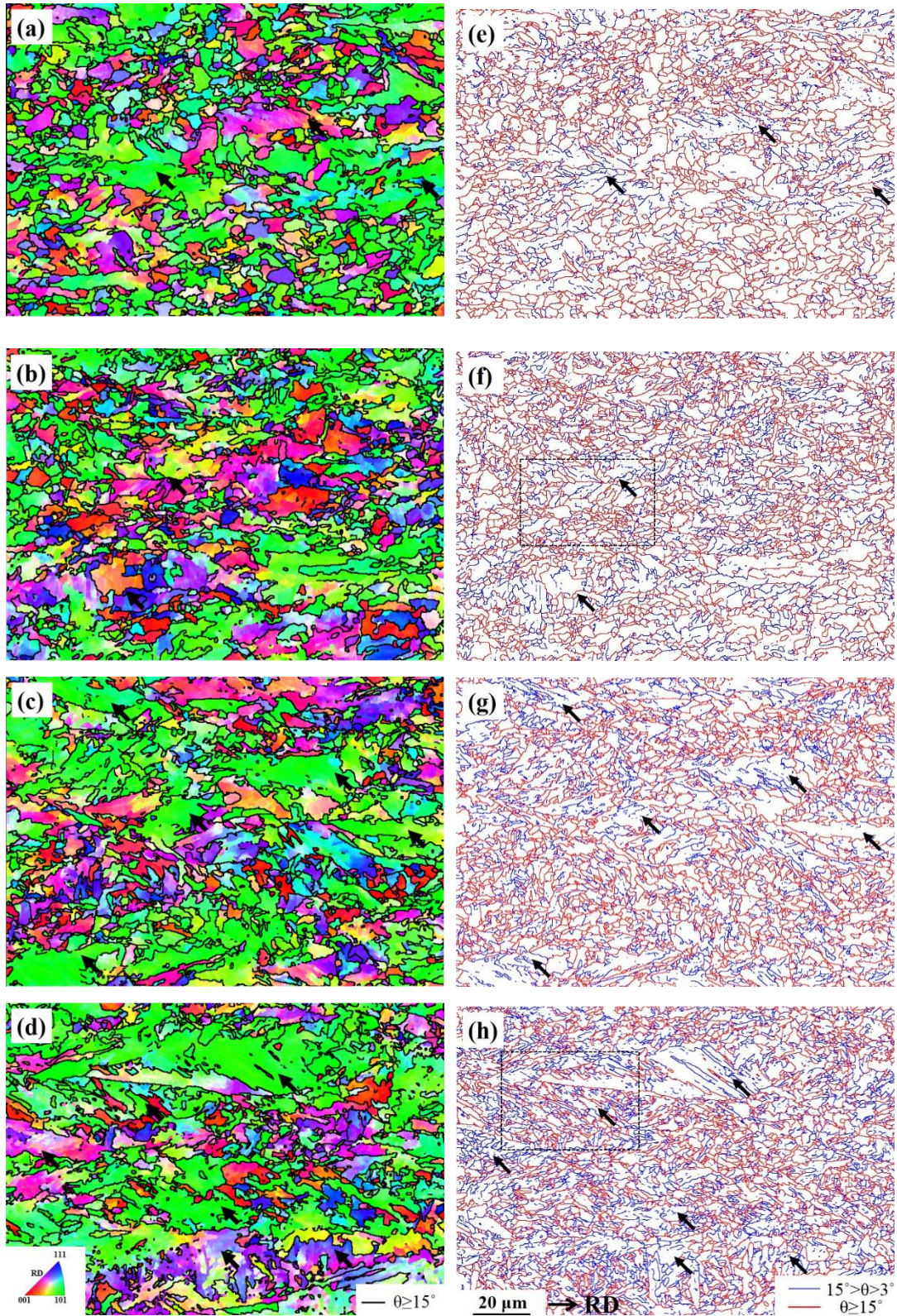
Figure 5-7 EBSD maps of the microstructures transformed from deformed austenite (strain2 = 0.5) with different continuous cooling rates: (a)~(d) inverse pole figure coloured orientation maps corresponding to microstructures with cooling rates of 5˚C/s,

10˚C/s, 20˚C/s and 50˚C/s respectively, where black lines represent high angle boundaries with disorientation greater than 15˚; (e)~(h) boundary maps corresponding to the same area in (a)~(d) respectively, where blue lines represent low angle boundaries with disorientation between 3˚ and 15˚ whilst red lines represent high angle boundaries with disorientation greater than 15˚.

To quantify the microstructural refinement, the grain size defined by different disorientation threshold values, 4˚ and 15˚ are measured by a linear intercept method in the Channel 5 software, owing to the reason explained in Section 3.3.2. The geometric mean of linear intercept lengths in both horizontal and vertical directions were calculated as in reference [146] and are shown in Figure 5-8.

Figure 5-8 Microstructure size parameter measured against two disorientation criteria: (a) 15˚ and (b) 4˚, as geometric mean of the linear interception lengths in horizontal and vertical direction from the EBSD maps, where error bars represent 95% confidence levels of the measurement.

For transformed microstructures from recrystallised austenite, the grain sizes defined by both disorientation threshold values of 4˚ and 15˚ are reduced with the cooling rate increasing from 0.5˚C/s to 50˚C/s. But the changes of grain size between cooling rates of 5˚C/s to 20 ˚C/s are not statistically significant as there are very large overlaps of their 95% CL error bars, corresponding very well to the results obtained from EBSD maps in Figure 5-6.

Differently, for microstructures transformed from deformed austenite, the change of grain size with cooling rate is more complicated. For the grain size defined by a disorientation threshold value of 4˚, the grain size is firstly reduced from 5.0 μm to 1.8 μm with the cooling rate increasing from 0.5˚C/s to 10˚C/s, and then the grain size is raised to 1.9 μm although this increase is not statistically significant. Finally, when the cooling rate reaches 50˚C/s, the grain size is further lowered to 1.7 μm. While for the grain size defined by a disorientation threshold

107

value of 15°, the effective grain size firstly is reduced from 5.7 μm to 2.9 μm with the cooling rate increasing from 0.5°C/s to 10°C/s, and then the effective grain size is increased continuously from 2.9 μm to 3.5 μm as the cooling rate is raised from 10°C/s to 50°C/s, although the effective grain size change between 10°C/s and 20°C/s is not statistically significant.

5.4 Discussion

5.4.1 Effect of austenite deformation at slow cooling rates

Without austenite deformation, the transformed microstructures cooled at 0.5°C/s and 1°C/s consist of PF/QF grains and BF packets. The occurrence of the BF microstructure can be attributed to the effect of niobium on the hardenability of the steel. It has been found by many researchers [171, 172] that the addition of niobium can suppress the allotriomorphic ferrite transformation, by lowering its nucleation rate at austenite grain boundaries, and promote bainitic transformation microstructures at the expense of allotriomorphic ferrite. The suppression effect of niobium on the allotriomorphic ferrite is evident when niobium is in solid solution. In past research [172], increasing the concentration of niobium in solution in austenite greatly retards the formation of allotriomorphic ferrite. However, a maximum suppression effect was found when the niobium concentration was beyond a certain level and it was explained that with a high niobium concentration, the precipitation of niobium carbides or carbonitride happens before the ferrite transformation during cooling and even worse these precipitates can act as intragranular nucleation sites for the ferrite transformation.

Through thermodynamic calculation for the tested steel, the addition of niobium can only slightly change the austenite stability, due to the low niobium concentration in the tested steels (0.09%). And in microalloyed steels, the concentration of niobium is normally lower than 0.1% [26]. This indicates that

the effect of niobium on steel's hardenability should be very limited. The discrepancy between thermodynamic calculation and experimental results can be explained by the fact that niobium atoms do not evenly distribute in austenite but segregate at austenite grain boundaries and different transformation suppression mechanisms were proposed based on this segregation. In research [172], the retardation of allotriomorphic ferrite transformation was attributed to the solute-drag effect that the segregation of niobium to austenite/ferrite interface is assumed to modify the diffusivity of carbon and decrease interface advancing rate. Nevertheless, since niobium also affects the kinetics of the bainitic transformation [171] in which substitutional solid solution atoms including niobium are believed to be partitionless [2], the solute-drag explanation is not reasonable under this situation and other retardation mechanisms, such as the stabilisation of grain boundaries by segregation of niobium atoms, seem more plausible [173].

Differently, subjected to an austenite deformation below the $T_{5\%}$ temperature, the transformed microstructures cooled at 0.5˚C/s and 1˚C/s consist of finer PF/QF grains compared with those transformed from recrystallised austenite. The BF packets shown in Figure 5-2 (a)~(b) disappear in Figure 5-3 (a)~(b). The PF/QF grain refinement and the disappearance of BF after austenite deformation can be explained as follows.

Firstly, austenite deformation increases the stored strain energy in the austenite and during reconstructive transformations (PF/QF) under slow cooling rates, this strain energy can add up to the driving force and make the decomposition of austenite begin at a higher temperature. Therefore, the low-temperature transformation product, BF, disappears during the continuous cooling after austenite deformation.

Secondly, deformation of the austenite can increase the austenite grain boundary area per unit volume and introduce deformation substructures within austenite grains, such as deformation bands or cell boundaries which can act as

intragranular nucleation sites [75]. The increase of the ferrite nucleation site density accelerates the transformation kinetics of ferrite, and also refines the ferrite grain size. Therefore, the PF/QF dominant microstructures appear finer after austenite deformation. Another effect of austenite deformation is that the increased austenite grain boundaries and deformation substructures are also attractive to niobium atoms, leading to lowered niobium segregation levels at these defects. Therefore, the austenite grain boundary stabilisation effect of niobium atoms is weakened, which reduces the volume fractions of low-temperature transformation products.

Last but not least, strain-induced precipitation of niobium carbide or carbonitride during austenite deformation may further reduce the niobium content in solution and thus weaken the austenite grain boundary stabilisation effect of niobium.

Therefore, the effect of austenite deformation on the transformation at slow cooling rates can be explained in terms of increasing driving forces, raising nucleation site densities and weakening the effect of niobium on steel's hardenability.

5.4.2 Effect of cooling rates without austenite deformation

Without austenite deformation, the transformed microstructures cooled at 5~50°C/s mainly consist of BF. The phase identification was performed according to the procedures described in Section 2.7. As the cooling rate is increased, the effective grain size decreases gradually and the distribution of both HAGBs and LAGBs are changed. These changes in grain refinement and the distribution of HAGBs and LAGBs can be explained from the point view of variant selection which is illustrated in Section 2.6.

Although the differences of BF microstructures with cooling rates between 5°C/s to 20°C/s are very small, these BF microstructures are quite different from the transformed microstructure cooled at 50°C/s. Therefore, a comparison is

made between the BF microstructures cooling at 5°C/s and 50°C/s. Since displacive transformations cannot cross austenite grain boundaries, a prior-austenite grain was identified in each EBSD map of these two BF microstructures. The {100} pole figures of the BF orientations of these two prior-austenite grains are shown in Figure 6-11 (a), (c) and the orientation maps of them are illustrated in Figure 5-10 (a), (d) respectively. Since the Kurdjumov–Sachs (K–S) relationship ($\{111\}_\gamma$//$\{110\}_\alpha$, $<110>_\gamma$//$<111>_\alpha$) generally provides good predictions for the BF transformation in steels [100], it was adopted as the orientation relationship in this research and the method proposed by Tari et al. [174] was used to evaluate the orientations of these two parent austenite grains, and the results were used to calculate the 24 K-S variants of each austenite grain. These results are shown in Figure 6-11 (b), (d) respectively, and good matches can be found between the pole figures of the experimentally determined BF orientations and calculated ferrite orientation variants.

To reveal detailed crystallographic features, the colours in the orientation maps were changed to show different colours for different CP and Bain groups, which is introduced in Section 2.6.2. These maps are termed as CP and Bain group maps and are shown in Figure 5-10 (b), (e) and Figure 5-10 (c), (f) for the two BF microstructures transformed at different cooling rates, respectively.
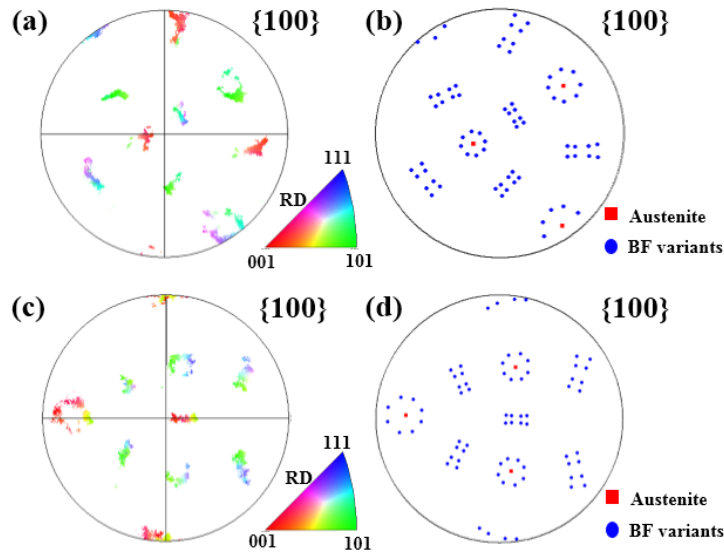
Figure 5-9 {100} pole figures of the BF orientation in single parent austenite grains with cooling rates of (a) 5˚C/s and (c) 50˚C/s; {100} pole figures of the calculated austenite orientations and corresponding ferrite orientation variants with cooling rates of (b) 5˚C/s and (d) 50˚C/s, respectively.
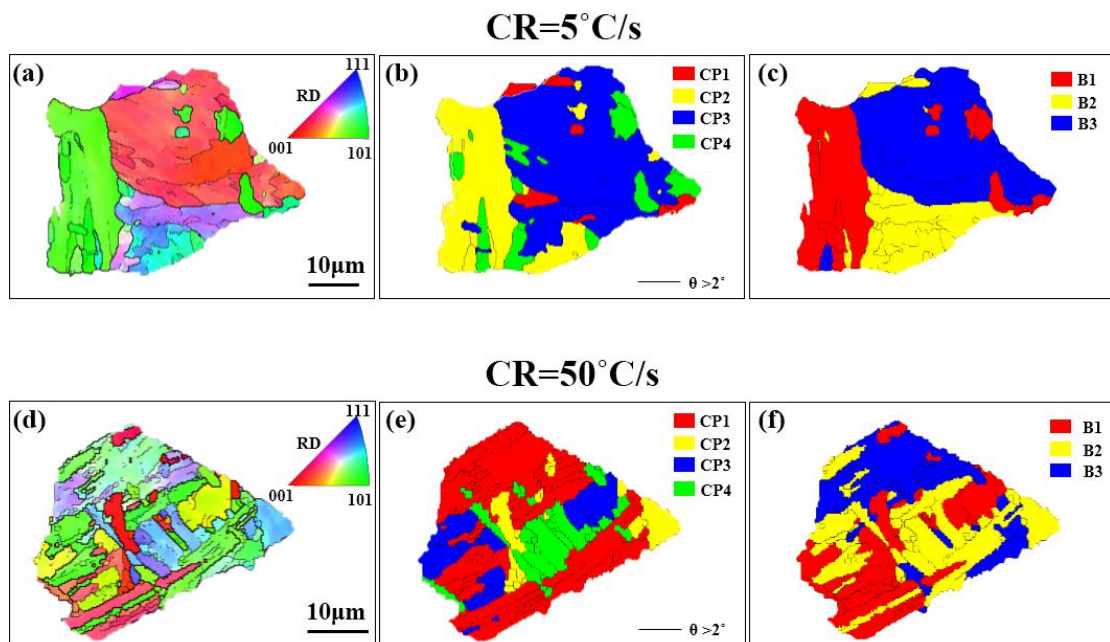
Figure 5-10 IPF coloured orientation maps (a) and (d), close-packed plane group maps (b) and (e) and Bain group maps (c) and (f) for BF microstructures in single parent austenite grains with cooling rates of 5˚C/s and 50˚C/s, respectively.

It can be seen clearly from Figure 5-9 that more intense variant selection happened at the cooling rate of 5˚C/s than at the cooling rate of 50˚C/s. Furthermore, the variant arrangements in these two microstructures are also quite different, as shown in Figure 5-10. At the cooling rate of 5˚C/s, variants belonging to the same Bain group are formed adjacently as shown in Figure 5-10 (c) and these variants may come from different CP groups, thus leading to intersecting CP groups as shown in Figure 5-10 (b). Differently, at the cooling rate of 50˚C/s, variants belonging to the same CP group are formed side by side as shown in Figure 5-10 (e) and these variants may come from different Bain groups, thus resulting in the typical packets morphology of BF.

These differences in the variant selection and the variant arrangement between two transformed BF microstructures cooled at 5˚C/s and 50˚C/s are similar to the results shown in Figure 2-40 and thus can be well explained by the influence of transformation driving force and accommodation method of transformation shape strain on variant selection. At the low cooling rate of 5˚C/s, BF transformation takes place at high temperatures and owing to the low BF transformation driving forces at high temperatures, intense variant selection happens. Due to the reason introduced in Section 2.6.3, variants belonging to the same Bain group are formed adjacently. While at the high cooling rate of 50˚C/s, BF transformation occurs at low temperatures and owing to the large BF transformation driving forces at low temperatures, variant selection is weakened. Due to the low transformation temperatures, the strength of austenite and BF are relatively high and thus the BF transformation shape strain cannot be relaxed easily by plastic accommodation. The transformation shape strain needs to be relaxed by self-accommodation through the formation of variants belonging to the same CP group but different Bain group in neighbours as introduced in Section 2.6.3. Since the boundaries between variants belonging to different Bain groups have disorientation angles higher than 47.1˚ as shown in Table 2-3, a higher density of HAGBs and thus a smaller effective grain size will be formed

113

at the cooling rate of 50˚C/s than at the cooling rate of 5˚C/s and some of these HAGBs exist within the BF packets. Based on the description above, it is reasonable to conceive that by further increasing the cooling rate and thus lowering the transformation temperature, the effective grain size will become increasingly small.

5.4.3 Conditions for the occurrence of AF transformation

In Chapter 4, it was found that austenite deformation below the recrystallisation-stop temperature promotes the transition from BF to AF by introducing deformation substructures as intragranular nucleation sites for AF transformation. Furthermore, BF dominates the transformed microstructures cooled at 5~50˚C/s without austenite deformation (strain2 of 0) as can be seen in Figure 5-2. Therefore, austenite deformation is required for the AF transformation in pipeline steels, which is quite different from the findings that AF-like microstructures can be found in continuous cooling products without deformation at slow cooling rates [89, 149, 170].

However, only meeting the condition of introducing intragranular nucleation sites by austenite deformation, AF transformation does not necessarily happen as shown in Figure 5-3 (d) at the cooling rate of 50˚C/s. For this specimen, a high density of intragranular nucleation sites had already been introduced into austenite grains by austenite deformation (strain2 = 0.5), but the transformed microstructure mainly consists of typical parallel BF laths and their nucleation mainly happened on the austenite grain boundaries. In other words, intragranular nucleation sites become inactive at this high cooling rate. Therefore, there must be another condition needed to be met for AF transformation to proceed.

It is very interesting to notice that in Figure 5-5 (b)~(c) where AF is the dominant microstructure, some short parallel laths along the PAGBs classified as BF can be seen clearly, and AF exists between these wide packets. While in the BF dominant microstructure as shown in Figure 5-5 (d), parallel BF laths

developed from PAGBs and extended across the whole austenite grain or impinged with others. To further confirm this microstructural characteristic, two areas were selected from the EBSD maps of microstructures transformed from deformed austenite and cooled at 10˚C/s and 50˚C/s respectively, indicated by black dashed blocks in Figure 5-7 (f) and (h) respectively. All Euler angle coloured orientation maps of these two areas with black lines representing boundaries with disorientation higher than 3˚ are shown in Figure 5-11 and Figure 5-12 respectively. Different parent austenite (PA) grains were separated from each other by carefully comparing the pole figure characteristics of different parts and PAGBs were highlighted by white dashed lines. The validity of the separation of these PA grains can be proved by the good correspondence between the {100} pole figures of the measured BF orientations and those of the transformed variants orientations of the calculated PA orientations. The method proposed by Tari et al. [174] was used to evaluate these PA orientations, following the Kurdjumov-Sachs (K-S) orientation relationship.
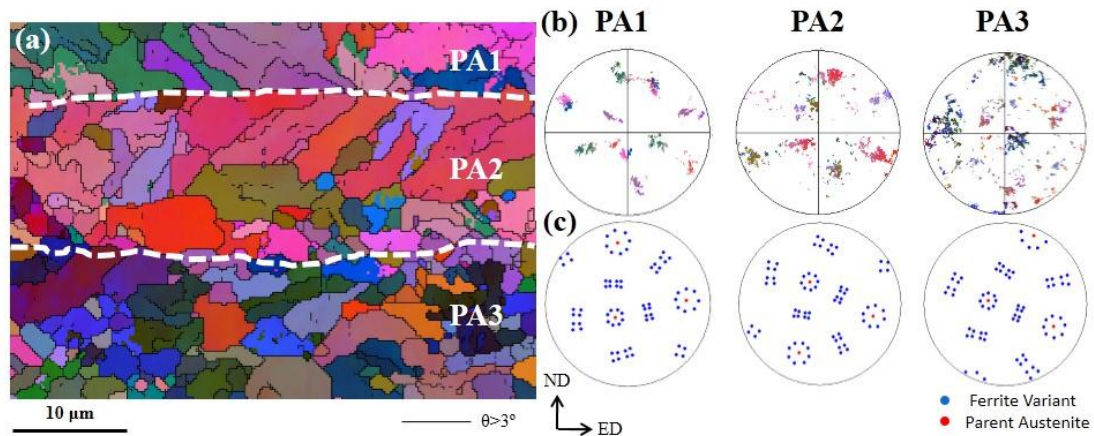
Figure 5-11 EBSD analysis of specimen with strain2 of 0.5 and cooling rate of 10˚C/s: (a) all Euler angle coloured orientation image map (black lines represent boundary disorientation>3˚ and PAGBs are shown by white dashed lines); (b) <100> pole figures of measured ferrite orientations in each parent austenite (PA) grain; (c) <100> pole figures of parent austenite (PA) orientations calculated and the orientations of their transformation variants respectively.

115
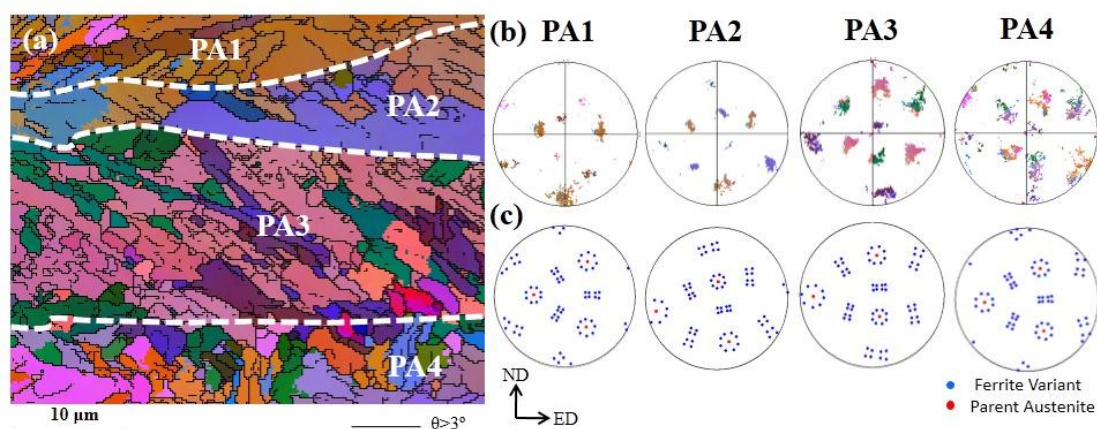
Figure 5-12 EBSD analysis of specimen with strain2 of 0.5 and cooling rate of 50°C/s: (a) all Euler angle coloured orientation image map (black lines represent boundary disorientation>3° and PAGBs are shown by white dashed lines); (b) <100> pole figures of measured ferrite orientations in each parent austenite (PA) grain; (c) <100> pole figures of parent austenite (PA) orientations calculated and the orientations of their transformation variants respectively.

In Figure 5-12 (a) where BF is the dominant microstructure, parallel BF laths forming packets with similar colours nucleated on PAGBs and extended across the whole grain or impinged with others. However, in Figure 5-11 (a) parallel laths nucleated on PAGBs and extended into PA2 were stopped and the remained austenite transformed into irregularly arranged AF laths, which corresponds very well to the characteristics observed in Figure 5-5 (b)~(c). It is also interesting to notice that in Figure 5-11 and Figure 5-12, the more refined and irregular the transformed microstructure, the more spreading of the ferrite orientations in the pole figures. There are some possible reasons for the spread of ferrite orientations. Under slow cooling rates, there may be some PF/QF grains which do not necessarily follow the orientation relationship with the parent austenite grains. The spreading of ferrite orientations may also reflect the disorientations induced by austenite deformation and the alleviated variant selection promoted by intragranular nucleation inside a single austenite grain.

116

Based on the above microstructure characteristic, in addition to the requirement for introducing intragranular nucleation sites, another prerequisite for the occurrence of AF transformation can be analysed as below.

Since austenite grain boundaries are very potent nucleation sites, BF laths firstly nucleate on the austenite grain boundaries during continuous cooling. When these laths develop across the whole austenite grain or impinge with other boundary nucleated laths, a BF dominant microstructure is formed. On the other hand, when these boundary nucleated laths are stopped prematurely due to certain mechanisms and thus cannot take up the whole parent austenite grain, AF transformation at intragranular nucleation sites happens during the following cooling process. The halting of BF laths should be another requirement for the occurrence of AF transformation.

Despite the nucleation promoting effect of austenite deformation illustrated in Section 4.4.2, it has been emphasised that displacive transformations involve the coordinated movement of atoms and such motion of a glissile interface can be halted if it encounters strong defects such as an austenite grain boundary or drastic deformation substructures. Less strong defects such as isolated dislocations also hinder the progress of such interfaces but can often be incorporated into the transformation product lattice. This means that austenite deformation can retard or hinder the displacive transformation. This retardation of the displacive transformation by plastic deformation is called mechanical stabilisation of austenite and has been found for all of the displacive transformations that occur in steels, which include Widmanstätten ferrite [175-177], bainite [178-180] and martensite [181, 182] transformations.

This mechanical stabilisation effect can be explained by a model [180] established by balancing the force driving the motion of the displacive transformation interface against the resistance of the dislocation debris created by austenite deformation. The mean shear stress τ needed to force dislocations past each other is:

$$\tau = \frac{Gb\rho^{\frac{1}{2}}}{8\pi(1-v)l} \qquad\qquad (5.1)$$

where G is the shear modulus, v the Poisson's ratio and ρ the dislocation density [183]. The stress τ_T driving the motion of the interface originates from the chemical free energy change $\varDelta G$ of the transformation,

$$\tau_T = \Phi\varDelta G \qquad\qquad (5.2)$$

where Φ is a constant assumed to be equal to unity. $\varDelta G$ varies with the transformation temperature and steel's composition. The chemical free energy change, $\varDelta G$, of the tested steel in this research was calculated using the thermodynamic calculation software Thermo-Calc which accesses thermodynamic data (TCFE6 database) to calculate phase stabilities and free energies. The stored strain energy due to the shape deformation accompanying bainite transformation comes to about 400 J/mol [184] which was subtracted from the Thermo-Calc calculation results. The values of bainitic ferrite transformation driving force (after the subtraction of the stored strain energy, 400 J/mol) at different temperatures are shown in Figure 5-13 (a). It can be seen that when temperature is lower than 645°C, bainitic transformation is thermodynamically possible for the tested steel composition.
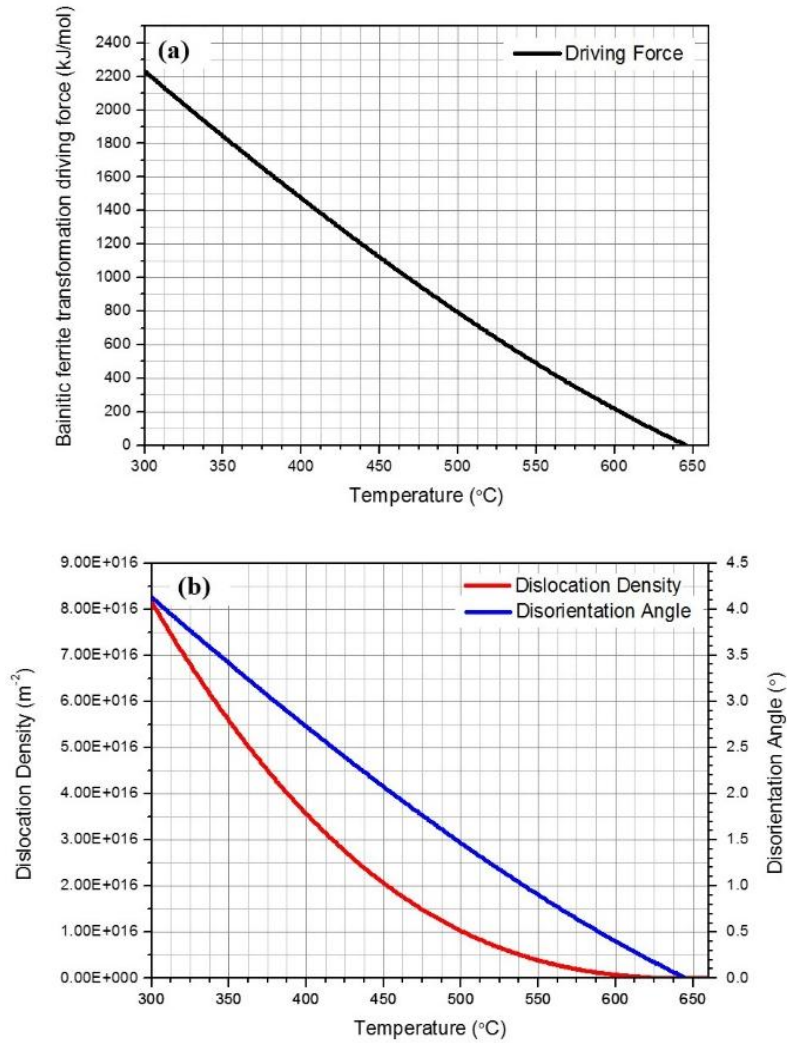
Figure 5-13 Variation of (a) bainitic ferrite transformation driving force and (b) interface halting dislocation density with corresponding disorientation angle of austenite as a function of transformation temperature.

The motion of the transformation interfaces halts when the stress driving it, τ_T, is lower than the resistance opposing it, τ. Therefore based on the driving force calculation results, the dislocation density in austenite which is high enough to halt the motion of the interface can be calculated using Equation (5.1) with austenite shear modulus 8×10^{10} Pa, Poisson's ratio 0.27 and Burgers vector 2.52×10^{-10} m. However, the dislocation density of deformed austenite is hard to measure. Therefore, the dislocation densities were roughly transferred to a sub-grain boundary disorientation angles according to the relationship:

119

$$b\rho^{\frac{1}{2}} \approx \theta \qquad\qquad (5.3)$$

where θ is the sub-grain boundary disorientation angle, and this relationship has been found effective for 304L stainless steel deformed in compression at 1000°C [185].

According to the transformation driving force values shown in Figure 5-13 (a), the dislocation densities and the corresponding sub-grain boundary disorientation angles capable of halting the transformation interface as a function of transformation temperature were calculated and are shown in Figure 5-13 (b). It can be seen that at relatively high transformation temperatures around 550°C, the motion of the transformation interface can be halted by sub-grain boundaries with disorientation angles higher than 0.9° which can be readily formed during the austenite deformation process with a strain = 0.5 as shown in research [186]. By lowering the transformation temperature, larger dislocation densities and thus higher sub-grain boundary disorientation angles are needed to stop the motion of the transformation interface. Furthermore, according to the scaling hypothesis [40] analysing the distribution of boundary spacing and disorientation angles, for sub-grain boundaries with disorientation angles above the mean disorientation angle, the higher the disorientation angle, the lower the frequency. Therefore, lowering the transformation temperature by increasing the cooling rate, the probability of a bainitic transformation interface being stopped is reduced resulting in relatively coarse BF packets.

It should be noted that an assumption is made here that the dislocations halting the advancing interface are all geometrically necessary dislocations (GNDs) which Equation (5.3) is applicable to. During austenite deformation, GNDs are needed to maintain lattice continuity while statistically stored dislocations (SSDs) are developed from random trapping processes [187]. Therefore, critical sub-grain boundary disorientation angles can be lowered with the presence of statistically stored dislocations.

Based on the mechanism illustrated above, it is feasible to conceive that if

the deformed austenite is cooled very fast from the deformation temperature to room temperature, there should be very few AF laths in the microstructure. Conversely, if the deformed austenite is cooled very fast from the deformation temperature to a relatively high temperature below the bainite transformation start temperature and then slowly cooled, AF dominant microstructures should be obtained. To test these conceptions, another two specimens were tested. Both of them underwent the same deformation profile with strain2 = 0.5, but one of them was water quenched to room temperature after deformation and the other one was fast cooled from 950˚C to 600˚C at 100˚C/s and then slowly cooled to 350˚C at 1˚C/s followed by a water quenching to room temperature. The transformed microstructures of these two specimens are shown in Figure 5-14. It can be seen clearly that for the water quenched specimen the microstructure mainly consists of BF and martensite and AF laths can hardly be found. For the other specimen, the transformed microstructure is AF dominant and this further proves that instead of cooling rates, transformation temperature is the critical parameter for the occurrence of AF transformation. This also explains the reason why an AF dominant microstructure is formed after austenite deformation in Chapter 4, because of the relatively slow cooling rate, 20˚C/s, used. And at higher cooling rates, e.g. 50˚C/s, the influence of austenite deformation on transformed microstructures will be less evident because both of the microstructures transformed from recrystallised and deformed austenite will be BF dominant.
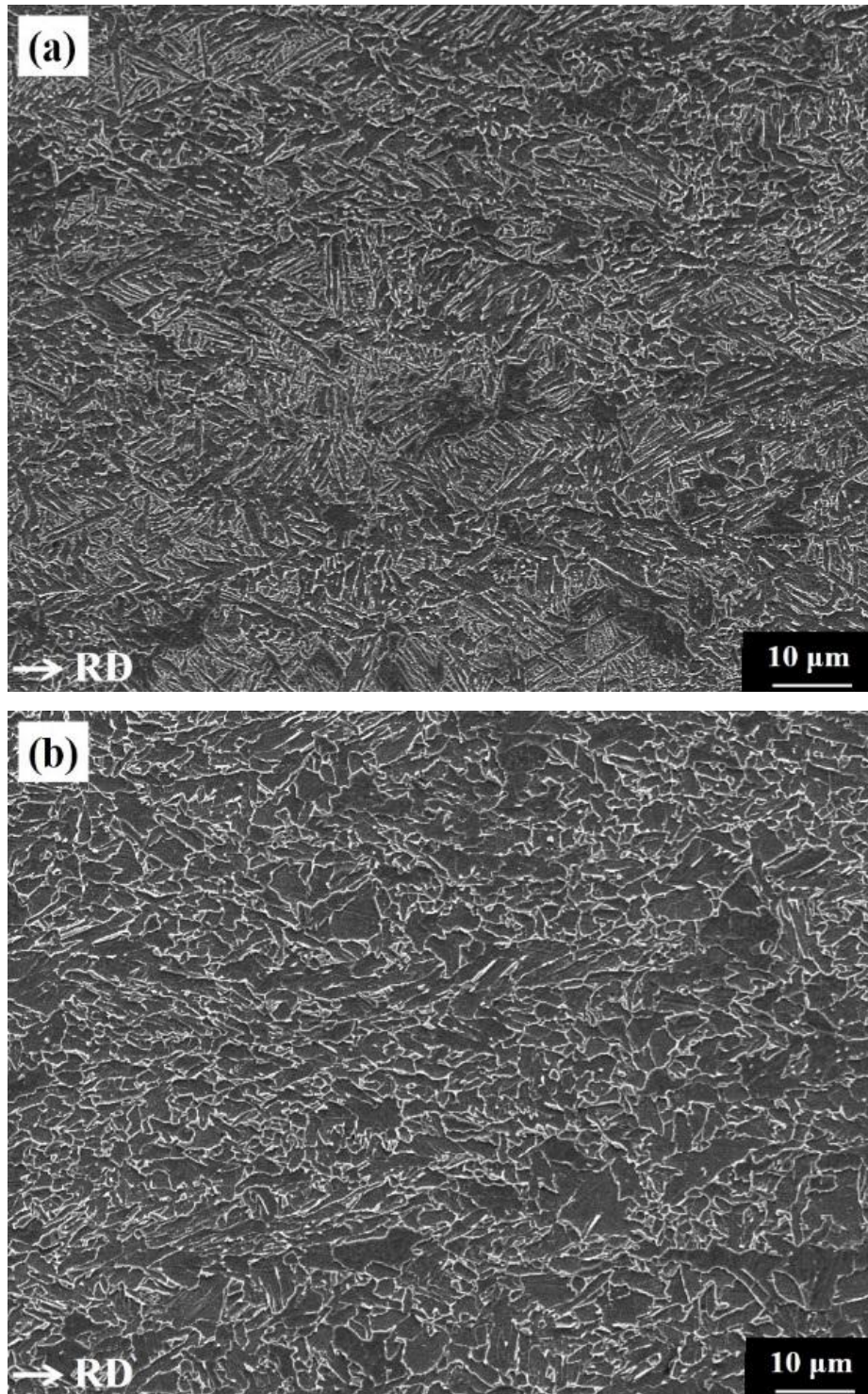
Figure 5-14 SEM secondary electron micrograph showing the microstructure of the transformed product after different cooling processes with austenite deformation strain2 = 0.5: (a) water quenched to room temperature; (b) cooled at 100 ˚C/s to 600 ˚C and then slowly cooled to 350˚C at 1˚C/s followed by water quenching to room temperature.

Some characteristics of the transformed AF microstructure need to be further explained.

(1) Although BF laths nucleated on austenite grain boundaries need to be stopped to give room for the AF intragranular nucleation, parallel BF laths as shown in Figure 5-5 (b)~(c) do not necessarily appear on each PAGB. This is because the deformation strain is not evenly distributed within each austenite grain. Normally strain at the austenite grain boundary is higher than that in the austenite grain interior and correspondingly sub-grain boundary disorientation angles near the austenite grain boundary will be higher than that in the grain interior. Therefore, boundary nucleated BF laths are more likely to be halted very near the austenite grain boundaries without forming BF packets.

(2) It is widely found in this research that if a BF packet is formed on one side of an austenite grain boundary, a BF packet will also be developed on the other side of the austenite grain boundary. This is because the strain across the austenite grain boundary is supposed to be continuous. If the deformation substructure developed on one side of the austenite grain boundary is not dense enough to stop the BF development, they are also not dense enough on the other side due to the continuity of the local strain.

(3) Even in AF dominant microstructures, there are still some long BF laths across the whole parent austenite grains. This can be attributed to the unevenly distributed deformation strains between different parent austenite grains, and the differences of deformation induced substructures between austenite grains with different orientations were investigated in research [186]. Furthermore, the microstructure changes from AF dominant to BF dominant is gradual with increased cooling rates.

(4) Although raising the transformation temperature will promote the mechanical stabilisation effect of austenite deformation and halt BF laths more effectively, the maximum possible transformation volume of AF and BF will be reduced with the rise of the transformation temperature and finally reaches zero

at the bainite transformation start temperature according to the incomplete transformation phenomenon of bainitic transformation [2]. This has already been shown in isothermal transformation results in research [85]. Therefore, the continuous cooling rate and the cooling interrupt temperature need to be selected carefully to stop the lengthening of BF laths and simultaneously get a high volume fraction of AF microstructure, and continuous cooling is more suitable than isothermal holding to get high volume fraction of AF.

(5) PF/QF transformation happened before AF and BF can consume the nucleation sites on austenite grain boundaries and more importantly, the solid solution atoms partitioned from PF/QF grains to austenite can stabilize their neighbour austenite and retard bainite nucleation, which has already been proved in research [188]. Moreover, PF/QF grains formed intragranularly can also halt the BF transformation interfaces. Therefore, the formation of PF/QF grains is beneficial to AF transformation. But the existence of PF/QF grains will undoubtedly lower the strength of the transformed microstructure, and the formation of PF/QF grains is not a prerequisite for AF transformation. In previous research [85], cooling from austenite deformation temperature 850°C to isothermal holding temperature 500~600°C at a rate of 75°C/s, the AF transformation still occurred without the aid of PF/QF transformation, and interestingly, it was observed that the PF transformation happened at PAGBs when AF and BF transformations were nearly finished. Similarly, in this research, it can be seen from Figure 5-14 (b) that with a cooling rate of 100°C/s to reduce the interference of the PF/QF transformation, AF still dominates the transformed microstructure. In other words, PF/QF transformation is not a prerequisite for AF transformation.

5.4.4 Effect of austenite deformation on grain refinement

As illustrated in Section 4.1, although many investigations have been conducted, the effect of austenite deformation on the grain refinement are still

controversial. In some investigations [85, 149, 150], it was found that the transformed microstructure is refined by austenite deformation and the volume fraction of AF increases with raised deformation. Contradicting this were results from another investigation [151] in which it was shown that the effective grain size of bainite was increased from 3.2 μm to 3.8 μm when the austenite was deformed by 30%. Furthermore, the block size of the bainite was found to be increased after austenite deformation [142], and the quantity of packets in each austenite grain also decreased after the austenite deformation [152]. More importantly, it was revealed from these investigations that even after significant austenite deformation, the transformation product consisted of parallel BF laths and the typical AF microstructure was absent.

Based on the experimental results in this chapter, it can be proposed that the effect of austenite deformation on the grain refinement is cooling rate dependent. Actually, the whole cooling rate range can be divided into four regions as shown in Figure 5-8 (a) and within each cooling rate region, the effect of austenite deformation on grain refinement is distinct.

In the cooling rate region 1, due to the low cooling rates (0.5˚C/s and 1˚C/s), the transformation products consist of PF/QF and BF (when transformed from fully recrystallised austenite) or PF/QF and microphases (when transformed from fully unrecrystallised austenite). Because of the influence of austenite deformation on the transformation driving force and the nucleation site density as illustrated in Section 5.4.1, the effective grain size is refined by austenite deformation in this region.

In the cooling rate region 2, the transformation products are BF (when transformed from fully recrystallised austenite) or AF dominant (when transformed from fully unrecrystallised austenite). Since for displacive transformation products lath boundaries are not necessarily HAGBs, therefore the grain refinement should be analysed from two aspects, the density of lath boundaries and the possibility of HAGB formation. Due to the relatively slow

125

cooling rates (5˚C/s and 10˚C/s) and thus, the high transformation temperatures, the transformed BF laths are very coarse, leading to a very low density of lath boundaries. Furthermore, at high transformation temperatures, during the BF transformation intense variant selection happens and variants belonging to the same Bain group are formed adjacently [99] as shown in Figure 5-10 (c). The possible reason for the formation of these particular variant pairs is explained in Section 2.6.3. Variants belonging to the same Bain group usually have disorientation angles small than 21.1˚ with each other as shown in Table 2-3. Therefore, a low density of HAGBs and thus a large effective grain size are found for the BF microstructures transformed from fully recrystallised austenite.

However, for the AF microstructures transformed from fully unrecrystallised austenite, due to the introduction of intragranular nucleation sites and the halting effect of the deformation substructures on the growth of displacive transformation products, both AF and BF laths are greatly refined as shown in Figure 5-5 (a)~(b), leading to a high density of lath boundaries. Furthermore, the introduction of intragranular nucleation sites can weaken the variant selection mechanism and thus more variants and variant pairs will be generated, leading to a high density of HAGBs and thus a small effective grain size as shown in Figure 5-7 (b)~(c) and Figure 5-8 (a) respectively. Actually, it has been found in research [189] that the formation of HAGBs is mainly attributed to the intragranular nucleation of the primary plates and not the plate interwoven morphology. Therefore, the effective grain size is refined by austenite deformation through the formation of intragranularly nucleated AF in region 2.

In the cooling rate region 3, the transformation products are BF (when transformed from fully recrystallised austenite) or AF+BF (when transformed from fully unrecrystallised austenite). For fully recrystallised austenite, due to the relatively high cooling rates (20˚C/s and 50˚C/s) and thus the low BF transformation temperatures, BF laths become thinner with the increased cooling rate, Figure 5-4 (c)~(d), and the factors weakening the variant selection are

126

increasingly strong so that more variants are formed in each austenite grain. Furthermore, owing to the occurrence of self-accommodation of the BF transformation shape strain at low transformation temperatures, typical packet structures are formed and within each packet variants belonging to different Bain groups are generated side by side as shown in Figure 5-10 (e)~(d). Therefore, a high density of HAGBs and thus a small effective grain size are found for the BF microstructures transformed from fully recrystallised austenite. More importantly, by increasing the cooling rates or lowering the transformation temperatures, the effective grain size can be further reduced.

In contrast, for the transformation products from fully unrecrystallised austenite, with the increased cooling rates or the lowered transformation temperatures, the intragranular nucleation sites for AF transformation gradually become inactive as explained in Section 5.4.3, and the fraction of AF is decreased while that of BF is raised as shown in Figure 5-7. For the BF transformation, the main nucleation sites are austenite grain boundaries, and austenite deformation can only result in a very limited increase of the austenite grain boundary area. Even worse, for a BF microstructure, austenite deformation can result in a strong variant selection that the BF variants with habit planes parallel to the active slip planes during austenite deformation are favoured [190]. This kind of variant selection can be found in PA2 and PA3 in Figure 5-12 (a). The traces of the lath boundaries on the RD-ND plane are around 32° away from the RD and based on the Schmid factor analysis for the main ideal texture component of austenite during plane strain compression [49] the traces of active slip planes in the RD-ND plane are 19.5°~ 45° away from the RD. Therefore, for deformed austenite, with the increased cooling rates, due to the raised BF fraction and the strong BF variant selection resulted from the austenite deformation, the effective grain size becomes increasingly large as shown in Figure 5-8 (a). More importantly, by increasing the cooling rates or lowering the transformation temperatures, the fraction of BF can be further increased as

illustrated in Section 5.4.3 and thus the effective grain size will be continuously increased.

Therefore, it is reasonable to conceive that the two lines in Figure 5-8 (a) can intersect at a certain cooling rate higher than 50°C/s and further increasing the cooling rates, the red line will be above the black line, which means in region 4 at very high cooling rates or low transformation temperatures, instead of refining, austenite deformation will lead to a coarser transformation microstructure. This conception has been confirmed in investigation [191] that at cooling rates higher than 20°C/s, the effective grain sizes of the microstructures transformed from fully unrecrystallised austenite are larger than those of the microstructures transformed from fully recrystallised austenite. The relevant results in investigation [191] are shown in Figure 5-15. The smaller intersecting cooling rate, 20°C/s, in investigation [191] maybe can be attributed to the large hardenability of the steel used in that research.
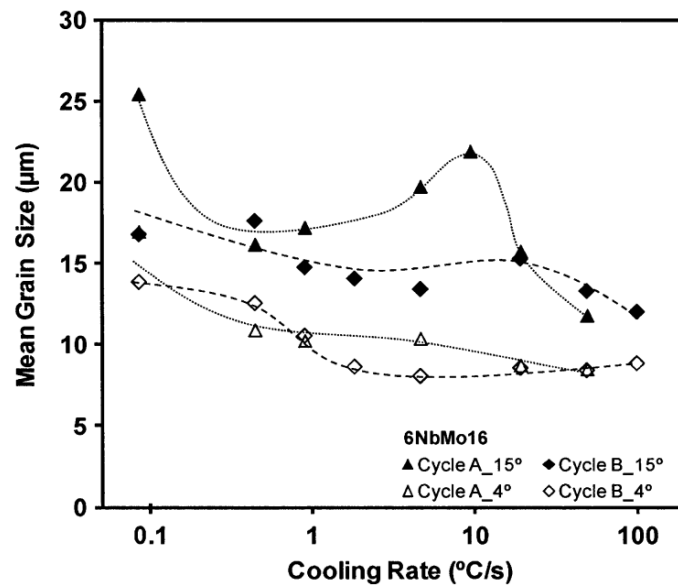
Figure 5-15 Effect of cooling rate on the mean grain size for both recrystallized (Cycle A) and unrecrystallised (Cycle B) austenite adopting 4° and 15° as threshold disorientation values in steel 6NbMo16 [191].

Based on the analysis above, the controversial effect of austenite deformation on grain refinement can be well understood. In investigations [85, 149, 150], due to the high transformation temperatures or the low cooling rates, the transformed microstructures are AF dominant so that the transformed microstructures are refined by austenite deformation as in region 2 or in region 3 in Figure 5-8 (a). However, in investigations [142, 151, 152], owing to the high cooling rates or the low transformation temperatures, BF microstructure dominates, therefore, the transformed microstructures are coarsened by austenite deformation as in region 4 in Figure 5-8.

5.5 Summary

In this chapter, the effects of austenite deformation and continuous cooling rates on the microstructural evolution were investigated. It was found that:

(1) Subjected to low cooling rates (0.5˚C/s and 1˚C/s), the transformation products consist of PF/QF and BF (when transformed from fully recrystallised austenite) or PF/QF and microphases (when transformed from fully unrecrystallised austenite). Because of the influence of austenite deformation on the transformation driving force, steel's hardenability and nucleation site density, the effective grain size is refined by austenite deformation and BF packets disappear in the transformation products from deformed austenite.

(2) Without austenite deformation, the transformed microstructures cooled at different cooling rates (5~50˚C/s) are all BF dominant. AF-like microstructures cannot be found in these continuous cooled microstructures covering a wide cooling rate range without austenite deformation, which proves that austenite deformation is required for the AF transformation in pipeline steels. For these BF dominant microstructures, effective grain size can be continuously reduced with the increased cooling rate.

(3) Subjected to the same austenite deformation (strain2 of 0.5), the fraction of AF decreases and BF becomes more and more dominant with the cooling rate increasing from 10˚C/s to 50˚C/s, which means a transition from AF to BF occurs. At the same time, the transformed microstructure is coarsened with the effective grain size being raised from 2.9 μm to 3.5 μm.

(4) Based on the results obtained from optical microscopy, scanning electron microscopy and electron backscattering diffraction mapping, the introduction of intragranular nucleation sites and halting of BF laths nucleated on austenite grain boundaries are found as two conditions that should be fulfilled for the occurrence of acicular ferrite transformation. Increasing austenite deformation strain can introduce a higher density of dislocation arrays into the austenite which can act as intragranular nucleation sites. Besides, the deformation substructures can also halt the lengthening of BF laths by the mechanism of mechanical stabilisation of austenite.

(5) Halting BF laths can only happen under relatively slower cooling rates or higher transformation temperature because high cooling rates result in a low transformation temperature which increases the driving force for transformation interfaces to overcome deformation substructures and leads to a BF or martensite dominant microstructure.

Chapter 6　Effect of austenite grain size on microstructure evolution

6.1　Introduction

Prior-austenite grain size (PAGS) is well acknowledged to have a remarkable effect on phase transformations in steel. But there are some differences in the influence of PAGS on various phase transformations [192-194]. For martensite transformation, the martensite-start temperature rises as the PAGS is increased [192]. As for pearlite transformation, it was argued in reference [193] that rising PAGS can delay isothermal pearlite transformation due to the reduction of grain edges which are the main nucleation sites for pearlite.

However, the effect of PAGS on the bainitic transformation is controversial [165, 194-196]. In some investigations [194, 196-198], it was found that the rate of bainite transformation was increased by a decrease in the PAGS, which was attributed to the fact that the reduction in PAGS brings about an increase in the grain boundary area per unit volume, and thus an enhanced nucleation rate. However, Davenport [199] observed that the PAGS had no observable effect on the bainite transformation kinetics. In contrast, investigation [200] indicated that a fine-grained austenite structure suppressed the growth of bainite and leads to a lower transformation rate. Additionally, it was shown that the influence of the PAGS does not appear to be continuous, and that there is a critical PAGS below which there is a distinct grain size effect [200]. To explain these controversial effects, Matsuzaki and Bhadeshia [195] discovered that for different steels the effects of PAGS on bainite transformation are distinct and the difference in kinetics was found together with evident discrepancy in transformed bainite microstructures. Whether the kinetics of bainite transformation are increased or decreased by reducing the PAGS depends on whether the kinetics are restricted by slow growth rate or limited number of nucleation sites. Despite the number

131

of studies concerning the effect of PAGS on BF transformation kinetics, there are few investigations regarding the influence of PAGS on BF microstructures.

Differently, for intragranularly nucleated transformation products, like the AF in steel welds, it has been found that the decomposition of supercooled austenite is a competition between the BF transformation nucleated on austenite grain boundaries and the AF transformation nucleated intragranularly on non-metallic inclusions [2]. It was found that increasing the PAGS, the fraction of intragranularly nucleated AF was increased, replacing the boundary nucleated BF, and this was attributed to the reduction of the austenite grain boundary density and thus the nucleation site density of BF [201]. Bhadeshia and Svensson [19] have performed systematic modelling research and established a collection of models to predict the transformed microstructures in steel welds. They found that increasing the PAGS can promote intragranularly nucleated transformations and consequently increase the AF volume fraction in steel welds. Since the AF in pipeline steels has been widely considered as an intragranularly nucleated transformation product of austenite [165-167], it is reasonable to assume that the fraction of AF will also be influenced by the PAGS.

Therefore, in this chapter, specimens with various austenite grain sizes were processed to investigate the effect of PAGS before continuous cooling (from fully recrystallised austenite) or before the finishing deformation (from fully unrecrystallised austenite) on the microstructural evolution and grain refinement.

6.2 Experimental

During the solid solution heat treatment and the thermomechanical processing illustrated previously in this thesis, parameters of the solid solution heat treatment, the reheating and the roughing deformation (strain1) can all influence the austenite grain size before the continuous cooling (strain2 = 0) or before the finishing deformation (strain2 = 0.5). However, attention must be paid on choosing the suitable parameters to generate different PAGSs, especially on

the reheating temperature and duration. During reheating, not only the PAGS but also the dissolution status of Nb precipitates are changed by altering the reheating temperatures and durations [22], which makes the investigation on the effect of PAGS biased. Differently, if the standard solid solution heat treatment can dissolve most of the Nb precipitates, prolonging the duration of the heat treatment can result in a larger PAGS without greatly changing the Nb dissolution status. In addition, changing the roughing deformation (strain1) also has little influence on the Nb precipitates dissolution status simply due to the high temperature (1100°C) of this deformation at which the solute supersaturation, and subsequently the extent of precipitation of Nb carbide or carbonitride is very low. Therefore, to generate austenite with different grain sizes, different parameters of the solid solution heat treatment and the roughing deformation (strain1) were used as shown in Table 6-1 and S, M, L and XL were designated to the specimens subjected to these different combinations of the heat treatment duration and the volume of strain1. The heat treatment temperature was selected as 1250°C based on the dissolution temperature of Nb carbide calculated for the tested steel from Equation (3.1), 1232°C, as illustrated in Section 3.2.2. After this solid solution heat treatment, all specimens were quenched in ice water.

Table 6-1 Heat treatment and austenite deformation parameters

Specimen names	S	M	L	XL
Heat treatment temperature (°C)	1250	1250	1250	1250
Heat treatment duration (s)	1800	1800	7200	7200
Strain1 magnitude	0.7	0.3	0.3	0
Prior-austenite grain size (μm)	22.3	37.0	52.4	62.8

The processing route is illustrated in Figure 6-1. The heat treated specimens

were reheated to 1200°C at a rate of 10°C/s, held for 2 minutes for equilibration, and then cooled at a rate of 5°C/s to 1100°C for a roughing deformation (strain1) at a constant true strain rate of $10s^{-1}$. After that, the specimens were cooled immediately to 950°C at a rate of 5°C/s for the finishing deformation with strain2, either 0 or 0.5. This finishing deformation was also performed at a constant true strain rate of $10s^{-1}$, and was followed by a controlled cooling from 950°C to 500°C at a rate of 10°C/s. After that, specimens were slowly cooled from 500°C to 350°C at a rate of 1°C/s and finally water quenched from 350°C to room temperature. Additionally, specimens S, M, L and XL were also water quenched directly from 950°C before or after the finishing deformation (strain2 = 0.5) to reveal the prior-austenite microstructures with different PAGSs.
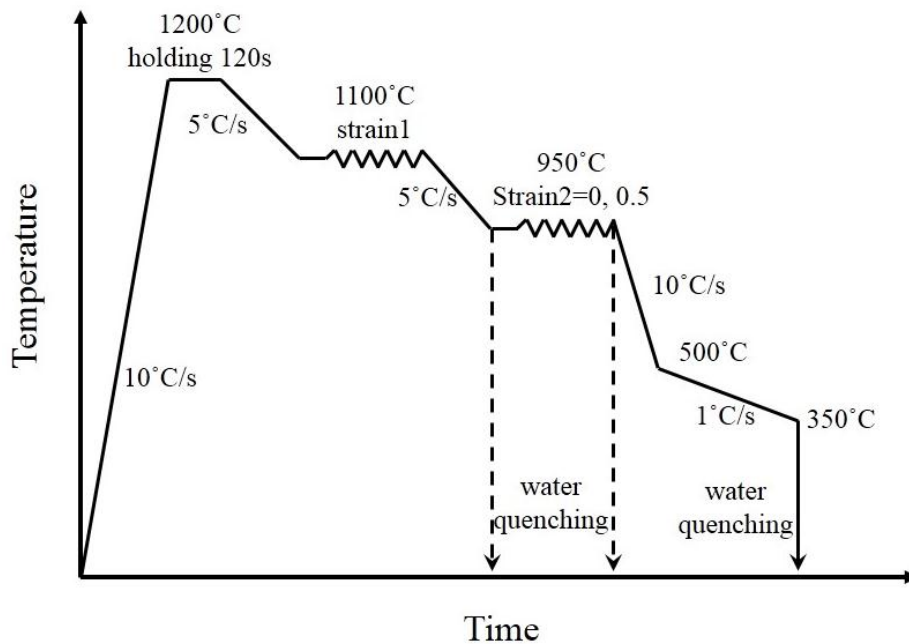
Figure 6-1 Schematic illustration of the thermomechanical testing profile.

Specimens for OM and SEM observation and EBSD mapping were prepared carefully as illustrated in Section 3.3. Specimens water quenched before the finishing deformation (strain2) were etched with a saturated picric acid aqueous solution to measure the PAGSs optically by the linear intercept method according to ASTM E112-13 standard [202]. The microstructures of the continuously

cooled specimens were observed after etching with 2% nital solution. EBSD analyses were carried out with a step size of 0.2 μm and accelerating voltage of 20 kV on the RD-ND plane of each specimen. Noise reduction and grain size measurement were performed as introduced in Section 3.3.2.

6.3 Results

6.3.1 Prior-austenite microstructures

Optical micrographs of the prior-austenite grain boundaries (PAGBs) both before and after strain2 for specimen S, M, L and XL are shown in Figure 6-2. It is clear from Figure 6-2 (a)~(d) that through adjusting the solid solution heat treatment durations and the magnitude of strain1, fully recrystallised austenite with different grain sizes were obtained before strain2 at 950˚C. PAGS measurement results are shown in Table 6-1, PAGS varying from 22.3 μm to 62.8 μm. After the finishing deformation (strain2 = 0.5), austenite grains of all specimens remain in a deformed state as shown in Figure 6-2 (e)~(h) and there is no sign for the occurrence of dynamic recrystallisation.
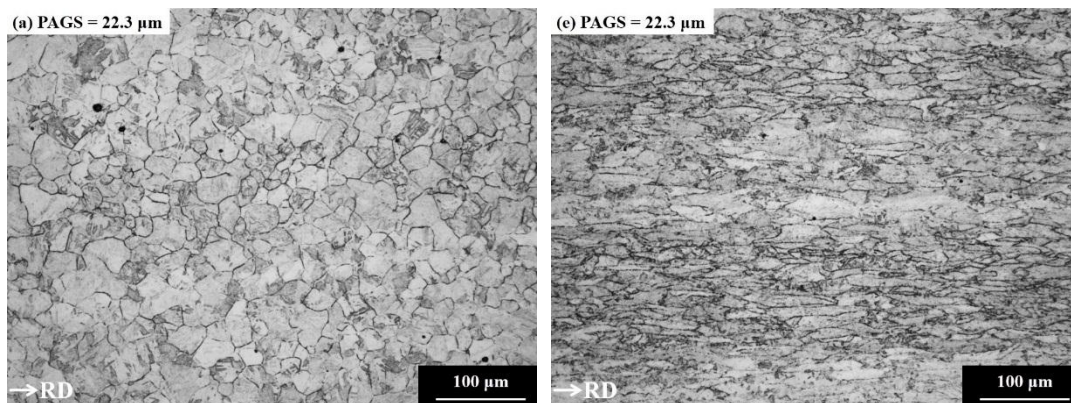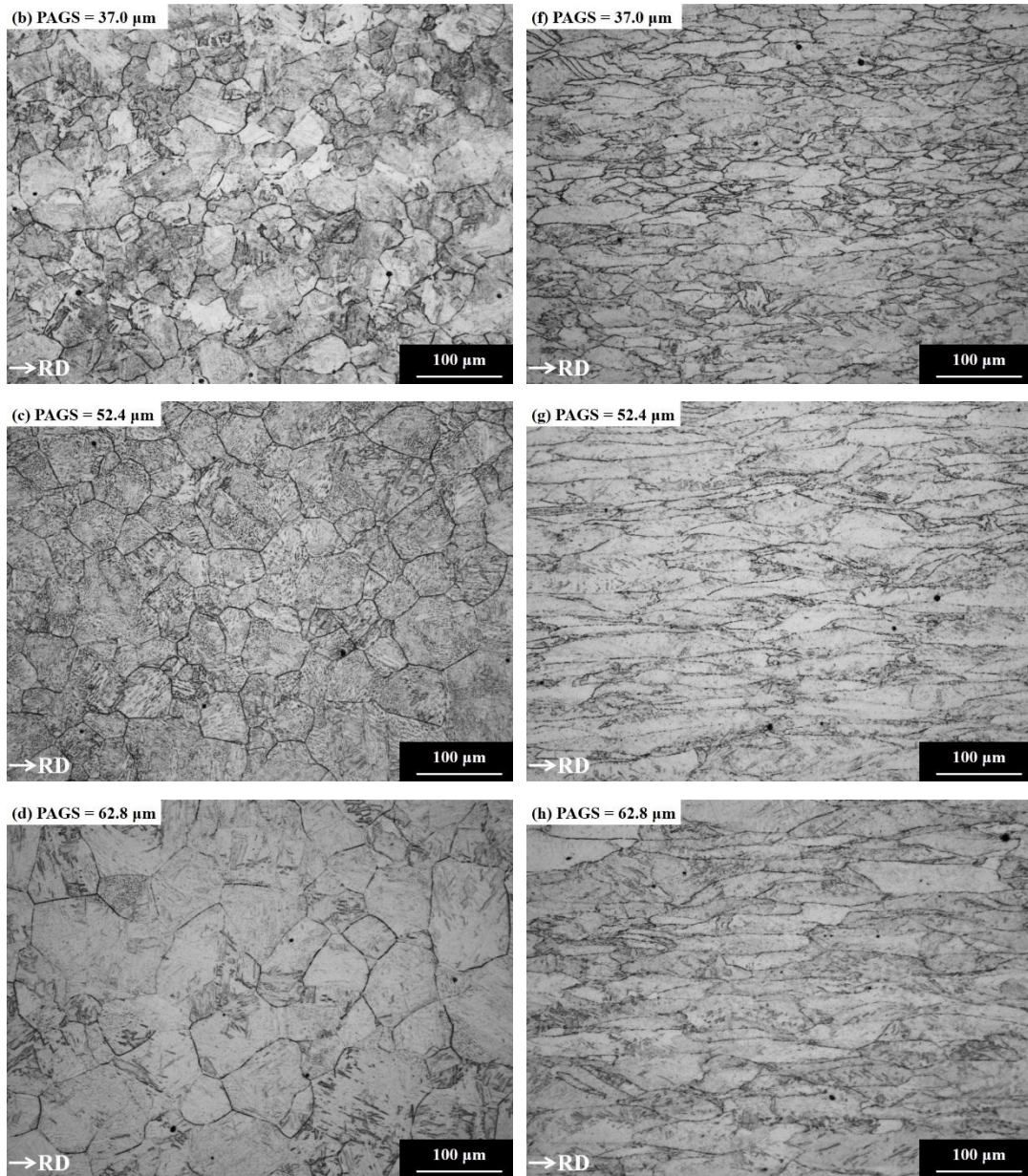
Figure 6-2 Optical micrographs of prior-austenite grain boundaries for specimen S, M, L and XL respectively: (a)~(d) before strain2 at 950˚C; (e)~(h) after strain2 of 0.5 at 950˚C.

6.3.2 Transformed microstructures

Optical micrographs of the continuously cooled microstructures transformed from recrystallised austenite (strain2 = 0) with different PAGSs are shown in Figure 6-3. The transformed microstructures all consist of BF but with clear

differences in their morphologies. With a PAGS of 37.0 μm, Figure 6-3 (b), the transformed microstructure mainly consists of packets of parallel BF laths. With an increased PAGS, Figure 6-3 (c)~(d), the BF lath boundaries are more and more obscure and irregularly shaped and the shape of the microphases, probably M/A constituents, also change from acicular to equiaxed. Due to the very small PAGS (22.3 μm), the microstructure in Figure 6-3 (a) is well refined and the morphology of the BF microstructure cannot be observed clearly from this optical micrograph.
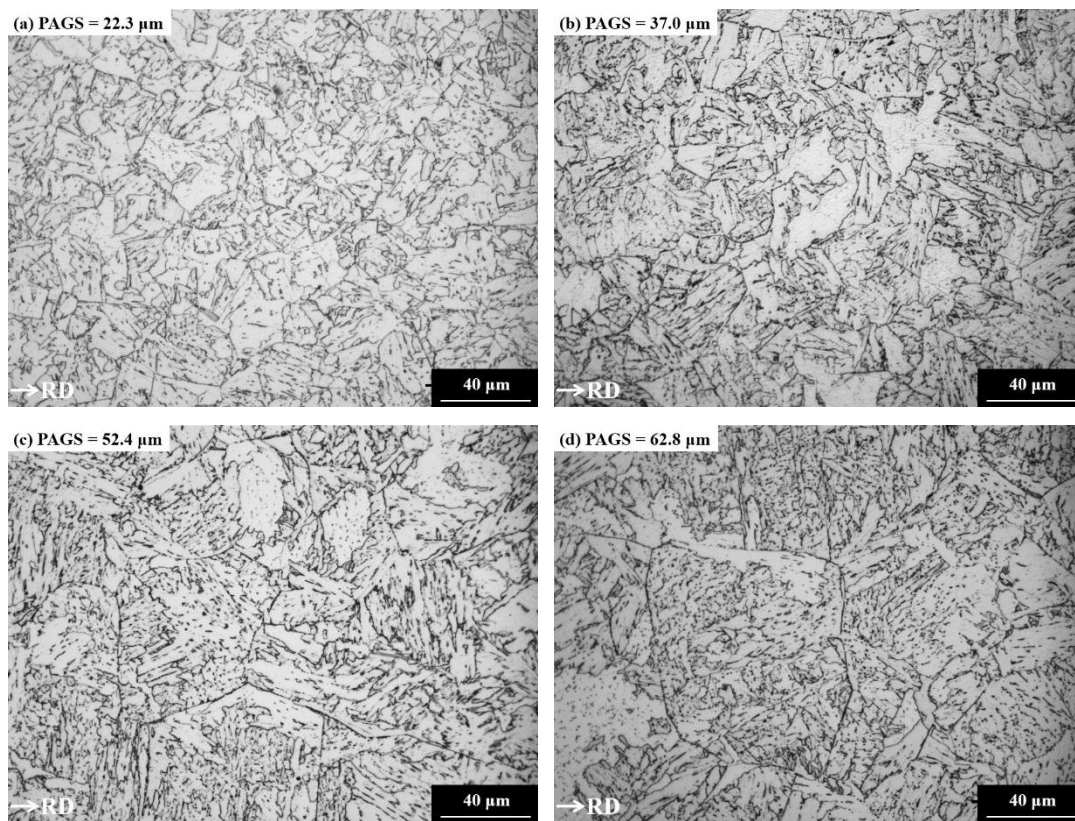
Figure 6-3 Optical micrographs depicting microstructures transformed from recrystallised austenite (strain2 = 0) with different PAGSs: (a) 22.3 μm, (b) 37.0 μm, (c) 52.4 μm and (d) 62.8 μm.

Optical micrographs of the continuously cooled microstructures transformed from deformed austenite (strain2 = 0.5) with different PAGSs are shown in Figure 6-4. From these micrographs we can see that the transformed

microstructures with the PAGSs of 22.3 μm and 37.0 μm are very similar and so are the transformed microstructures with the PAGSs of 52.4 μm and 62.8 μm. However, the transformed microstructures with the PAGSs of 22.3 μm and 37.0 μm are quite different from those with the PAGSs of 52.4 μm and 62.8 μm. Therefore, for transformation products from deformed austenite, the PAGSs can be divided into two groups, the small PAGS group (22.3 μm and 37.0 μm) and the large PAGS group (52.4 μm and 62.8 μm). With the small PAGSs, the transformed microstructures are AF dominant and consist of non-equiaxed ferrite laths with an irregular arrangement. While in the transformed microstructures with the large PAGSs, although a small fraction of AF still exists, the major transformation product is BF, organised and parallel laths nucleated on austenite grain boundaries and extended into grain interiors. Furthermore, the transformed microstructures with the small PAGSs are finer than those with the large PAGSs.
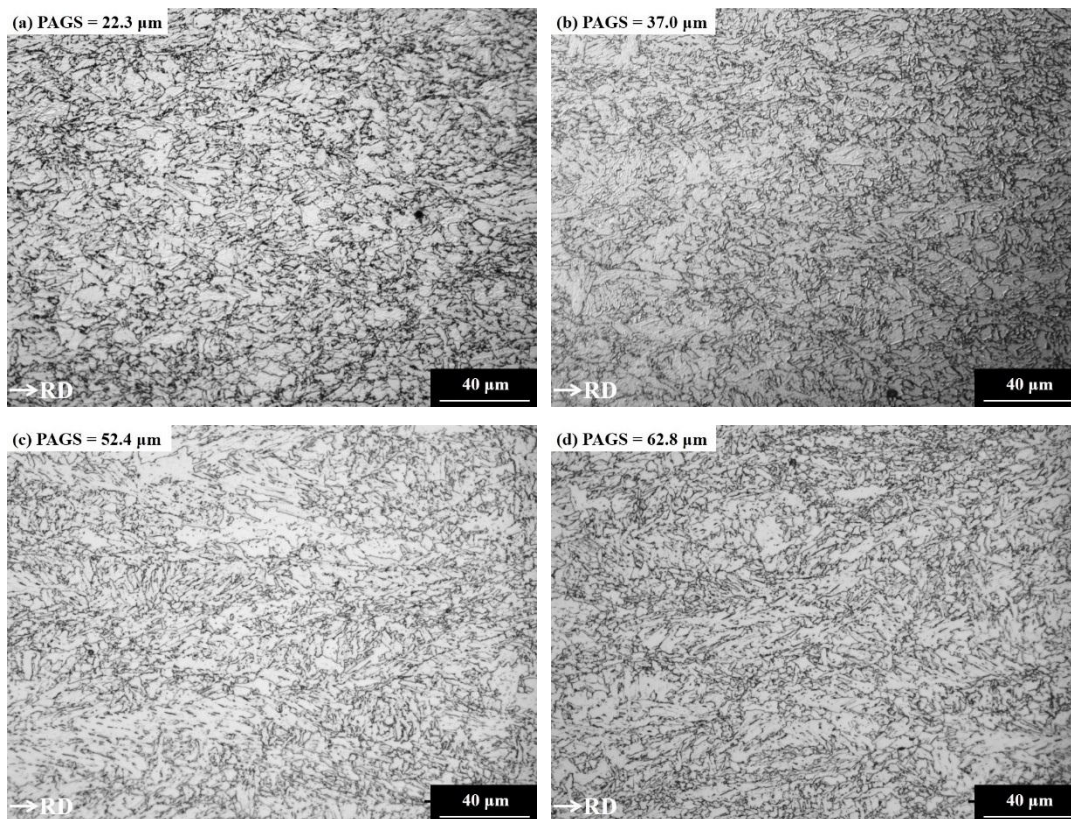
Figure 6-4 Optical micrographs depicting microstructures transformed from deformed

austenite (strain2 = 0.5) with different PAGSs: (a) 22.3 μm, (b) 37.0 μm, (c) 52.4 μm and (d) 62.8 μm.

To observe the microstructures in greater detail, SEM secondary electron micrographs of the continuously cooled microstructures transformed from recrystallised austenite (strain2 = 0) with different PAGSs are shown in Figure 6-5. With the PAGSs of 22.3 μm and 37.0 μm, BF laths with a parallel morphology can be observed clearly. However, as the PAGS is increased to 52.4 μm or 62.8 μm, more interlocking BF microstructures are observed in Figure 6-5 (c)~(d). In these microstructures, BF laths with different directions intersect with each other.
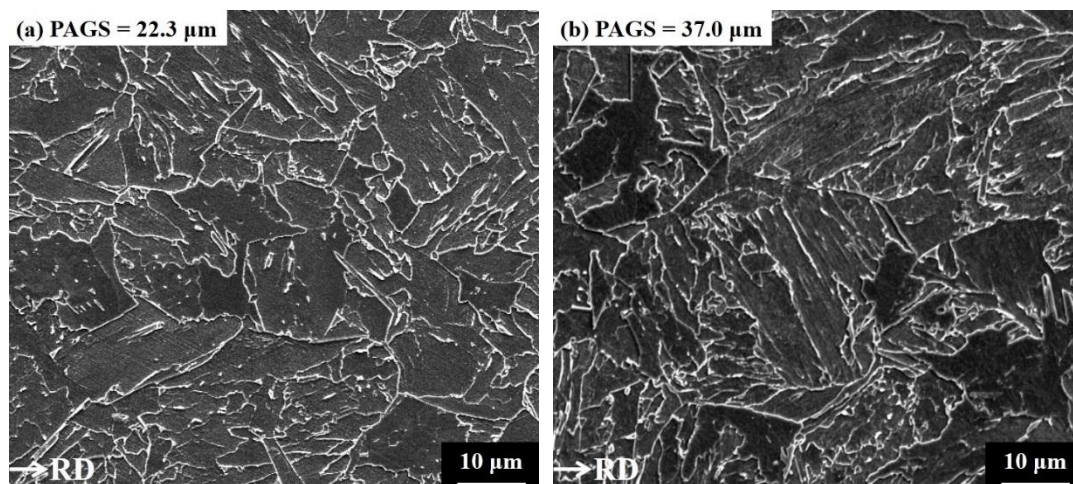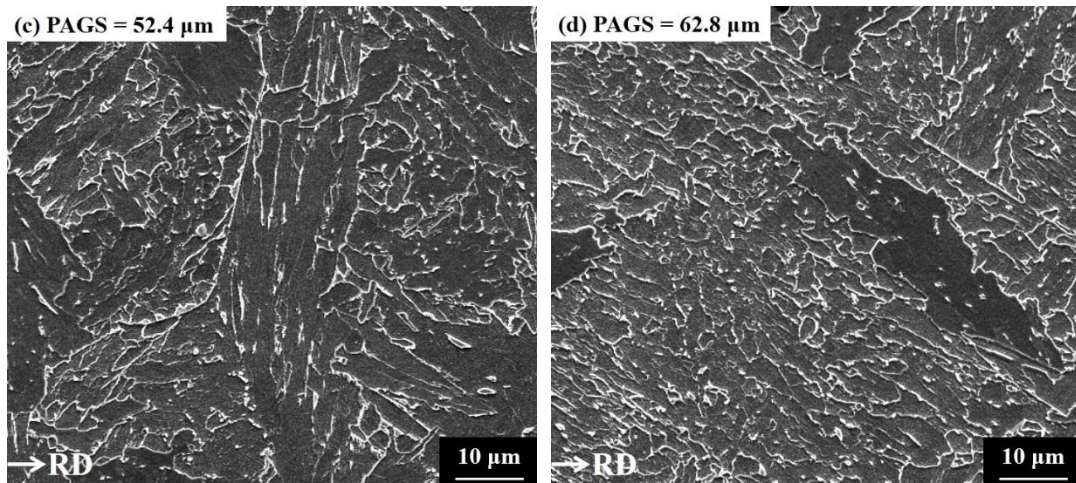
Figure 6-5 SEM secondary electron micrographs showing microstructures transformed from recrystallised austenite (strain2 = 0) with different PAGSs: (a) 22.3 μm, (b) 37.0 μm, (c) 52.4 μm and (d) 62.8 μm.

SEM secondary electron micrographs of the continuously cooled microstructures transformed from deformed austenite (strain2 = 0.5) with different PAGSs are shown in Figure 6-6. Similar results to those observed from optical micrographs can be obtained that with the small PAGSs, the transformed microstructures are AF dominant while for the large PAGSs, parallel BF laths are the main phase component. Therefore, there is a distinct effect of the PAGS on the microstructure evolution under present test conditions.
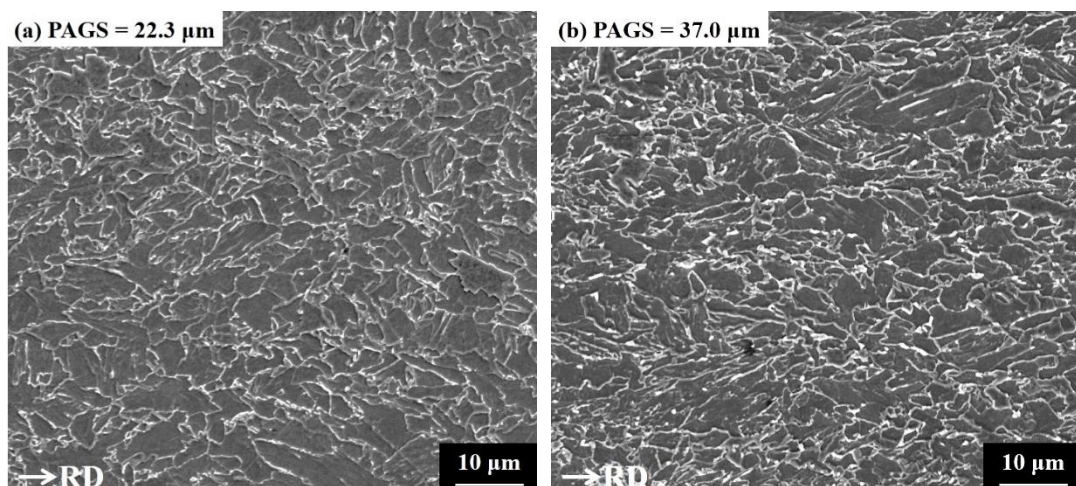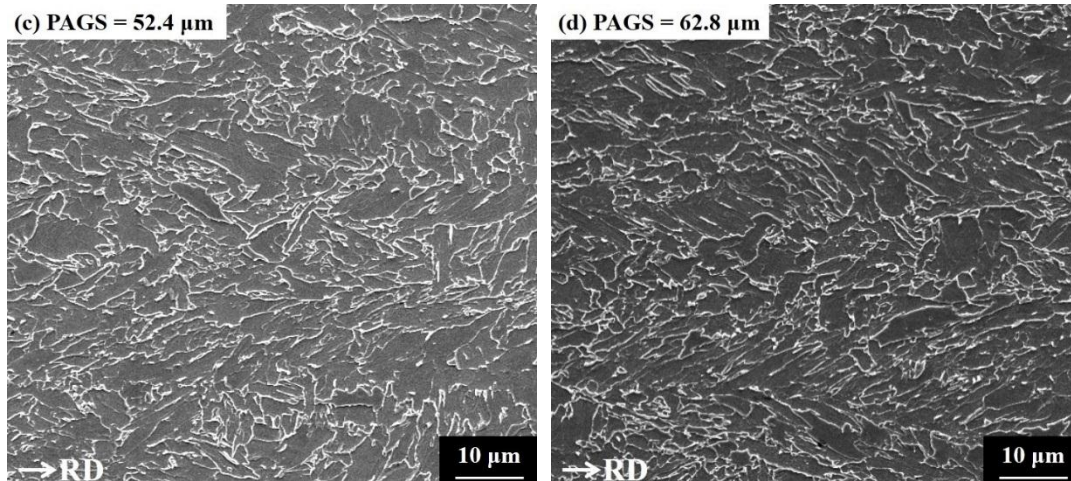
Figure 6-6 SEM secondary electron micrographs showing microstructures transformed from deformed austenite (strain2 = 0.5) with different PAGSs: (a) 22.3 μm, (b) 37.0 μm, (c) 52.4 μm and (d) 62.8 μm.

6.3.3 EBSD mappings

Following the noise reduction procedures illustrated in Section 3.3.2, a small area of each EBSD data set was used to plot an inverse pole figure (IPF) coloured orientation map and a boundary map. For a statistical analysis of the boundary interception length, each whole data set was used.

The selected area IPF coloured orientation maps and corresponding boundary maps of the continuously cooled microstructures transformed from fully recrystallised austenite with a different PAGS are shown in Figure 6-7. It can be seen from Figure 6-7 that with increasing PAGS, the density of HAGBs is reduced and the fraction of LAGBs is increased. More importantly, as the PAGS is increased, the shape of the LAGBs changes from parallel and straight to curved and irregularly arranged, and simultaneously the morphology of the transformed BF microstructures becomes increasingly intricate.

(a) PAGS = 22.3 μm
(e) PAGS = 22.3 μm
(b) PAGS = 37.0 μm
(f) PAGS = 37.0 μm
(c) PAGS = 52.4 μm
(g) PAGS = 52.4 μm
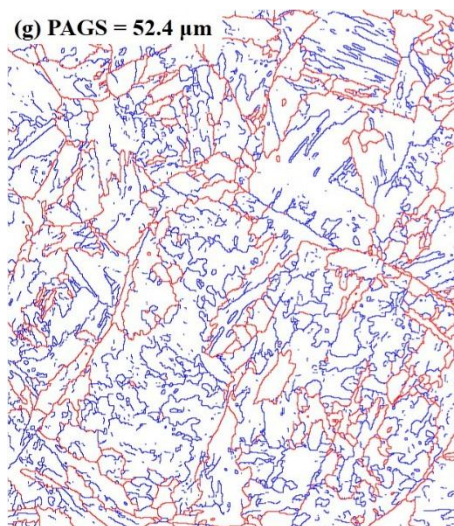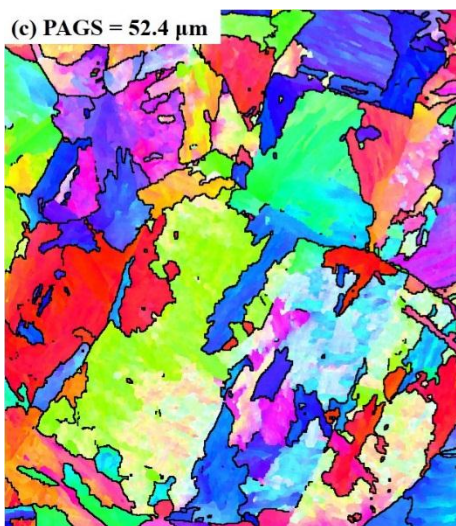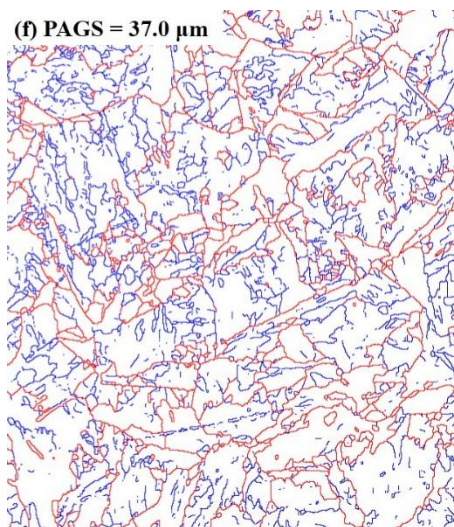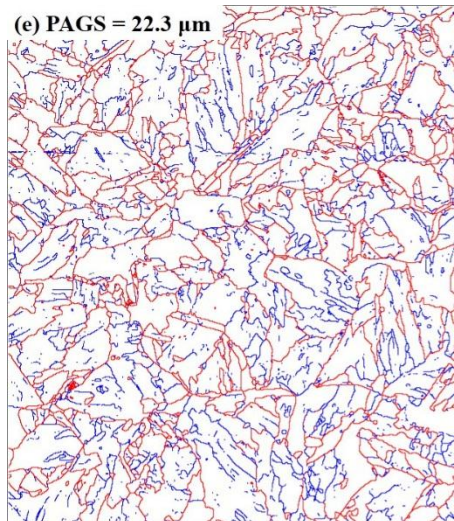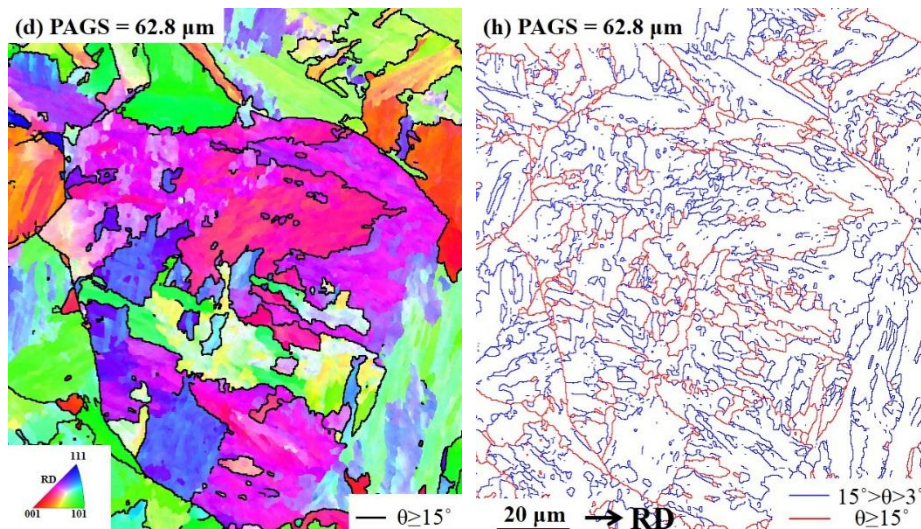
Figure 6-7 EBSD maps of the microstructures transformed from fully recrystallised austenite (strain2 = 0) with different PAGSs: (a)~(d) inverse pole figure coloured orientation image maps corresponding to microstructures with PAGS of 22.3 μm, 37.0 μm, 52.4 μm and 62.8 μm, respectively, where black lines represent high angle boundaries with disorientation greater than 15˚; (e)~(h) boundary maps corresponding to the same area in (a)~(d) respectively, where blue lines represent low angle boundaries with disorientation between 3˚ and 15˚ whilst red lines represent high angle boundaries with disorientation greater than 15˚.

The selected area IPF coloured orientation maps and corresponding boundary maps of the continuously cooled microstructures transformed from deformed austenite with different PAGSs are shown in Figure 6-8. From these maps, we can see that the transformation microstructures with the small PAGSs (22.3 μm and 37.0 μm) are finer and both the densities and fractions of HAGBs are higher than those with the large PAGSs (52.4 μm and 62.8 μm). Furthermore, relatively large BF regions like those found in Figure 5-7 which are rich in LAGBs but lack HAGBs can also be found in most of the transformed microstructures, and the fractions of these BF regions are considerably higher in microstructures with the large PAGS as shown in Figure 6-8 (g)~(h), indicating that a transition from AF to BF occurs by increasing the PAGS. In addition, AF regions which consist of fine and non-equiaxed laths bounded by HAGBs can

143

also be found in Figure 6-8 (g)~(h). Therefore, with large PAGSs very heterogeneous transformation microstructures were formed. The microstructure evolution characteristics observed in these EBSD maps correspond very well to those observed in the OM and SEM micrographs and thanks to the advantages of EBSD mapping, these microstructure changes can be well quantified.
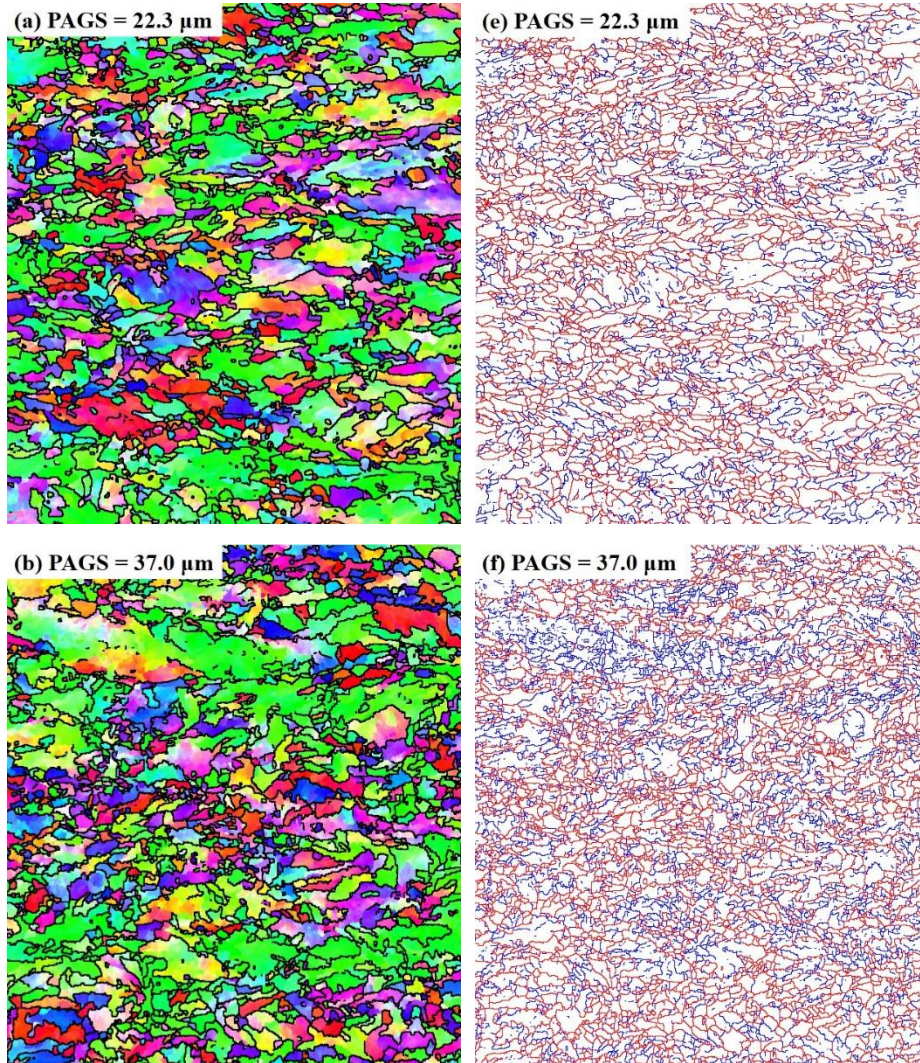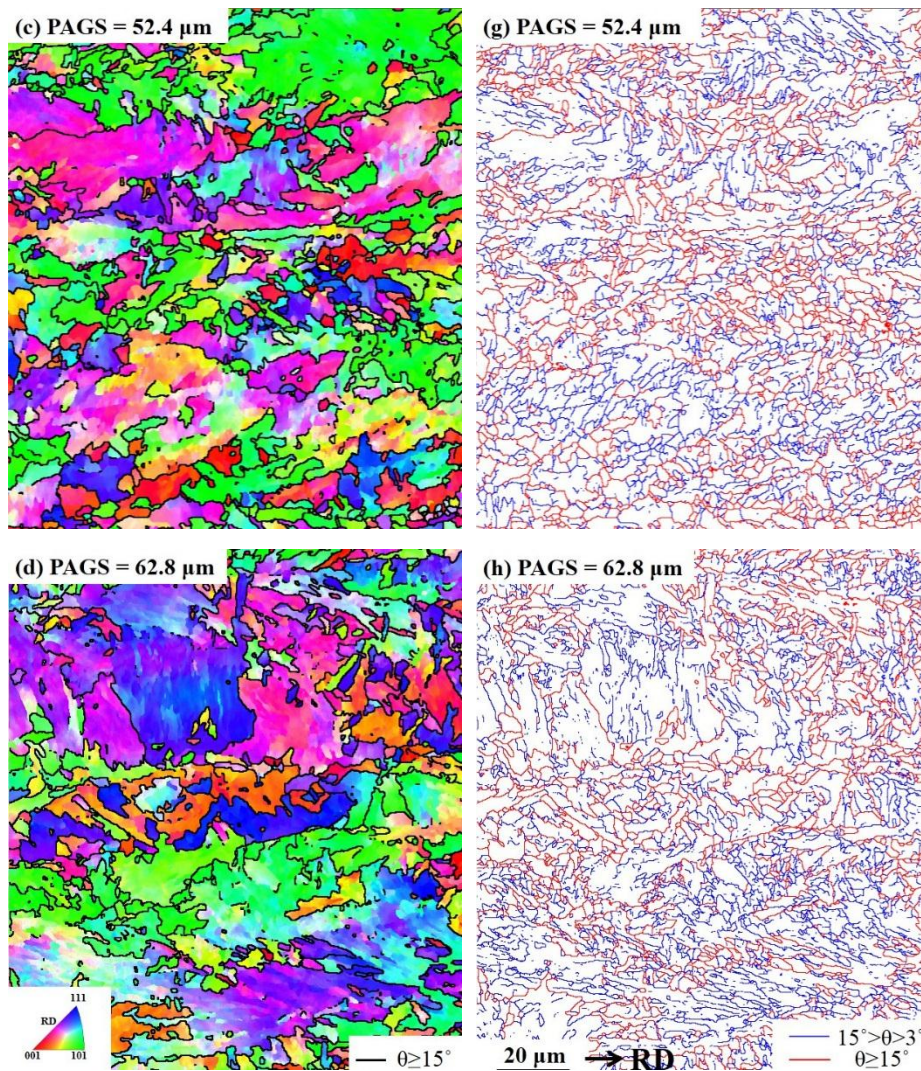
Figure 6-8 EBSD maps of the microstructures transformed from deformed austenite (strain2 = 0.5) with different PAGSs: (a)~(d) inverse pole figure coloured orientation image maps corresponding to microstructures with PAGS of 22.3 μm, 37.0 μm, 52.4 μm and 62.8 μm, respectively, where black lines represent high angle boundaries with disorientation greater than 15˚; (e)~(h) boundary maps corresponding to the same area in (a)~(d) respectively, where blue lines represent low angle boundaries with disorientation between 3˚ and 15˚ whilst red lines represent high angle boundaries with disorientation greater than 15˚.

To quantify the microstructural refinement, the grain size defined by different disorientation threshold values, 4˚ and 15˚ are measured by a linear intercept method in the Channel 5 software, owing to the reason explained in Section 3.3.2.

145

The respective geometric means of linear intercept lengths in both horizontal and vertical directions were calculated as in reference [146] and are shown in Figure 6-9.
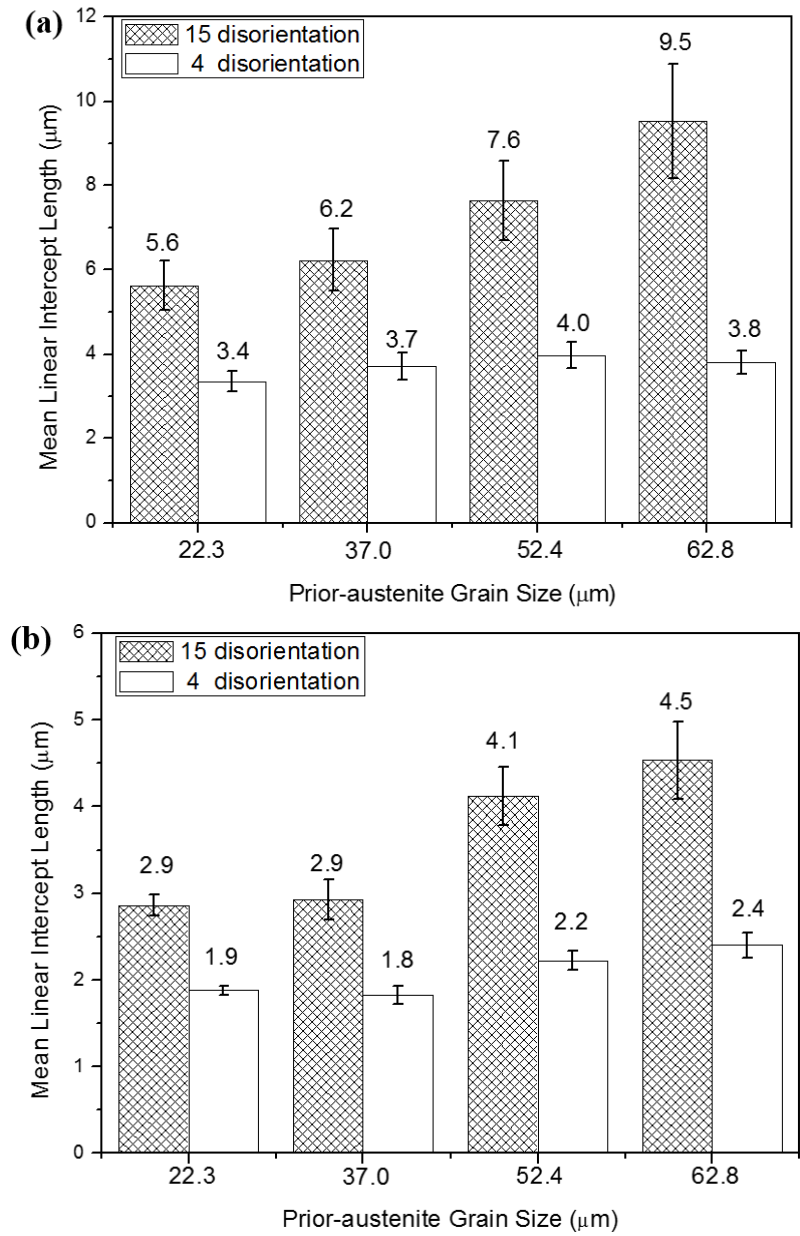
Figure 6-9 Microstructure size parameter measured against two disorientation criteria, 4° and 15°, as geometric mean of the linear interception lengths in horizontal and vertical direction from the EBSD maps measured from the microstructures transformed from: (a) fully recrystallised austenite (strain2 = 0) and (b) fully unrecrystallised austenite (strain2 = 0.5). Error bars represent 95% confidence levels of the

measurement.

In Figure 6-9 (a), we can see clearly that the mean linear intercept length following the disorientation threshold value of 15° decreases gradually with the reduction of PAGS from 62.8 μm to 22.3 μm, while the intercept lengths against the disorientation threshold value of 4° of these four microstructures are very similar. These results suggest that for BF microstructures transformed from fully recrystallised austenite, reducing the PAGS can effectively refine the transformed microstructures.

Differently, it can be seen in Figure 6-9 (b) that the mean linear intercept lengths following both disorientation threshold values firstly decrease with the reduction of PAGS from 62.8 μm to 37.0 μm and then level off when PAGS is further reduced to 22.3 μm. Furthermore, changes of the mean intercept lengths both between the transformed microstructures with the PAGSs of 52.4 μm and 62.8 μm and between the transformed microstructures with the PAGSs of 22.3 μm and 37.0 μm are not statistically significant as there are very large overlaps of the error bars. But the difference of the mean intercept length is quite evident between the transformed microstructures with the small and the large PAGSs. These grain refinement characteristics correspond very well to the microstructure observation from Figure 6-4.

The results above clearly show the effect of PAGS on the grain refinement of the microstructures transformed both from recrystallised and deformed austenite. However, by altering the PAGS before austenite deformation (strain2 = 0.5), not only the microstructure refinement but also the microstructure heterogeneity is influenced as shown in Figure 6-8. The microstructure heterogeneity also has a great impact on the toughness. In order to quantify the microstructure heterogeneity, the distributions of grain size defined by the diameter of equivalent circle against the disorientation angle criteria of 15° for the microstructures transformed from deformed austenite with different PAGSs

147

are shown in Figure 6-10. With the small PAGSs (22.3 μm and 37.0 μm), the AF dominant transformed microstructures both possess homogeneous grain size distributions and the difference is very small. As the PAGS is increased from 37.0 μm to 62.8 μm, an increase in the microstructure heterogeneity is observed and with the largest PAGS (62.8 μm) the grain size distribution is the wildest. According to research [191], a parameter $D_{c10\%}$ defined as the grain size for which 10 percent of the area fraction of grains have a size greater than that value is selected here to describe the relevance of coarse grain fractions in different microstructures. The corresponding $D_{c10\%}$ values for the transformed microstructures with the PAGS changing from 22.3 μm to 62.8 μm are 25.5 μm, 24.5 μm, 73.5 μm and 89.0 μm respectively. Therefore, it is straightforward to say that reducing the PAGS from 62.8 μm to 37.0 μm or 22.3 μm before austenite deformation can significantly refine and homogenise the transformed microstructure.
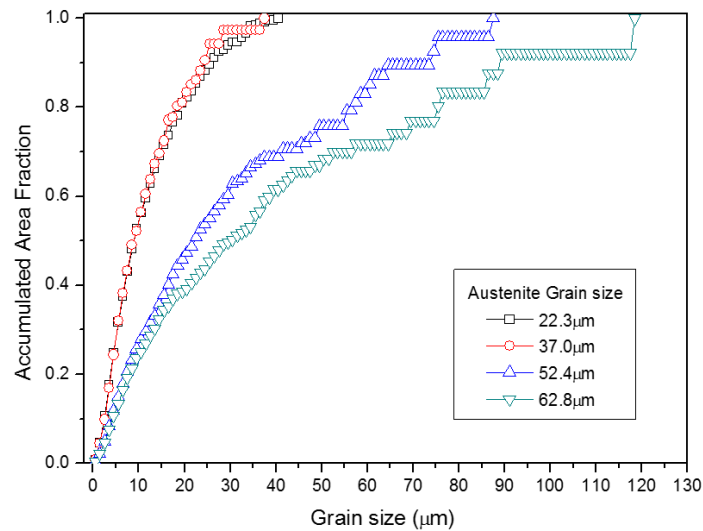
Figure 6-10 Grain size distributions of the microstructures transformed from fully unrecrystallised austenite (strain2 = 0.5) with different austenite grain sizes against the disorientation angle criteria of 15° plotted in terms of accumulated area fraction.

6.4 Discussion

6.4.1 Effect of PAGS on BF transformation and grain refinement

Without austenite deformation, the continuously cooled microstructures with different PAGSs, varying from 22.3 μm to 62.8 μm, mainly consist of BF laths. It can be seen from Figure 6-5 and Figure 6-9 (a) that altering the PAGS, both the morphology and the effective grain size of the transformed BF microstructure are changed. These changes can be explained from the point view of variant selection.

A comparison is made between the BF microstructures with the PAGSs of 37.0 μm (small) and 62.8 μm (large). A prior-austenite grain was identified in each EBSD map of these two BF microstructures. The {100} pole figures of the BF orientations of these two prior-austenite grains are shown in Figure 6-11 (a), (c) and the IPF coloured orientation maps of them are illustrated in Figure 6-12 (a) and (d) respectively. Since the Kurdjumov–Sachs (K–S) relationship ($\{111\}_\gamma//\{110\}_\alpha$, $<110>_\gamma//<111>_\alpha$) generally provides good predictions for the BF transformation in steels [100], it was adopted as the orientation relationship in this research and the method proposed by Tari et al. [174] was used to evaluate the orientations of these two parent austenite grains, and the results were used to calculate the 24 K-S variants of each austenite grain. These results are shown in Figure 6-11 (b), (d) respectively, and good matches can be found between the pole figures of the experimentally determined BF orientations and calculated ferrite orientation variants.

To reveal detailed crystallographic features, the colours in the orientation maps were changed to show different colours for different CP and Bain groups, which is introduced in Section 2.6.2. These maps are termed as CP and Bain group maps and are shown in Figure 6-12 (b), (e) and Figure 6-12 (c), (f) for the two microstructures transformed with different PAGSs, respectively.

149
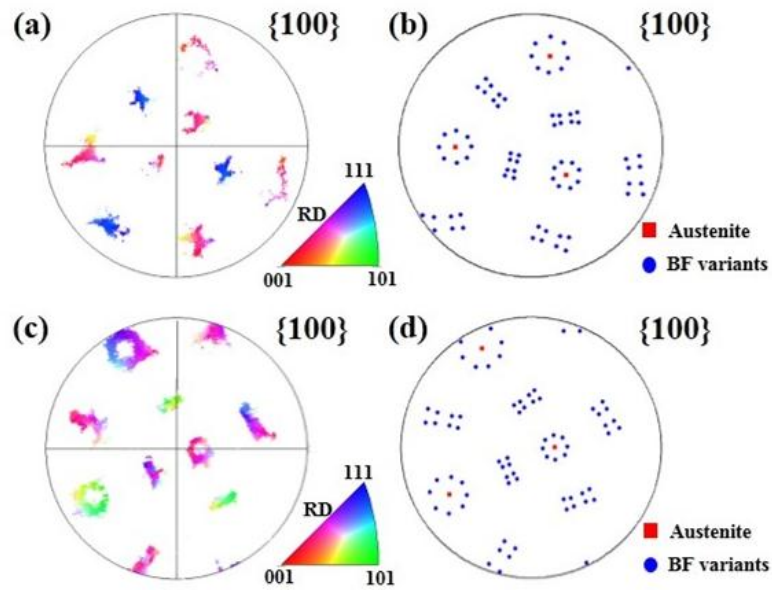
Figure 6-11 {100} pole figures of the BF orientation in single parent austenite grains with (a) small (37.0 μm) and (c) large (62.8 μm) PAGS; {100} pole figures of the calculated austenite orientations and corresponding ferrite orientation variants with (b) small and (d) large PAGS.
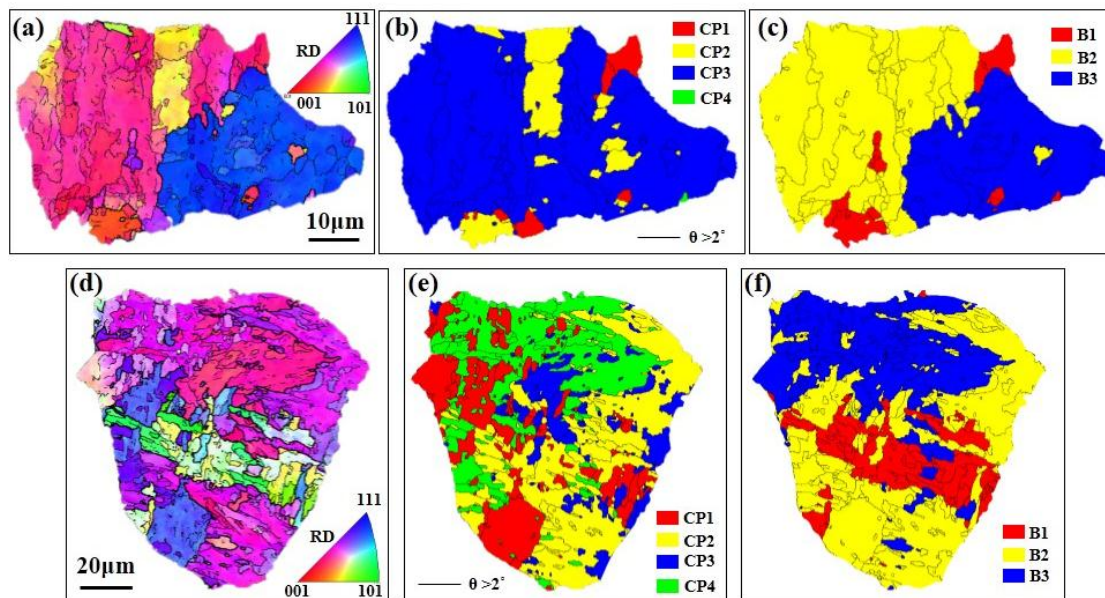
Figure 6-12 IPF coloured orientation maps (a) and (d), close-packed plane group maps (b) and (e) and Bain group maps (c) and (f) for BF microstructures in single parent austenite grains with the small (37.0 μm) and large (62.8 μm) PAGS respectively.

150

For the BF microstructure with a small PAGS (37.0 μm), Figure 6-12 (a), parallel BF laths can be clearly revealed by low angle grain boundaries. It is also evident from Figure 6-11 (a), (b) that an intense variant selection occurred, and only a small fraction of the 24 K-S variants formed. Furthermore, the entire austenite grain is dominated by a single CP group with blue colour as shown in the CP map, Figure 6-12 (b), but consists of two Bain groups, yellow and blue, as shown in the Bain group map, Figure 6-12 (c).

For the BF microstructure with the large PAGS shown in Figure 6-12 (d), a more complicated BF microstructure was formed, and nearly all the 24 K-S variants exist, Figure 6-11 (c), (d). From the CP group map shown in Figure 6-12 (e), it is evident that the entire austenite grain is occupied by intersecting CP groups, signifying variants from the same CP groups are no longer preferentially formed side by side. Interestingly, although adjacent laths come from different CP groups, they mainly belong to the same Bain group as shown in the Bain group map in Figure 6-12 (f), except in the central part of the parent austenite grain where different Bain groups intersect.

The above analysis clearly shows that there is a limited number of BF orientation variants formed in the smaller austenite grain. This suggests that after nucleation on the most potent austenite grain boundaries, the BF laths rapidly develop across the whole parent grain before nucleation sites on other austenite grain boundaries become potent enough. However, for the larger austenite grain, and because of the larger intercept length and higher volume, before the initially nucleated BF laths expand across the complete austenite grain, other austenite grain boundaries become potent enough, and there is still enough volume of austenite left for the development of these nuclei. Since variant selection happens during the BF nucleation on austenite grain boundaries through the reduction of the BF/austenite boundary energy and other mechanisms [203], the variants selected on the austenite grain boundaries varies with the austenite grain

boundary characteristics. Therefore, in austenite grains with a large PAGS, BF laths of different variant types can develop, and the variant selection is less intense than that observed in the small-grained austenite. This is consistent with previous research [204, 205], where austenite grains with a small PAGS transformed into limited types of variants compared with large-grained austenite. Additionally, it was found in research [205] that the size of BF blocks which consisted of variants with a similar orientation, was nearly equal to the linear intercept length of the parent austenite when the size of parent austenite was smaller than ~30 μm. In austenite with a grain size higher than this value, the block size was found to be considerably smaller than the size of the austenite grain, indicating that more blocks will be formed in coarse-grained austenite.

Besides variant selection, the arrangements of CP and Bain groups are also quite different between small-grained and large-grained austenite. During the bainite transformation, the parent austenite grain is usually segmented into packets, each of which consists of a group of laths with nearly the same trace direction on a polished surface due to their habit planes being in close proximity to each other. Since the variants belonging to the same CP group have the closest habit planes [203], packets usually consist of variants coming from the same CP group. In other words, BF laths belonging to the same CP group are usually formed side by side. However, this is only the case in austenite with a small PAGS as shown in Figure 6-3 (b) and Figure 6-12 (b). For the austenite with a large PAGS, the parent austenite grains cannot be clearly divided into packets as shown in Figure 6-3 (d) and the BF laths belonging to different CP groups are formed adjacently and are well-intersected, Figure 6-12 (e). In this case, austenite grains are more conveniently described as being divided by Bain groups instead of CP groups. This is consistent with previous research [99] that the variants belonging to the same Bain group are created adjacently in bainite transformed at higher temperatures and subsequent smaller driving forces.

Obviously, it is these differences in the arrangement of CP groups between

austenite grains with small and large PAGS that result in the differences in optical morphology. For the transformed microstructure with a small PAGS, a single CP group is dominant, and the boundaries between parallel laths are quite continuous, Figure 6-12 (a), and thus can be identified easily in optical micrographs or SEM micrographs. However, in the transformed microstructure with a large PAGS, the BF laths belonging to different CP groups were observed to be adjacent to each other, thus forming an interlocking morphology. Because of the incomplete transformation phenomenon of bainite [2] and this interlocking morphology of BF laths, granular M/A constituents are found between BF laths. Furthermore, the lath boundaries are less continuous as shown in the upper part of Figure 6-12 (a), therefore they are not obvious from optical micrographs. Although it is possible to say that it is the impingement between different Bain groups that results in this interlocking morphology, it also exists in the area where a single Bain group is dominant, as shown in the upper part of the austenite grain in Figure 6-12 (c). This latter situation is consistent with the results from previous research [110], where adjacent non-parallel sets of BF laths were found belonging to the same Bain group and presented as one grain in the optical micrographs. Although the thickening of the BF laths during continuous cooling usually covers up this interlocking morphology in optical micrographs, it can be clearly revealed in the partially transformed microstructures [57, 110, 121].

The possible formation mechanism of a variant pair belonging to different CP groups but the same Bain group was explained in Section 2.6.3 in terms of the strain-induced nucleation of BF, the reduction of plastic deformation in austenite and the reduction of lath boundary energy. Interestingly, this variant pairing mechanism is not dominant in the BF microstructure with the small PAGS. Although the austenite grain size exhibits an effect on the bainite start temperature and transformation kinetics, the possibility of transformation temperature acting as the dominant factor can be excluded. This is due to the fact that the same differences resulted from PAGS were also observed in isothermally

transformed bainite microstructures [121], although no explanation was provided.

A review of the martensite transformation shows that there is a very similar nucleation process to what this research has found in large-grained austenite. This process is known as autocatalysis, which describes the situation where plates of martensite form and induce new embryos that are then available for further transformation [2]. Autocatalysis accounts for the bursts of transformation that the initial formation of a plate stimulates a disproportionately large degree of further transformation and most importantly, it was found that the burst temperature of martensite is decreased with the reduction of austenite grain size [206, 207]. This effect of austenite grain size is attributed to the fact that the burst of martensite transformation arises because of the intense elastic and plastic disturbance of the austenite adjacent to a martensite plate [2]. It is the displacive transformation strain that causes this disturbance. The intensity of the stress and strain field generated by a plate is proportional to the plate size. For the primary plates nucleated first their size can be thought to be restricted by the PAGS. Therefore, the formation of plates in a larger austenite grain will generate a higher degree of the elastic and plastic disturbance and thus a higher burst temperature [206]. However, the situation is different in the BF transformation, where sub-units are stopped below a certain size due to the plastic accommodation of the transformation strain in the austenite, and the formation of laths actually lowers the average transformation strain magnitude from around 0.23 to 0.13 [2]. Therefore, the elastic and plastic disturbance of the austenite should not be significantly influenced by the size difference of laths and thus PAGS.

A more reasonable explanation could be based on the driving force of BF transformation from austenite near the BF/austenite interface. Because of the fact that the post-transformation carbon content of BF tends to be significantly higher than equilibrium and the diffusion coefficient of carbon in austenite is

significantly lower than that in ferrite, there are carbon enriched regions in the austenite around the existing BF sub-units [208]. Since the grain boundary area per unit volume is lower in the large-grained austenite, fewer BF laths form per unit volume at a certain time than those in the small-grained austenite, as schematically shown in Figure 6-13. Furthermore, BF grows under a relatively small driving force, which is only adequate for the development of a low carbon nucleus [2]. Therefore, the carbon concentration of the austenite near the existing BF laths can be reduced sufficiently in large-grained austenite to a level that strain-induced nucleation sites become potent enough to generate BF, whereas in small-grained austenite the carbon diffusion fields of adjacent BF laths are more likely to overlap, keeping the carbon concentration higher than the level to allow nucleation sites to be potent enough. The low cooling rate in the present research also provides enough time at high temperatures, which facilitates the carbon diffusion in austenite. However, more details on the transformation strain plastic accommodation and carbon distribution profile are needed to propose a definite answer.
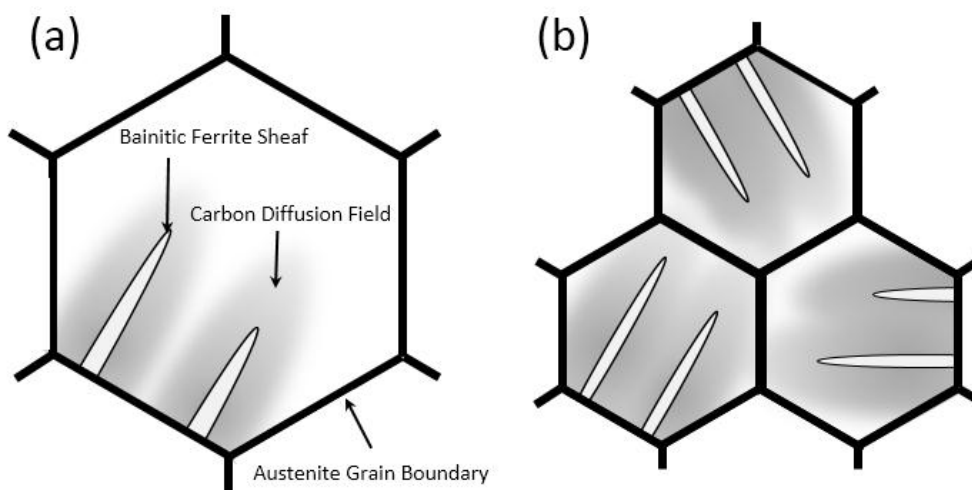
Figure 6-13 Schematic illustration of the difference in carbon diffusion fields in the austenite with (a) large and (b) small PAGS.

155

Due to the difference in variant selection as shown in Figure 6-11, the chance of forming HAGBs within each austenite grain is lower for the small-grained austenite compared to the large-grained austenite as illustrated in the Bain group maps in Figure 6-12 (c) and (f). However, with the reduction of PAGS from 62.8 μm to 22.3 μm, the effective grain size gradually decreases from 9.5 μm to 5.6 μm, indicating the density of HAGB is higher in the transformed microstructure with a smaller PAGS. This discrepancy can be explained by analysing the densities and fractions of HAGBs shown in Figure 6-14.
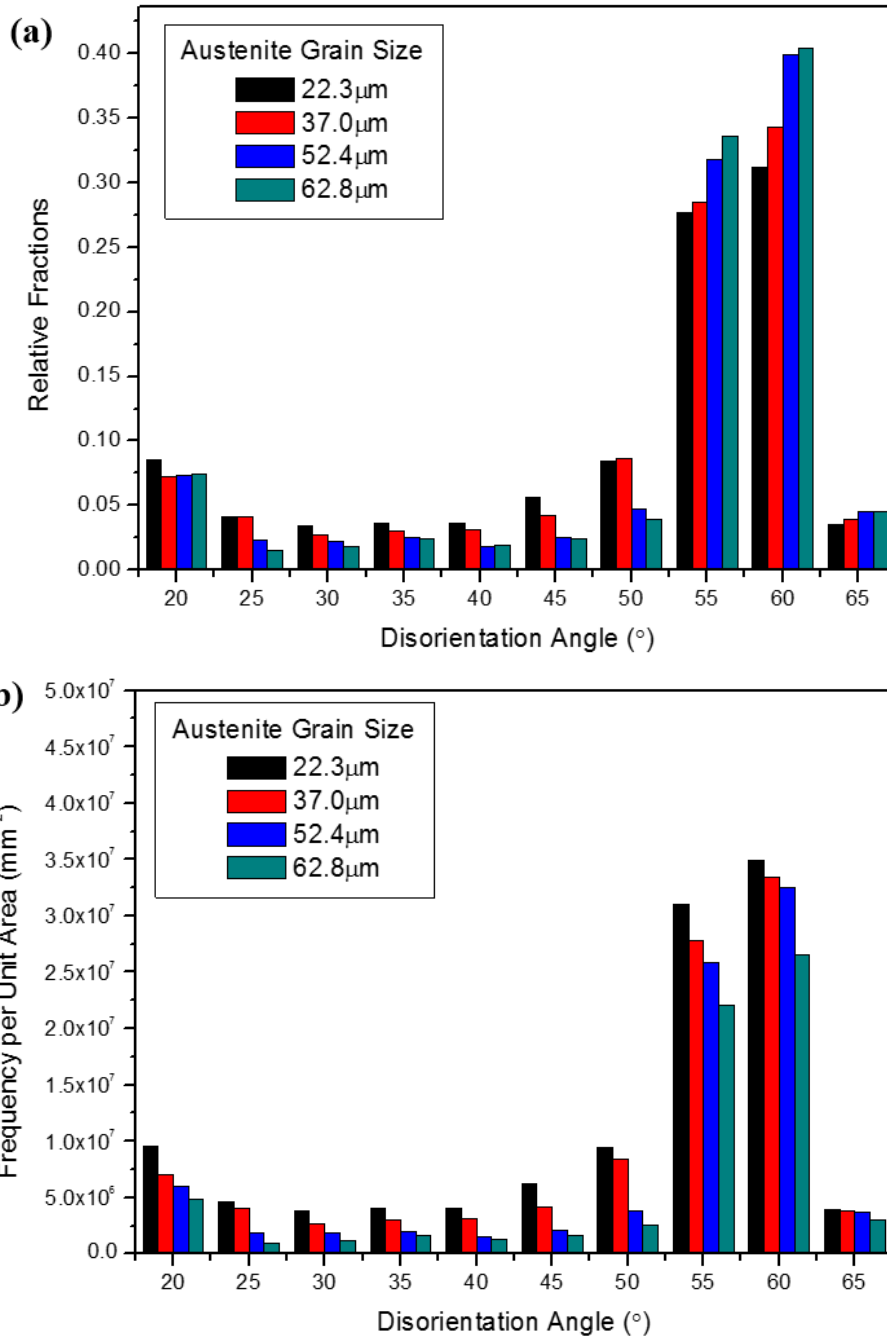
Figure 6-14 Histograms showing (a) the relative fractions of boundaries and (b) the boundary densities in terms of absolute number per unit area with different disorientation angles from 15˚ to 62.8˚.

As described in Section 4.3.3 and Section 4.4.3, boundaries with different disorientation angles are formed by different mechanisms. The whole disorientation angle scope can be divided into four ranges, range 1 (θ<10˚), range

2 (10°≤θ<21°), range 3 (21°≤θ<47°) and range 4 (47°≤θ≤62.8°). For HAGBs, only the disorientation angle ranges 2~4 are involved.

HAGBs with disorientation angles within range 2 are mainly the boundaries between variants transformed in the same austenite grain and belonging to the same Bain group. HAGBs with disorientation angles within range 3 are the boundaries between variants transformed from different austenite grains at PAGBs. HAGBs with disorientations angles within range 4 are mainly the boundaries between variants transformed in the same austenite grain but belonging to different Bain groups.

In Figure 6-14 (a), we can see that with the decrease of PAGS, the fractions of HAGBs with disorientation angles within range 3 are increased, while the fractions of HAGBs with disorientation angles within range 4 are reduced. No great changes are found in the fractions of HAGBs with disorientation angles within range 2. These results indicate that the chance of forming HAGBs within each austenite grain is lower for the small-grained austenite compared to the large-grained austenite and for the small-grained austenite more fractions of HAGBs are formed at the PAGBs, leading to the increased fraction of HAGBs within range 3 as the PAGS is reduced. But, with the reduction of PAGS, the quantity of prior-austenite grains and also the total area of PAGBs per unit volume are increased, leading to the increased absolute densities of HAGBs within the disorientation angle ranges 2~4 as shown in Figure 6-14 (b).

Furthermore, besides range 3, the disorientation angles of boundaries formed between variants transformed from different austenite grains can also fall into other disorientation angle ranges 1, 2 and 4. With the reciprocal increase of the total PAGB area per unit volume as the PAGS is reduced, the influence of PAGB on boundary densities within the ranges 1, 2 and 4 are more and more evident.

Therefore, although intense variant selections exist in transformed microstructures with small PAGSs, due to the large austenite grain quantity and

the large total PAGB area, the transformed microstructure is refined with the reduction of PAGS.

6.4.2 Effect of PAGS on AF transformation and grain refinement

Since the AF in pipeline steels is considered as a kind of intragranularly nucleated transformation product of austenite [165-167], according to the results of investigations [19][201] that increasing PAGS, the dominant transformation product changes from the boundary nucleated phase to the intragranularly nucleated phase, the volume fraction of AF in this situation should be raised with the increase of PAGS. However, as shown in Figure 6-8 the volume fraction of AF actually is reduced with the increase of PAGS from 37.0 μm to 62.8 μm. Furthermore, due to the fact that AF microstructures have a high density of HAGBs, the reduction of AF volume fraction also results in a coarsening of the transformed microstructure as shown in Figure 6-9 (b). The discrepancy between the experimental results and the prediction based on the models in research [19][201] can be explained in terms of the conditions for the occurrence of AF transformation in pipeline steels and the differences in the austenite deformed microstructures with various PAGS.

As proposed in Section 5.4.3, the introduction of intragranular nucleation sites and the halting of BF laths nucleated on the austenite grain boundaries are the two conditions that should be fulfilled for the occurrence of acicular ferrite transformation in pipeline steels. Since AF shows a similar transformation behaviour to that of BF, which is agreed by many researchers [1, 88, 209], the nucleation mechanisms of AF and BF should be similar. When austenite is heavily deformed, the dislocations and stacking faults introduced into austenite grains can act as intragranular nucleation sites of AF as illustrated in Section 4.4.2. Besides that, when the driving force of BF transformation is smaller than the resistance exerted by the deformation substructures in austenite, these deformation substructures can halt the lengthening of BF laths nucleated on the

austenite grain boundaries through the mechanism of mechanical stabilisation. Therefore, AF transformation strongly depends on the austenite deformation substructures and the transformation temperatures.

After the deformation of austenite below the recrystallisation-stop temperature ($T_{5\%}$), several changes in the state of austenite are made, including austenite grain shape, density of deformation substructures, annealing twin boundaries (transformed into normal HAGBs during austenite deformation) and bulging of austenite grain boundaries [210].

The change in the densities of austenite grain boundaries can be evaluated by the effective nucleation area per unit volume, S_v (mm^{-1}), which is introduced in Section 2.2 as a quantitative characterisation of the deformed austenite microstructure [16]. The expression of the total area of deformed austenite grain boundaries per unit volume, S_v(GB), was proposed in [18] as:

$$S_v(GB) = [1.67(R - 0.1) + 1](\frac{2}{D})$$

(6.1)

where R is the reduction ratio and D is the PAGS before austenite deformation. It is clear that under the same reduction ratio, namely the same strain2, the total area of PAGBs per unit volume has a reciprocal relationship with the PAGS.

The density of deformation induced dislocations can be approximated by the sum of the density of statistically stored dislocations (SSDs), ρ_s, and the density of geometrically necessary dislocations (GNDs), ρ_g, these two types of dislocations are accumulated by different mechanisms. In research [187] it was proposed that for polycrystalline materials, if each grain is assumed to undergo its uniform strain, overlaps of materials occur in some places while voids appear in others. Dislocations should be introduced into each grain to correct the overlaps or voids to keep strain compatibility everywhere and these dislocations are geometrically necessary and thus called geometrically necessary dislocations (GNDs). Differently, dislocations accumulated by trapping one another in a random way without geometry requirements are called statistically stored dislocations (SSDs). The expressions of the densities of these two kinds of

dislocations are given as follows [211]:

$$\rho_s = \frac{C_1 \varepsilon}{b l_1} \tag{6.2}$$

and

$$\rho_g = \frac{C_2 \varepsilon}{b l_2} \tag{6.3}$$

where l_1 and l_2 are the average slip lengths for SSD and GND respectively, C_1 and C_2 constants, ε the strain and b the magnitude of the Burgers vector. In polycrystals, l_2 is a characteristic of the microstructure which is independent of strains and is proportional to the grain size, while l_1 is often regarded as the diameter to which a dislocation ring expands before it stops and l_1 varies with strain. It is expected that the increase of ρ_g also can influence the ρ_s. Due to the increase of the density of GNDs, the chance that a dislocation is trapped by others will be increased, leading to a higher ρ_s. Therefore, changing the austenite grain size before deformation can influence the total dislocation density in the deformed austenite microstructure. The total dislocation density will be increased reciprocally with the reduction of the austenite grain size before deformation according to the Hall-Petch relationship [187], Equation (2.1), and the relationship between the flow stress, σ, and the dislocation density, ρ, proposed as:

$$\sigma = \alpha G b \rho^{\frac{1}{2}} \tag{6.4}$$

in research [212], where α is a numerical constant of order unity, G the shear modulus.

Based on the illustration above, it is clear that although the total area of austenite grain boundaries per unit volume is increased reciprocally with the reduction of PAGS, the total dislocation density is also raised with a reciprocal relationship with the decrease of PAGS. More importantly, since the austenite deformation substructures can halt the lengthening of the BF laths nucleated on austenite grain boundaries through the mechanism of mechanical stabilisation of

austenite [178-180], the total area of BF-nucleation active austenite grain boundaries per unit volume will be lower than the calculated S_v value, and each of the active nucleation sites on austenite grain boundaries may only generate a very limited volume of BF. Therefore, with the reduction of PAGS, the increase of dislocation densities and thus the increase of intragranular nucleation site densities for AF is more dominate than the rise of the nucleation site densities of BF, leading to the increase of the AF fraction. As illustrated in Section 4.4.3, the increased fraction of AF can weaken the variant selection and thus generate a higher density of HAGBs, finally leading to a more refined microstructure. The relatively smaller influence of reducing PAGS from 62.5 μm to 52.4 μm than decreasing PAGS from 52.4 μm to 37.0 μm on the microstructure refinement shown in Figure 6-9 (b) can also be explained by the reciprocal relationship between the austenite dislocation density and the PAGS as schematically illustrated in Figure 6-15.
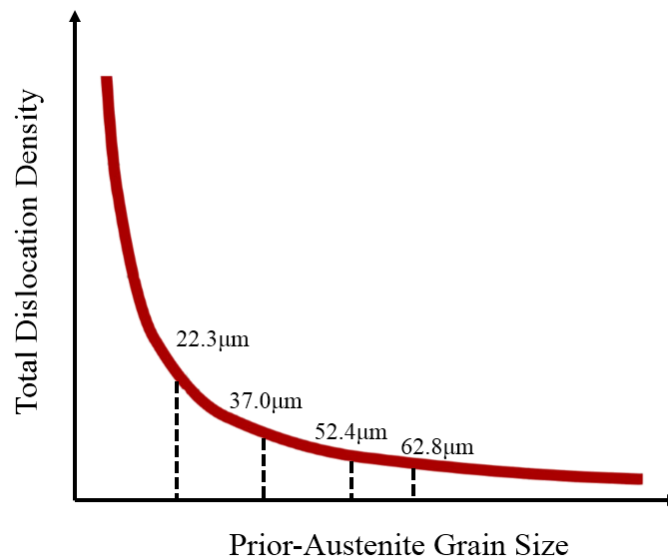
Figure 6-15 Schematical illustration of the reciprocal relationship between the total dislocation density and the PAGS before deformation.

Differently, it is universally acknowledged that the AF in steel welds

162

nucleates on the non-metallic inclusions introduced during welding [2], and after welding, the densities of the non-metallic inclusions and thus the possible nucleation sites of AF are fixed. Furthermore, it is known that for recrystallised austenite grains, the total area of austenite grain boundaries per unit volume increases reciprocally with the reduction of PAGS, Equation (2.3). Therefore, for steel welds, decreasing the PAGS, the total area of the austenite grain boundaries per unit volume is increased reciprocally, while the density of the intragranular nucleation sites is fixed, leading to a promotion of the transformation product nucleated on austenite grain boundaries and thus a reduction of the AF fraction in steel welds as shown in research [19][201].

Although some researchers still claimed that the AF in pipeline steels also nucleates on non-metallic inclusions, the results in this research that the fraction of AF is increased with the reduction of PAGS, add as indirect evidence that the intragranular nucleation sites of AF in pipeline steels are deformation substructures instead of non-metallic inclusions. Furthermore, the advance in steel making technology has significantly improved the cleanness of modern high strength low alloy (HSLA) steels and a high purity is also a prerequisite for modern HSLA steels. Clean steels are characterised by very small amounts of oxides and sulphides preferably in a globular form [213] and it is difficult to find high enough quantity of non-metallic inclusions in high grade pipeline steels to support AF transformation as in weld metals. But to obtain the weld metal AF-like microstructures in structural steels, inoculated acicular ferrite steels have been developed, in which inclusion particles that are effective in stimulating AF nucleation are deliberately brought in by controlling the de-oxidation process during steel making [2]. The particles formed are generally a mixture of various oxides and sulphides, but the effective phase for AF nucleation is Ti_2O_3 [72].

Although as the PAGS is decreased from 62.8 μm to 37.0 μm, the fraction of AF is increased and the transformed microstructure is refined, reducing the PAGS further to 22.3 μm, there are not significant changes on the transformed

microstructures and the grain refinement as shown in Figure 6-8 and Figure 6-9 (b), respectively. Since fractions of AF and grain refinement both are closely related to the density of the deformation induced substructure, it is reasonable to argue that as the PAGS is reduced from 37.0 μm to 22.3 μm, the trend of the deformation substructure being increased as predicted in Figure 6-15 is weakened or prohibited due to the operation of certain mechanisms.

It is well known that under the same deformation conditions, decreasing the starting austenite grain size, the critical strain for the onset of dynamic recrystallisation (DRX) is reduced [214] and once DRX is triggered during the deformation, not necessary to a large extent, static recrystallisation (SRX) and meta-dynamic recrystallisation (MDRX) can proceed during the following continuous cooling and result in an evident restoration as shown in Section 4.4.1. Therefore, it is reasonable to conceive that with the PAGS of 22.3 μm, DRX was triggered during the austenite deformation and resulted in a decrease of the deformation substructure density. However, after strain2 of 0.5, the austenite grains remain unrecrystallised as shown in Figure 6-2 (e), which means that DRX is not triggered during the austenite deformation with the PAGS of 22.3 μm. However, SRX could still happen during the subsequent continuous cooling. As stated in Section 4.4.1, the continuously cooled specimen with PAGS of 22. 3 μm was etched with a saturated aqueous picric acid solution to reveal the PAGBs. The optical micrograph depicting the PAGBs before phase transformation is shown in Figure 6-16. As can be seen from this figure, the shape of the prior-austenite grains cannot be observed as clearly as in Figure 4-9. Therefore, it is difficult to determine whether SRX happens during the continuous cooling directly from the optical micrograph of the PAGBs.
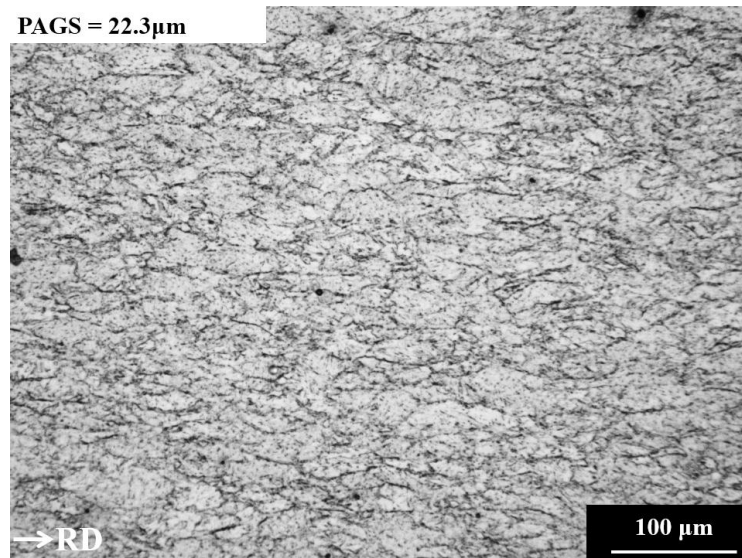
Figure 6-16 Optical micrograph depicting prior-austenite grain boundaries of the continuously cooled specimen with PAGS of 22.3 μm.

Fortunately, the texture information of the transformed microstructure can also be used as evidence to see whether SRX occurs during the continuous cooling. The principal texture component presented in the recrystallised austenite is the cube ({001} <010>) texture component and after displacive transformations, its products are the Goss ({110} <001>), the rotated Goss ({110} <110>) and the rotated cube ({001} <110>) texture components [215]. The presence of the Goss and the rotated Goss texture components is a sign that austenite is recrystallised or partially recrystallised before transformation and the presence of the rotated cube texture component alone does not necessarily indicate the occurrence of austenite recrystallisation because the rotated cube texture component can also be transformed from the Brass ({110} <112>) texture component [215]. The texture of the transformation product with PAGS of 22.3μm measured by EBSD technique are represented by the $\varphi_2 = 45°$ section of orientation density function (ODF) in Figure 6-17 (a) and positions of the relevant texture components in the $\varphi_2 = 45°$ section are shown in Figure 6-17 (b). From Figure 6-17 we can see that although the rotated cube texture component exists in the texture of the transformed microstructure, the absence of the Goss

165

and the rotated Goss texture components suggest that austenite was unrecrystallised before transformation even with the PAGS as small as 22.3 µm. Therefore, both DRX and SRX did not happen in the present research and thus are not responsible for the cessation of microstructure refinement when the PAGS is reduced from 37.0 µm to 22.3 µm.
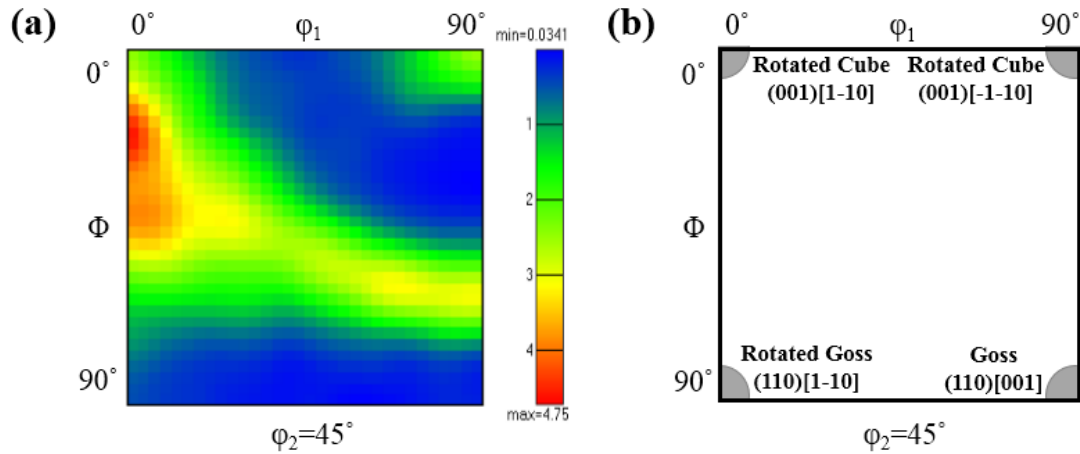
Figure 6-17 (a) $\varphi_2 = 45°$ section of the ODF measured by EBSD technique for the transformed microstructure with PAGS of 22.5 µm, (b) positions of the relevant texture components in the $\varphi_2 = 45°$ section.

Interestingly, the experimental results in research [216, 217] may provide an explanation for the cessation of microstructure refinement when the PAGS is reduced from 37.0 µm to 22.3 µm. In research [216] after AISI 304 stainless steel specimens with PAGSs of 40 µm and 15 µm were deformed with a strain of 1.0 at 900°C and a strain rate of $0.5s^{-1}$, from the EBSD maps shown in Figure 6-18, it was found that in the coarse-grained austenite, Figure 6-18 (a), uniformly distributed substructures can be found in the unrecrystallised austenite grains, while in the fine-grained austenite, Figure 6-18 (b), relatively dense substructures exist only near the austenite grain boundaries, leaving the interior lacking in sub-grain boundaries. Similarly, in investigation [217] after AISI 304 stainless steel specimens with PAGSs of 35 µm and 8 µm were deformed at

900˚C with a strain of 1.0 and a strain rate of $0.01s^{-1}$, it was found from the EBSD maps that in the coarse-grained austenite two types of deformation substructures exist, dense cell structures and elongated dislocation boundaries with large distances between them, but in fine-grained austenite the major part of substructures are the elongated dislocation boundaries and the density of substructures is significantly less than that in the coarse-grained austenite. As for the reason of these differences, in research [216] it was proposed that during the deformation of the fine-grained austenite, grain boundary shearing and/or sliding take place at austenite grain boundaries which can lead to the development of inhomogeneous deformation substructures near the grain boundaries and also in the fine-grained austenite dynamic recovery is promoted due to an acceleration of dislocations spreading into austenite grain boundaries, while in research [217] grain boundary sliding in the fine-grained austenite was taken as the main cause.
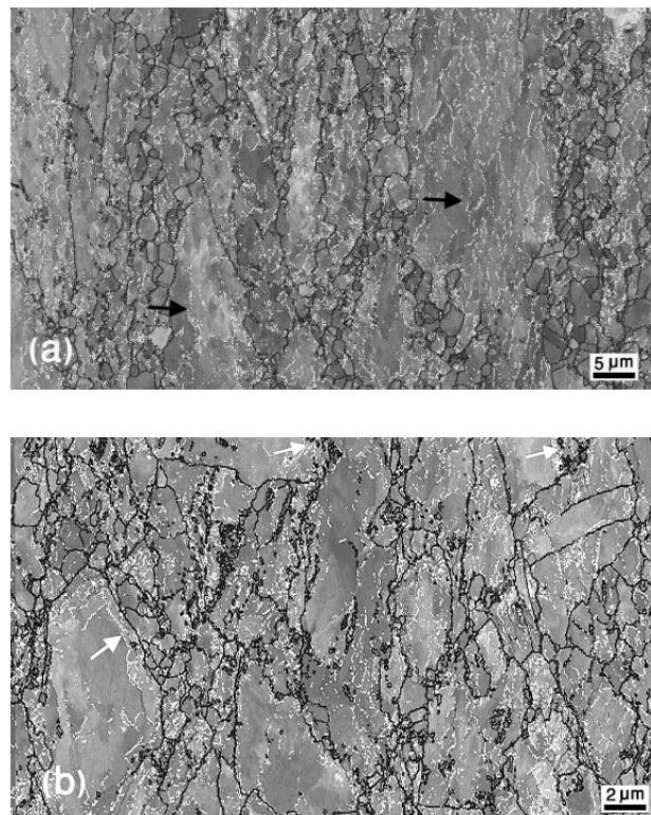
Figure 6-18 EBSD maps of the specimens with different PAGSs, (a) 40 μm and (b) 15

μm, deformed at 900°C with a strain rate of 0.5s^{-1} and strain of 1.0 [216].

Based on the results of these investigations [216, 217], it is clear that the type, distribution, and density of the deformation substructures are different as the PAGSs change from 40 μm to 15 μm or from 35 μm to 8 μm. Therefore, a similar change in the deformation substructures could be expected in the present case with the reduction of PAGS from 37.0 μm to 22.3 μm and it could be these changes that are responsible for the cessation of microstructure refinement. However, further investigations on the austenite deformation substructure with small PAGSs are required to get a definite answer.

6.4.3 Relationship between S_v and effective grain sizes

Based on the effective grain size results of specimens with different PAGSs and strain2 magnitude which have the same accelerated cooling process (10°C/s), the relationship between the effective grain sizes of the transformed microstructures and the S_v values calculated according to Equation (2.3) and Equation (2.4) are shown in Figure 6-19. Like the result for ferrite grain size in Figure 2-2, the effective grain size of continuously cooled transformation products (BF for fully recrystallised austenite, AF for largely unrecrystallised austenite and a mixture of BF and AF for slightly deformed austenite) has a reciprocal relationship with the S_v values. Although S_v was originally proposed to quantify the total effective nucleation site area of PF/QF per unit volume [16] and the nucleation site density of AF cannot be quantified by the S_v value, the factors affecting the effective grain sizes of BF and AF, including PAGS and austenite deformation, are also involved in the expressions of S_v for recrystallised and deformed austenite, Equation (2.3) and Equation (2.4).
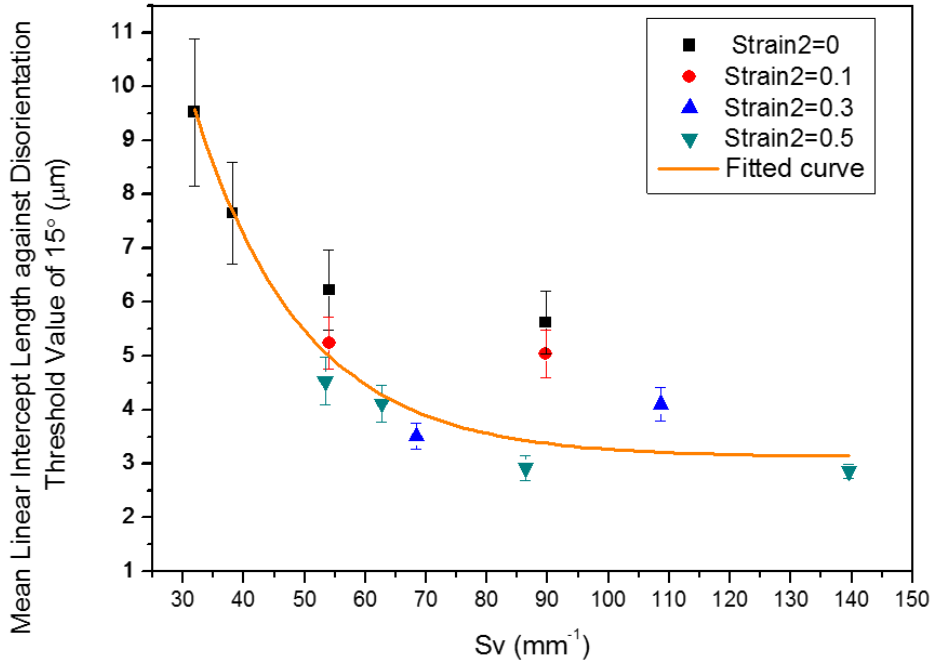
Figure 6-19 Relationship between the effective grain size of transformed microstructure after an accelerated cooling (10˚C/s) and the S_v value.

Although generally a reciprocal relationship between the effective grain sizes and the S_v values can be found in Figure 6-19, some discrepancies can be identified as well. With nearly the same S_v values (around 55 mm^{-1} and 90 mm^{-1}), the effective grain sizes of recrystallised (strain2 = 0), slightly deformed (strain2 = 0.1) and largely deformed austenite (strain2 = 0.5) are quite different and these differences raise with the increased S_v values. Therefore, with the same S_v value, deformation of austenite with a large austenite grain size is more effective than refining austenite grain size to a small value but without deformation in transformation product grain refinement and this advantage of austenite deformation is more evident at higher S_v values.

6.5 Summary

In this chapter, different parameters of the solid solution heat treatment and the roughing deformation were used to generate austenite with different grain sizes and the effects of austenite grain size on the microstructural evolution

transformed from both recrystallised austenite and deformed austenite were investigated. For microstructures transformed from recrystallised austenite with different prior-austenite grain sizes, it was found that:

(1) The continuously cooled microstructures with different PAGSs, varying from 22.3 μm to 62.8 μm, mainly consist of BF laths. Under a relatively slow continuous cooling rate, intense BF variant selection occurs for small-grained austenite and BF laths, belonging to the same CP group, tend to grow side by side forming packet structures that are visible in optical micrographs.

(2) For large-grained austenite, nearly all the variants are formed and variants from different CP groups but the same Bain group tend to grow together forming an interlocking structure, which is difficult to distinguish in optical micrographs. This morphology difference may be attributed to possible lower carbon concentrations near the BF and austenite interfaces in the large-grained austenite than those in the small-grained austenite.

(3) Although intense variant selections exist in transformed microstructures with small PAGSs, due to the large austenite grain quantity and thus the large total PAGB area per unit volume, the transformed microstructure is refined with the reduction of PAGS.

For microstructures transformed from deformed austenite with different prior-austenite grain sizes, it was found that:

(1) With the small PAGSs (22.3 μm and 37.0 μm), the transformed microstructures are AF dominant consisting of non-equiaxed ferrite laths with an irregular arrangement. While in the transformed microstructures with the large PAGSs (52.4 μm and 62.8 μm), although a small fraction of AF still exists, the major transformation product is BF, organised and parallel laths nucleated on austenite grain boundaries and extended into the grain interior.

170

(2) Reducing the PAGS from 62.8 μm to 37.0 μm before austenite deformation, the volume fraction of AF is increased indicating the intragranular nucleation sites of AF in pipeline steels are austenite deformation substructures instead of non-metallic inclusions as in steel welds.

(3) The reduction of the PAGS from 62.8 μm to 37.0 μm before austenite deformation can significantly refine and homogenise the transformed microstructure by introducing an increased density of austenite deformation substructures which promote the AF transformation.

(4) Reducing the PAGS further from 37.0 μm to 22.3 μm, there are not significant changes on the transformed microstructures and the grain refinement. Restoration processes like DRX and SRX are excluded and the differences in the type, distribution, and density of the deformation substructures between deformed austenite with PAGSs of 37.0 μm and 22.3 μm are proposed to be responsible for the cessation of microstructure refinement.

Based on the effective grain size results of specimens with different PAGSs and different deformation magnitude which have the same accelerated cooling process (10˚C/s), a reciprocal relationship between the effective grain sizes and the S_v values can be found generally and with the same S_v value, deformation of austenite with a large austenite grain size is more effective than refining austenite grain size to a small value but without deformation in transformation product grain refinement and this advantage of austenite deformation is more evident at higher S_v values.

Chapter 7   Conclusions

In this research, by conducting plane strain compression (PSC) tests followed by continuous cooling, the effect of various thermomechanical controlled processing (TMCP) parameters on the transformation products of a high temperature processing (HTP) steel were investigated. Not only their individual effects but also their combined influences were studied. The effects of austenite deformation below the recrystallisation-stop temperature ($T_{5\%}$) on the austenite restoration behaviour, the evolution of transformed microstructures and the grain refinement were studied and the possible nucleation mechanism of acicular ferrite (AF) was presented in Chapter 4. The influences of different continuous cooling rates, for both recrystallised austenite and deformed austenite, on the evolution of transformed microstructures and the grain refinement were investigated and the conditions for the occurrence of AF transformation were proposed in Chapter 5. In Chapter 6, the effects of different austenite grain sizes, for both recrystallised austenite and deformed austenite, on the evolution of transformed microstructures and the grain refinement were studied. To summarise the entire research, the following conclusions can be made.

With an increase of strain in the austenite below the recrystallisation-stop temperature ($T_{5\%}$), transition from bainitic ferrite (BF) to AF occurs, and the grain boundary density and microhardness increase with the rise of the AF fraction in the transformed microstructure. Meanwhile, the effective grain size decreases with the increased accumulated strain, indicating toughness improvement. However, further increasing the strain above a critical value triggers dynamic recrystallisation and leads to the onset of static recrystallisation/meta-dynamic recrystallisation during continuous cooling. This partially recrystallised austenite microstructure results in a drop of microhardness and leads to an inhomogeneous and coarse microstructure with AF regions surrounded by blocky bainitic ferrite packets.

172

Without austenite deformation, the transformed microstructures cooled at different cooling rates are all BF dominant. AF-like microstructures cannot be found in these continuous cooled microstructures covering a wide cooling rate range without austenite deformation, which proves that austenite deformation is required for the AF transformation in pipeline steels. Subjected to the same austenite deformation, the fraction of AF decreases and the BF becomes more and more dominant with the increase of cooling rates, which means a transition from AF to BF occurs. Based on the results obtained, the introduction of intragranular nucleation sites and halting of BF laths nucleated on austenite grain boundaries are found as two conditions that should be fulfilled for the occurrence of acicular ferrite transformation in pipeline steels. Increasing the austenite deformation strain can introduce a higher density of dislocation arrays into the austenite which can act as intragranular nucleation sites. Besides, the deformation substructures can also halt the lengthening of BF laths by the mechanism of mechanical stabilisation of austenite. Halting BF laths can only happen under relatively slower cooling rates or higher transformation temperature because high cooling rates result in a low transformation temperature which increases the driving force for transformation interfaces to overcome austenite deformation substructures and leads to a BF or martensite dominant microstructure.

For microstructures transformed from recrystallised austenite with different prior-austenite grain sizes, the continuously cooled microstructures mainly consist of BF laths under a relatively slow continuous cooling rate. Intense BF variant selection occurs for small-grained austenite and BF laths, belonging to the same CP group, tend to grow side by side forming packet structures that are visible in optical micrographs. For large-grained austenite, nearly all the variants are formed and variants from different CP groups but the same Bain group tend to grow together forming an interlocking structure, which is difficult to distinguish in optical micrographs. This morphology difference may be

attributed to possible lower carbon concentrations near the BF and austenite interfaces in the large-grained austenite than those in the small-grained austenite. Although intense variant selections exist in transformed microstructures with small PAGSs, due to the large austenite grain quantity and thus the large total PAGB area per unit volume, the transformed microstructure is refined with the reduction of PAGS.

For microstructures transformed from deformed austenite with small prior-austenite grain sizes, the transformed products are AF dominant consisting of non-equiaxed ferrite laths with an irregular arrangement. While for microstructures transformed from deformed austenite with large prior-austenite grain sizes, although a small fraction of AF still exists, the major transformation product is BF, organized and parallel laths nucleated on austenite grain boundaries and extended into the grain interior.

Based on the results from this research, the implications for industrial practices are given as follows. First, to get AF dominant microstructures under industrial continuous cooling conditions, deformation below the recrystallisation-stop temperature ($T_{5\%}$) should be high enough to encourage the transition from BF to AF, but not so high that restoration processes can be triggered which will lower the accumulated strain in austenite and weaken the effect of austenite deformation on the AF transformation promotion, grain refinement and strengthening. Second, AF transformation can only happen under relatively slow cooling rates or high transformation temperatures, therefore the continuous cooling processes must be designed carefully. If the cooling rate is too large or the transformation temperatures is too low, BF or martensite microstructure will become dominant and the grain-refining effect of austenite deformation will be weakened, and under some conditions, it is possible that the transformed microstructures are coarsen by austenite deformation. Last but not least, under the same accelerated cooling condition, a reciprocal relationship between the effective grain sizes and the S_v values can be found generally and

174

with the same S_v value, deformation of austenite with a large austenite grain size is more effective in the grain refinement of transformation products than refining austenite grain size to a small value but without deformation. And this advantage of austenite deformation is more evident at higher S_v values. Therefore, a reasonable allocation of the total rolling reduction to the rough rolling and the finish rolling is required.

Chapter 8   Future work

Based on the results from this research, the following suggestions for future research are proposed:

8.1 Crystallographic characteristics of acicular ferrite

Although the conditions for the occurrence of acicular ferrite transformation in pipeline steels have been proposed in this thesis, since the transformation mechanism of AF is also displacive, the crystallographic characteristics of AF, including the orientation relationship between AF and parent austenite, variant selection and variant pairing, are necessary for a complete characterisation and deeper understanding of the AF microstructure in pipeline steels.

8.2 Plastic accommodation of BF transformation strain

The reason why variant pairs come from the same Bain group but belonging to different CP group are still unclear. It is possible that the dislocations introduced into the austenite during the plastic accommodation of the transformation shape strain lead to the development of such a kind of variant pair. Therefore, identifying the dislocations in the austenite resulted from plastic accommodation is helpful to understand this variant-pairing mechanism.

8.3 Deformation substructures in small-grained austenite

In this research, it was found that reducing the PAGS from 37.0 μm to 22.3 μm before austenite deformation, there are not significant changes on the transformed microstructures and the grain refinement. Differences in the type, distribution, and density of the deformation substructures between deformed austenite with PAGSs of 37.0 μm and 22.3 μm were proposed to be responsible for the cessation of microstructure refinement. However, evidence can only be found in the investigations with the deformation of AISI 304 stainless steel at

very low strain rates, $0.5s^{-1}$ in research [216] and $0.01s^{-1}$ in research [217]. Further investigations on the austenite deformation substructure with small austenite grain sizes at high strain rates are required to get a definite answer.

8.4 Microstructure with small effective grain size and high strength

Based on the results in this research, acicular ferrite transformation can only happen under relatively slower cooling rates or higher transformation temperatures, which means there is a strength limit for the AF dominant microstructures because the strength of displacive transformation products is closely related to the transformation temperature. To get a higher strength, low transformation temperature is needed. However, if the cooling rate is too large or the transformation temperature is too low, BF or martensite microstructure will become dominant and the effective grain size will be increased, which means the toughness will be compromised. Therefore, it is imperative to find new methods to obtain microstructures with small effective grains and high strengths.

References

1. Y.M. Kim et al., "Effects of molybdenum and vanadium addition on tensile and charpy impact properties of API X70 linepipe steels," Metallurgical and Materials Transactions A, 38 (2007) 1731-1742.

2. H.K.D.H. Bhadeshia, Bainite in steels (Inst. of Metals, 1992).

3. M.C. Zhao et al., "The effects of thermo-mechanical control process on microstructures and mechanical properties of a commercial pipeline steel," Materials Science and Engineering: A, 335 (2002) 14-20.

4. S. Shanmugam et al., "Microstructure and high strength–toughness combination of a new 700MPa Nb-microalloyed pipeline steel," Materials Science and Engineering: A, 478 (2008) 26-37.

5. Y.M. Kim et al., "Effect of microstructure on the yield ratio and low temperature toughness of linepipe steels," ISIJ international, 42 (2002) 1571-1577.

6. F. Grimpe et al., "Development, production and application of heavy plates in grades up to X120," 1st International Conference "Super-High Strength Steels" Rome, Italy November, 2005, 2-4.

7. I. Takeuchi et al., "The prospects for high-grade steel pipes for gas pipelines," Pipes and Pipelines International, 48 (2003) 33-43.

8. Y. Smith et al., Manganese-Molybdenum-Niobium Acicular Ferrite Steels with High Strength and Toughness, Toward improved ductility and toughness, Climax Molybdenum Company (Japan) Ltd, Kyoto, 1972, pp. 119-142.

9. W. Wang et al., "Study of high strength pipeline steels with different microstructures," Materials Science and Engineering: A, 502 (2009) 38-44.

10. M.C. Zhao et al., "Role of microstructure on sulfide stress cracking of oil and gas pipeline steels," Metallurgical and Materials Transactions A, 34 (2003) 1089-1096.

11. Y. Zhong et al., "In situ TEM study of the effect of M/A films at grain boundaries on crack propagation in an ultra-fine acicular ferrite pipeline steel," Acta materialia, 54 (2006) 435-443.

12. C. Chiou et al., "The effect of prior compressive deformation of austenite on toughness property in an ultra-low carbon bainitic steel," Materials chemistry and physics, 69 (2001) 113-124.

13. E. Hall, "The deformation and ageing of mild steel: III discussion of results," Proceedings of the Physical Society. Section B, 64 (1951) 747.

14. N. Petch, "The cleavage strength of polycrystals," J. Iron Steel Inst., 174 (1953) 25-28.

15. F. Pickering and T. Gladman, Iron and Steel Institute Special Report No. 81, Iron and Steel Institute, , Tokyo, 1963, pp. 10.

16. G. Speich et al., "Formation of ferrite from control-rolled austenite," Phase transformations in ferrous alloys, (1983) 341-389.

17. A. Thorvaldsen, "The intercept method—2. Determination of spatial grain size," Acta materialia, 45 (1997) 595-600.

18. C. OUCHI et al., "The Effect of Hot Rolling Condition and Chemical Composition on the Onset Temperature of γ-α Transformation after Hot Rolling," Transactions of the Iron and Steel Institute of Japan, 22 (1982) 214-222.

19. E. Palmiere et al., "The influence of niobium supersaturation in austenite on the static recrystallization behavior of low carbon microalloyed steels," Metallurgical and Materials Transactions A, 27 (1996) 951-960.

20. I. Kozasu et al., Hot Rolling as a High-Temperature Thermo-Mechanical Process, Microalloying 75, Union Carbide, Washington, D.C., 1977, pp. 120-135.

21. L. Sun, "The effects of strain path reversal on austenite grain subdivision, recrystallisation and phase transformations in microalloyed steel," (Ph.D. thesis, University of Sheffield, 2012).

22. C. Heckmann et al., "Development of low carbon Nb–Ti–B microalloyed steels for high strength large diameter linepipe," Ironmaking & steelmaking, 32 (2005) 337-341.

23. A.J. Deardo, "Accelerated Cooling - a Physical Metallurgy Perspective," Canadian Metallurgical Quarterly, 27 (1988) 141-154.

24. C. Ouchi, "Development of steel plates by intensive use of TMCP and direct quenching processes," ISIJ international, 41 (2001) 542-553.

25. M. Umemoto et al., "Effect of cooling rate on grain size of ferrite in a carbon steel," Materials science and technology, 3 (1987) 249-255.

26. K. Hulka and J. Gray, "High Temperature Processing of Line Pipe Steels," Proceedings of the International Symposium Niobium, 2001, 587-612.

27. H. TAMEHIRO et al., "Effect of accelerated cooling after controlled rolling on the hydrogen induced cracking resistance of line pipe steel," Transactions of the Iron and Steel Institute of Japan, 25 (1985) 982-988.

28. F. Humphreys and M. Hatherly, Recrystallization and related annealing phenomena (Elsevier, 2004).

29. S. Curtze and V.-T. Kuokkala, "Dependence of tensile deformation behavior of TWIP steels on stacking fault energy, temperature and strain rate," Acta materialia, 58 (2010) 5129-5141.

30. R.W. Hertzberg, "Deformation and fracture mechanics of engineering materials," John Wiley & Sons, 1983, (1983) 697.

31. H. Idrissi et al., "Is there a relationship between the stacking fault character and the activated mode of plasticity of Fe–Mn-based austenitic steels?," Scripta Materialia, 60 (2009) 941-944.

32. P.J. Ferreira and P. Müllner, "A thermodynamic model for the stacking-fault energy," Acta Materialia, 46 (1998) 4479-4484.

33. S. Allain et al., "Correlations between the calculated stacking fault energy and the plasticity mechanisms in Fe–Mn–C alloys," Materials Science and Engineering: A, 387 (2004) 158-162.

34. Y.K. Lee and C.S. Choi, "Driving force for $\gamma \rightarrow \varepsilon$ martensitic transformation and stacking fault energy of γ in Fe-Mn binary system," Metallurgical and Materials Transactions A: Physical Metallurgy and Materials Science, 31 (2000) 355-360.

35. W. Charnock and J. Nutting, "The effect of carbon and nickel upon the stacking-fault energy of iron," Metal Science Journal, 1 (1967) 123-127.

36. N. Hansen and R.F. Mehl, "New discoveries in deformed metals," Metallurgical and materials transactions A, 32 (2001) 2917-2935.

37. Q. Liu et al., "Microstructure and strength of commercial purity aluminium (AA 1200) cold-rolled to large strains," Acta materialia, 50 (2002) 3789-3802.

38. D.A. Hughes and N. Hansen, "Microstructure and strength of nickel at large strains," Acta Materialia, 48 (2000) 2985-3004.

39. V. Ananthan et al., "Cell and band structures in cold rolled polycrystalline copper," Materials science and technology, 7 (1991) 1069-1075.

40. D. Hughes and N. Hansen, "High angle boundaries formed by grain subdivision mechanisms," Acta materialia, 45 (1997) 3871-3886.

41. N. Hansen and D.J. Jensen, "Development of microstructure in FCC metals during cold work," Philosophical Transactions of the Royal Society of London A: Mathematical, Physical and Engineering Sciences, 357 (1999) 1447-1469.

42. C. Barlow and N. Hansen, "Plastic deformation of metals and alloys," (2014).

43. W. Pantleon and N. Hansen, "Dislocation boundaries—the distribution function of disorientation angles," Acta Materialia, 49 (2001) 1479-1493.

44. N. Hansen et al., "Effect of grain boundaries and grain orientation on structure and properties," Metallurgical and Materials Transactions A, 42 (2011) 613-625.

45. G. Winther and X. Huang, "Dislocation structures. Part II. Slip system dependence," Philosophical Magazine, 87 (2007) 5215-5235.

46. X. Huang and G. Winther, "Dislocation structures. Part I. Grain orientation dependence," Philosophical Magazine, 87 (2007) 5189-5214.

47. G. Taylor, "Plastic strain in metals, 28 th May Lecture to the Institute of Metals," May, 4 (1938) 307-324.

48. N. Hansen, "Cold deformation microstructures," Materials science and technology, 6 (1990) 1039-1047.

49. A.S. Taylor et al., "Orientation dependence of the substructure characteristics in a Ni–30Fe austenitic model alloy deformed in hot plane strain compression," Acta Materialia, 60 (2012) 1548-1569.

50. A.S. Taylor et al., "Comparison of 304 stainless steel and Ni–30wt.% Fe as potential model alloys to study the behaviour of austenite during thermomechanical processing," Acta Materialia, 59 (2011) 5832-5844.

51. T. Araki, "Atlas for bainitic microstructures," Atlas for Bainitic Microstructures, 1 (1992) 4-5.

52. G. Krauss and S.W. Thompson, "Ferritic microstructures in continuously cooled low-and ultralow-carbon steels," ISIJ international, 35 (1995) 937-945.

53. S. Ghasemi Banadkouki and D. Dunne, "Formation of ferritic products during continuous cooling of a Cu-bearing HSLA steel," ISIJ international, 46 (2006) 759-768.

54. H.K. Bhadeshia, "Diffusional formation of ferrite in iron and its alloys," Progress in Materials Science, 29 (1985) 321-386.

55. G. Krauss, Steels: processing, structure, and performance (ASM International, 2005).

56. E. Wilson, "The gamma-> alpha transformation in low carbon irons," ISIJ Int., 34 (1994) 615-630.

57. D. Tian et al., "Correlation between microstructural features of granular bainite, roughness of fracture surface and toughness of simulated CGHAZ in QT type HSLA steels," Scandinavian Journal of Metallurgy, 25 (1996) 87-94.

58. H.J. Jun et al., "Effects of deformation and boron on microstructure and continuous cooling transformation in low carbon HSLA steels," Materials Science and Engineering: A, 422 (2006) 157-162.

59. P. Cizek et al., "Effect of composition and austenite deformation on the transformation characteristics of low-carbon and ultralow-carbon microalloyed steels," Metallurgical and Materials Transactions A, 33 (2002) 1331-1349.

60. H. Bhadeshia and R. Honeycombe, Steels: microstructure and properties: microstructure and properties (Butterworth-Heinemann, 2011).

61. P. Yan and H.K.D.H. Bhadeshia, "Mechanism and Kinetics of Solid-State Transformation in High-Temperature Processed Linepipe Steel," Metallurgical and Materials Transactions A, 44 (2013) 5468-5477.

62. I. Madariaga et al., "Upper acicular ferrite formation in a medium-carbon microalloyed steel by isothermal transformation: Nucleation enhancement by CuS," Metallurgical and Materials Transactions A, 29 (1998) 1003-1015.

63. S. Babu and H. Bhadeshia, "Transition from bainite to acicular ferrite in reheated Fe–Cr–C weld deposits," Materials Science and Technology, 6 (1990) 1005-1020.

64. S.S. Babu, "The mechanism of acicular ferrite in weld deposits," Current Opinion in Solid State and Materials Science, 8 (2004) 267-278.

65. J. Yang and H.K.D.H. Bhadeshia, "Acicular ferrite transformation in alloy-steel weld metals," Journal of materials science, 26 (1991) 839-845.

66. J. Yang and H. Bhadeshia, "Orientation relationships between adjacent plates of acicular ferrite in steel weld deposits," Materials science and technology, 5 (1989) 93-97.

67. J. Yang et al., "Acicular ferrite transformation in deformed austenite of an alloy-steel weld metal," Journal of materials science, 30 (1995) 5036-5041.

68. A.-F. Gourgues et al., "Electron backscattering diffraction study of acicular ferrite, bainite, and martensite steel microstructures," Materials Science and Technology, 16 (2000) 26-40.

69. S. Babu and H. Bhadeshia, "Stress and the acicular ferrite transformation," Materials Science and Engineering: A, 156 (1992) 1-9.

70. M. Chandrasekharaiah et al., "An atom probe study of retained austenite in ferritic weld metal," Welding journal, 71 (1992) 247s-251s.

71. M. Díz-Fuentes et al., "Analysis of different acicular ferrite microstructures in low-carbon steels by electron backscattered diffraction. Study of their toughness behavior," Metallurgical and Materials Transactions A, 34 (2003) 2505-2516.

72. H. Homma et al., "Improvement of HAZ toughness in HSLA steel by introducing finely dispersed Ti-oxide," Weld J, 66 (1987) 301-305.

73. J.-S. Byun et al., "Inoculated acicular ferrite microstructure and mechanical properties," Materials Science and Engineering: A, 319 (2001) 326-331.

74. T.S. Janzen and W.N. Horner, "Alliance Pipeline - a design shift in long distance gas transmission," 1998, 83-88.

75. F. Xiao et al., "Acicular ferritic microstructure of a low-carbon Mn–Mo–Nb microalloyed pipeline steel," Materials Characterization, 54 (2005) 305-314.

76. H. Fang et al., "Bainite transformation," Beijing: Science Press, 2 (1999) 59.

77. T. Araki et al., "Atlas for Bainitic Microstructures," ISIJ, Tokyo, 1 (1992) 1-165.

78. T. Araki et al., "Reviewed Concept on the Microstructural Identification and Terminology of Low Carbon Ferrous Bainites," Materials Science Forum, Trans Tech Publ, 1991, 275-280.

79. L. Collins et al., "Microstructures of linepipe steels," Canadian Metallurgical Quarterly, 22 (1983) 169-179.

80. M. Pontremoli et al., "Development of grade API X80 pipeline steel plates produced by controlled rolling," Metals Technology, 11 (1984) 504-514.

81. R. Cryderman et al., "Controlled-Cooled Structural Steels Modified with Columbium, Molybdenum and Boron," ASM TRANS QUART, 62 (1969) 561-574.

82. A. Coldren and J. Mihelich, "Acicular ferrite HSLA steels for line pipe," Metal Science and Heat Treatment, 19 (1977) 559-572.

83. W. Wang et al., "Relation among rolling parameters, microstructures and mechanical properties in an acicular ferrite pipeline steel," Materials & Design, 30 (2009) 3436-3443.

84. C.P.a.A. DeVito, "High-strength microalloyed pipe steels resistant to hydrogen-induced failures," MiCon 78: Optimization of Processing, Properties, and Service Performance Through Microstructural Control, 672 (1979) 53.

85. Y.M. Kim et al., "Transformation behavior and microstructural characteristics of acicular ferrite in linepipe steels," Materials Science and Engineering: A, 478 (2008) 361-370.

86. C. Shang et al., "Forming and controlling of the acicular ferrite in low carbon microalloyed steel," Acta Metallurgica Sinica(China), 41 (2005) 471-476.

87. M.-C. Zhao et al., "Difference in the role of non-quench aging on mechanical properties between acicular ferrite and ferrite-pearlite pipeline steels," ISIJ international, 45 (2005) 116-120.

88. Z. Tang and W. Stumpf, "The role of molybdenum additions and prior deformation on acicular ferrite formation in microalloyed Nb–Ti low-carbon line-pipe steels," Materials Characterization, 59 (2008) 717-728.

89. J.L. Lee et al., "The intermediate transformation of Mn-Mo-Nb steel during continuous cooling," Journal of materials science, 22 (1987) 2767-2777.

90. M.C. Zhao et al., "Continuous cooling transformation of undeformed and deformed low carbon pipeline steels," Materials Science and Engineering: A, 355 (2003) 126-136.

91. R. Zhang and J. Boyd, "Bainite transformation in deformed austenite," Metallurgical and Materials Transactions A, 41 (2010) 1448-1459.

92. S. Okaguchi et al., "Morphology of Widmanstatten and Bainitic Ferrites," Materials Transactions, JIM(Japan), 32 (1991) 697-704.

93. G. Kurdjumov and G. Sachs, "Over the mechanisms of steel hardening," Z. Phys, 64 (1930) 325-343.

94. Z. Nishiyama, "X-ray investigation of the mechanism of the transformation from face centered cubic lattice to body centered cubic," Sci. Rep. Tohoku Univ, 23 (1934) 637-664.

95. G. Wassermann, "Influence of the--transformation of an irreversible Ni steel onto crystal orientation and tensile strength," Arch. Eisenhüttenwes, 126 (1933) 647.

96. P.M. Kelly et al., "The orientation relationship between lath martensite and austenite in low carbon, low alloy steels," Acta Metallurgica Et Materialia, 38 (1990) 1075-1081.

97. A.B. Greninger and A.R. Troiano, "The mechanism of martensite formation," Trans. AIME, 185 (1949) 590-598.

98. P.M. Kelly, "Crystallography of lath martensite in steels," Materials Transactions, JIM, 33 (1992) 235-242.

99. N. Takayama et al., "Effects of transformation temperature on variant pairing of bainitic ferrite in low carbon steel," Acta Materialia, 60 (2012) 2387-2396.

100. M. Butrón-Guillén et al., "A variant selection model for predicting the transformation texture of deformed austenite," Metallurgical and Materials Transactions A, 28 (1997) 1755-1768.

101. S. Zhang et al., "Variant selection of low carbon high alloy steel in an austenite grain during martensite transformation," ISIJ international, 52 (2012) 510-515.

102. A.-F. Gourgues, "Microtexture induced by the bainitic transformation in steels during welding. Effect on the resistance to cleavage cracking," Materials Science Forum, 426 (2003) 3629-3634.

103. M. Abbasi et al., "An approach to prior austenite reconstruction," Materials Characterization, 66 (2012) 1-8.

104. K. Iwashita et al., "Formation mechanism of the hierarchic structure in the lath martensite phase in steels," Philosophical Magazine, 91 (2011) 4495-4513.

105. H.K.D.H. Bhadeshia and D.V. Edmonds, "The bainite transformation in a silicon steel," Metallurgical Transactions A, 10 (1979) 895-907.

106. H.K.D.H. Bhadeshia and D.V. Edmonds, "Mechanism of bainite formation in steels," Acta Metallurgica, 28 (1980) 1265-1273.

107. B.P.J. Sandvik, "The Bainite reaction in Fe-Si-C Alloys: The primary stage," Metallurgical Transactions A, 13 (1982) 777-787.

108. H. Ling and W. Owen, "A model of the thermoelastic growth of martensite," Acta Metallurgica, 29 (1981) 1721-1736.

109. K.i. Shimizu et al., "The association of martensite platelets with austenite stacking faults in an Fe-8Cr-1C alloy," Acta Metallurgica, 18 (1970) 1005-1011.

110. A. Lambert-Perlade et al., "Austenite to bainite phase transformation in the heat-affected zone of a high strength low alloy steel," Acta Materialia, 52 (2004) 2337-2348.

111. A. Lambert-Perlade et al., "Mechanisms and modeling of cleavage fracture in simulated heat-affected zone microstructures of a high-strength low alloy steel," Metallurgical and Materials Transactions A: Physical Metallurgy and Materials Science, 35 (2004) 1039-1053.

112. T. Furuhara and T. Maki, "Variant selection in heterogeneous nucleation on defects in diffusional phase transformation and precipitation," Materials Science and Engineering: A, 312 (2001) 145-154.

113. T. Furuhara et al., "Key factors in grain refinement of martensite and bainite," Materials Science Forum, Trans Tech Publ, 2010, 3044-3049.

114. T. Furuhara et al., "Variant selection in grain boundary nucleation of upper bainite," Metallurgical and Materials Transactions A, 39 (2008) 1003-1013.

115. K. Tsuzaki et al., "Potency of grain boundaries as martensitic nucleation sites," Le Journal de Physique IV, 5 (1995) C8-167-C168-172.

116. G. Olson and M. Cohen, "A general mechanism of martensitic nucleation: Part II. FCC→ BCC and other martensitic transformations," Metallurgical and Materials Transactions A, 7 (1976) 1905-1914.

117. M. Ueda et al., "Effect of grain boundary character on the martensitic transformation in Fe–32at.% Ni bicrystals," Acta materialia, 49 (2001) 3421-3432.

118. M. Ueda et al., "Controlling factor for nucleation of martensite at grain boundary in Fe-Ni bicrystals," Acta materialia, 51 (2003) 1007-1017.

119. T. Furuhara et al., "Crystallography of upper bainite in Fe–Ni–C alloys," Materials Science and Engineering: A, 431 (2006) 228-236.

120. S. Morito et al., "The morphology and crystallography of lath martensite in Fe-C alloys," Acta Materialia, 51 (2003) 1789-1799.

121. L. Lan et al., "Effect of austenite grain size on isothermal bainite transformation in low carbon microalloyed steel," Materials Science and Technology, 27 (2011) 1657-1663.

122. S. Morito et al., "The morphology and crystallography of lath martensite in alloy steels," Acta materialia, 54 (2006) 5323-5331.

123. T. Swarr and G. Krauss, "The effect of structure on the deformation of as-quenched and tempered martensite in an Fe-0.2 pct C alloy," Metallurgical Transactions A, 7 (1976) 41-48.

124. K. Zhu et al., "Characterization and quantification methods of complex BCC matrix microstructures in advanced high strength steels," Journal of Materials Science, 48 (2013) 413-423.

125. K. Shibata and K. Asakura, "Transformation behavior and microstructures in ultra-low carbon steels," ISIJ international, 35 (1995) 982-991.

126. P. Cizek et al., "The Effect of Simulated Thermomechanical Processing on the Transformation Behavior and Microstructure of a Low-Carbon Mo-Nb Linepipe Steel," Metallurgical and Materials Transactions A, 46 (2014) 407-425.

127. J.-Y. Kang et al., "Phase analysis of steels by grain-averaged EBSD functions," ISIJ international, 51 (2011) 130-136.

128. S. Zaefferer et al., "EBSD as a tool to identify and quantify bainite and ferrite in low‐alloyed Al‐TRIP steels," Journal of Microscopy, 230 (2008) 499-508.

129. D.G. Stalheim, "The use of high temperature processing (HTP) steel for high strength oil and gas transmission pipeline applications," Iron & Steel, 40 (2005) 699-704.

130. M. Mirza and C. Sellars, "Modelling the hot plane strain compression test Part 2– Effect of friction and specimen geometry on spread," Materials science and technology, 17 (2001) 1142-1148.

131. J.S. Hinton, "Laboratory simulation of microstructural evolution in AISI 430 Ferritic Stainless Steel during the Steckel Mill Process," (Ph.D. thesis, University of Sheffield, 2006).

132. E. Palmiere et al., "Compositional and microstructural changes which attend reheating and grain coarsening in steels containing niobium," Metallurgical and Materials Transactions A, 25 (1994) 277-286.

133. A. Gorni and J.D. da Silveira, "Accelerated cooling of steel plates: the time has come," Quenching and Cooling, Residual Stress and Distortion Control,ed. ASTM International,(ASTM International, 2010),

134. M. Brammer, "Plate mills for higher-strength products," Ironmaking & steelmaking, 33 (2006) 353-356.

135. B. Xiao, "Multipass Laboratory Simulations of Steel Plate Hot Rolling for Improved Steel Productivity," (Ph.D. thesis, University of Sheffield, 2013).

136. D. Jorge-Badiola et al., "Influence of Thermomechanical Processing on the Austenite-Pearlite Transformation in High Carbon Vanadium Microalloyed Steels," Isij International, 50 (2010) 546-555.

137. S. Hashimoto and M. Nakamura, "Effects of microalloying elements on mechanical properties of reinforcing bars," Isij International, 46 (2006) 1510-1515.

138. M. Mirza and C. Sellars, "Modelling the hot plane strain compression test Part 1– Effect of specimen geometry, strain rate, and friction on deformation," Materials Science and Technology, 17 (2001) 1133-1141.

139. M. Mirza and C. Sellars, "Modelling hot plane strain compression test Part 3– Effect of asymmetric conditions," Materials science and technology, 23 (2007) 567-576.

140. S.L. Shrestha et al., "An automated method of quantifying ferrite microstructures using electron backscatter diffraction (EBSD) data," Ultramicroscopy.

141. J. Wu et al., "Image quality analysis: a new method of characterizing microstructures," ISIJ international, 45 (2005) 254-262.

142. H. Kawata et al., "Crystallography of ausformed upper bainite structure in Fe–9Ni–C alloys," Materials Science and Engineering: A, 438 (2006) 140-144.

143. O. Engler and V. Randle, Introduction to texture analysis: macrotexture, microtexture, and orientation mapping (CRC press, 2009).

144. K. Mingard et al., "Grain size measurement by EBSD in complex hot deformed metal alloy microstructures," Journal of microscopy, 227 (2007) 298-308.

145. S. Valcke et al., "Electron backscattered diffraction as a tool to quantify subgrains in deformed calcite," Journal of microscopy, 224 (2006) 264-276.

146. L. Sun et al., "Mapping microstructure inhomogeneity using electron backscatter diffraction in 316L stainless steel subjected to hot plane strain compression tests," Materials Science and Technology, 26 (2010) 1477-1486.

147. H. Kitahara et al., "Crystallographic features of lath martensite in low-carbon steel," Acta Materialia, 54 (2006) 1279-1288.

148. S. Kim et al., "Relationship between yield ratio and the material constants of the Swift equation," Metals and Materials International, 12 (2006) 131-135.

149. F.R. Xiao et al., "Challenge of mechanical properties of an acicular ferrite pipeline steel," Materials Science and Engineering: A, 431 (2006) 41-52.

150. D. Bai et al., "Effect of deformation and cooling rate on the microstructures of low carbon Nb-B steels," ISIJ international, 38 (1998) 371-379.

151. N.Y. Zolotarevskii et al., "Effect of the Grain Size and Deformation Substructure of Austenite on the Crystal Geometry of Bainite and Martensite in Low-Carbon Steels," Metal Science and Heat Treatment, 55 (2014) 550-558.

152. L. Malet et al., "Variant selection during the γ-to-α$_b$ phase transformation in hot-rolled bainitic TRIP-aided steels," Scripta materialia, 61 (2009) 520-523.

153. B. Dutta and E. Palmiere, "Effect of prestrain and deformation temperature on the recrystallization behavior of steels microalloyed with niobium," Metallurgical and Materials Transactions A, 34 (2003) 1237-1247.

154. M. Loveday et al., "Measurement of flow stress in hot plane strain compression tests," Materials at High Temperatures, 23 (2006) 85-118.

155. I. Yakubtsov and J. Boyd, "Bainite transformation during continuous cooling of low carbon microalloyed steel," Materials science and technology, 17 (2001) 296-301.

156. P. Uranga et al., "Transition between static and metadynamic recrystallization kinetics in coarse Nb microalloyed austenite," Materials Science and Engineering: A, 345 (2003) 319-327.

157. J.W. Brooks et al., "Direct observations of martensite nuclei in stainless steel," Acta Metallurgica, 27 (1979) 1839-1847.

158. G.B. Olson and M. Cohen, "A mechanism for the strain-induced nucleation of martensitic transformations," Journal of the Less Common Metals, 28 (1972) 107-118.

159. M. Suezawa and H. Cook, "On the nucleation of martensite," Acta Metallurgica, 28 (1980) 423-432.

160. H.K. Yeddu et al., "Strain-induced martensitic transformation in stainless steels: A three-dimensional phase-field study," Acta Materialia, 61 (2013) 6972-6982.

161. X. Li et al., "Influence of prior austenite grain size on martensite–austenite constituent and toughness in the heat affected zone of 700MPa high strength linepipe steel," Materials Science and Engineering A, 616 (2014) 141-147.

162. C. Magee, "Nucleation of martensite," PAPER FROM PHASE TRANSFORMATIONS, ASM. 1970, 115-156, (1970).

163. J. Christian, "The mechanism of phase transformations in crystalline solids," Institute of Metals, London, 231 (1969) 129-142.

164. T. Shigeta et al., "The Effects of Ausforming on Variant Selection of Martensite in Cr-Mo Steel," Quarterly Journal of the Japan Welding Society, 31 (2013) 178s-182s.

165. S. Yamamoto et al., "Effects of the austenite grain size and deformation in the unrecrystallized austenite region on bainite transformation behavior and microstructure," ISIJ international, 35 (1995) 1020-1026.

166. J. Yang et al., "The influence of plastic deformation and cooling rates on the microstructural constituents of an ultra-low carbon bainitic steel," ISIJ international, 35 (1995) 1013-1019.

167. K. Fujiwara et al., "Effect of hot deformation on bainite structure in low carbn steels," ISIJ international, 35 (1995) 1006-1012.

168. M. Olasolo et al., "Effect of austenite microstructure and cooling rate on transformation characteristics in a low carbon Nb–V microalloyed steel," Materials Science and Engineering: A, 528 (2011) 2559-2569.

169. H. Bhadeshia, "Some phase transformations in steels," Materials science and technology, 15 (1999) 22-29.

170. F. Xiao et al., "Acicular ferritic microstructure of a low-carbon Mn-Mo-Nb microalloyed pipeline steel," Materials Characterization, 54 (2005) 305-314.

171. G. Rees et al., "The effect of niobium in solid solution on the transformation kinetics of bainite," Materials Science and Engineering: A, 194 (1995) 179-186.

172. M. Thomas and G. Michal, The Influence of Niobium and Nb (C, N) Precipitation on the Formation of Proeutectic Ferrite in Low-Alloy Steels, in: H.I. Aaronson (Ed.) Solid to Solid Phase Transformations, TMS-AIME, Warrendale, PA 1981, pp. 469-473.

173. R. de Avillez, "Niobium Technical Report," NbTR, 1   82.

174. V. Tari et al., "Back calculation of parent austenite orientation using a clustering approach," Journal of Applied Crystallography, 46 (2013) 210-215.

175. P. Shipway and H. Bhadeshia, "The mechanical stabilisation of Widmanstätten ferrite," Materials Science and Engineering: A, 223 (1997) 179-185.

176. R.H. Larn and J.R. Yang, "The effect of compressive deformation of austenite on the bainitic ferrite transformation in Fe-Mn-Si-C steels," Materials Science and Engineering A, 278 (2000) 278-291.

177. R. Larn and J. Yang, "The effect of compressive deformation of austenite on the Widmanstätten ferrite transformation in Fe–Mn–Si–C steel," Materials Science and Engineering: A, 264 (1999) 139-150.

178. P. Shipway and H. Bhadeshia, "Mechanical stabilisation of bainite," Materials science and technology, 11 (1995) 1116-1128.

179. S. Singh and H. Bhadeshia, "Quantitative evidence for mechanical stabilization of bainite," Materials science and technology, 12 (1996) 610-612.

180. S. Chatterjee et al., "Mechanical stabilisation of austenite," Materials Science and Technology, 22 (2006) 641-644.

181. W.C. Leslie and R.L. Miller, "The stabilization of austenite by closely spaced boundaries," ASM Trans. Q., 57 (1964) 972-979.

182. E.S. Machlin and M. Cohen, "Burst phenomenon in the martensitic transformation," Trans. AIME, 191 (1951) 746-754.

189

183. R.W.K. Honeycombe, "The plastic deformation of metals," (1975).

184. H. Bhadeshia, "A rationalisation of shear transformations in steels," Acta Metallurgica, 29 (1981) 1117-1130.

185. D. Hughes et al., "Geometrically necessary boundaries, incidental dislocation boundaries and geometrically necessary dislocations," Scripta Materialia, 48 (2003) 147-153.

186. A. Taylor et al., "Orientation dependence of the substructure characteristics in a Ni–30Fe austenitic model alloy deformed in hot plane strain compression," Acta materialia, 60 (2012) 1548-1569.

187. M. Ashby, "The deformation of plastically non-homogeneous materials," Philosophical Magazine, 21 (1970) 399-424.

188. S. Babu and H. Bhadeshia, "Mechanism of the transition from bainite to acicular ferrite," Materials Transactions, JIM(Japan), 32 (1991) 679-688.

189. M. Díaz-Fuentes and I. Gutiérrez, "Analysis of different acicular ferrite microstructures generated in a medium-carbon molybdenum steel," Materials Science and Engineering: A, 363 (2003) 316-324.

190. G. Miyamoto et al., "Variant selection of lath martensite and bainite transformation in low carbon steel by ausforming," Journal of Alloys and Compounds, (2012).

191. N. Isasti et al., "Effect of Composition and Deformation on Coarse-Grained Austenite Transformation in Nb-Mo Microalloyed Steels," Metallurgical and Materials Transactions A, 42 (2011) 3729-3742.

192. A. Garcia-Junceda et al., "Dependence of martensite start temperature on fine austenite grain size," Scripta Materialia, 58 (2008) 134-137.

193. M. Umemoto et al., "Prediction of hardenability effects from isothermal transformation kinetics," Journal of Heat Treating, 1 (1980) 57-64.

194. M. Umemoto et al., "Transformation kinetics of bainite during isothermal holding and continuous cooling," Tetsu-to-Hagane, 68 (1982) 461-470.

195. A. Matsuzaki and H. Bhadeshia, "Effect of austenite grain size and bainite morphology on overall kinetics of bainite transformation in steels," Materials Science and Technology, 15 (1999) 518-522.

196. S.-J. Lee et al., "Effect of austenite grain size on the transformation kinetics of upper and lower bainite in a low-alloy steel," Scripta Materialia, 59 (2008) 87-90.

197. J. Barford and W. Owen, "The effect of austenite grain size and temperature on the rate of bainita transformation," Metal Science and Heat Treatment, 4 (1962) 359-360.

198. G. Rees and H. Bhadeshia, "Bainite transformation kinetics Part 1 Modified model," Materials Science and Technology, 8 (1992) 985-993.

199. E. Davenport et al., "Influence of Austenite Grain Size upon Isothermal Transformation Behavior of SAE 4140 Steel," Trans. AIME, 145 (1941) 301.

200. G. Xu et al., "A new approach to quantitative analysis of bainitic transformation in a superbainite steel," Scripta Materialia, 68 (2013) 833-836.

201. R. Farrar et al., "The effect of prior austenite grain size on the transformation behaviour of C-Mn-Ni weld metal," Journal of materials science, 28 (1993) 1385-1390.

202. Standard Test Methods for Determining Average Grain Size, ASTM International, 2013.

203. T. Furuhara et al., "Key factors in grain refinement of martensite and bainite," Materials Science Forum, 638 (2010) 3044-3049.

204. V. Pancholi et al., "Self-accommodation in the bainitic microstructure of ultra-high-strength steel," Acta Materialia, 56 (2008) 2037-2050.

205. L. Rancel et al., "Measurement of bainite packet size and its influence on cleavage fracture in a medium carbon bainitic steel," Materials Science and Engineering: A, 530 (2011) 21-27.

206. J. Guimarães and J. Gomes, "A metallographic study of the influence of the austenite grain size on martensite kinetics," Acta Metallurgica, 26 (1978) 1591-1596.

207. M. Umemoto and W. Owen, "Effects of austenitizing temperature and austenite grain size on the formation of athermal martensite in an iron-nickel and an iron-nickel-carbon alloy," Metallurgical transactions, 5 (1974) 2041-2046.

208. S. Mujahid and H. Bhadeshia, "Partitioning of carbon from supersaturated ferrite plates," Acta metallurgica et materialia, 40 (1992) 389-396.

209. S. Lee et al., "Transformation strengthening by thermomechanical treatments in C-Mn-Ni-Nb steels," Metallurgical and Materials Transactions A, 26 (1995) 1093-1100.

210. T. Kvackaj and I. Mamuzic, "A quantitative characterization of austenite microstructure after deformation in nonrecrystallization region and its influence on ferrite microstructure after transformation," ISIJ international, 38 (1998) 1270-1276.

211. N. Hansen and B. Ralph, "The strain and grain size dependence of the flow stress of copper," Acta Metallurgica, 30 (1982) 411-417.

212. H. Mecking and U. Kocks, "Kinetics of flow and strain-hardening," Acta Metallurgica, 29 (1981) 1865-1875.

213. R. Cochrane, "The effect of second-phase particles on the mechanical properties of steel," The Iron and Steel Institute, (1971) 101-106.

214. J.J. Jonas et al., "The Avrami kinetics of dynamic recrystallization," Acta Materialia, 57 (2009) 2748-2756.

215. J.J. Jonas, "Transformation textures associated with steel processing," Microstructure and Texture in Steels,ed. Springer,(Springer, 2009), 3-17

216. J. Rasti et al., "Influence of grain size on the dynamic recrystallization behavior of AISI 304 stainless steel during hot deformation," International Journal of Materials Research, 103 (2012) 483-489.

217. A. Dehghan-Manshadi and P. Hodgson, "Dependency of recrystallization mechanism to the initial grain size," Metallurgical and Materials Transactions A, 39 (2008) 2830-2840.